CENTRIFUGE CRATER SCALING EXPERIMENT II

Material Strength Effects

AD A106424

Boeing Aerospace Company
P.O. Box 3999
Seattle, Washington 98124

1 May 1979

Interm Report for Period 31 January 1978—31 January 1979

CONTRACT No. DNA 001-78-C-0149

> APPROVED FOR PUBLIC RELEASE;
> DISTRIBUTION UNLIMITED.

DTIC
ELECTE
NOV 2 1981

A

DTIC FILE COPY

Prepared for
Director
DEFENSE NUCLEAR AGENCY
Washington, D. C. 20305

REPORT DOCUMENTATION PAGE	READ INSTRUCTIONS BEFORE COMPLETING FORM

1. REPORT NUMBER	2. GOVT ACCESSION NO.	3. RECIPIENT'S CATALOG NUMBER
DNA 4999Z	AD-A106 422	

4. TITLE (and Subtitle)	5. TYPE OF REPORT & PERIOD COVERED
CENTRIFUGE CRATER SCALING EXPERIMENT II. Material Strength Effects	Report, for Period 1 Jan 79
	6. PERFORMING ORG. REPORT NUMBER

7. AUTHOR(s)	8. CONTRACT OR GRANT NUMBER(s)
R. M. Schmidt	
K. A. Holsapple	DNA 001-78-C-0149

9. PERFORMING ORGANIZATION NAME AND ADDRESS	10. PROGRAM ELEMENT, PROJECT, TASK AREA & WORK UNIT NUMBERS
Boeing Aerospace Company P.O. Box 3999 Seattle, Washington 98124	Subtask Y99QAXSD070-42

11. CONTROLLING OFFICE NAME AND ADDRESS	12. REPORT DATE
Director Defense Nuclear Agency Washington, D.C. 20305	1 May 1979
	13. NUMBER OF PAGES
	176

14. MONITORING AGENCY NAME & ADDRESS(if different from Controlling Office)	15. SECURITY CLASS. (of this report)
	UNCLASSIFIED
	15a. DECLASSIFICATION DOWNGRADING SCHEDULE N/A

16. DISTRIBUTION STATEMENT (of this Report)

Approved for public release; distribution unlimited.

17. DISTRIBUTION STATEMENT (of the abstract entered in Block 20, if different from Report)

18. SUPPLEMENTARY NOTES

19. KEY WORDS (Continue on reverse side if necessary and identify by block number)

Accelerated Frame Testing	Crater Scaling	PETN
Alluvium	Dimensional Analysis	Saturated Sand
Centrifuge	Gravity-Scaling	Similitude Requirements
Cratering	Lead Azide	Soil Material Strength
Crater Aspect Ratio	Ottawa Sand	Soil Moisture Content

20. ABSTRACT (Continue on reverse side if necessary and identify by block number)

Direct simulation of large-scale explosive events can be performed at subscale using the elevated gravity field of a centrifuge. This technique allows prediction of different soil-media effects in a well-controlled manner over many orders of magnitude in explosive energy. Cratering experiments were conducted in desert alluvium, dry Ottawa sand, saturated sand, and an oil-base clay. Both lead-azide and pentaerythritol-tetra-

DD FORM 1473 EDITION OF 1 NOV 65 IS OBSOLETE
1 JAN 73

20. ABSTRACT (Continued)

nitrate (PETN) explosives were used. These various experiments incorporated large differences in explosive specific energy Q_e, soil cohesion c, soil angle of internal friction ϕ, charge weight W and gravitational acceleration, g. Experimental results show substantial differences in cratering phenomena.

The gravity-scaled yield $[\pi_2 = (g/Q_e)(W/\delta)^{1/3}]$, previously used to correlate centrifuge cratering results in dry Ottawa sand, has been modified to accurately account for the effects of variations in c and ϕ. When cratering efficiency is plotted as a function of this strength-gravity-scaled yield $\bar{\pi}_2$, all experimental results fall on a single curve.

These results show that at small actual yields soil cohesion dominates the cratering process. At larger yields, the cohesion has little effect, but the angle of internal friction becomes an important variable because of the large overburden. The behavior of a material such as alluvium, having nonzero values for both c and ϕ, shows cube-root scaling at low yields but becomes asymptotic to dry sand behavior at large yields. Neither behaves as a zero-strength material, and neither shows quarter-root scaling for scaled yields approaching megatons of TNT.

SUMMARY

The use of increased gravity as a necessary and sufficient condition to correctly simulate large-scale cratering events with small laboratory experiments was theoretically and experimentally verified in the previous year's work. During that program cratering experiments were carried out for a range of almost 11 decades of gravity-scaled energy in dry Ottawa sand. In addition, a highly successful simulation of the JOHNIE BOY nuclear event was performed by a combination of a nuclear high-explosive (HE) equivalence generated by a code calculation, together with the small-scale simulation of the resulting HE event on the centrifuge.

The program reported here was intended to investigate variations in cratering phenomena due to differing cratering media. In particular, parts of the program included:

1) a series of experiments in a nominal 4-percent moisture desert alluvium over the maximum gravity-scaled energy range of about 11 decades,

2) experiments in alluvium with moisture content from near zero to 7-1/2 percent,

3) experiments in a fully saturated, dense Ottawa sand, and

4) experiments in an oil-base modeling clay.

All of the experiments were conducted with half-buried spherical charges.

In addition to the experimental program, supporting theoretical analyses were conducted to organize and interpret the experimental results and to generate a rational prediction method for other materials. A theory was constructed which correlates the experimental results using a single gravity-size-strength parameter, $\bar{\pi}_2$. This parameter correctly measures the equivalence of all combinations of gravity, charge size, medium and charge properties considered.

The theory identifies two distinct regimes. For a given soil and charge type, a cohesion-dominated regime exists for small charge size. In this regime, cube-root scaling of crater volume is predicted. The value of the cratering efficiency in this regime depends directly on the cohesion of the

1

material. If cohesion is zero, such as for dry granular materials, this regime is not observed.

A transition to a lithostatic-pressure-dominated regime occurs at a value of charge size which depends upon the relation between the cohesion and the angle of internal friction. For charge sizes sufficiently larger than this value, the cratering efficiency decreases with increasing charge size. This decrease approaches a straight line on a log-log plot. However, a decrease to the classical "quarter-root" scaling, suggested in the literature, is not observed. This failure is attributed to the dependence of the coupling efficiency on the specific energy of the explosive and on the other variables included in the theory.

The results of this program illustrate the utility of the centrifuge as a tool to explore the dependence of cratering phenomena on a multitude of parameters in a precise and inexpensive way. The results of the desert alluvium experiments explain the discrepancy between the small-scale experiments at 1 G and the large field shots, and furthermore clarify the variations found in 1-G experiments in different materials such as saturated sand.

PREFACE

The authors would like to thank CDR T. J. Deevy of the Defense Nuclear Agency who was the technical monitor for this program. His keen interest and enthusiasm contributed to the success of the endeavor. We would also like to acknowledge and thank C. R. Wauchope of The Boeing Aerospace Company for his tireless work on the data reduction task including all the plots, tables and artwork in this report.

TABLE OF CONTENTS

LIST OF ILLUSTRATIONS

LIST OF ILLUSTRATIONS (Continued)

LIST OF TABLES

SECTION 1

INTRODUCTION

Crater size and shape depends upon both the soil type and the explosive type for a fixed source geometry. Differences are attributed to the influence of material properties. Significant variations have been observed in the many field experiments in materials ranging from water, on one extreme, to granite, on the other, and for energy sources consisting of various high explosives, nuclear explosives, and hypervelocity-impact projectiles.

The data scatter inherent in large-scale field events has made it difficult to determine quantitatively how medium and source properties affect cratering mechanisms. On the other hand, the more precise laboratory tests at small scale do not always reproduce the phenomenology of large scale events.

Previous results of a theoretical and experimental program (Schmidt and Holsapple, 1978a) demonstrate that large explosive events can be directly simulated at small scale, if the test is performed at elevated gravity. These conditions are obtained by performing the experiments on a centrifuge, with a gravity variation from 10 to greater than 500 G. Both theoretical and experimental results verify that, for large- and small-scale tests performed in the same material with the same explosive, all aspects of the cratering phenomena are correctly simulated. A possible anomalous effect of centrifuge testing, e.g., Coriolis force, has not proven to be significant. The energy of the simulated large-scale test is equal to g^3E, where E is the energy of the small-scale test conducted at elevated gravity g. Consequently, a variation of gravity from 1 to 500 G allows a simulation of explosive events over a range of $(500)^3 = 125 \times 10^6$, or more than 8 decades of energy.

Extending this earlier work, experiments were successfully performed in both dry and wet Ottawa sand, desert alluvium of various moisture content, and an oil-base clay during the current program. Both lead-azide (PbN_6) and PETN explosive charges were used. These experiments gave data over a large range of soil strengths, explosive properties, charge mass and gravitational acceleration. The cratering results are reproducible and consistent with existing field events. These data, together with a consideration of the variations in material properties and energy sources, provide an empirical base for the construction of a theory that predicts the effects of media strength and energy-source properties on crater volume, radius and depth.

9

SECTION 2
EXPERIMENTAL RESULTS

2-1   CENTRIFUGE DESCRIPTION

The Boeing 600-G geotechnical centrifuge was used in this study. This machine has a dynamic load rating of 60,000 G-kg (66 G-tons) at 620 rpm and was constructed using the aerodynamic housing and main shaft assembly from a Gyrex Model 2133 centrifuge. The rotor was designed and fabricated by the Boeing Company to incorporate symmetric swing baskets for geotechnic applications. The arm radius to the fully extended base plate is 139.7 cm. The maximum payload mass is 250 kg on each rotor end. An overall view is shown in Fig. 2.1; the details of the swing basket and soil-sample container are shown in Fig. 2.2. Power is provided by a 30-horsepower Eaton Dynamatic Model ACM-326-910B drive unit incorporating an adjustable speed, constant-torque eddy-current clutch. The unit has electrical dynamic braking, allowing shut-down from maximum rpm in less than 30 seconds. The constant speed motor and variable drive unit are shock mounted and coupled to the main shaft with a belt to minimize vibration.

The rotor shaft is equipped with 24 slip rings for instrumentation channels, three 220-V.a.c.-power slip rings and a hydraulic slip ring which can accommodate either gas or liquid. A pair of motor-driven Nikon F2 35-mm still cameras are hub-mounted in a stereo configuration. These cameras provide stereophoto coverage of the number-one rotor end with a maximum framing rate of six per second. A 16-mm movie camera is also hub-mounted and operates at up to 500 frames per second, giving movie coverage of the number-one rotor end. Illumination for all cameras is provided by three 600-watt quartz-halogen lamps. An alternate scheme uses Sylvania FF-33 long-duration (3-sec) flash lamps.

2-2   RESULTS OF SMALL-SCALE EXPERIMENTS

Various small-scale explosive experiments were performed on the centrifuge. Spherical explosive charges manufactured by the R. Stresau Laboratories of Spooner, Wisconsin were used exclusively. These included three different sizes of PETN (0.49 gm, 1.34 gm and 4.08 gm) and one of PbN_6 (1.70 gm). All were centrally initiated by applying 40 V.d.c. to a notched 0.0127-cm-diameter tungsten wire. The PETN charges contained a nominal 0.130-gm

10

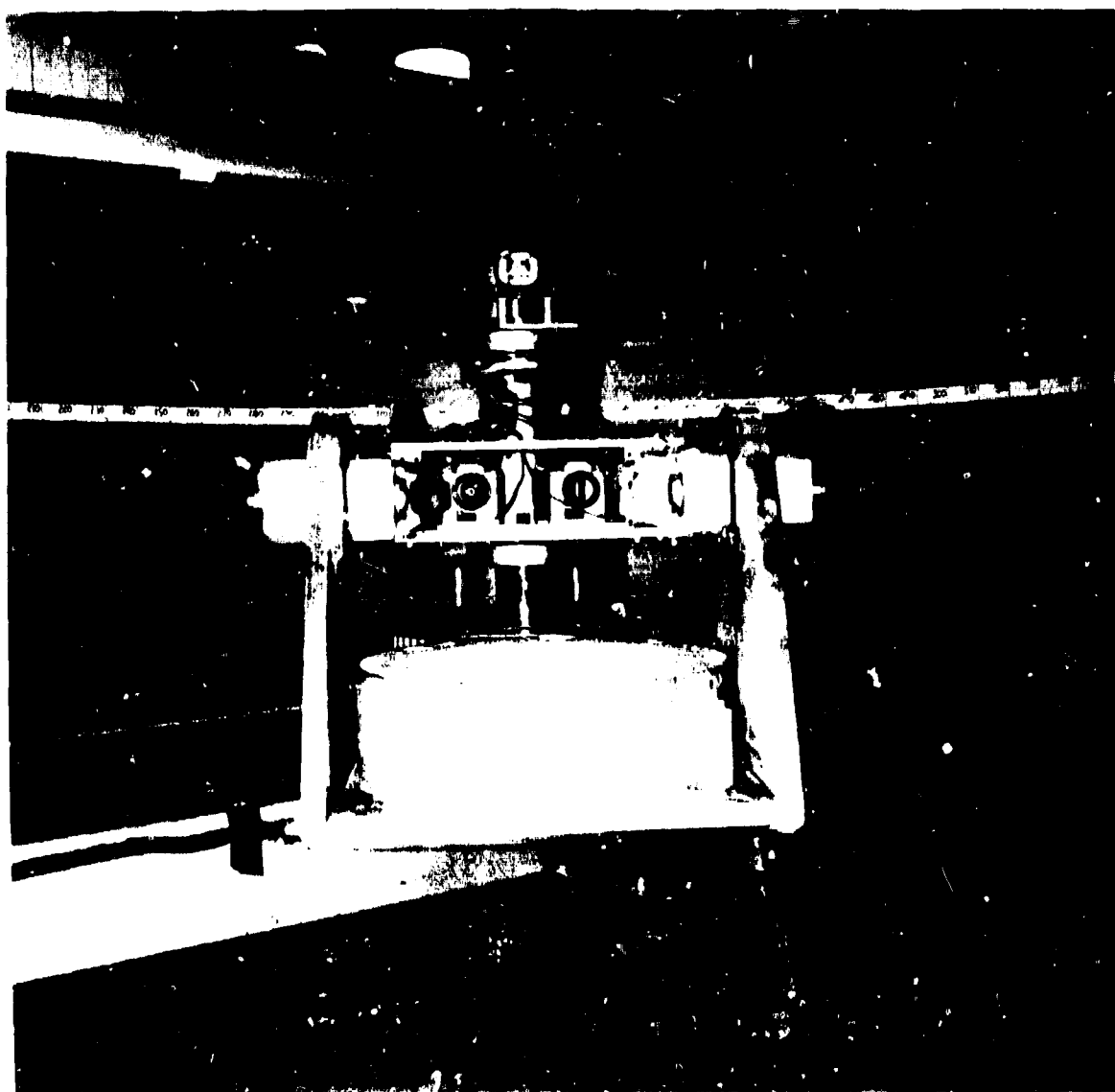Fig. 2.1   Boeing 500-G geotechnic centrifuge.

Fig. 2.2 Sample container and stereo-camera configuration.

concentric sphere of silver azide to facilitate ignition. In each test the explosive sphere was half-buried by excavating a small hole after screening the final surface on the soil sample.

The soils tested included dry Ottawa sand, desert alluvium obtained from Kirtland AFB (with moisture content from near zero up to 7.5 percent) and an oil-base modeling clay. In addition, several shots were made in a nearly saturated Ottawa sand demonstrating the feasibility of conducting such experiments. Details of the experimental technique describing soil sample preparation, determination of explosive properties, test procedure and crater measurement scheme is given by Schmidt and Holsapple (1978a).

A complete list of experimental conditions and the resulting crater dimensions is given in Tables 2.1 through 2.4. Appropriate nondimensional quantities to be used in the analysis to follow are also tabulated. The analysis of these data is considered in the following sections.

2-3   SATURATED-SAND EXPERIMENTS

The final series of shots was designed to assess the feasibility of using a centrifuge to examine cratering behavior in saturated media. Four shots in Ottawa sand at 100 G were conducted first. The first two (Run 26, Table 2.4) provided a comparison of grain size effects for comparable dense sands. Ottawa Sawing sand (nominal range of grain size 0.30-0.60 mm) was wetted to a final wet density of 2.08 gm/cc. This was contrasted to Ottawa Banding sand (nominal range of grain size 0.10-0.20 mm) that was wetted to a final wet density of 2.06 gm/cc. Identical charges consisting of 1.70 gm spheres of lead azide were half buried in each sample. The crater formed in the coarser grain Sawing sand was 2.23 times larger in volume than that produced in the Banding sand.

A Photo-Sonic 16-mm movie camera run at 400 frames/sec was used to record the shot in the coarser Sawing sand. The camera was started after the centrifuge was at the appropriate rpm just prior to firing, providing a preshot reference. The centrifuge was held at 100 G for 60 seconds after firing to observe any post-excavation shape modification, due to possible liquefaction or slumping. The 400-foot film, which recorded for 42 seconds showed no evidence of any shape change following crater formation. In addition to the movie coverage, a stereo-still-picture sequence confirms that no significant shape change took place during deceleration of the centrifuge. This is especially significant

13

Table 2.1   Summary of data for apparent crater shape in dry Ottawa sand.

Shot Number	Gravity $\frac{g}{(G)}$	Sand Type	Sand Density ρ (gm/cc)	Charge Type	Charge Mass W (gm)	Energy Release E (erg)	Specific Energy Q_0 (erg/gm)	Mass Density δ (gm/cc)	Charge Radius a (cm)	Depth of Burst d (cm)	Volume V (cc)	Radius r (cm)	Depth h (cm)	π_2 $\frac{g}{Q_0}\left(\frac{W}{\delta}\right)^{\frac{1}{3}}$	π_V $\frac{V_0}{W}$	π_r $r\left(\frac{\delta}{W}\right)^{\frac{1}{3}}$	π_h $h\left(\frac{\rho}{W}\right)^{\frac{1}{3}}$	$\bar{\pi}_2$ See Eqs. 3.26
10-X*	465	SAWING	1.774	PbN₆	1.79	2.24E10	1.32E10	3.10	0.508	0	27.1	3.87	0.89	2.82E-5	28.3	3.93	0.72	2.26E-5
10-O	463	SAWING	1.781	PETN	0.49	2.24E10	4.54E10	1.93	0.390	0	17.1	3.56	0.71	6.33E-6	62.2	5.47	1.09	5.06E-4
11-X	451	FLINTSHOT	1.776	PETN	1.34	7.18E10	5.34E10	1.78	0.565	0	35.1	4.38	0.99	7.54E-6	46.7	4.82	1.09	6.03E-4
11-O	451	FLINTSHOT	1.781	PETN	1.34	7.18E10	5.34E10	1.78	0.565	0	38.0	4.37	0.97	7.54E-6	50.5	4.74	1.07	6.03E-4
12-X	451	BANDING	1.677	PETN	4.08	2.27E11	5.56E10	1.73	0.826	0	96.3	6.33	1.28	1.06E-5	39.6	4.71	0.95	8.48E-4
12-O	451	FLINTSHOT	1.778	PETN	4.08	2.27E11	5.56E10	1.73	0.826	0	101.0	6.41	1.31	1.06E-5	44.0	4.86	0.99	8.48E-4
13-X	306	BANDING	1.677	PETN	4.08	2.27E11	5.56E10	1.73	0.826	0	119.0	6.65	1.56	7.19E-6	48.9	4.94	1.16	5.75E-4
13-O	306	FLINTSHOT	1.782	PETN	4.08	2.27E11	5.56E10	1.73	0.826	0	128.0	6.88	1.37	7.19E-6	55.0	5.22	1.04	5.75E-4
15-X	10	FLINTSHOT	1.784	PETN	0.49	2.24E10	4.54E10	1.93	0.390	0	94.8	6.40	1.23	1.37E-7	345.	9.85	1.94	1.10E-7
15-O	10	FLINTSHOT	1.784	PETN	0.49	2.24E10	4.54E10	1.93	0.390	0	95.2	6.40	1.27	1.37E-7	347.	9.85	1.95	1.10E-7
UDRI-9**	1	FLINT HOT	1.802	PbN₆	1.70	2.24E10	1.32E10	3.10	0.508	0	436.0	10.20	2.29	6.08E-8	462.	10.4	2.33	4.86E-8
UDRI-22	1	FLINTSHOT	1.802	PbN₆	1.70	2.24E10	1.32E10	3.10	0.508	0	420.0	10.10	2.35	6.08E-8	445.	10.3	2.40	4.86E-8
UDRI-117	1	FLINTSHOT	1.802	PETN	0.49	2.24E10	4.54E10	1.93	0.390	0	274.0	8.76	2.06	1.37E-8	1008.	13.5	3.18	1.10E-8
UDRI-120	1	FLINTSHOT	1.796	PETN	0.49	2.24E10	4.54E10	1.93	0.390	0	292.0	8.88	2.13	1.37E-8	1070.	13.7	3.28	1.10E-8
UDRI-146	1	FLINTSHOT	1.796	PETN	0.49	2.24E10	4.54E10	1.93	0.390	0	284.0	8.89	2.02	1.37E-8	1041.	13.7	3.11	1.10E-8
UDRI-642	1	FLINTSHOT	1.802	PETN	1.34	7.18E10	5.34E10	1.78	0.565	0	640.0	11.80	2.50	1.67E-8	861.	13.0	2.76	1.34E-8
UDRI-644	1	FLINTSHOT	1.802	PETN	1.34	7.18E10	5.34E10	1.78	0.565	0	706.0	12.00	2.66	1.67E-8	949.	13.2	2.94	1.34E-8
UDRI-643	1	FLINTSHOT	1.802	PETN	4.08	2.27E11	5.56E10	1.73	0.826	0	1677.0	16.30	3.39	2.35E-8	741.	12.4	2.58	1.88E-8
UDRI-645	1	FLINTSHOT	1.802	PETN	4.08	2.27E11	5.56E10	1.73	0.826	0	1751.0	16.40	3.54	2.35E-8	773.	12.5	2.76	1.88E-8

*Schmidt & Holsapple (1978a)

**A.J. Piekutowski (1974, 1975 and unpublished data)

14

Table 2.2   Summary of data for apparent crater shape in KAFB desert alluvium.

Shot Number	Gravity g/G	Moisture Content w (%)	Soil Density ρ (gm/cc)	Charge Type	Charge Mass W (gm)	Energy Release E (erg)	Specific Energy Q_e (erg/gr)	Mass Density δ (gm/cc)	Charge Radius a (cm)	Depth of Burst d (cm)	Volume V (cc)	Radius r (cm)	Depth h (cm)	π_g $g\left(\frac{W}{Q_e}\right)^{1/3}$	π_v $\frac{V\delta}{W}$	π_r $r\left(\frac{\delta}{W}\right)^{1/3}$	π_h $h\left(\frac{\delta}{W}\right)^{1/3}$	$\frac{\pi_h}{\pi_r}$ See Eqs. 3.26
UDRI-646	1	~4.0	1.622	PbN6	1.70	2.24 E10	1.32 E10	3.10	0.508	0	58.7	6.47	1.85	6.08 E-8	56.0	6.37	1.82	7.98 E-6
UDRI-647	1	~4.0	1.581	PbN6	1.70	2.24 E10	1.32 E10	3.10	0.508	0	72.4	6.90	1.95	6.08 E-8	67.3	6.74	1.90	8.19 E-6
UDRI-648	1	~4.0	1.600	PbN6	1.70	2.24 E10	1.32 E10	3.10	0.508	0	45.0	5.84	1.75	6.08 E-8	42.4	5.72	1.71	8.09 E-6
UDRI-649	1	~4.0	1.57	PETN	1.34	7.18 E10	5.34 E10	1.78	0.565	0	103.0	6.88	2.40	1.67 E-8	121.0	7.25	2.53	2.04 E-6
UDRI-652	1	~4.0	1.587	PETN	1.34	7.18 E10	5.34 E10	1.78	0.565	0	66.6	6.44	2.00	1.67 E-8	78.9	6.81	2.12	2.02 E-6
UDRI-650	1	~4.0	1.555	PETN	4.08	2.27 E11	5.56 E10	1.73	0.826	0	196.0	8.28	2.86	2.35 E-8	74.7	6.00	2.57	1.98 E-6
UDRI-651	1	~4.0	1.584	PETN	4.08	2.27 E11	5.56 E10	1.73	0.826	0	175.0	8.52	2.90	2.35 E-8	67.9	6.22	2.54	1.95 E-6
16-X	451	~4.0	1.449	PETN	1.34	7.18 E10	5.34 E10	1.78	0.565	0	48.1	4.70	1.91	7.54 E-6	52.0	4.32	1.90	7.66 E-6
16-O	451	~4.0	1.429	PETN	1.34	7.18 E10	5.34 E10	1.78	0.565	0	51.0	4.78	2.18	7.54 E-6	54.4	4.36	2.13	7.69 E-6
17-X	451	2.7	1.607	PETN	1.34	7.18 E10	5.34 E10	1.79	0.565	0	36.2	4.22	1.58	7.54 E-6	36.2	4.43	1.43	7.45 E-6
17-O	306	2.7	1.609	PETN	4.08	2.27 E11	5.56 E10	1.73	0.826	0	96.5	5.23	1.57	1.25 E-5	38.1	4.57	1.44	7.11 E-6
19-X	345	4.2	1.576	PETN	1.34	7.18 E10	5.34 E10	1.78	0.565	0.645	116.0	6.08	2.76	5.77 E-6	136.0	6.42	2.59	6.20 E-6
19-O	345	4.1	1.570	PETN	1.34	7.18 E10	5.34 E10	1.73	0.565	0.362	77.7	5.37	2.26	5.77 E-6	91.0	5.66	2.38	6.21 E-6
20-X	10	4.0	1.579	PETN	0.49	2.24 E10	4.54 E10	1.93	0.390	0	26.1	4.61	1.28	1.37 E-7	347	6.81	1.89	2.47 E-6
20-O	10	3.9	1.582	PbN6	1.70	2.24 E10	1.32 E10	3.10	0.508	0	43.4	5.36	1.37	6.08 E-7	40.4	5.23	1.34	8.58 E-6
21-X	520	4.3	1.584	PbN6	1.70	2.24 E10	1.32 E10	3.10	0.508	0	23.7	3.69	1.58	3.16 E-5	22.1	3.60	1.54	3.70 E-5
21-O	520	4.1	1.596	PETN	4.08	2.27 E11	5.56 E10	1.73	0.826	0	103.0	5.99	2.37	1.22 E-5	40.3	4.38	1.73	1.08 E-5
23-X	93	4.0	1.570	PETN	4.08	2.27 E11	5.56 E10	1.73	0.826	0	169.3	7.52	2.50	2.78 E-6	65.7	5.47	1.82	3.53 E-6
23-O	179	3.8	1.566	PETN	0.49	2.24 E10	4.54 E10	1.93	0.390	0	19.7	3.96	1.28	2.45 E-6	61.0	5.83	1.99	4.17 E-6
24-X	306	7.5	1.657	PETN	4.08	2.27 E11	5.56 E10	1.73	0.826	0	135.8	6.10	3.25	7.19 E-6	55.2	4.52	2.41	7.26 E-6
24-O	306	<0.7	1.540	PETN	4.08	2.27 E11	5.56 E10	1.73	0.826	0	107.9	6.7	1.97	7.19 E-6	40.7	4.85	1.38	7.20 E-6

*..Preliminary unpublished data.
**Schmidt's metallurgic 1974.

Table 2.3   Summary of data for apparent crater shape in "Permoplast" oil-base clay.

Shot Number	g Gravity (G)	Test Temperature (°C)	ρ Soil Density (gm/cc)	Charge Type	W Charge Mass (gm)	E Energy Release (erg)	Q_0 Specific Energy (erg/gm)	δ Mean Density (gm/cc)	a Charge Radius (cm)	d Depth of Burst (cm)	V Volume (cc)	r Radius (cm)	h Depth (cm)	π_2 $\frac{g}{Q_0}\left(\frac{W}{\delta}\right)^{1/3}$	π_V $\frac{V\rho}{W}$	π_r $r\left(\frac{\rho}{W}\right)^{1/3}$	π_h $h\left(\frac{\rho}{W}\right)^{1/3}$	π_t See Eqn. 3.26
14-X	309	22.8	1.53	PETN	4.04	2.77 E11	5.56 E10	1.73	0.826	0	249.	5.91	4.22	7.26 E-6	93.4	4.26	3.04	2.22 E-6
14-O	454	22.8	1.53	PETN	1.34	7.18 E10	5.34 E10	1.78	0.565	0	85.8	4.27	2.79	7.59 E-6	98.0	4.44	2.92	2.32 E-6
22X-1	557	24.4	1.53	PbN₆	1.70	2.24 E10	1.32 E10	3.10	0.508	0	40.4	3.32	2.37	3.39 E-5	36.4	3.21	2.29	9.76 E-6
22X-2	10	24.4	1.53	PbN₆	1.70	2.24 E10	1.32 E10	3.10	0.508	0	53.4	3.24	2.92	6.08 E-7	48.1	3.13	2.82	5.77 E-6
25-X	517	23.3	1.53	PETN	4.08	2.77 E11	5.56 E10	1.73	0.826	0	150.	5.74	2.73	1.21 E-5	56.2	4.14	1.97	2.80 E-6
25-O	10	23.3	1.53	PETN	4.08	2.77 E11	5.56 E10	1.73	0.826	0	498.	6.82	6.01	2.35 E-7	187.	4.92	4.33	1.30 E-6
29-X	504	21.7	1.53	PETN	0.49	2.24 E10	4.54 E10	1.93	0.390	0	17.6	2.56	1.84	6.90 E-6	55.0	3.74	2.69	2.48 E-6
29-O	294	22.2	1.53	PETN	4.08	2.77 E11	5.56 E10	1.73	0.826	0	211.	5.70	3.77	6.90 E-6	79.1	4.11	2.72	2.18 E-6
25-X	518	~22		Test for stability of crater shape: 100 seconds at 518 G.	4.08						142.	5.72	2.53	1.22 E-5	53.2	4.12	1.82	2.77 E-6
25-O	518	~22									235.	6.77	3.23	1.22 E-5	88.1	4.88	2.33	2.77 E-6

*Schmidt & Holsapple (1979d)

16

Table 2.4   Summary of data for apparent crater shape in saturated Ottawa sand.

Shot Number	g Gravity (G)	Sand Type	ρ Wet Density (gm/cc)	Dry Density (gm/cc)	Charge Type	W Charge Mass (gm)	E Energy Release (erg)	Q_0 Specific Energy (erg/gm)	δ Mass Density (gm/cc)	a Charge Radius (cm)	d Depth of Burst (cm)	V Volume (cc)	r Radius (cm)	h Depth (cm)	$\frac{g}{Q_0}\left(\frac{W}{\delta}\right)^{1/3}$	$\frac{V\delta}{W}$	$r\left(\frac{\delta}{W}\right)^{1/3}$	$h\left(\frac{\delta}{W}\right)^{1/3}$
UDRI-375	1	Flintshot	2.13	1.81	PbN	1.70	2.24 E10	1.32 E10	3.10	0.508	0	98.0	6.78	1.51	6.08 E-8	120.	7.31	1.63
UDRI-395	1	Flintshot	2.13	1.81	PbN	1.70	2.24 E10	1.32 E10	3.10	0.508	0	95.4	6.81	1.55	6.08 E-8	120.	7.34	1.67
UDRI-406	1	Flintshot	2.13	1.81	PbN	1.70	2.24 E10	1.32 E10	3.10	0.508	0	118.	8.05	1.60	6.08 E-8	148.	8.68	1.72
UDRI-471	1	Flintshot	2.13	1.81	PbN	1.70	2.24 E10	1.32 E10	3.10	0.508	0	104.	7.74	1.48	6.08 E-8	130.	8.34	1.60
UDRI-473	1	Flintshot	2.13	1.81	PbN	1.70	2.24 E10	1.32 E10	3.10	0.508	0	82.2	6.68	1.37	6.08 E-8	103.	7.20	1.48
UDRI-514	1	Flintshot	2.13	1.81	PbN	1.70	2.24 E10	1.32 E10	3.10	0.508	0	112.	7.15	1.80	6.08 E-8	140.	7.77	1.94
26-X	100	Bumping	2.056	≈1.70	PbN	1.70	2.24 E10	1.32 E10	3.10	0.508	0	54.8	4.80	1.91	6.08 E-6	66.3	5.11	2.03
26-O	100	Sewing	2.078	≈1.73	PbN	1.70	2.24 E10	1.32 E10	3.10	0.508	0	122.	6.88	2.09	6.08 E-6	149.	7.36	2.23
27-X	100	Flintshot	2.113	1.802	PbN	1.70	2.24 E10	1.32 E10	3.10	0.508	0	86.6	6.09	1.78	6.08 E-6	108.	6.55	1.91
27-O	100	Flintshot	2.113	1.802	PbN	1.70	2.24 E10	1.32 E10	3.10	0.508	0	73.8	6.03	1.77	6.08 E-6	91.7	6.48	1.90
28-X	10	Flintshot	2.109	1.792	PbN	1.70	2.24 E10	1.32 E10	3.10	0.508	0	67.5	5.81	1.45	6.08 E-7	83.7	6.24	1.56
28-O	520	Flintshot	2.107	1.798	PbN	1.70	2.24 E10	1.32 E10	3.10	0.508	0	34.1	4.68	1.13	3.16 E-5	42.3	5.03	1.21

*A.J. Piekutowski (unpublished data)

**Z diameter only

17

because the water table goes through a shape change as the sample is accelerated from 1-G conditions. In the centrifuge environment the water conforms to a cylindrical geopotential surface, whereas the sand surface remains flat. Therefore to achieve a water table that is tangent to the ground surface at shot point (127.1 cm from the centrifuge axis), the sand surface must be 2.1 cm below the rim of the 46-cm-diameter container. Under these conditions the water table, initially sufficiently above the sand surface, will contour and become tangent to the surface along the diameter of the sample that is parallel to the centrifuge axis of rotation. Excess water will run over the edge. An alternative to this configuration would be to contour the sand surface to conform to the cylindrical geopotential surface. In either case, however, there will be a relative motion of the water as the centrifuge rotor accelerates from rest. For large enough arm radius, this curvature effect can be neglected as long as the relative water motion does not disturb the sand upon start up or shut down of the centrifuge.

The second pair of shots (Run 27, Table 2.4) was a carefully controlled reproducibility test. Ottawa Flintshot sand was pluviated to a dry density state of 1.802 gm/cc. Water was carefully added to provide a final wet density of 2.113 gm/cc. Within the accuracy of these measurements and an assumed grain specific gravity of 2.65 gm/cc, the degree of saturation was greater than 97 percent. The goal was to achieve sand states comparable to those of Piekutowski (unpublished data) allowing direct comparison of the centrifuge data.

The results indicate a high degree of reproducibility. The crater radius and the crater depth were within 1 percent, respectively, for the two craters. The crater volumes differed from each other by 15 percent. The coefficient of variation (c.o.v.) for the two 100-G centrifuge shots was ± 11 percent. This compares favorably with c.o.v. of ± 13 percent for the six 1-G shots performed by Piekutowski. Considering the complexity of charge placement and other experimental constraints, associated with the centrifuge, these results indicate that cratering experiments in saturated (or nearly saturated) media can be satisfactorily performed at high G in the centrifuge. On Run 27 the movie camera framing rate was 50 per second permitting sufficient recording time to follow the deceleration phase, confirming the observations of the previous run regarding crater stability.

The final pair of shots extended the range of gravity variation to 500 G and provided a data point at 10 G. Some water wave washing of the crater was

18

observed on the movie coverage of the 10-G shot (28-X). This filled in the crater somewhat creating the asymmetry seen in the profile plots in Appendix A.

2-4   STRESS-WAVE MEASUREMENTS

A series of soil-stress measurements were made using carbon gages placed at known distances from the explosive charge. Thirteen shots were made under various operating conditions. Some were fired with the centrifuge not running. These provided a check on the slip rings in the static condition versus direct connection to the oscilloscope, bypassing the rings. Six stress gage shots were made with the centrifuge in operation at 200 G and at 500 G. These were in addition to the crater formation shots discussed below.

About half of the shots were successful in producing stress profiles. The remaining shots failed due to premature trigger problems due to electrical coupling in the slip ring circuitry from the charge firing current. A 3-mm diameter piezo pin in contact with the charge works very well as a scope trigger and provides a reliable time reference for shock initiation into the soil. From this preliminary series of tests, it is concluded that dynamic on-board measurements can be made. Appropriate calibration methods need to be developed. This includes not only stress amplitude but a technique to place the gage without disturbing the sample as well as knowing its exact location. The slip ring transmission appears adequate but cross talk and electrical noise can be a problem under some circumstances. This can be eliminated using on-board recording systems which are currently under development.

2-5   SOIL MATERIAL PROPERTY TESTS

To facilitate the correlation of cratering with soil material properties, certain laboratory tests were performed. The bulk of the tests were performed under subcontract to Shannon and Wilson, Inc., Geotechnic Consultants, Seattle, WA. These consisted of unconsolidated-undrained triaxial tests and also some direct shear tests. The reported laboratory test data supplied by Shannon and Wilson are included in Appendix B.

Mechanical property data were obtained for Kirtland Air Force Base (KAFB) alluvium at various moisture contents, dry Ottawa sand of three different grain sizes and Permoplast oil-base clay. Two series of triaxial tests were

performed, the first was conducted at high confining pressures, up to 27.5 bars. A second series was performed at lower confining pressures, on the order of 1.4 bars and lower. From these latter tests, soil cohesion and angle of internal friction were determined for use in the analytical model for crater volume (developed in Section 3), incorporating soil material properties. The direct shear tests were performed to bracket the zero-confining-pressure cohesion intercept. These values are considerably lower than the extrapolated intercept from the low-pressure triaxial tests. This may be due in part to the nonuniform stress state encountered in this type of test. For calculational purposes, the direct shear values were assumed to be a lower limit for the cohesion and the low-pressure triaxial test to be an upper bound. The high-pressure triaxial tests show some reduction of tan ϕ, which is commonly observed for soils. Representative values for all three soil types are given in Sections 3 and 5. The actual test results are included in Appendix B.

SECTION 3

A MATERIAL STRENGTH MODEL FOR CRATER VOLUME

3-1 DIMENSIONLESS PARAMETERS

The basis for direct simulation of large field events using small laboratory experiments at large gravity results from an analysis of the similarity requirements between the two experiments. A complete similarity analysis of the governing equations of continuum mechanics in their general form has been presented by Schmidt and Holsapple (1978a, 1980) and will not be reproduced here. When restricted to experiments with a finite set of governing variables, a set of dimensionless parameters can be derived. Two experiments are similar when each of these dimensionless parameters has the same value for both experiments.

For the application here, consider the case of a half-buried (zero depth of burst) spherical explosive detonated in a homogeneous soil medium. The dependent variable of interest is the apparent crater volume V. It is assumed to depend on soil density ρ, soil strength Y, explosive mass W, explosive specific energy Q_e, explosive mass density δ, and gravity g. Furthermore, a Mohr-Coulomb strength model for soil is assumed

$$Y = c + P \tan \phi \tag{3.1}$$

so that the strength Y under confining pressure P is determined by the cohesion c and the angle of internal friction ϕ. Therefore, the dependent variable V is assumed to be determined by seven independent variables, ρ, c, ϕ, W, Q_e, δ, g, for a total of eight variables. These eight variables can be formed into five dimensionless groups defined and referred to as follows:

$$\pi_v = \frac{V\rho}{W} \qquad \text{(cratering efficiency)} \tag{3.2a}$$

$$\pi_2 = \frac{g}{Q_e} \left(\frac{W}{\delta}\right)^{1/3} \qquad \text{(gravity-scaled yield)} \tag{3.2b}$$

$$\pi_3 = \frac{\rho}{\delta} \qquad \text{(mass density ratio)} \tag{3.2c}$$

21

$$\pi_4 = \frac{c}{\rho Q_e} \qquad \text{(cohesion parameter)} \qquad (3.2d)$$

$$\pi_5 = \tan \phi \qquad \text{(internal friction parameter)} \quad (3.2e)$$

Therefore, the dependent pi-group π_v must be determined by the remaining four,

$$\pi_v = F (\pi_2, \pi_3, \pi_4, \pi_5) . \qquad (3.3)$$

For a given soil-explosive combination, π_3, π_4 and π_5 are fixed, and π_v becomes a function solely of π_2. Two experiments in the same material using the same explosive are similar whenever π_2 has the same value and they will have the same value for the cratering efficiency π_v. These two experiments can differ in explosive mass W and in gravity g, but, in order to be similar, the product $g^3 W$ must be the same. Thus, an experiment with four grams of explosive at 500 G is similar to and directly simulates an experiment of 500 tons of the same explosive at 1 G.

The function F in Eq. 3.3 can be determined using experimental results and its dependence upon the explosive and the soil properties is the focus of this report. The differences in the observed π_2 dependence for the various soil-explosive pairs determine the influence of the material property parameters π_3, π_4 and π_5. The form of this latter dependence is suggested by a consideration of the fundamental physics of the phenomena, as will be shown.

3-2   EFFECTS OF MATERIAL STRENGTH AND EXPLOSIVE PROPERTIES

A theory that unifies the experimental results presented in Fig. 3.1 is desired. This theory must account for and quantify the variations due to medium and explosive properties.

The previously identified variables segregating the different materials include the density ρ, cohesion c and angle of internal friction ϕ of the soil medium, and the density δ and specific energy Q_e of the explosive. These variables enter into the three dimensionless pi-groups π_3, π_4 and π_5.

The process of cratering by a high explosive is a complex result of the kinematics and dynamics initiated by the detonation. This detonation
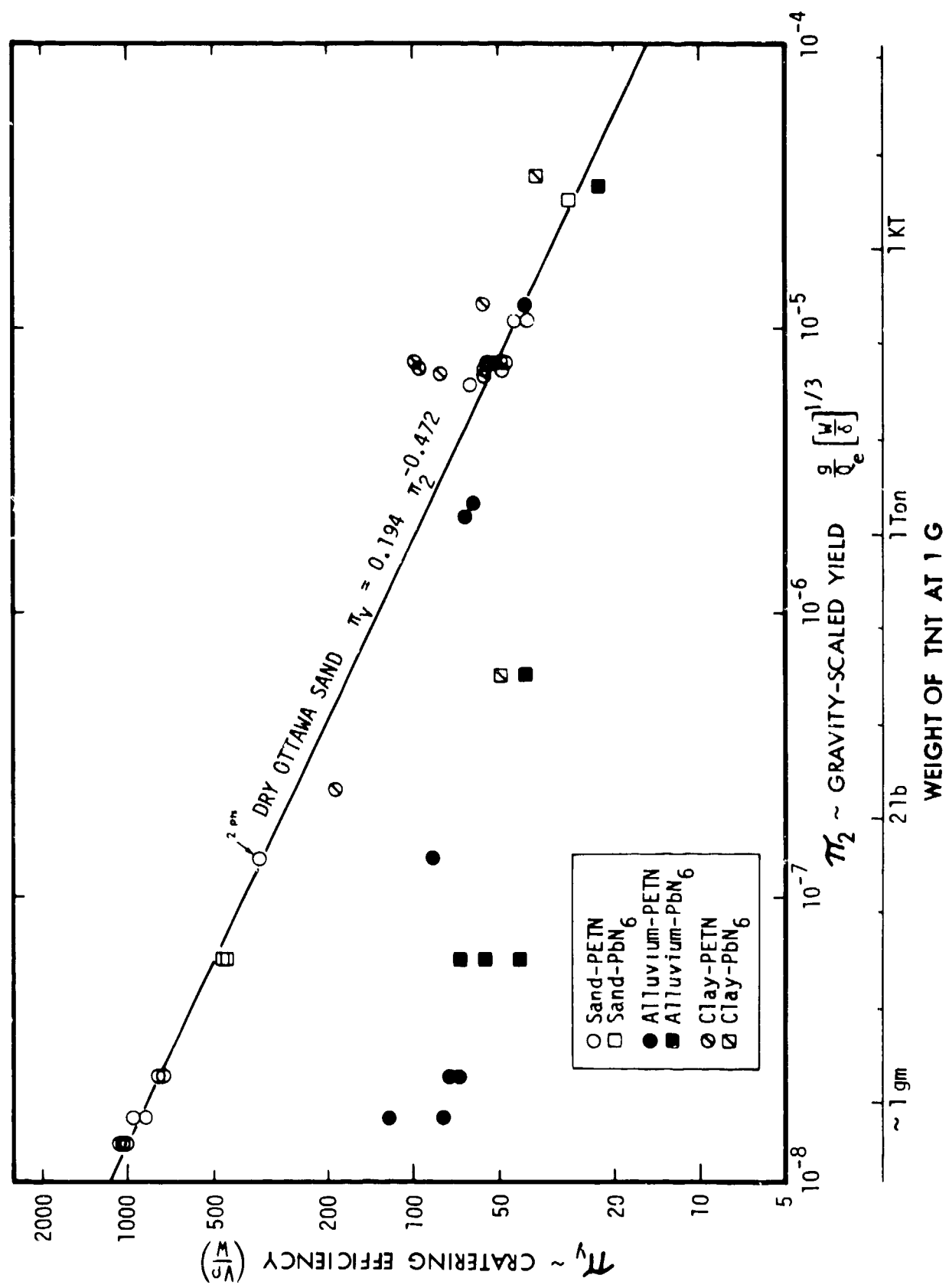
22

Fig. 3.1 Cratering efficiency versus gravity-scaled yield for various soil-explosive combinations.

process is commonly modeled as a shock propagating through the explosive, with the detonation products assumed to behave as a perfect gas. The pressure behind the shock is given by the Chapman-Jouguet pressure

$$P_{CJ} = 2(\gamma - 1)\delta Q_e \qquad (3.4)$$

where γ, the ratio of the specific heats, is taken to be constant.

The effects of this shock on the soil can be studied by considering an energy balance for that material. The equation expressing the balance of mechanical and thermodynamic energy for the motion of a general continuum can be written as (Truesdell and Toupin 1960)

$$\Delta(KE) = \int_0^t P dt + \int_0^t Q dt - \Delta(IE) \qquad (3.5)$$

with

$$P = \oint_S \vec{t} \cdot \vec{v} \, da + \int_R \rho \vec{b} \cdot \vec{v} \, dv \qquad (3.6)$$

$$Q = \int_R \rho \, r \, dv - \oint_S \vec{q} \cdot \vec{n} \, da, \qquad (3.7)$$

and where the symbols are defined as

$\Delta(KE)$: increment of kinetic energy

$\Delta(IE)$: increment of internal energy

P: rate of work due to forces

Q: rate of heating

$\vec{t}$: surface actions

$\vec{v}$: velocity of material particles

ρ: mass density

$\vec{b}$: body force per unit mass

r: internal heating rate per unit mass

$\vec{q}$: heat flux vector

da: area differential element

24

dv: volume differential element

dt: time differential

$\vec{n}$: unit vector normal to da

and R is any material region enclosed by the closed surface S.

In the present application, these equations are applied to the region of soil material excavated to create the crater, the region labeled as R in Fig. 3.2. The coupling of the source energy is via a pressure pulse transmitted across the source-soil and the air-soil interface, denoted as the surface S_1 in Fig. 3.2. Energy transport via radiation or heat conduction is inconsequential for high-explosive sources: consequently, $Q = 0$. The rate of mechanical work across this interface S_1 is given by

$$P_1 = \int_{S_1} \vec{t} \cdot \vec{v} \, da. \qquad (3.8)$$

This rate of work, integrated over the duration of the process, is that fraction of the total energy that does work on the excavated material. For near-surface events, much of the energy is released to the atmosphere. Other fractions of the total energy lost are in the shock compression and subsequent adiabatic unloading of the ground material and in the internal shearing of the material being retained as internal energy. Recognizing these loss mechanisms, it is assumed that

$$\int_0^t P_1 \, dt - \Delta(IE) = nE \qquad (3.9)$$

where E is the total energy of the explosive and n is that fraction that contributes to the crater excavation. Consequently, if S_2 denotes the interface between the excavated and the remaining soil (the crater boundary interface, Fig. 3.2), and work at the soil-air interface is ignored, then

$$nE = \Delta(KE) - \int_0^t \left[\int_{S_2} \vec{t} \cdot \vec{v} \, da + \int_R \vec{\cdot} \vec{v} \, dv \right] dt \qquad (3.10)$$

25
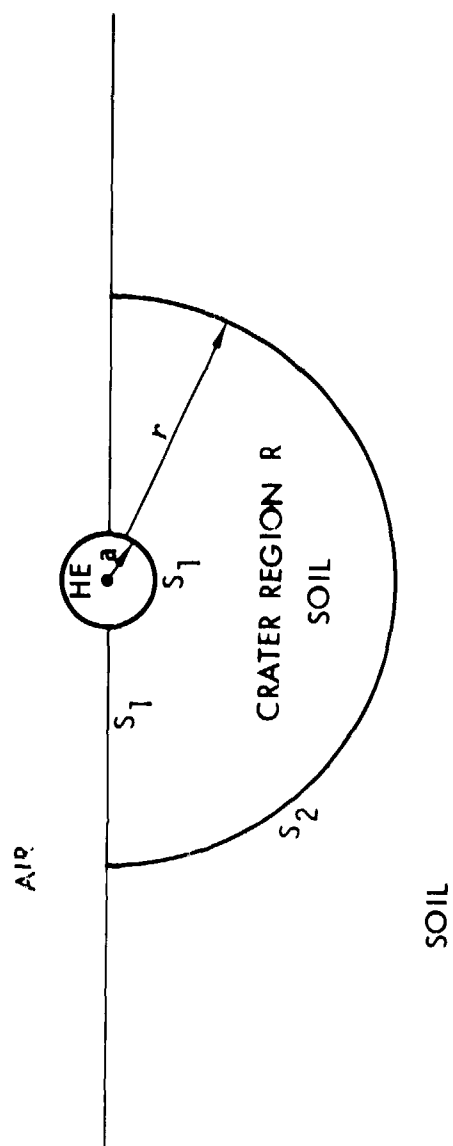
Fig. 3.2 Definition of crater region for explosive cratering.

which states that the energy nE produces an increment in kinetic energy and does work against the body forces and along the crater interface. The net change in kinetic energy is zero at the termination of the process. The work against the gravity-induced body forces can be written as an increment of potential energy. Thus,

$$nE = \Delta(PE) + W_Y \tag{3.11}$$

where
$$\Delta(PE) = -\int_0^t \left[\int_R \rho \vec{b} \cdot \vec{v} \, dv \right] dt$$

is the increment of potential energy,

and
$$W_Y = -\int_0^t \left[\int_{S_2} \vec{t} \cdot \vec{v} \, da \right] dt \tag{3.12}$$

is the work done on the excavated material at the crater boundary. This balance equation states that the energy nE goes into two parts: the change in potential energy required during the excavation and the work done as the excavated material shears along the crater boundary. Since this deformation requires overcoming the strength of the soil material, it is referred to as the work done against the material strength. This fundamental energy balance, but without the n coupling factor, was attributed to Charters and Summers (1959) and by Gault and Wedekind (1977).

The exact value of the two terms on the right in Eq. 3.11 will depend on the details of the flow field during the cratering process and on the final crater configuration. However, by using certain simplifying assumptions and considering the dimensions involved, the form of these two terms can be deduced.

In particular, it is now assumed that

1) the crater is hemispherical with radius r;
2) the work at the crater interface is proportional to the material strength Y;

27

3) the material strength Y is given by the Mohr-Coulomb model (Eq. 3.1), where c is the cohesion, P the confining pressure, and ϕ the angle of internal friction; and

4) A measure of the confining pressure P is the lithostatic pressure ρ_r at the bottom of the crater.

If the strength Y (Eq. 3.1) is substituted for the stress $\vec{t}$ in Eq. 3.12, two terms result. The first is proportional to the cohesion c and the second to tan ϕ. An integration over the crater surface S_2, taken here to be a hemisphere for convenience, will give the form:

$$W_Y = C_1(cr^3) + C_2 (\rho gr^4 \tan \phi), \qquad (3.13)$$

where C_1 and C_2 are two numerical constants which depend upon the crater geometry. The form of Eq. 3.13 is general and applies to any axi-symmetric family of crater shapes where the depth is a given fraction of the radius.

The first term results from the cohesion c acting on a surface area proportional to r^2 and shearing along a distance proportional to r. The second term is due to a confining pressure proportional to ρgr acting on the same surface that is proportional to r^2 and sheared over a distance proportional to r.

Likewise, the potential energy term is given by

$$\Lambda(PE) = C_3 \rho gr^4 . \qquad (3.14)$$

where the excavated volume is proportional to r^3, the elevation change is proportional to r and the constant C_3 is determined by the geometry of the crater shape. Consequently, the energy balance has the general form

$$\eta E = C_1 (cr^3) + C_2 (\rho gr^4 \tan \phi) + C_3(\rho gr^4). \qquad (3.15)$$

The values of C_1, C_2, and C_3 also depend on the flow field leading to the crater excavation. For example, Gault and Wedekind (1977) give a similar form, but without the η factor, or the tan ϕ term, and with values for C_1 and C_3 based upon additional simplifying assumptions.

The energy of the explosive given in terms of the charge radius, a, is

28

$$E = (4\pi/3) \ a^3 \ \delta Q_e. \tag{3.16}$$

The numerical factor, $4\pi/3$, can be combined with the other coefficients in Eq. 3.15 when Eq. 3.16 is used to get

$$\eta = \overline{C}_1 \ \frac{c}{\delta Q_e} \ (\frac{r}{a})^3 + (\frac{\rho g a}{\delta Q_e}) \ (\frac{r}{a})^4 \ (\overline{C}_2 \ \tan \phi + \overline{C}_3). \tag{3.17}$$

The dimensionless groups defined in Eqs. 3.2 can be rewritten as

$$\pi_v = \frac{V\rho}{W} = (\frac{\rho}{\delta}) \ (\frac{2\pi}{3} \ r^3) \ (\frac{4\pi}{3} \ a^3)^{-1} = \frac{1}{2} \ (\frac{\rho}{\delta}) \ (\frac{r}{a})^3 \tag{3.18a}$$

$$\pi_2 = \frac{g}{Q_e} \ (\frac{W}{\delta})^{1/3} = (\frac{4\pi}{3})^{1/3} \ \frac{ga}{Q_e} \tag{3.18b}$$

$$\pi_3 = \frac{\rho}{\delta} \tag{3.18c}$$

$$\pi_4 = \frac{c}{\rho Q_e} \tag{3.18d}$$

$$\pi_5 = \tan \phi. \tag{3.18e}$$

Therefore Eq. 3.17 can be written as

$$\eta = K_1 (\pi_4) \ (\pi_v) + (\pi_2) \ (\pi_1)^{4/3} \ (\pi_3)^{-1/3} \ (K_2 \ \pi_5 + K_3). \tag{3.19}$$

The factor $\pi_3 = \rho/\delta$, which occurs to the negative 1/3 power, does not vary significantly over the range of experiments considered here. As a simplification, it is assumed to be constant and is henceforth included in the K_2 and K_3 coefficients giving

$$\eta = K_1 \ \pi_4 \ \pi_v + (K_2 \ \pi_5 + K_3) \ \pi_2 \ \pi_v^{4/3}. \tag{3.20}$$

Equation 3.20 can be used to express π_v as a function of the other parameters π_2, π_3 and π_4, recognizing that the coupling factor η is expected to depend upon π_2, π_3 and π_4. Only after specifying this dependence is it possible

29

to determine the explicit form of the solution to this equation. However, it is instructive to consider certain limiting cases. For example, consider a series of experiments in a medium having zero cohesion c. In this case, $\pi_4 = 0$, π_5 is a constant and Eq. 3.20 reduces to

$$\pi_v \propto n^{3/4} \, \pi_2^{-3/4} \, .$$

(3.21)

For a series of experiments in a cohesionless material for a given explosive, and assuming that the efficiency n is independent of π_2,

$$V \propto E^{3/4} \, g^{-3/4} \, .$$

(3.22)

In this case, at fixed gravity, each crater linear dimension varies with the one-quarter root of the energy, often referred to as quarter-root scaling. However, experimental results (Piekutowski, 1975; Schmidt and Holsapple, 1978a, 1980) indicate that the coupling efficiency n depends upon Q_e and g; hence, n is not independent of π_2. Furthermore, it can also be expected to depend on π_3. Consequently, quarter-root scaling has not been observed for half-buried high explosive charges, even in cohesionless materials; whereas for hypervelocity impact into water, Gault (1978) obtained cratering data that approaches quarter-root scaling--1/3.83.

A second special case arises when the term with π_2 is small compared to the first term in Eq. 3.20. This occurs if either g or the charge energy E is sufficiently small, and the material has non-zero cohesion. Then, noting that π_4 is constant for a given soil-explosive combination, the cratering efficiency is proportional to the coupling factor,

$$\pi_v \propto n.$$

(3.23)

Furthermore, if n is independent of π_2 and π_3, then the cratering efficiency is constant and

$$V \propto E \, ,$$

(3.24)

resulting in the cube-root scaling.

In the general case for a soil with finite cohesion, allowing the coupling efficiency n to be a variable, the solution for the cratering efficiency π_v will be determined by all the terms in Eq. 3.20. That is

$$\pi_v = G [n, \pi_4, \pi_2 (\pi_5 + k_1)] \qquad (3.25a)$$

where $\qquad k_1 = K_3/K_2. \qquad\qquad (3.25b)$

A study of the experimental cratering data for a given soil-explosive combination shows that the results follow a consistent trend with increasing charge weight. At small values of π_2 (small charge size), the cratering efficiency π_v approaches a constant (horizontal asymptote). As π_2 increases, π_v decreases, approaching a different asymptote for large π_2. What is desired is a functional relationship that fits this general trend. In Eq. 3.25a, the variables π_2 and π_5 occur in a particular combination. Consequently the cratering efficiency can be expected to depend on this combined parameter and separately on π_4. This additional parameter π_4, which is in principle a completely distinct variable, is included as a simple sum

$$\bar{\pi}_2 = \pi_2 (\pi_5 + k_1) + k_2 \pi_4 \qquad (3.26a)$$

$$= \frac{g}{Q_e} \left(\frac{W}{\delta}\right)^{1/3} [\tan \phi + k_1] + k_2 \frac{c}{\rho Q_e} \; . \qquad (3.26b)$$

This single variable $\bar{\pi}_2$ includes the strength measures c and $\tan \phi$, as well as the gravity-scaled-yield parameter π_2 and the specific energy measure of the explosive Q_e. Whether it alone can be used to account for dependences on π_2, π_4 and π_5 separately can only be determined from experiments. Assuming that it can, then

$$\pi_v = H (\bar{\pi}_2) \qquad (3.27)$$

for all soils and explosives.

For the specific case of the dry-Ottawa-sand experiments, the cohesion c is zero. Therefore, π_4 is zero and Eq. 3.26a becomes

$$\bar{\pi}_2 = (\tan \phi + k_1)\pi_2 \qquad (3.28)$$

31

where the sum $(\tan \phi + k_1)$ is a constant. The $\bar{\pi}_2$ variable is, therefore, only a constant multiple different from the gravity-scaled-yield parameter π_2. As shown in Fig. 3.1, the sand data are well represented by a power law of the form (Schmidt and Holsapple 1978a, 1980)

$$\pi_v = 0.194 \ \pi_2^{-0.472} \ . \tag{3.29}$$

In terms of the $\bar{\pi}_2$ variable, Eq. 3.29 can also be written

$$\pi_v = 0.194 \left(\frac{\bar{\pi}_2}{\tan \phi + k_1} \right)^{-0.472} \ . \tag{3.30}$$

The measured value of ϕ for this material was 35° giving $\tan \phi = 0.70$. Experimental results for materials with different values for $\tan \phi$ determine the empirical constant k_1. A value of 0.1 was chosen to be consistent with the various soils tested. The factor k_1 is a measure of the relative importance of the potential energy term compared to the Mohr-Coulomb confining-pressure strength term in the energy balance (Eq. 3.15). The fact that k_1 is relatively small compared to $\tan \phi$ for granular materials indicates that the dominant influence of increased gravity or increased charge size in crater formation is not the increasing potential energy contribution, but the increased lithostatic pressure. Only for a material with zero angle of internal friction will this dependence on increasing size be dominated by the potential energy contribution.

For $k_1 = 0.1$, Eq. 3.30 becomes

$$\pi_v = \frac{0.194}{(0.7 + 0.1)^{-0.472}} \ \bar{\pi}_2^{-0.472} \tag{3.31}$$

giving the form of the function H in Eq. 3.27

$$(\bar{\pi}_2) = 0.174 \ \bar{\pi}_2^{-0.472} \tag{3.32}$$

The usefulness of the particular combination of terms defining $\bar{\pi}_2$, (Eqs. 3.26) is shown in Fig. 3.3 for various soil-explosive pairs. For all
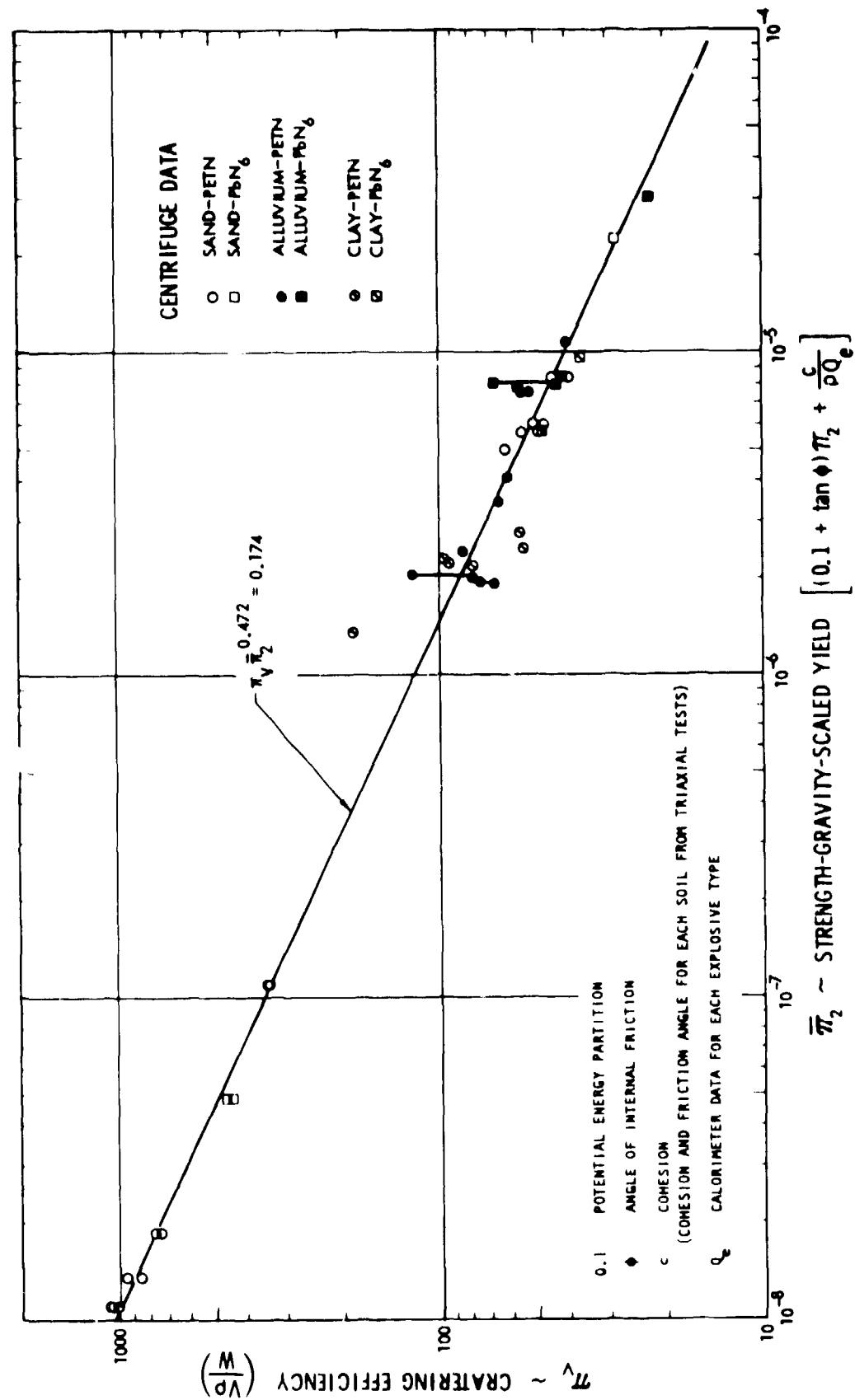
Fig. 3.3   Cratering efficiency as a function of the combined strength-gravity-scaled yield parameter, $\bar{\pi}_2$.

33

materials tested, π_v versus the parameter $\bar{\pi}_2$ can be fitted by a single straight line on a log-log plot.

The evaluation of the $\bar{\pi}_2$ parameter requires values for the strength properties of the various soils, as well as the material properties of the explosives. Experimentally determined values for the cohesion c and the angle of internal friction ϕ were measured using static triaxial tests (see Appendix B). These values are listed in Table 3.1 for dry Ottawa sand, KAFB desert alluvium, and the oil-base clay. Table 3.2 lists the values of specific energy Q_e and mass density δ for the various charges used in this study. The three sizes of PETN charges have different Q_e, because a fixed amount of silver azide initiator was used in each of the various sizes. The value of the specific energy Q_e for each composite charge was calculated by dividing the energy release due to both the silver azide and the PETN by the sum of their masses.

A value of unity for the other empirical constant k_2 in Eq. 3.26, was determined by trial and error. The final results are shown as a curve of π_v versus $\bar{\pi}_2$ for the three materials and the two different explosives in Fig. 3.3. In contrast to Fig. 3.1, the combined gravity-yield-strength parameter $\bar{\pi}_2$ accounts for the differences in gravity, size, strength and charge properties, with particularly good agreement for the sand and alluvium experiments. All the data points lie near a single straight line. Only the clay data shows appreciable scatter, which is discussed below. These results provide experimental justification of the particular combination of parameters defining the $\bar{\pi}_2$ parameter.

It is instructive to rewrite the function $\pi_v = H(\bar{\pi}_2)$ in terms of the gravity-scaled-yield parameter π_2, and the strength parameters π_4 and π_5. Substituting Eq. 3.26a into Eq. 3.32 gives

$$\pi_1 = \frac{V\rho}{W} = 0.174 \left[\frac{c}{\rho Q_e} + \frac{g}{Q_e} \left(\frac{W}{\delta} \right)^{1/3} (\tan \phi + 0.1) \right]^{-0.472}. \qquad (3.33)$$

Curves generated from this equation for each different combination of soil cohesion and charge properties are shown in Fig. 3.4. It is seen that this equation does reproduce the observed experimental trends and values. The agreement is particularly good for the sand and the alluvium data and correctly matches the shape for both explosive types in the clay which exhibits some

34

Table 3.1. Soil Properties.

Cratering Medium	Cohesion (dyne/cm^2)	Internal Friction Angle (degree)	Density (gm/cm^3)
Dry Ottawa Sand	0.0	35	1.80
Dry Desert Alluvium	1.7×10^5	32	1.60
Modeling Clay	1.1×10^5	1.2	1.53

Table 3.2. Explosive Properties

Explosive Type	Mass (gm)	Energy (erg)	Specific Energy (erg/gm)	Density (gm/cm^3)
PETN	0.49	2.24×10^{10}	4.54×10^{10}	1.93
PETN	1.34	7.18×10^{10}	5.34×10^{10}	1.78
PETN	4.08	2.27×10^{10}	5.56×10^{10}	1.73
PbN$_6$	1.70	2.24×10^{10}	1.32×10^{10}	3.10
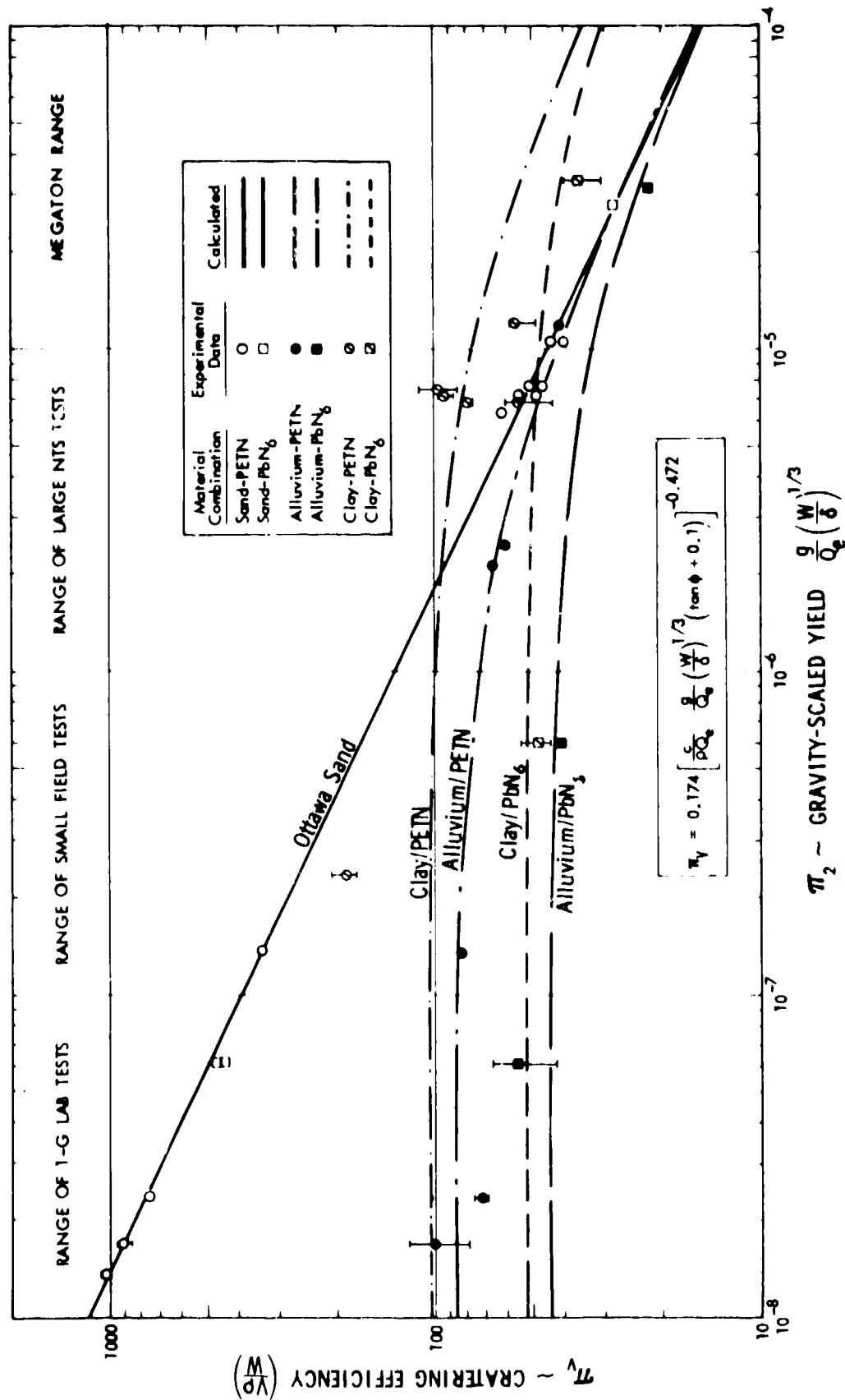
Fig. 3.4 Comparison of material strength model for cratering efficiency with centrifuge experimental results.

36

scatter. Possible causes of this scatter include rate effects which violate the similarity requirements at fixed π_2, sample preparation, aging of the clay and dependence of material properties upon temperature which varied slightly from shot to shot (see Table 2.3). Additional experiments are required to better define the clay behavior leading to the observed scatter. Nevertheless the mean values are in good agreement.

For small values of π_2 (small charge mass W), π_v approaches a constant value given by

$$\pi_v = 0.174 \; (\frac{c}{\rho Q_e})^{-0.472} \tag{3.34}$$

and is therefore determined by the cohesion and density of the cratering medium and the specific energy of the explosive. Equation 3.34 agrees with the differences in the observed asymptotes for the various combinations tested. Only if c is zero will this cube-root regime not be observed, as is the case for the dry Ottawa sand data.

For sufficiently large values of charge size, the π_2 term in Eq. 3.26a will dominate. In this large-charge-size regime, the curves generated from Eq. 3.33 are asymptotic to the equation

$$\pi_v = 0.174 \; [\frac{g}{Q_e} \; (\frac{W}{\delta})^{1/3} \; (\tan \phi + 0.1)]^{-0.472} \tag{3.35}$$

which is independent of the cohesion of the material. This is a straight line on a log-log plot of π_v versus π_2.

3-3   GENERALIZATION TO OTHER SOIL TYPES

Figure 3.5 shows the expected behavior for a generic material having both finite cohesion and finite angle of internal friction. The horizontal asymptote described above is shown, as well as the asymptote for large values of charge size. The transition value of π_2, corresponding to the intersection of these two straight line asymptotes, is

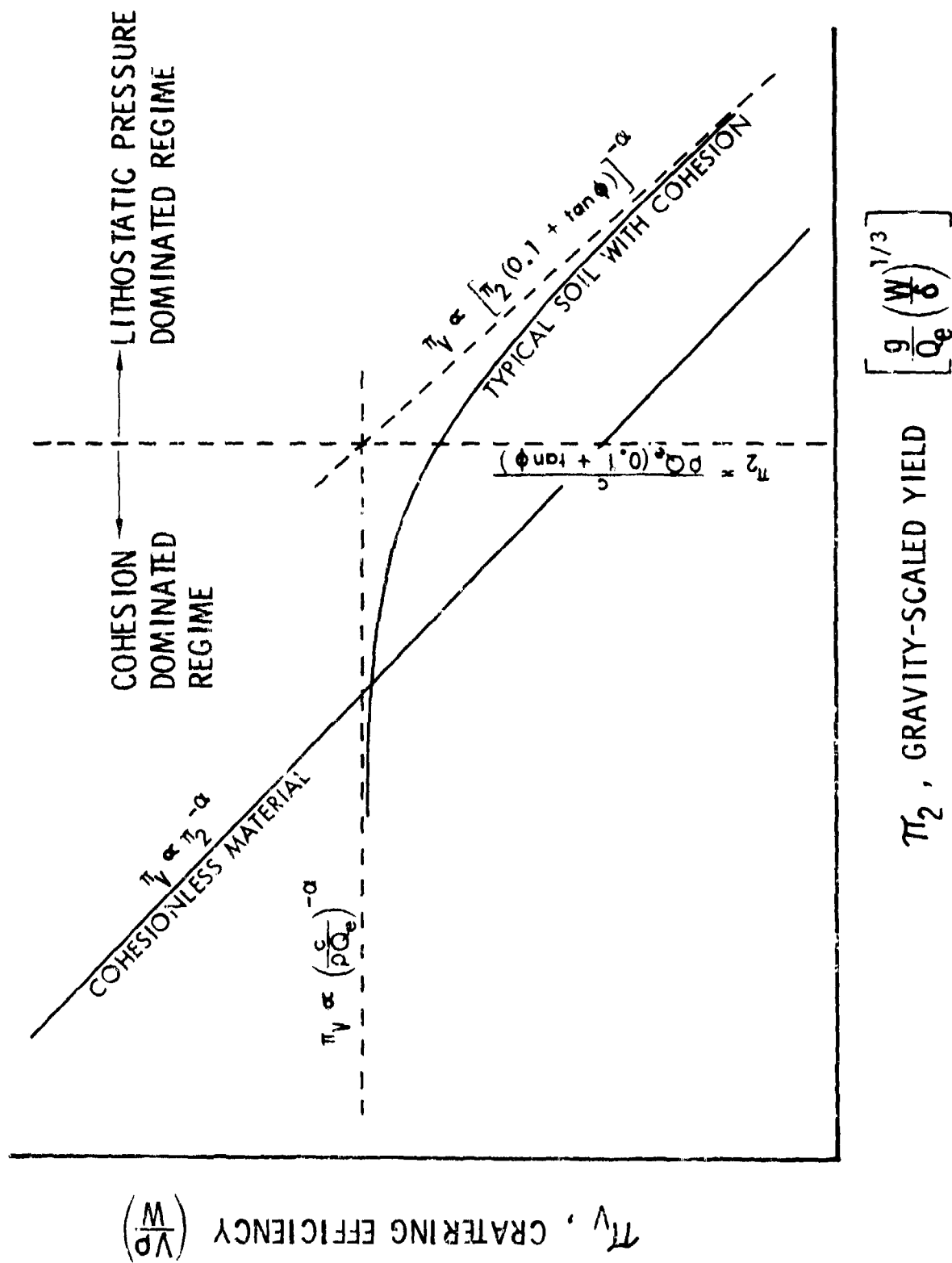$$\pi_2 = \frac{c}{\rho Q_e (0.1 + \tan \phi)} \; , \tag{3.36}$$

37

Fig. 3.5   General form of cratering efficiency versus gravity-scaled yield for a typical soil.

38

which is determined by the cohesion, the angle of internal friction, the soil density and the specific energy.

Using the definition of π_2, the critical charge mass corresponding to this transition is

$$W = \delta \left[\frac{c}{\rho g \ (\tan \phi + 0.1)} \right]^3 . \qquad (3.37)$$

A curve depicting the transitional charge size for TNT in terms of the strength parameter c/ρ $(\tan \phi + 0.1)$ for various values of gravity g is shown in Fig. 3.6. The strength ranges for common soils are indicated on this figure in a very approximate way. This figure indicates, for example, that at 1 G the transitional charge mass for alluvial materials is in the range of a ton to a kiloton of TNT.

These results explain some of the apparent discrepancies observed in explosive cratering tests. In alluvium, for example, small-scale tests do not extrapolate to large-scale field tests, as can be seen based upon the strength model given here. Small tests in alluvium at 1 G are in the cohesion-dominated, cube-root regime. Existing large-scale field tests are around the transition charge size. These field data (Chabai, 1965) are compared with the calculated behavior for TNT explosive ($Q_e = 4.19 \times 10^{10}$ erg/gm) in desert alluvium as shown in Fig. 3.7. The predicted crater volume is based entirely upon the centrifuge experimental results, using charge sizes on the order of a few grams of either PETN or PbN_6. The 5000-lb shot lies right on the predicted curve. There is some scatter among the three 256-lb shots, but the mean value lies on the curve.

Another interesting result is a comparison of the clay and the sand cratering efficiencies. At small π_2 values (small charge size) the clay volumes were substantially below those for sand. This is consistent with the idea that sand is "strengthless" and clay has finite cohesion. For large π_2 (large charge size) the cratering efficiency in clay is greater than in dry sand. In this regime, the cratering efficiency is dominated by the angle of internal friction, which introduces an effective strength due to the large lithostatic pressure. Clay has a near-zero angle of internal friction. Consequently, for large confining pressure, the dry sand is "stronger" than the clay, which explains the observed crater volumes. This general behavior is in qualitative agreement with calculated results of O'Keefe and Ahrens (1978) who used a Mohr-Coulomb strength model with a high-pressure cutoff.
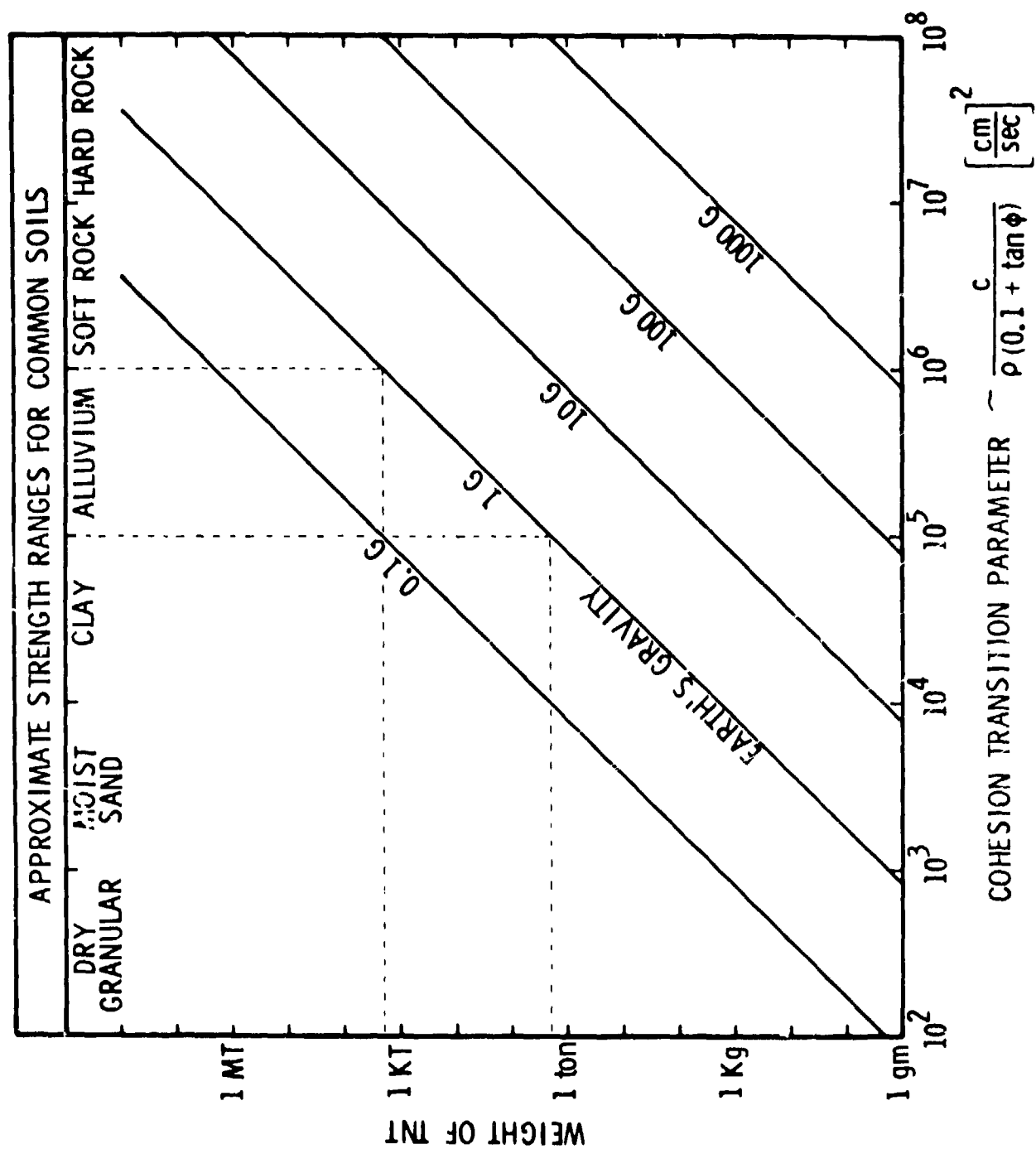
39

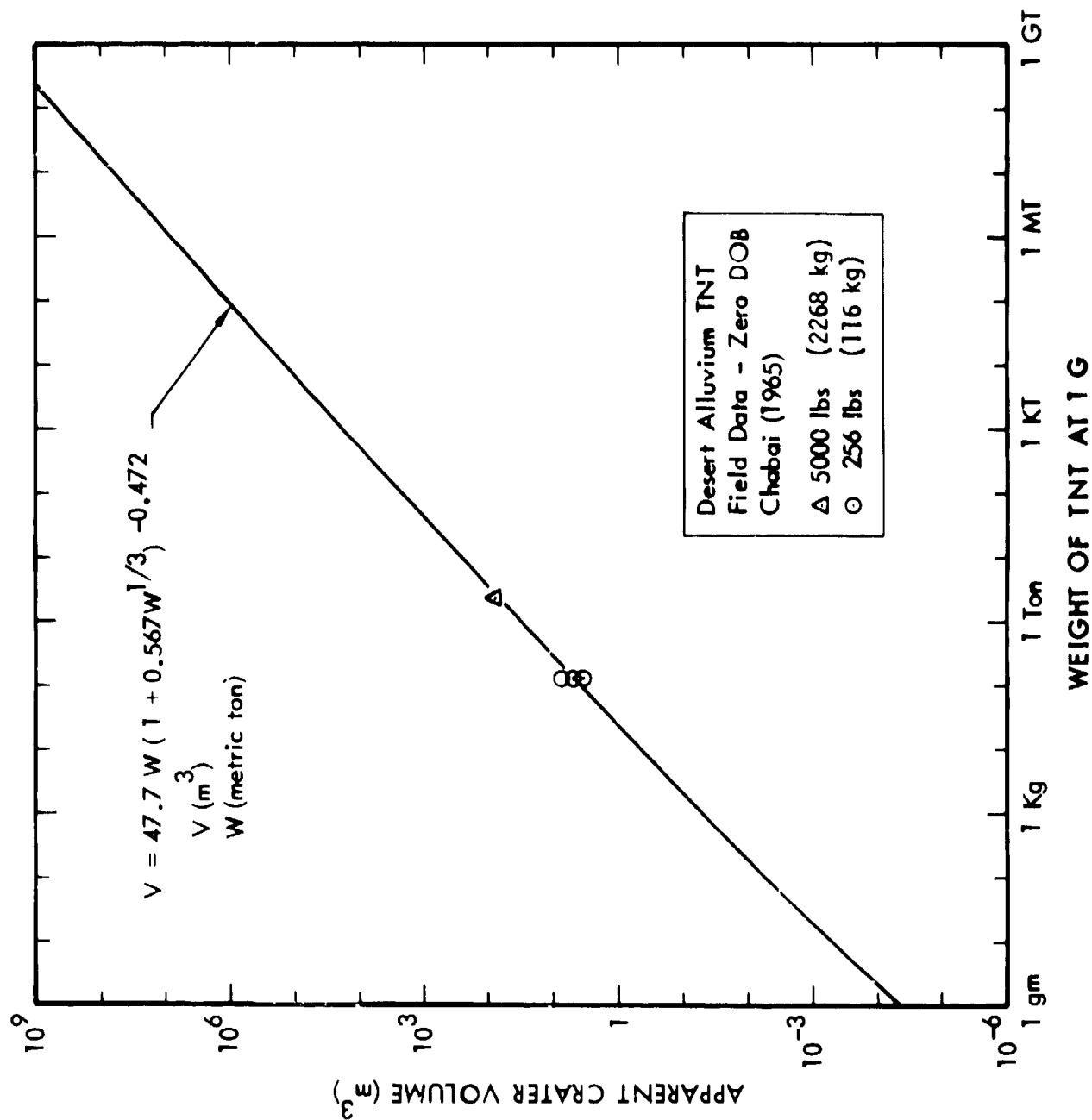Fig. 3.6   Transitional yield of TNT versus material-strength parameter.

40

Fig. 3.7   Comparison of field data with an analytical model based solely upon centrifuge experimental results.

41

SECTION 4
CRATER RADIUS AND CRATER DEPTH

Significant variations in crater shape versus scaled energy were observed for the different soil-explosive combinations tested. These variations include differences in overall shape, as measured by the aspect ratio (ratio of the radius to depth), and more detailed features, such as terraces and central mounds. For the purposes of this report only the differences in radius and maximum depth, are considered.

Nondimensional forms for the crater radius r and the crater depth h are

$$\pi_r = r \left(\frac{\rho}{W}\right)^{1/3} \tag{4.1}$$

$$\pi_h = h \left(\frac{\rho}{W}\right)^{1/3} \tag{4.2}$$

All the results obtained to date for π_r and for π_h for dry sand, clay, and 4-percent moisture alluvium at zero depth of burst are shown in Figs. 4.1 and 4.2 as a function of the gravity-scaled-yield parameter π_2. The data points for dry Ottawa sand are, as given previously (Schmidt and Holsapple 1978a), along the curves described by

$$\pi_r = 0.766 \; \pi_2^{-0.159} \tag{4.3}$$

and

$$\pi_h = 0.154 \; \pi_2^{-0.164} \tag{4.4}$$

which give very good straight-line fits using these logarithmic scales.

For the alluvium data points, considering only those with (approximately) 4-percent moisture, the acquisition of additional data has led to an interpretation, incorporating the cohesion of the medium, different than that previously given (Schmidt and Holsapple 1978a). The data for the radius has the same qualitative trend as does the crater volume data. A functional form for a quantitative model is given below. The trend of the depth data, however, is not even qualitatively the same as that for either the volume or the radius.
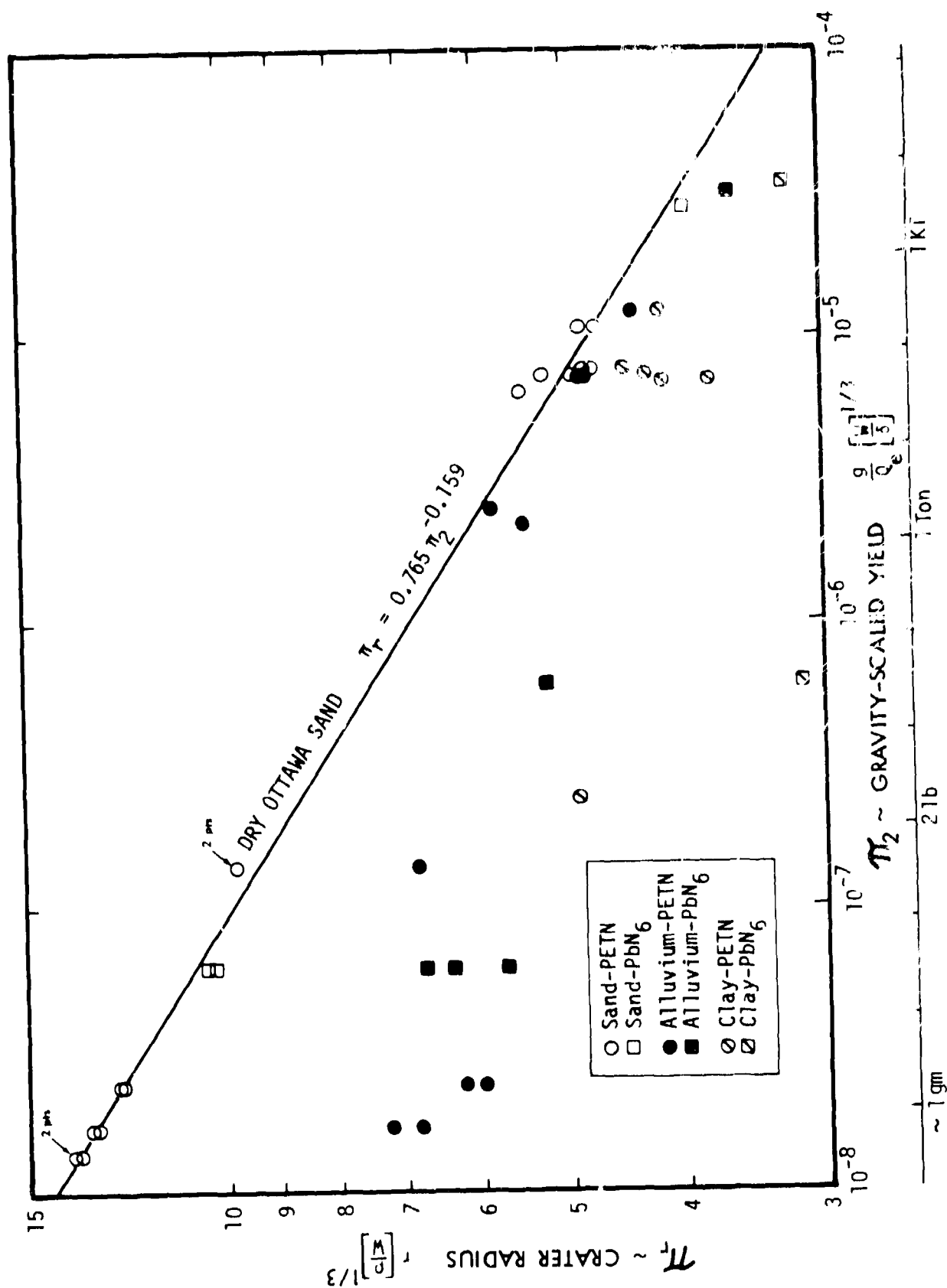
42

Fig. 4.1 Radius parameter versus gravity-scaled yield for various soil-explosive combinations.
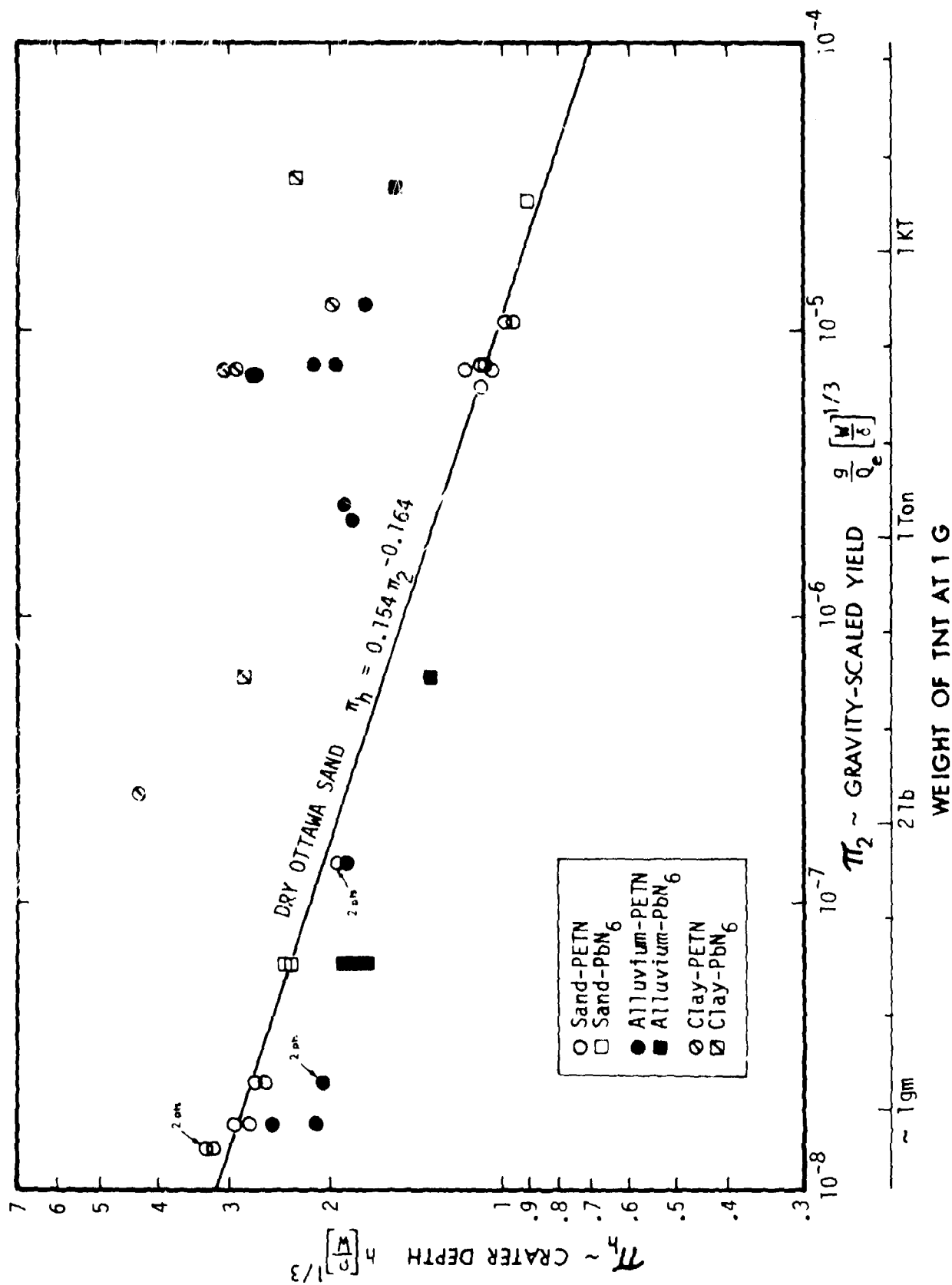
43

Fig. 4.2 Depth parameter versus gravity-scaled yield for various soil-explosive combinations.

An attempt was made to model both the radius and depth data using the same strength model developed for the volume data (Section 3). However, the data do not appear to be consistent with this interpretation. Some reasons for this are discussed.

The strength model for volume was based on the energy available and upon the work necessary to excavate the crater. However, the dependence of the work required on the specific shape of the crater was not considered. Thus, the theory is expected to be more suitable for the volume, than for shape variables such as radius and depth. Since the volume is approximately proportional to the radius squared times the depth, the radius is the dominant dimension determining the volume. Consequently, the radius behavior might be expected to exhibit the same trend as the volume and, perhaps, the depth to a lesser degree.

It is clear that slope stability considerations may rule out certain crater shapes as either the explosive size or gravity is increased. For example, McKinnon and Melosh (1978) have shown for craters with vertical walls and flat bottoms that there is a maximum depth, due to the initiation of slumping. The value depends upon the parameters $\rho g h/c$ and $\tan \phi$. Subsequent work by Melosh and McKinnon (1979) indicates that craters of parabolic shape also cannot exceed some maximum depth. This trend is consistent with observations of James (1977, 1978).

From the following equality

$$\frac{\rho g h}{c} = h(\frac{\rho}{W})^{1/3} \quad \frac{g}{Q_e} (\frac{W}{\delta})^{1/3} \quad \frac{\rho Q_e}{c} \quad (\frac{\delta}{\rho})^{1/3} \tag{4.5a}$$

$$= \pi_h \, \pi_2/(\pi_4 \, \pi_3^{1/3}), \tag{4.5b}$$

a limiting value on $\rho g h/c$ implies a limit on the crater depth variable as a function of π_2 for a given soil-explosive combination which determines π_4 and π_3.

$$\pi_h \leq K \, \pi_4 \, \pi_3^{1/3} \, \pi_2^{-1} \tag{4.6}$$

The constant K depends on $\tan \phi$ and crater shape profile. If, to first order, it can be assumed that slumping due to stability limits does not change the crater volume, the prediction of crater volume only requires a consideration

of the energy balance. The radius is influenced to some degree by stability considerations, and the depth and the aspect ratio (r/h) may be dominated by stability.

The centrifuge does give a tool for direct simulation of large-scale craters. For the soils and explosives over the range of scaled energy tested, the data points in Figs. 4.1 and 4.2 give predictive values for both radius and depth. For granular materials, like sand and alluvium, π_r versus π_2 can be explained with a functional form like that obtained for the volume. The clay craters were significantly different in shape, and the theory generated from energy balance considerations alone was not sufficient to explain the data.

At small values of the gravity-scaled size parameter π_2, the π_r variation for the alluvium is essentially constant (independent of π_2). This is a regime of cube-root scaling where all the crater dimensions are determined by the cohesion of the material. The dry sand, which has essentially no cohesion, does not show this behavior.

As the variable π_2 is increased, the results become more influenced by lithostatic pressure. As discussed in Section 3, this is due to two factors: the increased strength, due to the lithostatic pressure and the angle of internal friction; and the additional work that must be done to excavate the crater as the size or the gravity increases. For the volume variable π_v, the data show a transition regime, curving from the constant π_v asymptote for small π_2 values to a sloped straight-line asymptote (on log-log plot) for large π_2 values. The radius parameter π_r for alluvium shows the same general trend, but the exact form of the function that fits the data is different.

As given above, the effects of strength for the various materials considered can be measured by a generalization of the combined strength-gravity-scaled yield parameter $\bar{\pi}_2$ given by Eq. 3.26b as follows

$$\bar{\pi}_2 = \frac{g}{Q_e} \left(\frac{W}{\delta}\right)^{1/3} [A_1 \tan \phi + A_2] + A_3 \frac{c}{\rho Q_e} . \tag{4.7}$$

There are three terms in this parameter. The $A_1 \tan \phi$ term is a measure of the work against the material strength increase due to confining pressure. The A_2 term is a measure of the work against gravity, and the A_3 term measures the work to overcome the cohesion during the crater excavation. The values of each of the constants determine the relative importance of each of these terms.

46

For the volume data, A_1 was taken as unity, A_2 was taken to be 0.1, and A_3 as 1.0, as discussed in Section 3. However, for the radius data, different values are seen to be more appropriate. This is not surprising, since the different work terms vary in importance in determining radius, as compared to the depth or the volume.

As shown in Fig. 4.1, the values for π_r for alluvium and dry Ottawa sand all converge at large values of π_2. This indicates that there is little or no dependence on tan ϕ, since this strength contribution determines any variation in dependence on π_2 for large values of π_2. Thus, for the radius data, A_1 was taken to be zero and $\bar{\pi}_2$ can be divided by A_2 giving

$$\bar{\pi}_2' = \frac{g}{Q_e} \left(\frac{W}{\delta}\right)^{1/3} + A_4 \frac{c}{\rho Q_e} , \tag{4.8a}$$

where now

$$A_4 = A_3/A_2 . \tag{4.8b}$$

To find the best value of A_4, the cohesion-determined asymptotes at small values of π_2 can be used. The functional form expected, based on the results of Section 3, is

$$\pi_r = K \, \bar{\pi}_2^{-\alpha} . \tag{4.9}$$

For dry Ottawa sand with zero cohesion, Eq. 4.8a gives

$$\bar{\pi}_2' = \pi_2 = \frac{g}{Q_e} \left(\frac{W}{\delta}\right)^{1/3} , \tag{4.10}$$

so that the fit for π_r, Eq. 4.3 becomes

$$\pi_r = 0.766 \, \bar{\pi}_2'^{-0.159} . \tag{4.11}$$

Hence for the Ottawa sand radius data

$$K = 0.766 \tag{4.12a}$$

and

$$\alpha = 0.159. \tag{4.12b}$$

For materials other than sand this result can be generalized by substituting the complete definition of $\bar{\pi}'_2$ (Eq. 4.8a) into Eq. 4.11, giving

$$\pi_r = 0.766 \left[\frac{g}{Q_e} \left(\frac{W}{\delta}\right)^{1/3} + A_4 \frac{c}{\rho Q_e} \right]^{-0.159} . \tag{4.13}$$

The constant A_4 is determined by the value of the cohesion-dominated asymptotes at small values of π_2. Setting $\pi_2 = 0$,

$$\pi_r = 0.766 \ (A_4)^{-0.159} \left(\frac{c}{\rho Q_e}\right)^{-0.159}. \tag{4.14}$$

Alluvium data for π_r at small π_2 values are taken from Piekutowski (unpublished data)--shot numbers UDRI-646 through UDRI-651 in Table 2.2. For these shots, $A_4 = 0.5$ gives a good fit. This completely fixes the dependence of π_r on the other variables and the final result is

$$\pi_r = 0.766 \left[\frac{g}{Q_e} \left(\frac{W}{\delta}\right)^{1/3} + 0.5 \frac{c}{\rho Q_e} \right]^{-0.159} \tag{4.15}$$

The curves generated from this equation, together with the data points for dry Ottawa sand and alluvium, are shown in Fig. 4.3.

As a final measure of crater shape, the aspect ratio, r/h, will be discussed. As suggested above, slope stability considerations are expected to play an important role in determining values of this crater dimension. The slope stability depends upon the material strength, which has two components: the cohesion and the angle of internal friction. For a material with zero cohesion and non-zero angle of internal friction (such as the dry Ottawa sand), stability is independent of gravity and size. That is, stability of a certain shape at small scale or at small gravity implies stability at large scale or at large gravity. This follows from the fact that, while increased size or gravity requires greater strength, the strength increases as the size or gravity increases due to the increased lithostatic confining pressure (i.e., strength proportional to $\rho g h \tan \phi$).
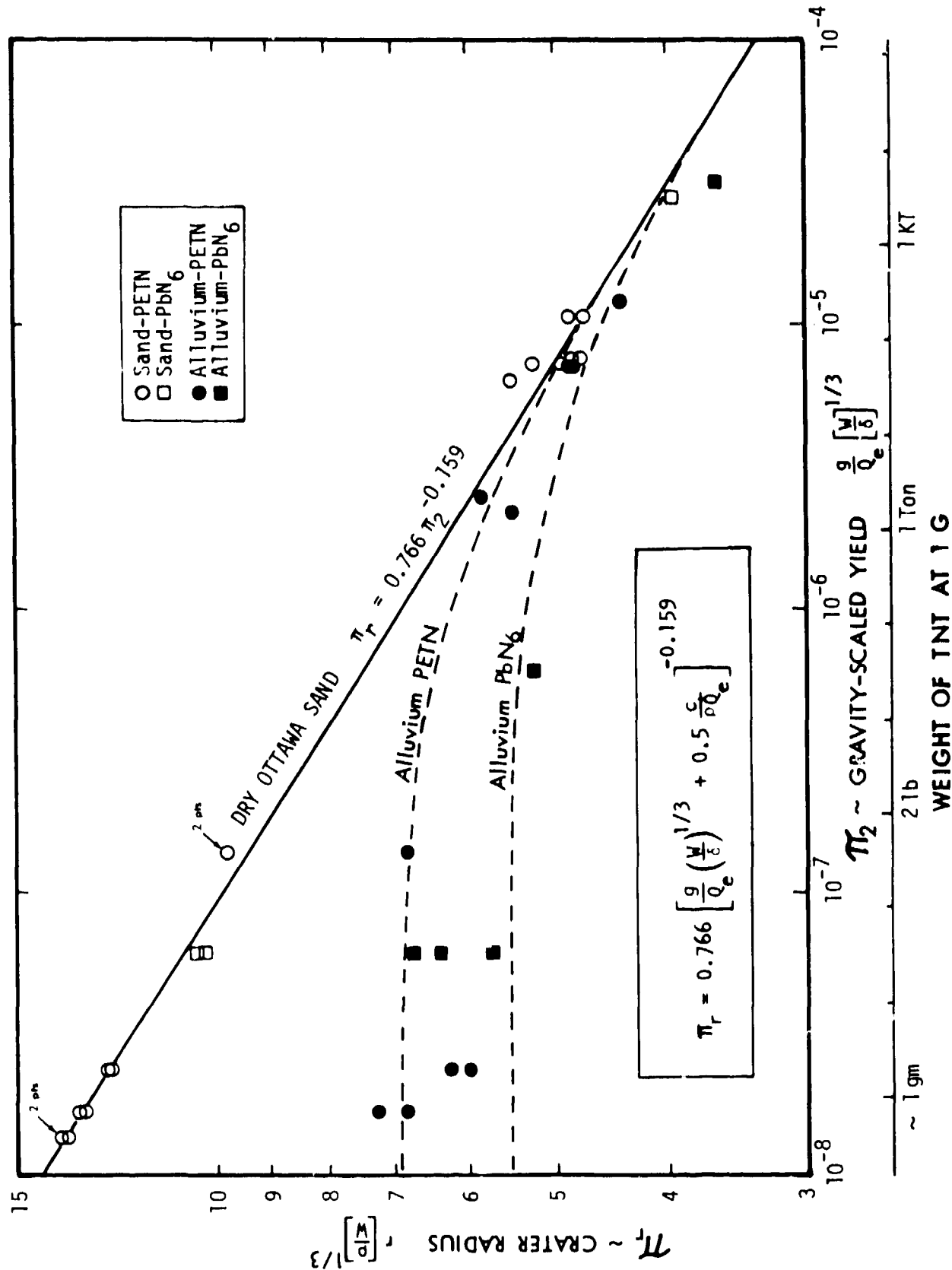
48

Fig. 4.3 Comparison of material strength model for radius parameter with centrifuge experimental results.

49

On the other hand, the stability of a material with small angle of internal friction but large cohesion will depend both on the scaled size and on gravity. Consequently, a variation of shape is ant.:ipated with increasing size.

The parameter π_2 correlates all crater-size data very well. It accounts for differences of size, gravity and source energy density. However, for shape measures such as the aspect ratio, π_2 may not be the most appropriate independent parameter. For example, energy-density effects may not play a role in crater shape. The stability arguments given above suggest that for a cohesive material the dimensionless parameter $\rho gh/c$ may be more significant. (It should be noted that this pi-group is not independent but merely a combination of the original set as shown in Eq. 4.5b.)

Figures 4.4, 4.5 and 4.6 show aspect ratio results for the various soils. Figure 4.4 is a composite plot showing the aspect ratio for all three materials versus π_2. Figure 4.5 shows the alluvium aspect ratio versus $\rho gh/c$, and Fig. 4.6 shows the same for clay. The expectations are supported by the data. For dry Ottawa sand, the aspect ratio is essentially independent of scaled size, as indicated on Fig. 4.4. The value is about 4.6 with ± 10 percent variation.

For the alluvium, Fig. 4.5 is thought to be more meaningful than Fig. 4.4. In Fig. 4.5, with the stability parameter $\rho gh/c$ as the abscissa, the aspect ratio shows as a gradual decrease (more hemispherical shape) as the parameter increases. For comparison, the equivalent 1-G crater depth is shown on the top as a second abscissa scale. This trend is not expected to continue to ever-increasing crater sizes. For very large sizes, slope stability dictates that the crater walls can never get steeper than the angle of friction for the material. A lower limit on r/h should be given by the reciprocal of $\tan\phi$. For alluvium, this limit value is r/h = 1.6 as shown in Fig. 4.5. With increasing crater depth the aspect ratio is expected to become asymptotic to this limit. Interestingly, the TEAPOT ESS crater, whose depth was 20.4 m, had the smallest aspect ratio of all the large NTS alluvium craters, a value equal to 1.62.

Figure 4.6 shows the clay results as a plot of aspect ratio versus the stability parameter. For small values of $\rho gh/c$, the craters are nearly hemispherical. As the stability parameter increases, there is a gradual increase in the aspect ratio. Only one data point, shot 25-X has a uniquely
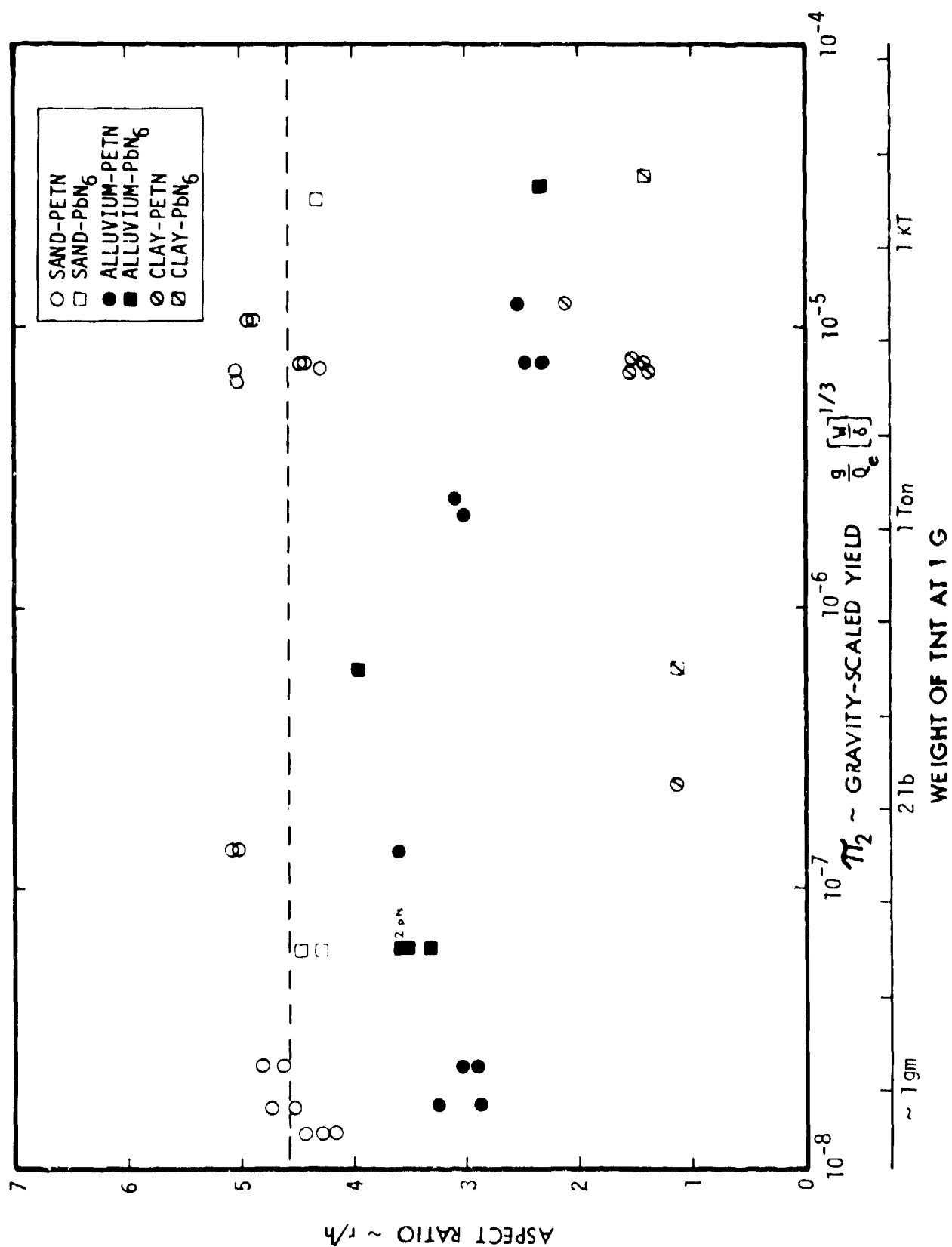
50

Fig. 4.4 Crater aspect ratio versus gravity-scaled yield for various soil-explosive combinations.
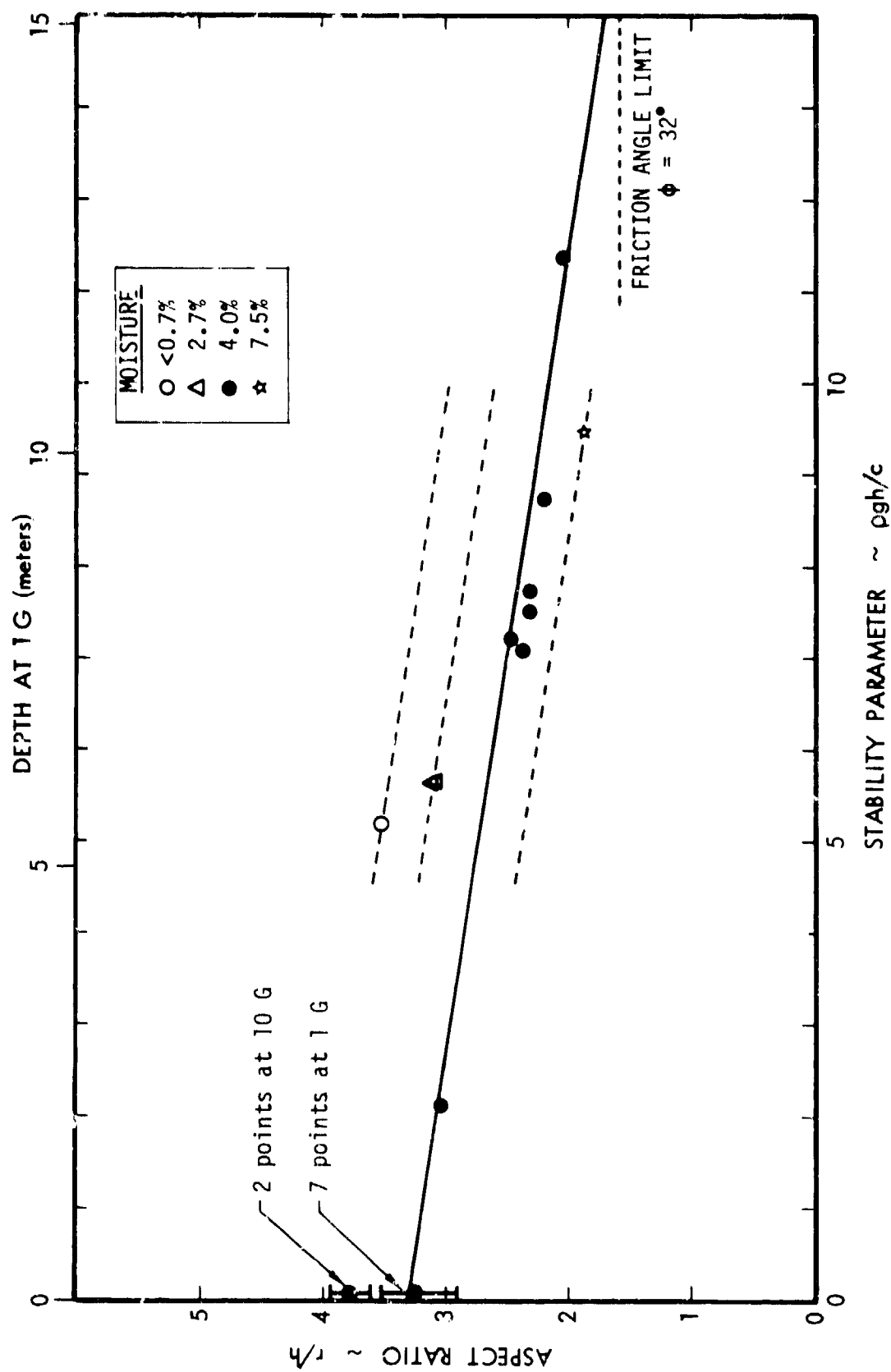
51

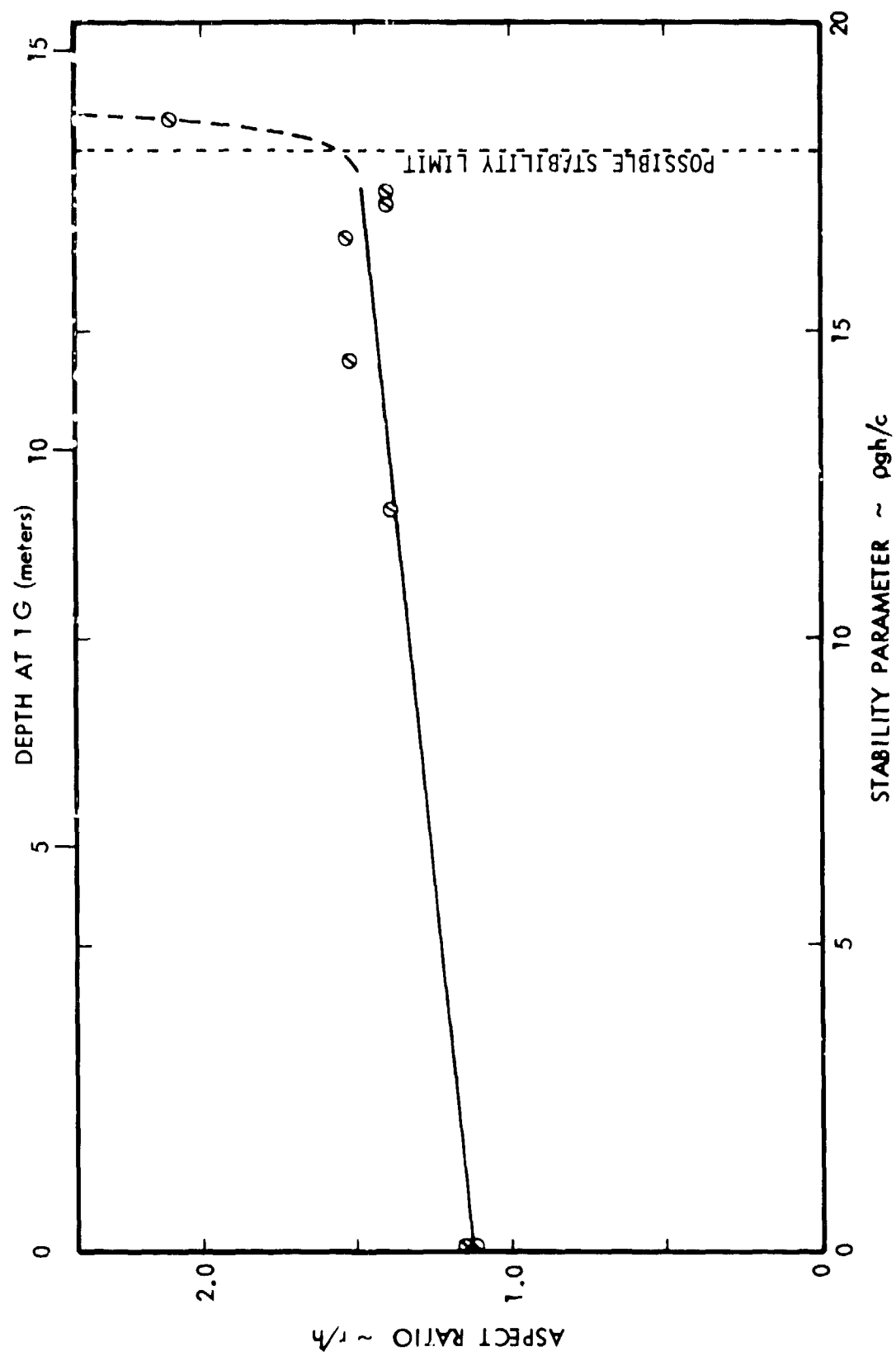Fig. 4.5 Crater aspect ratio versus stability parameter for KAFB alluvium.

Fig. 4.6 Crater aspect ratio versus stability parameter for oil-base clay.

greater aspect ratio (flatter crater). It also has the largest value of the stability parameter, which probably accounts for its unique flat profile. McKinnon and Melosh (1978) have found, for "transient" craters with a cake-pan shape, that a stability limit occurs at a definite value of $\rho gh/c$ for a given material with a given $\tan \phi$. For cake-pan-shaped craters, they found the value to be about 6.0. For the present experiments, craters seem to retain a lower value of aspect ratio, up to a value of $\rho gh/c$ equal to approximately 18. This is equivalent to a value of ρgh equal to 2.1×10^6 dyne/cm^2. Shot 25-X is the only shot over this threshold.

A check on the existence of a stability limit based on $\rho gh/c$ was made as an adjunct to shot 25-0. This crater was formed at low G with a resulting $\rho gh/c$ equal to 0.8. Subsequent to the cratering event, the gravity was increased to 518 G for 100 seconds, which would have resulted in a $\rho gh/c$ equal to 42 had the crater shape remained constant. However, the crater slumped considerably as can be seen in Figure 4.7. The final aspect ratio was 2.1, about the same as that for crater 25-X which was formed at high G. The final slumped values of $\rho gh/c$ for 25-0 was equal to 23, and ρgh was 2.5×10^6 dynes/cm^2. This gives compelling evidence that, for this clay, all large volume craters will have a limiting value of ρgh equal to 2.5×10^6 gm/cm-sec^2. At 1 G, with $\rho = 1.53$ gm/cm^3, the limiting depth is about 16 meters for all charge sizes.

Crater 25-X, formed at high G, was also subjected to the 518-G environment for 100 seconds to provide a control point. As can be seen in Fig. 4.7, it underwent negligible shape change suggesting that a stable shape was formed upon excavation. This was confirmed when both craters, 25-0 and 25-X, were cut in two using a thin wire to reveal the crater cross sections.

The low-G crater, 25-0, showed marked evidence of flow and collapse of the transient crater formed at low G, whereas the high-G crater, 25-X, showed no evidence of a transient crater or any significant flow or slumping. Figure 4.8 is a comparison of the two cross sections. They show the same approximate final shapes, but were arrived at by very different processes.

In this experiment, using the oil-base clay material, the crater formed at high G, corresponding to a 1-G field event of 564 metric tons of PETN, did not go through a transient stage and collapse.
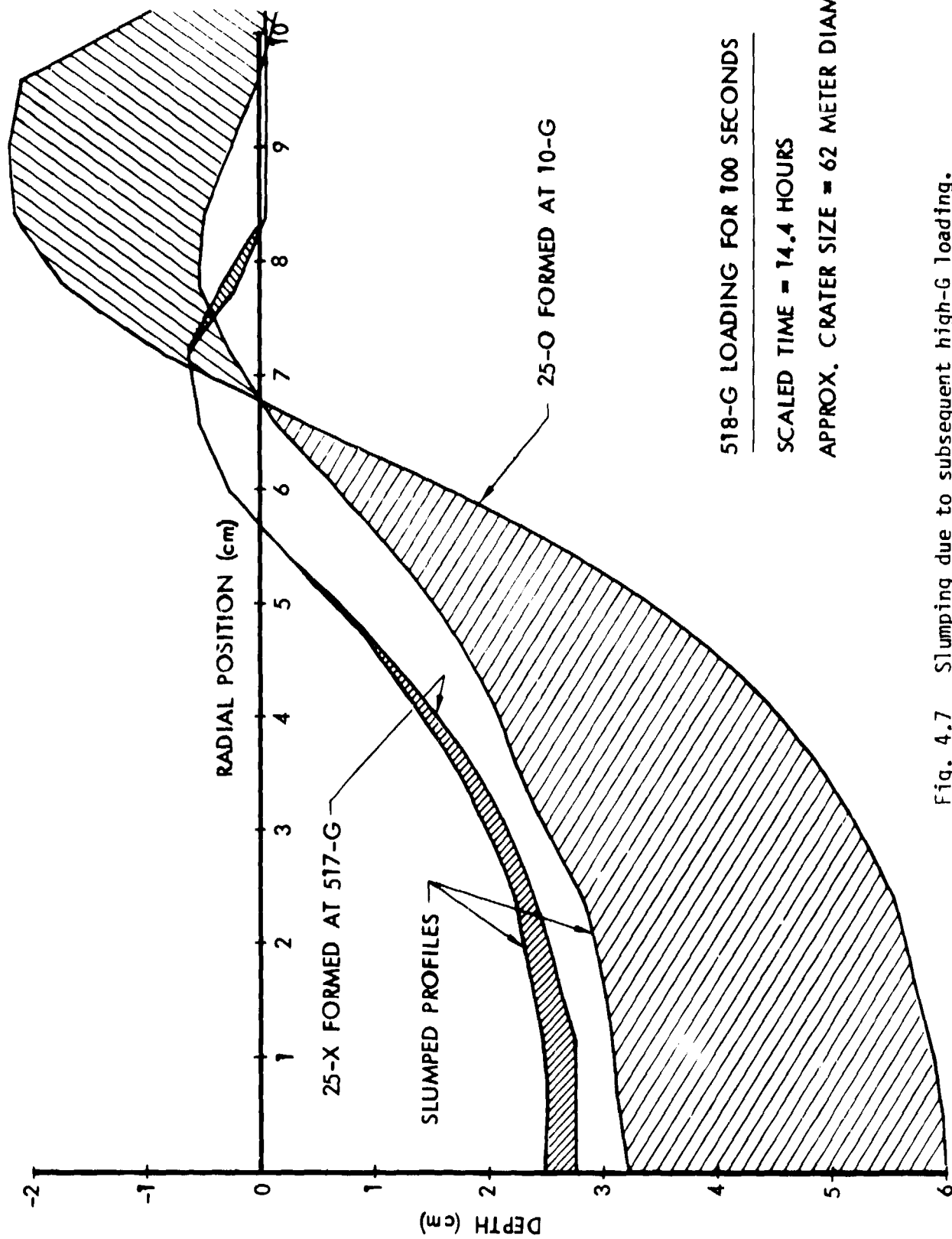
54

RADIAL POSITION (cm)

518-G LOADING FOR 100 SECONDS

SCALED TIME = 14.4 HOURS

APPROX. CRATER SIZE = 62 METER DIAMETER

25-O FORMED AT 10-G

25-X FORMED AT 517-G

SLUMPED PROFILES

DEPTH (cm)

Fig. 4.7   Slumping due to subsequent high-G loading.
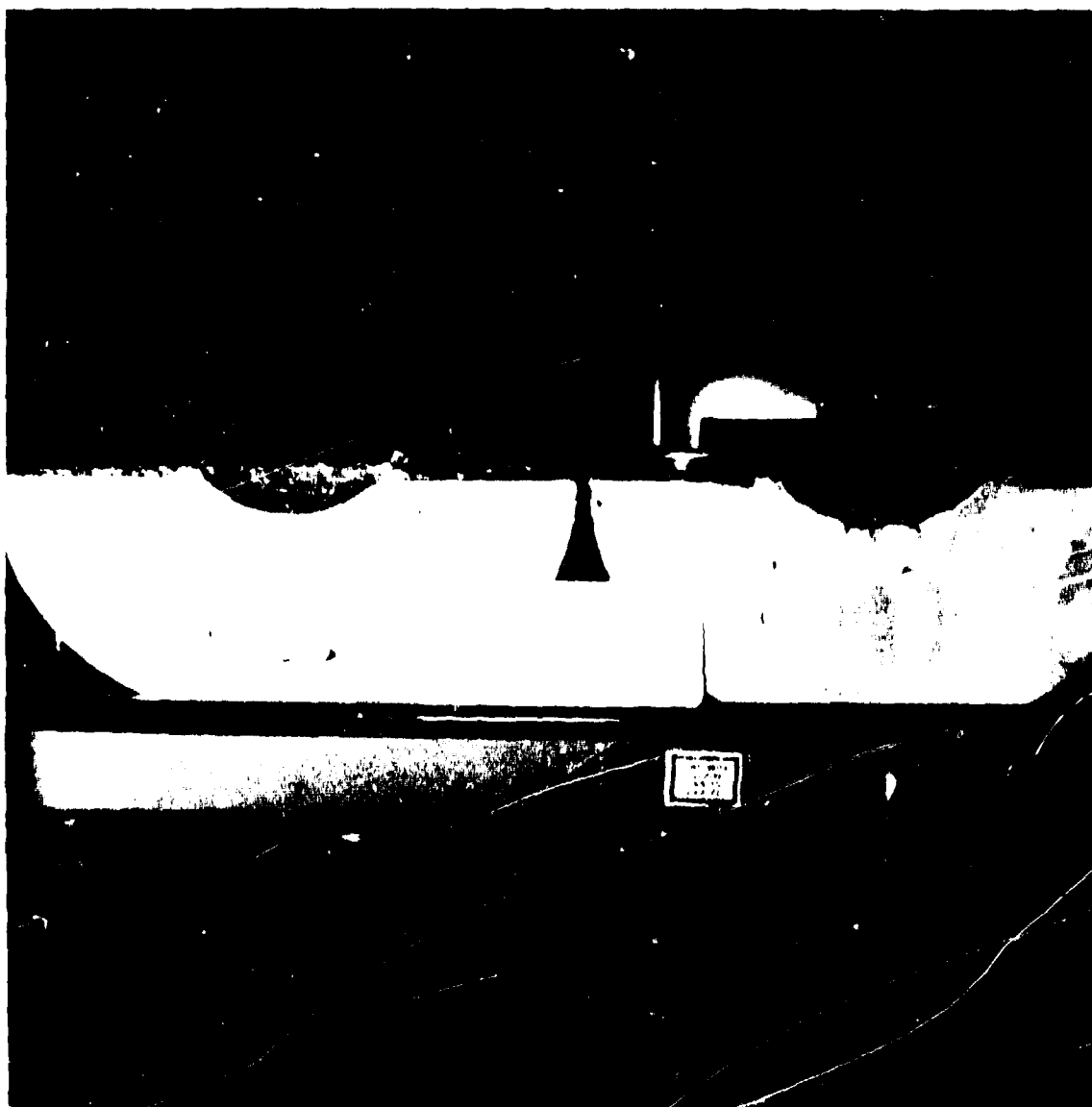(Also see Figs. A23-A26, Fig. 4.8 and text.)

55

Fig. 4.8.   Comparison of crater cross sections. Shot 25-0 formed at
10 G shown to the right. Shot 25-X formed at 517 G shown
to the left. Both craters were subsequently spun at 518 G
for 100 seconds. Note flow pattern and structure of crater
floor in 10-G crater. (Also see Figs. A23-A26, Fig. 4.7 and
text.)

56

SECTION 5
MOISTURE CONTENT

Several shots were designed to determine the effect of moisture content on cratering phenomena in desert alluvium. Four shots with moisture contents from less than 0.7 percent to 7.5 percent were made in addition to the series of shots at approximately 4-percent moisture.

Significant differences due to moisture content were found. Static triaxial tests were performed on specimens with various moisture contents. The strength properties were found to depend strongly upon moisture content. Consequently, it is expected that differences in cratering behavior should be observed. The results of the static material-property tests are summarized in Table 5.1. Two values of cohesion are shown for each case. One of these is based on the zero-confining-pressure intercept from triaxial tests. The other is obtained by a direct shear test.

All variable moisture tests were performed at a gravity-scaled-yield parameter π_2 about equal to 7×10^{-6}. This corresponds to about 70 metric tons of TNT at 1 G. The variation of cratering efficiency π_v with moisture content at this π_2 value is shown in Fig. 5.1 (also see Fig. 3.4). The dependence of aspect ratio r/h on moisture is shown in Fig. 5.2.

Although an explicit correlation to measured strengths was not attempted since all the data were for a fixed scaled size, certain qualitative behavior is noteworthy. Both the crater size and shape depend markedly on moisture content at this scaled size. The cratering efficiency decreases as the moisture content decreases, with the largest changes occurring as the alluvium becomes more dry. This is probably due to the significantly larger angle of internal friction noted for the dry alluvium. At this scaled size, the value of π_2 is in the regime where that friction angle is the dominant strength contribution.

Since all samples with moisture content greater than about 2 percent have about the same angle of friction, small changes in cratering efficiency would be expected. The results are consistent with this expectation, except for shots 17-X and 17-O. These two shots, while consistent with each other, seem to be small compared to the others. Figure 5.3 shows the measured wet density versus moisture content. Note that the samples with 2.7-percent moisture appear anomalous on this curve also. It may be that sample preparation variations for

Table 5.1. Summary of material property tests on KAFB desert alluvium.
(See Appendix B.)

| Moisture Content % | Cohesion | | Angle of Internal Friction (degree) |
	Triaxial test (dyne/cm^2)	Direct Shear (dyne/cm^2)	
<1.0	2.8 x 10^5	0.4 x 10^5	46
2.4 (high pressure)	2.0 x 10^5	--	36
3.0-4.0	6.5 x 10^5	0.7 x 10^5	36.5
4.4 (high pressure)	1.7 x 10^5	--	32
7.2	3.2 x 10^5	2.1 x 10^5	37
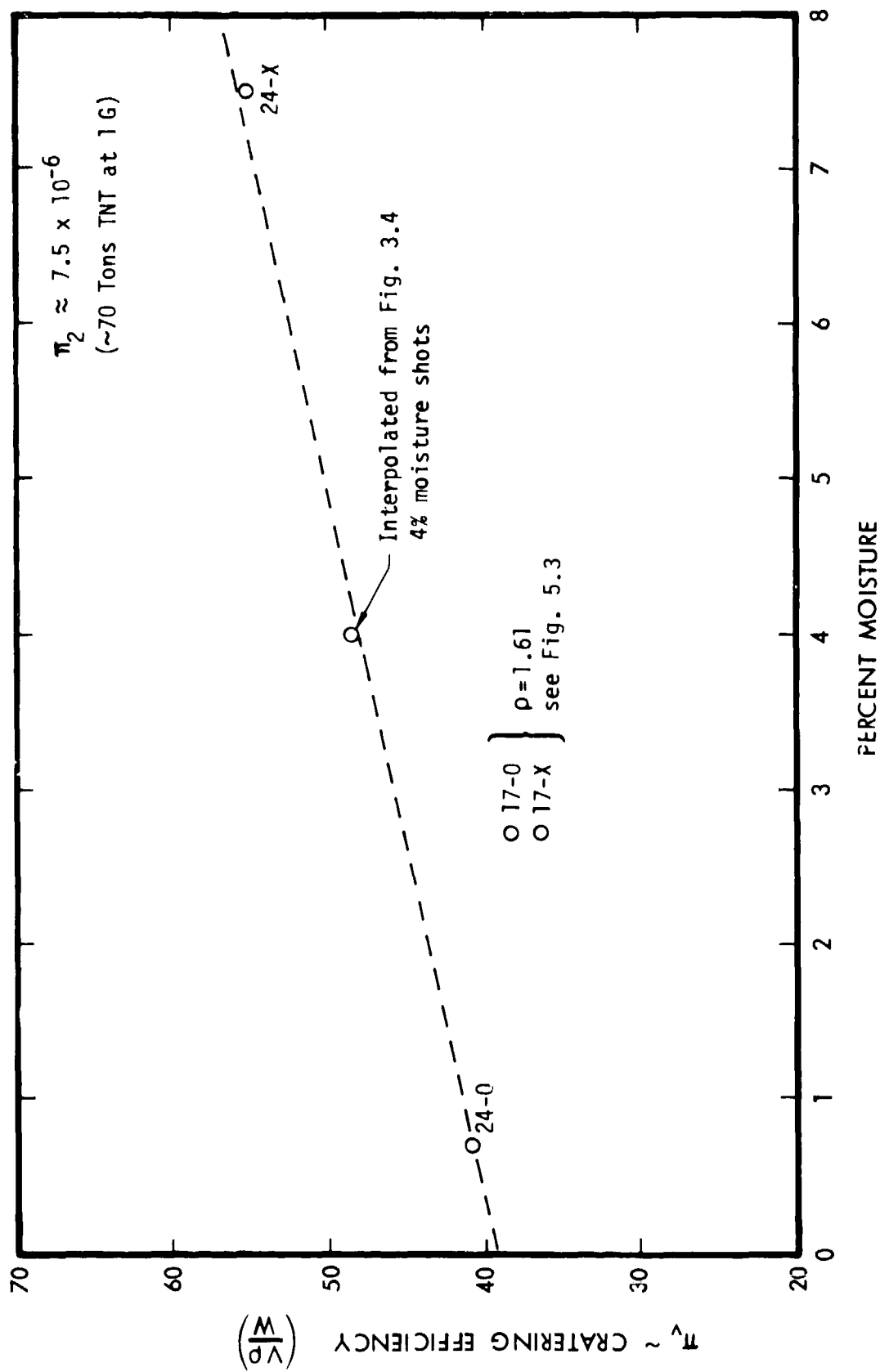
Fig. 5.1 Variation of cratering efficiency with moisture content of KAFB alluvium for constant π_2 (equivalent to 70 Tons TNT).
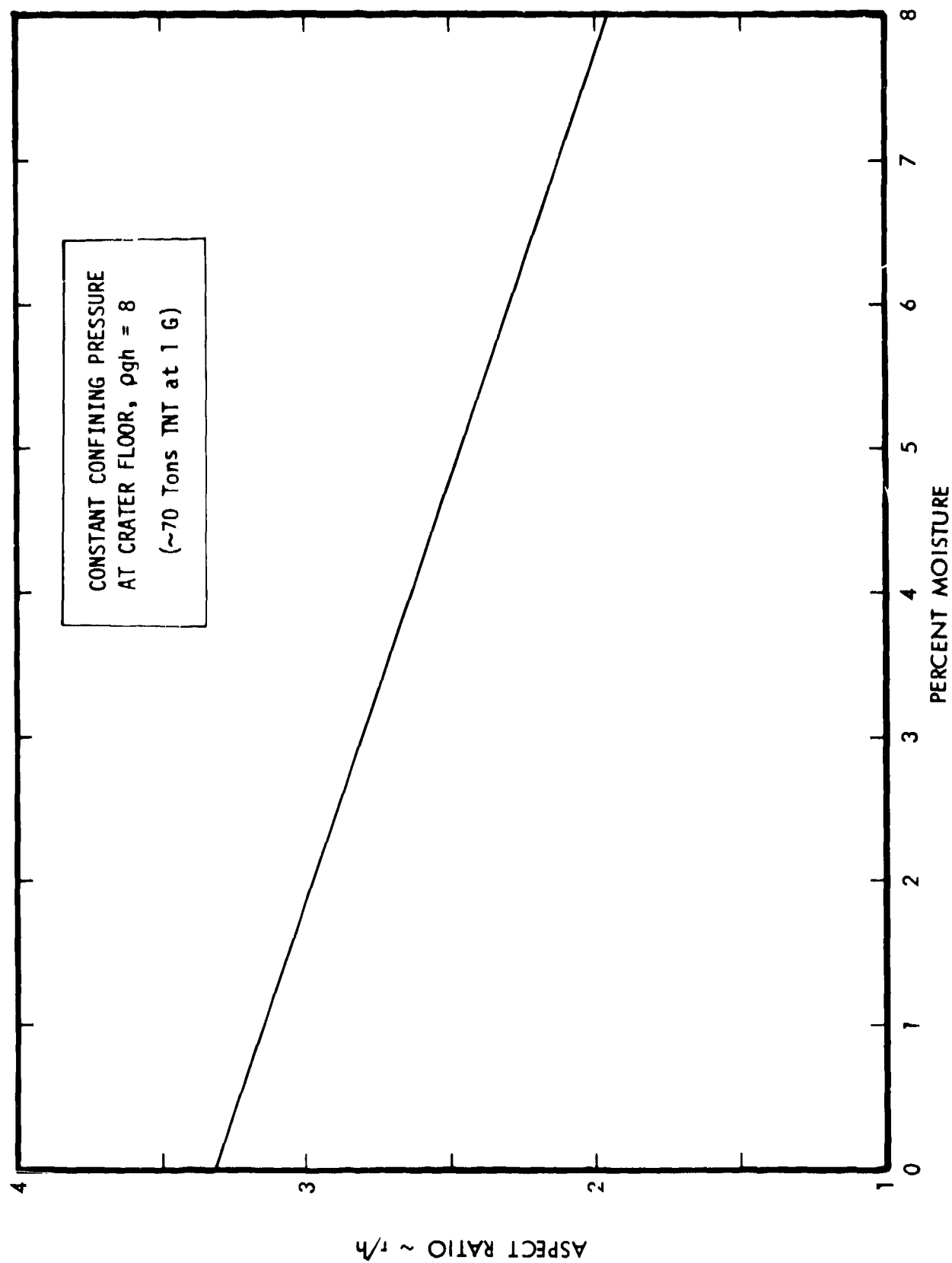
Fig. 5.2 Crossplot at constant value of ρgh (from Fig. 4.5) for crater aspect ratio as a function of moisture content of KAFB alluvium.
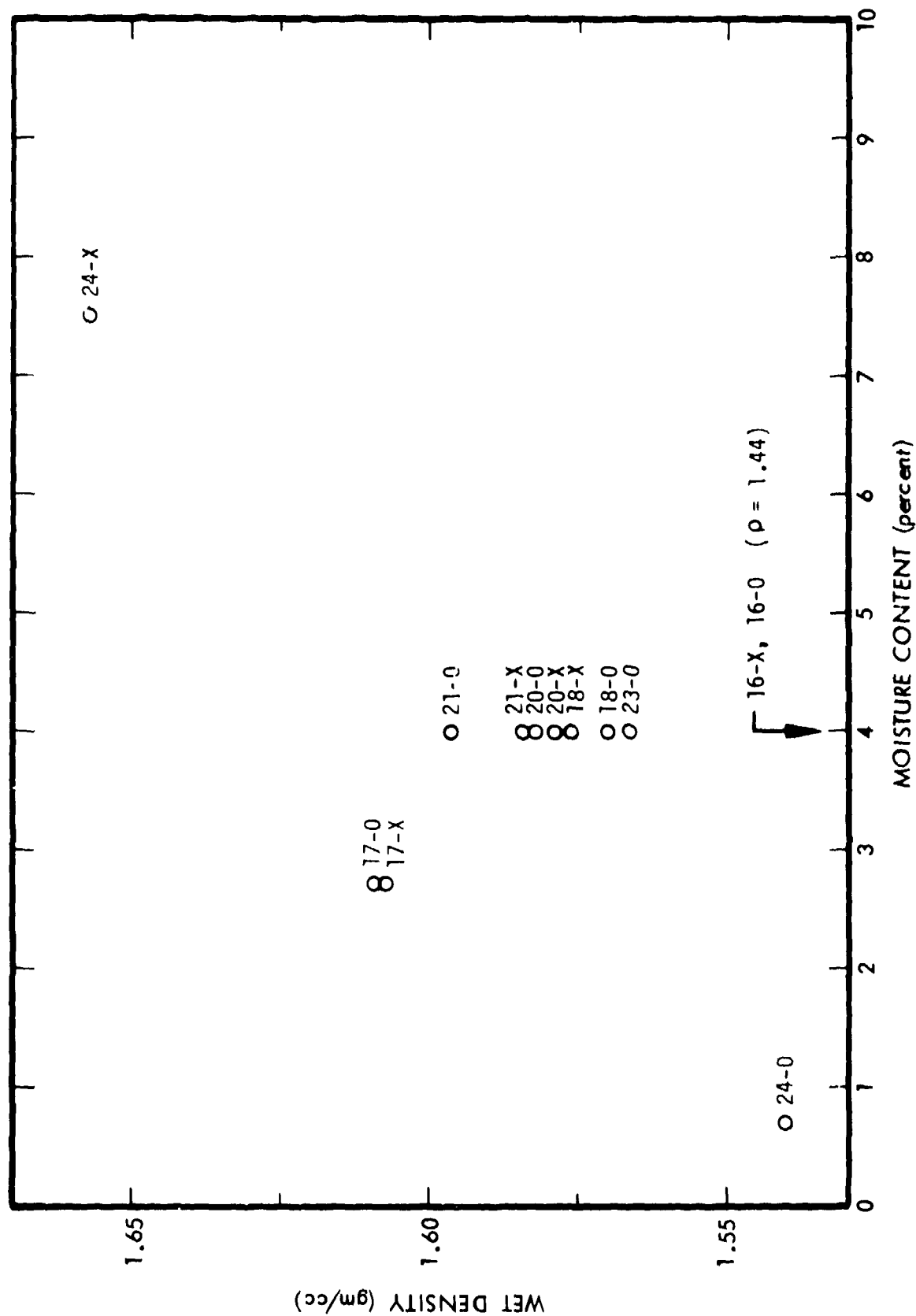
Fig. 5.3 Bulk density of KAFB alluvium versus moisture content. (Samples were each centrifuged for 10 minutes at 500 G to achieve uniform stable soil conditions; the shot number is shown by each point.)

the 2.7-percent-moisture experiments explain the results of 17-X and 17-0.

The variation of aspect ratio with moisture, as shown in Fig. 5.2, again shows a consistent trend. As the moisture content is decreased, the crater becomes flatter. For large moisture content, the crater becomes more nearly hemispherical. There was no consistent variation in the measured values of angle of friction for specimens with moisture in excess of about 2 percent. The only consistent variation in strength for these samples was the cohesion measured in the direct shear tests, as shown in Table 5.1. This leads to the conclusion that it is the decreasing cohesion that causes the flattening of the craters as the moisture content is decreased. At the other extreme, the 7.5-percent-moisture specimen with the greatest cohesion has a bowl shape very nearly the same as the clay.

SECTION 6
SATURATED SAND RESULTS

The feasibility of performing centrifuge cratering experiments in saturated sand was assessed. Six shots were performed in three different types of sand. The results are in qualitative agreement with the strength theory developed above and because of their importance to interpreting the Pacific Proving Ground (PPG) nuclear cratering events, a discussion is included here.

Figure 6.1 shows the results of these six experiments as a plot of the cratering efficiency π_v versus the gravity-scaled-yield parameter π_2. Also shown are the results of six 1-G shots by Piekutowski (unpublished data). The line representing the dry Ottawa sand results is shown for comparison.

At small values of π_2, the data show significantly reduced cratering efficiency as compared to the dry sand. Shot 28-X at 10 G, shows a much lower cratering efficiency. However, for this crater some lateral washing, due to wave motion, was observed on the high-speed-movie coverage during the slowdown of the centrifuge. This was consistent with a reduced crater cross section. For that reason, it is thought to have partially filled in an actual crater volume that was larger. This occurrence is also suggested by the shape of that crater, which was much flatter than all others.

If shot 28-X is discounted (or considered a lower limit), the data are consistent and show the same trend as that observed for the 4-percent-moisture alluvium. At low values of π_2, the cratering efficiency is independent of π_2. This cohesion-dominated, cube-root range corresponds to an "apparent" cohesion (Scott, 1963). As the size parameter π_2 increases, the cratering efficiency crosses over the dry-sand curve, and the saturated-sand cratering efficiency is greater than that for dry sand.

This general behavior is entirely consistent with the strength theory given in Section 3, if the apparent cohesion and the strength envelope of a saturated soil is considered. Seed and Lee (1967) show that the total-stress failure envelope for a saturated sand under undrained conditions is distinctly different than for drained conditions. The undrained test, which corresponds to dynamic phenomena, allows the pore water to carry significant portions of the total pressure or to cavitate, which can influence the effective strength. For dense sands the net strength envelope has an apparent cohesion even though the dry sand itself has none. Furthermore, for sufficiently large confining
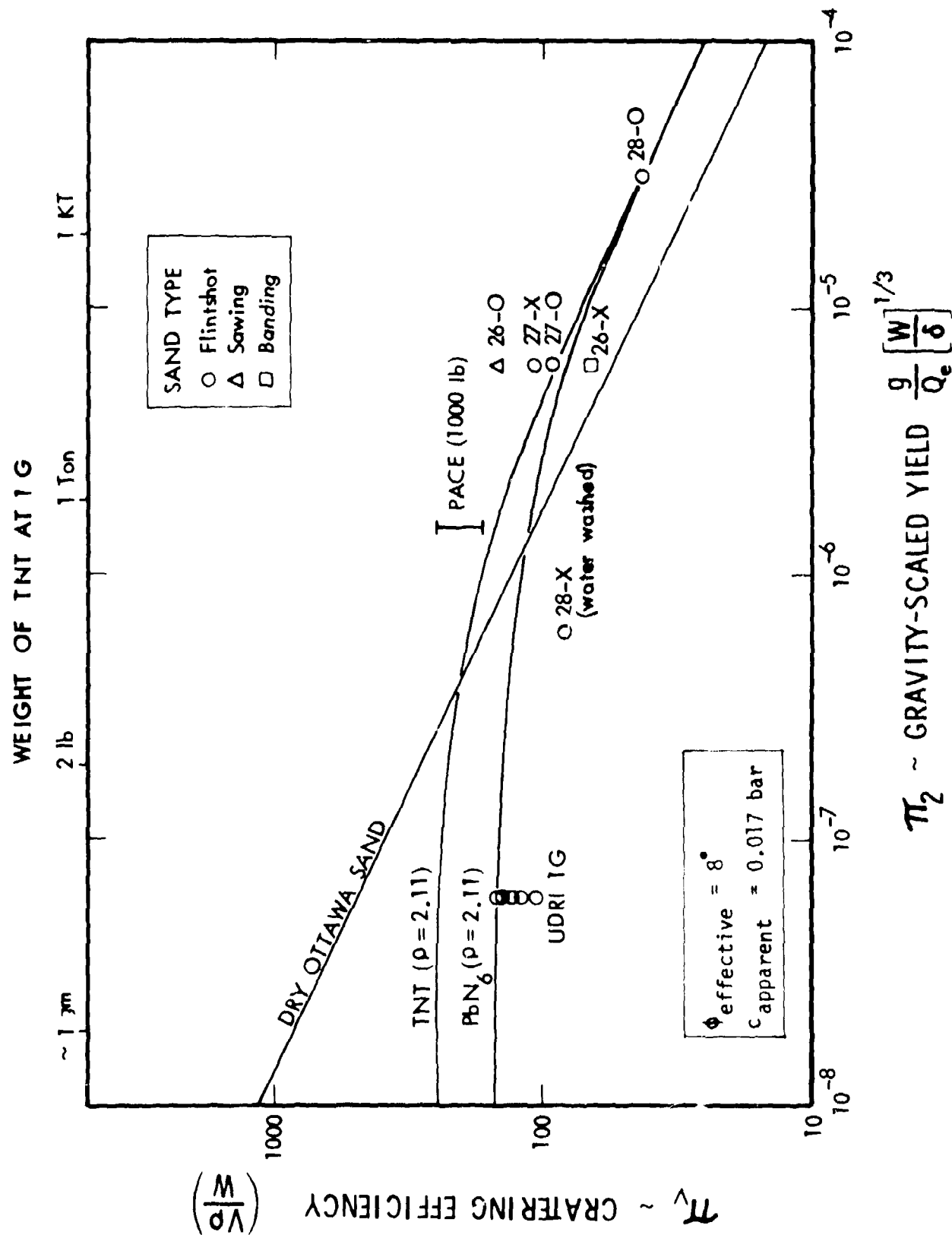
63

Fig. 6.1 Comparison of material strength model for cratering efficiency with centrifuge experimental results for saturated sand.

pressure, the angle of internal friction for the total stress envelope is much smaller than that of the dry sand material itself. Seed and Lee (1967) present data for undrained tests on saturated Sacramento River sand of various porosities. For initially consolidated conditions, the angle of friction for large confining pressure is on the order of 7-8 degrees, as opposed to 37 degrees for the dry sand. For unconsolidated initial conditions and large confining pressure the angle is zero.

These considerations, in conjunction with the strength theory of Section 3, indicate that at small π_2 a saturated sand should behave as a cohesive material and have a cube-root, cohesion-dominated regime. As π_2 is increased, a transition to a gravity-dominated response is expected. For sufficiently large π_2, the effective angle of friction is zero or very small, and the cratering efficiency should be greater than that for dry sand.

The values of the aspect ratio r/h for the saturated sand centrifuge shots are shown versus $\rho g h$ in Fig. 6.2. If the angle of friction is small for large values of π_2, then the stability considerations given for the clay results would also apply to the saturated sand. That is, for large sizes, there would be a limiting value to $\rho g h/c$ and sufficiently large craters would have much greater aspect ratios (r/h). This trend is, of course, observed in the PPG nuclear craters as seen in the comparison plot for aspect ratio in Fig. 6.3. To facilitate the comparison between the centrifuge-formed craters and the field data, a scaled abscissa is used. For the field shots G equals one and the actual depth is shown. For the centrifuge shots the actual crater depth is multiplied by test condition G value. The intent of this figure is to illustrate how the crater aspect ratio increases with crater depth for the saturated sand.
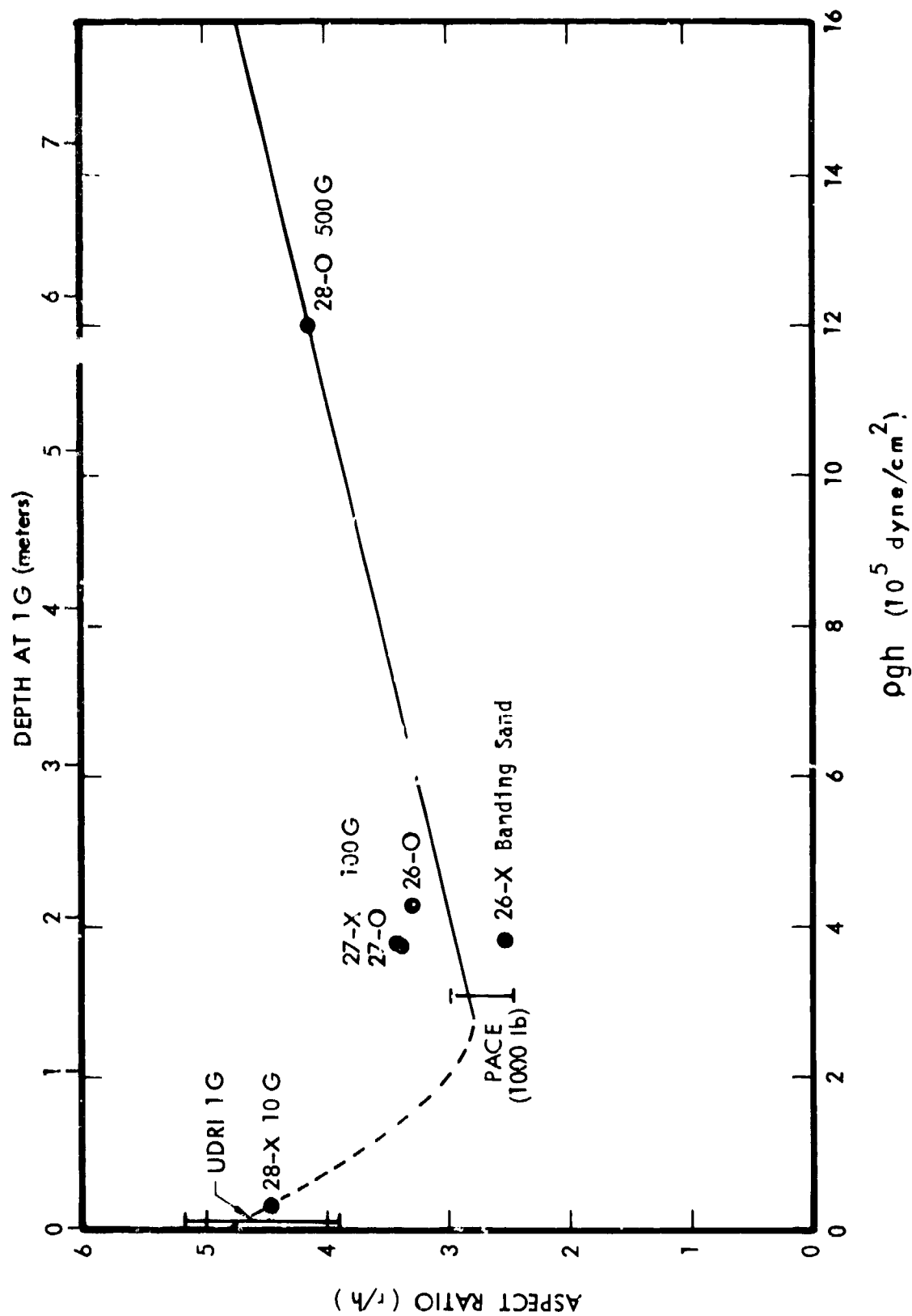
65

Fig. 6.2 Saturated sand results for crater aspect ratio versus lithostatic confining pressure corresponding to crater depth.
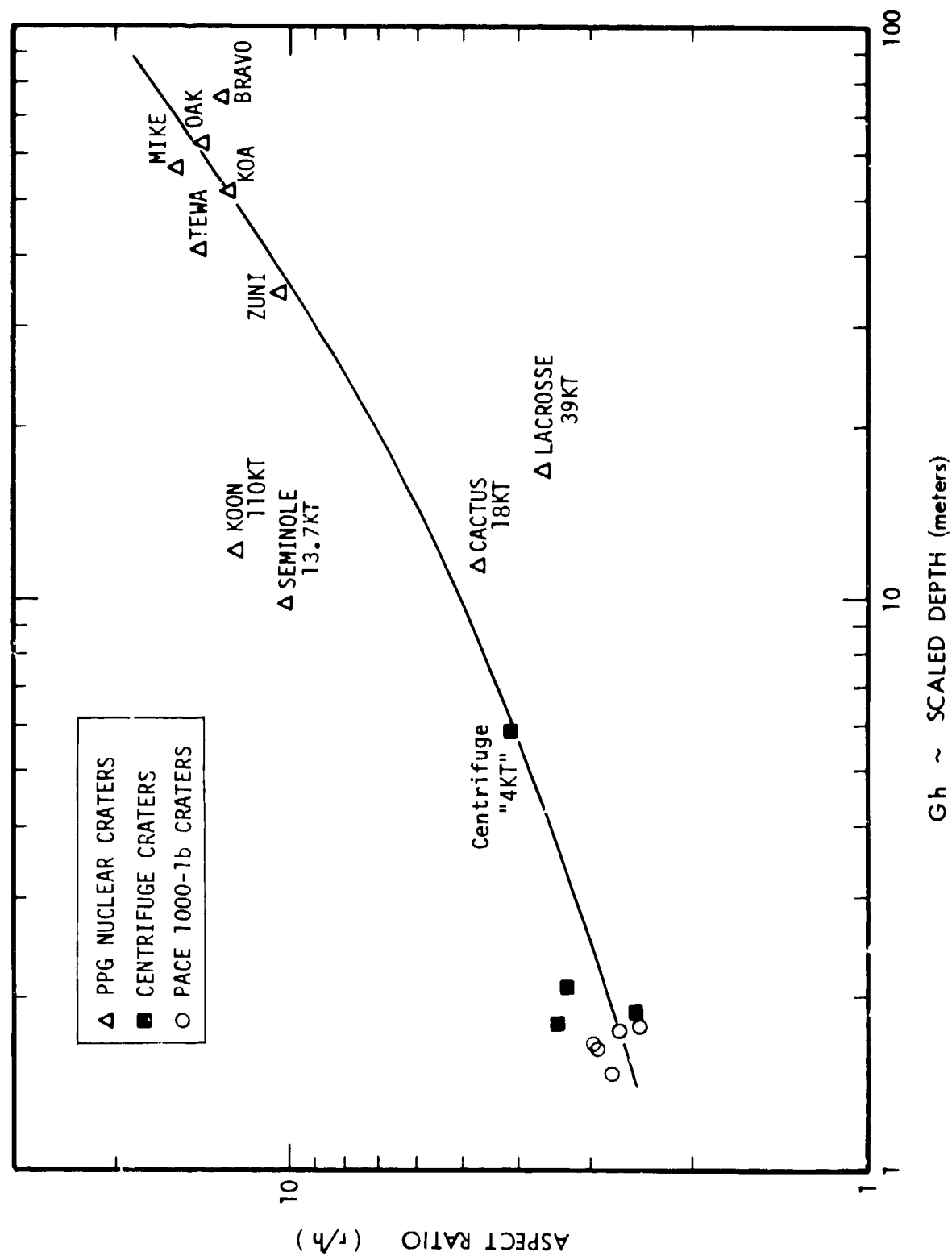
Fig. 6.3 Comparison of centrifuge results for crater aspect ratio with data from PPG nuclear and high-explosive craters.

SECTION 7

CONCLUSIONS

The simulation of large-scale cratering events at subscale on a centrifuge has been successfully extended to a variety of important materials. These include desert alluvium with various moisture contents, water-saturated sand, and an oil-base clay. The results clearly illustrate the dependence of crater volume and shape on gravity and, consequently, the need for elevated gravity in order to correctly model large-scale events at subscale. The accumulated data, in conjunction with previous 1-G results, have identified three differing mechanisms that dominate in different size regimes. The results have been unified into a soil-strength mathematical model that can be used to predict cratering in a variety of materials, and with various high-explosive sources.

It has proved feasible to conduct tests in water-saturated sands. At small-scaled sizes, the cratering efficiency in this material is less than that in dry sand. This is attributed to the "apparent cohesion" of a dense saturated granular medium under undrained conditions. At large scaled-sizes, the cratering efficiency exceeds that of dry sand. This is attributed to the small friction angle of the material when the pressure is in excess of the critical confining pressure of the sand. These interpretations are consistent with the soil-strength model that has been presented.

Tests have also been performed in desert alluvium with various controlled moisture contents. The data show a strength-dominated regime at small-scaled sizes and become more-or-less asymptotic to the dry-sand behavior at scaled explosive-source sizes in the kiloton and above range. Small variations in the moisture content had a significant effect on both crater size and structure, consistent with the measured material-strength properties and the model presented.

Material property differences also produced large differences in crater shape and structure. The dry sand craters had essentially constant shape with varying scaled size. The alluvium craters, at a fixed moisture content, showed a trend toward shallower craters at decreasing size. For fixed scaled-source size, shallower craters were observed with decreasing moisture content.

The most dramatic change of shape with size was observed for the clay and the saturated-sand craters. In both cases there was a threshold above which

the craters became increasingly shallow. This threshold has been interpreted as a slope-stability limit. There is also evidence from the clay-crater data that large-scale shallow craters do not necessarily go through a transient deeper bowl-shaped phase as commonly suggested.

The shape of the saturated-sand craters is consistent with the PACE field experiments. Extrapolation of the observed reduction of aspect ratio (radius/depth) with yield is consistent with the trend observed for the PPG nuclear craters.

This experimental study successfully examined the applicability of the centrifuge technique to a variety of real-world materials. The material properties were sufficiently well controlled and characterized so that a meaningful mathematical model that predicts the effects of material properties on cratering behavior has been generated. Its validity has been demonstrated over a range of more than nine orders of magnitude of scaled yield and the model can be used as a high-explosive baseline for nuclear yields of interest. Included in the scaled-yield parameter is a dependence upon source energy density. The validity of this parameter has been demonstrated over a range of four to one in energy density for high explosives. For impact cratering, a range of more than two orders of magnitude on energy density is in agreement with this same scaled-yield parameter (Schmidt and Holsapple, 1978a). Furthermore, using a "working gas" concept as defined by Butkovich (1967) to establish a value for nuclear energy density appropriate to the time-scale of crater excavation, this source model promises to provide a scaling tool allowing application of these centrifuge results to the prediction of nuclear craters (Schmidt et al. 1979).

Results obtained are only for half-buried charges. They have convincingly demonstrated that the centrifuge provides a viable method to determine cratering behavior for various soils at large explosive yields of interest. In particular it can be used to examine conditions leading to the slumping of transient bowl-shape craters. Further, this is of particular interest in the case of saturated media which may undergo blast-induced liquefaction and thereby reduce the shear strength to below that required for stability.

Recommendations are to extend the data base to include tangent-above charge configurations. As height-of-burst is increased, the transition between the strength-dominated cube-root regime and the gravity-dominated regime is expected to be different from that observed for half-buried charges.

69

Preliminary h.o.b. data for scaled yields above this transition indicate that the scaling exponent is slightly less (1/3.8) than observed for half-buried explosives (1/3.6). This behavior must be examined in particular for water-saturated soils of varying porosity. Small differences in the scaling leads to large discrepancies in predictions for large yields. Centrifuge techniques provide a means to test these various mechanisms.

SECTION 8
REFERENCES

Butkovich T. R. (1967) The gas equation of state for natural materials, UCRL-14729, Lawrence Radiation Laboratory, Livermore, CA.

Chabai A. J. (1965) On scaling dimensions of craters produced by buried explosives. J. Geophys. Res. 70, p. 5075-5098.

Charters A. C. and Summers J. L. (1959) Some comments on the phenomena of high speed impact. NOLR 1238, U. S. Naval Ordnance Laboratory, White Oak, Silver Springs, MD, p. 200-221.

Gault D. E. and Wedekind J. A. (1977) Experimental hypervelocity impact into quartz sand--II, Effects of gravitational acceleration. Impact and Explosion Cratering, p. 1231-1244 (D. J. Roddy, R. O. Pepin and R. B. Merrill, editors) Pergamon Press.

Gault D. E. (1978) Experimental impact "craters" formed in water: gravity scaling realized (abstract). Trans. Am. Geophysc. Union 59 (12) p. 1121.

Gaffney E. S. (1978) Effects of gravity on explosive-craters. Proc. Ninth Lunar and Planetary Sci. Conf. p. 3831-3842.

James R. G. (1977) Cratering experiments on the centrifuge. University of Cambridge, England, Dept. of Civil Engineering Report.

James R. G. (1978) Cratering experiments on the centrifuge (2nd series) University of Cambridge, England, Dept. of Civil Engineering Report.

McKinnon W. B. and Melosh H. J. (1978) Further investigation into the role of plastic failure in crater modification (Abstract). Lunar and Planetary Science IX, p. 729-731. Lunar and Planetary Institute, Houston, TX.

Melosh H. J. and McKinnon W. B. (1979) Theoretical and experimental study of crater collapse (Abstract). Lunar and Planetary Science X, p. 830-832. Lunar and Planetary Institute, Houston, TX.

O'Keefe J. A. and Ahrens T. J. (1978) Late stage crater flows and the effect of strength on transient crater depth (abstract). Lunar and Planetary Science IX, March 1978, p. 823-825.

Piekutowski A. J. (1974) Laboratory-scale high-explosive cratering and ejecta phenomenology studies. Air Force Weapons Laboratory report AFWL-TR-72-155, Albuquerque, NM., 328 pp.

Piekutowski A. J. (1975) A comparison of crater effects for lead azide and PETN explosive charges. Air Force Weapons Laboratory Report AFWL-TR-74-182, Albuquerque, NM., 140 pp.

Piekutowski A. J. (1977) University of Dayton Research Institute, Dayton, OH, Private Communication.

Schmidt R. M. (1978) Centrifuge simulation of the JOHNIE BOY 500-ton cratering event. Proc. Ninth Lunar and Planetary Sci. Conf. p. 3877-3889.

Schmidt R. M. and Holsapple K. A. (1978a) Centrifuge cratering scaling experiments I: Dry granular soils. Defense Nuclear Agency Report 4568F, Washington, D.C., 172 pp.

Schmidt R. M. and Holsapple K. A. (1978b) A gravity-scaled energy parameter relating impact and explosive crater size (abstract). Trans. Am. Geophys. Union, 59 (12), p. 1121.

Schmidt R. M. and Holsapple K. A. (1980) Theory and experiments on centrifuge cratering. J. Geophys. Res. 85, B, p. 235-252.

Schmidt R. M., Holsapple K. A. and Wauchope C. R. (1979) Nuclear cratering: Why a centrifuge? Proc. Defense Nuclear Agency Strategic Structures Biennial Review Conf. p. IV-13 SRI International Menlo Park, CA.

Seed, H. B. and Lee K. L. (1967) Undrained strength of characteristics of cohesionless soils. J. of Soil Mechanics and Foundation Div. ASCE, SM6, p. 333-360.

Scott, R. F. (1963) Principles of soil mechanics, Addison-Wesley Publishing Co. Inc., p. 361-362, Reading, MA.

Truesdell C. and Toupin R. (1960) The classical field theories, Handbuch der Physik, edited by S. Flugge, Springer-Verlag, Berlin, 1960, Vol. III/1, p. 226-902.

APPENDIX A
CENTRIFUGE SHOT RECORDS

This section contains all the data for the elevated gravity centrifuge experiments. A table is given for each run which includes the test conditions for the two shots performed at the opposing rotor ends. Following each table is a figure which contains a comparison plot for the two craters and a set of documentary photographs.

SHOT NUMBER	14-0	14-X
DATE	9/19/77	9/19/77
PURPOSE	π_2 Test	π_2 Test
CHARGE DESCRIPTION	CICS-1.265(B-3)	CICS-4(B-5)
CHARGE MASS (gm)	0.13 AgN_3/1.23 PETN	0.13 AgN_3/3.94 PETN
CHARGE RADIUS (cm)	0.565	0.826
CHARGE CONFIGURATION	Half-Buried Sphere	Half-Buried Sphere
TEST BED MATERIAL	Permoplast Clay (#52)	Permoplast Clay (#47)
TEST BED DENSITY (gm/cc)	1.53	1.53
MOISTURE CONTENT (%)	--	--
TEST BED GEOMETRY	Homogeneous	Homogeneous
CENTRIFUGE SPEED (rpm)	571	471
GROUND ZERO RADIUS (cm)	124.5	124.5
CENTRIFUGAL ACCELERATION (G)	454	309
CRATER VOLUME (cc)	75.4	244
CRATER RADIUS (cm)	4.17	5.91
MAX CRATER DEPTH (cm)	2.59	4.23
CRATER ASPECT RATIO (r/h)	1.61	1.40
CRATER C/L DEPTH (cm)	2.59	4.23
LIP RADIUS (cm)	5.05	7.20
LIP HEIGHT (cm)	0.90	1.22
LIP VOLUME (cc)	35	79.3
PI_2	7.59E-6	7.26E-6
PI_V	98.0	93.4
PI_R	4.46	4.26
PI_H	2.92	3.04

A2

| SHOT NUMBER RANGE (cm)	14-0 DEPTH (cm)	14-X DEPTH (cm)
0.0	2.594	4.231
0.6	2.526	3.986
1.2	2.397	3.942
1.8	2.226	3.826
2.4	1.923	3.575
3.0	1.440	3.196
3.6	0.774	2.948
4.2	-0.045	2.366
4.8	-0.749	1.590
5.4	-0.824	0.800
6.0	-0.430	-0.136
6.6	-0.046	-0.829
7.2	-0.049	-1.223
7.8	-0.059	-0.859
8.4	--	-0.212
9.0	--	0.008
9.6	-0.065	0.022
10.2	--	--
10.8	--	--
11.4	-0.097	0.055
12.0	--	--
12.6	--	--
13.2	-0.134	0.047
13.8	--	--
14.4	--	--
15.0	-0.201	0.025
15.6	--	--
16.2	--	--
16.8	-0.311	0.008
17.4	--	--
18.0	--	--
18.6	--	--
19.2	--	--
19.8	--	--
20.4	--	--
21.0	--	--

A3
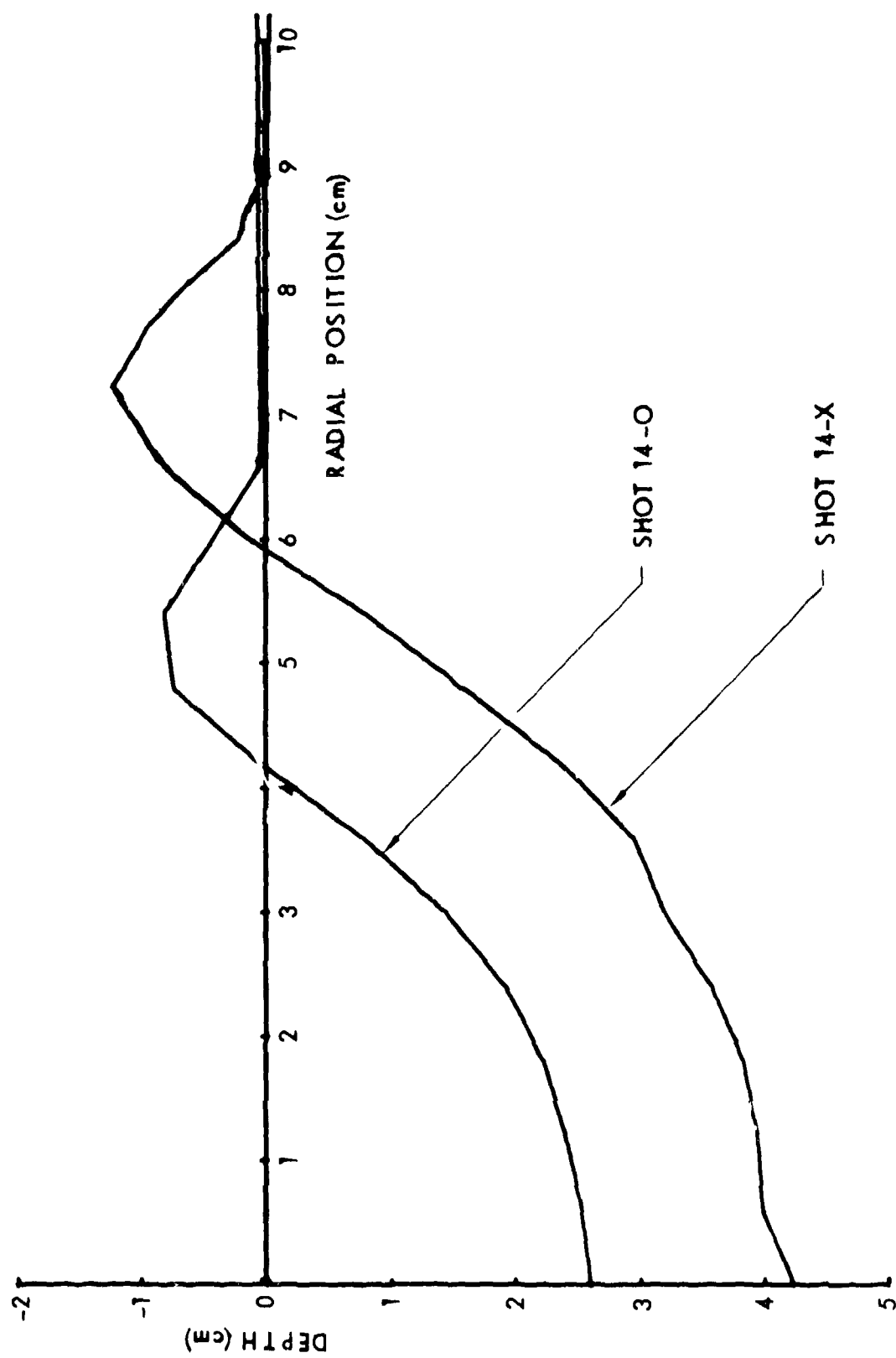
Fig. A1.   Comparison of crater profiles.
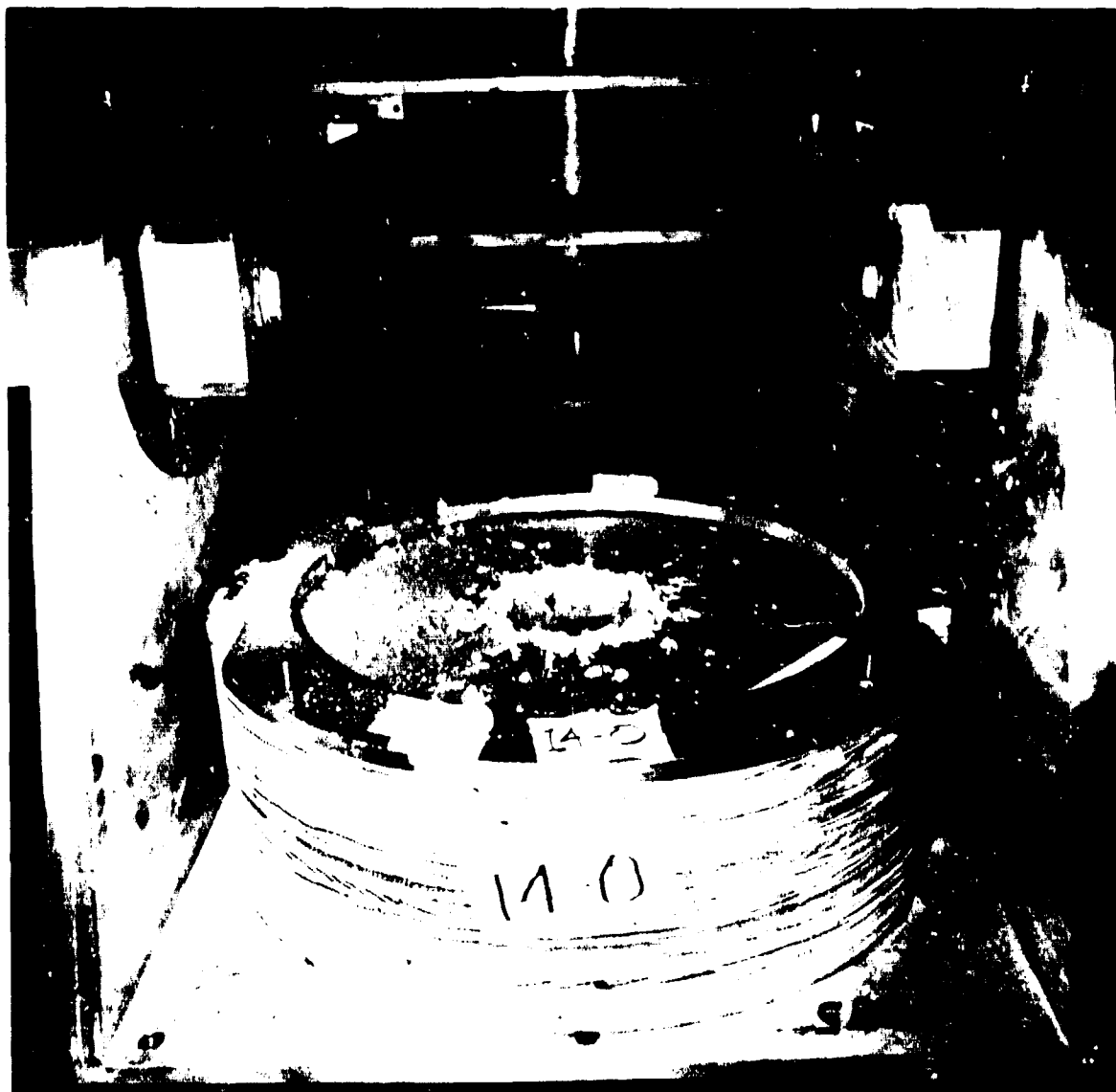
Fig. A2. Shot 14-0, crater formed at 454 G by spherical 1.34-gm PETN charge half-buried in "Permoplast" oil-base clay.

A5

Fig. A3.   Shot 14-X, crater formed at 309 G by spherical 4.08-gm PETN
charge half-buried in "Permoplast" oil-base clay.

SHOT NUMBER	20-0	20-X
DATE	5/18/78	5/18/78
PURPOSE	10-G Check on	10-G Check on
	UDRI Data	UDRI Data
CHARGE DESCRIPTION	CILAS-13(B-3)	CICS-5(B-5)
CHARGE MASS (gm)	1.71 PbN_6	0.13 AgN_3/0.36 PETN
CHARGE RADIUS (cm)	0.508	0.390
CHARGE CONFIGURATION	Half-Buried Sph re	Half-Buried Sphere
TEST BED MATERIAL	KAFB D.A. #10/#11	KAFB D.A. #8/#9
TEST BED DENSITY (gm/cc)	1.582	1.579
MOISTURE CONTENT (%)	3.9	4.0
TEST BED GEOMETRY	Homogeneous	Homogeneous
CENTRIFUGE SPEED (rpm)	84.6	84.6
GROUND ZERO RADIUS (cm)	125	125
CENTRIFUGAL ACCELERATION (G)	10	10
CRATER VOLUME (cc)	43.4	26.1
CRATER RADIUS (cm)	5.36	4.61
MAX CRATER DEPTH (cm)	1.37	1.28
CRATER ASPECT RATIO (r/h)	3.91	3.60
CRATER C/L DEPTH (cm)	1.37	1.28
LIP RADIUS (cm)	7.80	7.20
LIP HEIGHT (cm)	0.16	0.14
LIP VOLUME (cc)	48.3	42.4
PI_2	6.08E-7	1.37E-7
PI_V	40.4	84.1
PI_R	5.23	6.81
PI_H	1.34	1.89

| SHOT NUMBER	20-0	20-X
RANGE (cm)	DEPTH (cm)	DEPTH (cm)
0.0	1.368	1.283
0.6	1.306	1.251
1.2	1.126	0.958
1.8	0.822	0.583
2.4	0.777	0.472
3.0	0.653	0.439
3.6	0.507	0.295
4.2	0.366	0.111
4.8	0.158	-0.053
5.4	-0.017	-0.105
6.0	-0.070	-0.107
6.6	-0.111	-0.119
7.2	-0.149	-0.139
7.8	-0.164	-0.133
8.4	-0.145	-0.103
9.0	-0.117	-0.100
9.6	-0.113	-0.078
10.2	-0.095	-0.068
10.8	-0.081	-0.059
11.4	-0.076	-0.050
12.0	-0.066	-0.046
12.6	-0.037	-0.031
13.2	-0.036	-0.027
13.8	-0.026	-0.022
14.4	-0.021	-0.020
15.0	-0.019	-0.014
15.6	-0.007	-0.014
16.2	-0.005	-0.014
16.8	-0.001	-0.002
17.4	0.000	-0.002
18.0	0.006	-0.004
18.6	0.006	-0.005
19.2	0.014	-0.002
19.8	--	-0.009
20.4	--	-0.018
21.0	--	--
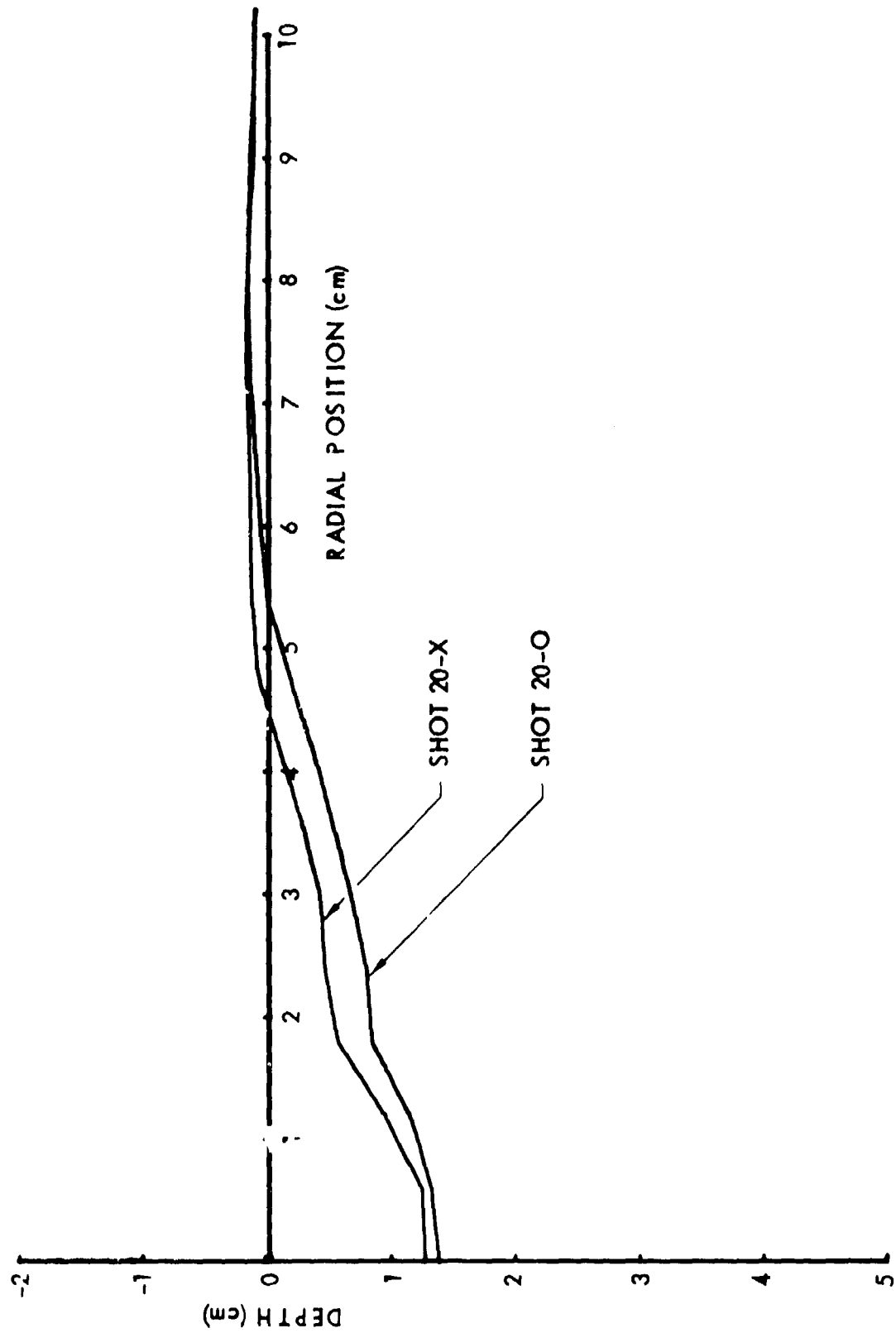
Fig. A4. Comparison of crater profiles.
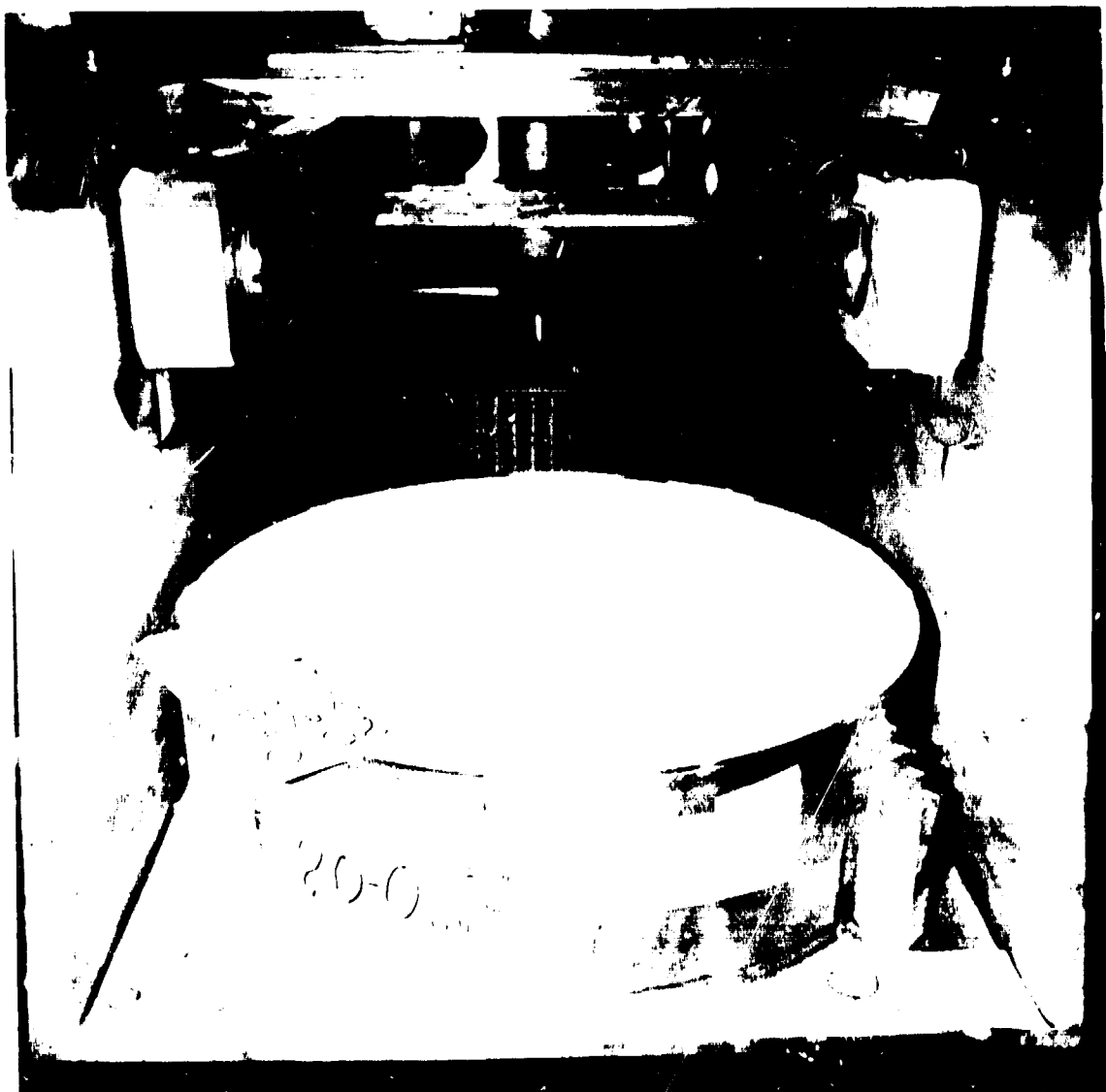
Fig. A5.   Shot 20-0, crater formed at 10 G by spherical 1.70-gm PbN$_6$ charge half-buried in KAFB desert alluvium.
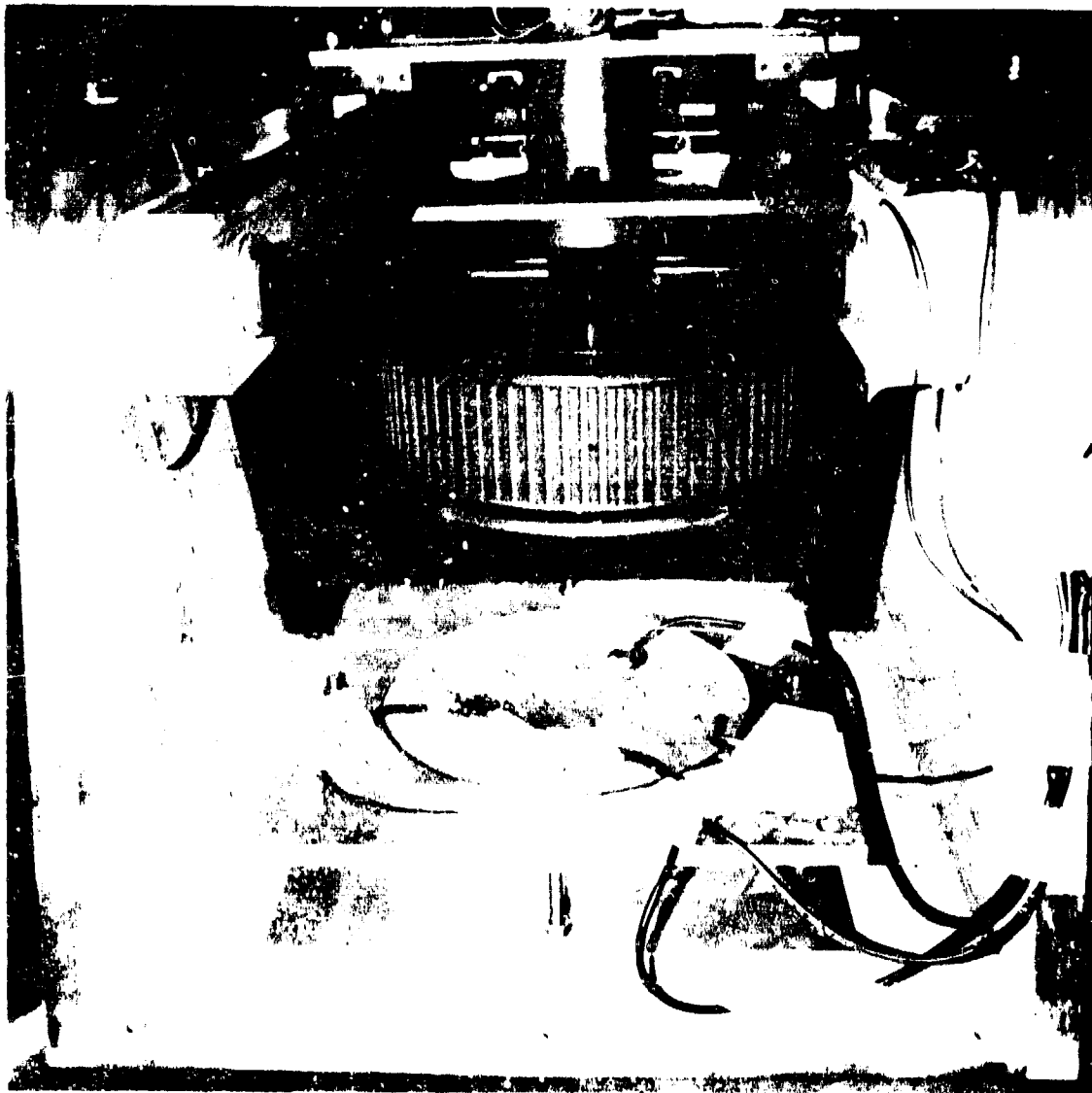
Fig. A6.   Shot 20-X, crater formed at 10 G by spherical 0.49-gm PETN
charge half-buried in KAFB desert alluvium.

SHOT NUMBER	21-0	21-X
DATE	5/26/78	5/26/78
PURPOSE	Maximum π_2	Maximum π_2
CHARGE DESCRIPTION	CICS-4(B-12)	CILAS-13(B-4)
CHARGE MASS (gm)	0.13 AlN_3/3.94 PETN	1.71 PbN_6
CHARGE RADIUS (cm)	0.826	0.508
CHARGE CONFIGURATION	Half-Buried Sphere	Half-Buried Sphere
TEST BED MATERIAL	KAFB D.A. #11	KAFB D.A. #12
TEST BED DENSITY (gm/cc)	1.596	1.584
MOISTURE CONTENT (%)	4.1	4.3
TEST BED GEOMETRY	Homogeneous	Homogeneous
CENTRIFUGE SPEED (rpm)	610	610
GROUND ZERO RADIUS (cm)	125	125
CENTRIFUGAL ACCELERATION (G)	520	520
CRATER VOLUME (cc)	103	23.7
CRATER RADIUS (cm)	5.99	3.69
MAX CRATER DEPTH (cm)	2.37	1.58
CRATER ASPECT RATIO (r/h)	2.53	2.34
CRATER C/L DEPTH (cm)	2.37	1.58
LIP RADIUS (cm)	7.20	4.80
LIP HEIGHT (cm)	0.32	0.19
LIP VOLUME (cc)	47.7	12.6
PI_2	1.22E-5	3.16E-5
PI_V	40.3	22.1
PI_R	4.38	3.60
PI_H	1.73	1.54

SHOT NUMBER	21-0	21-X
RANGE (cm)	DEPTH (cm)	DEPTH (cm)
0.0	2.374	1.579
0.6	2.351	1.568
1.2	2.367	1.282
1.8	2.237	0.696
2.4	1.908	0.548
3.0	1.333	0.334
3.6	0.945	0.038
4.2	0.737	-0.188
4.8	0.504	-0.189
5.4	0.245	-0.113
6.0	-0.002	-0.066
6.6	-0.215	-0.037
7.2	-0.315	-0.020
7.8	-0.265	-0.013
8.4	-0.183	-0.004
9.0	-0.124	-0.003
9.6	-0.092	-0.002
10.2	-0.060	0.001
10.8	-0.031	0.004
11.4	-0.031	0.011
12.0	-0.015	0.012
12.6	-0.012	0.014
13.2	-0.010	0.012
13.8	-0.006	0.006
14.4	-0.010	0.004
15.0	-0.003	0.010
15.6	0.002	0.005
16.2	0.001	0.010
16.8	-0.002	0.001
17.4	-0.000	0.001
18.0	-0.004	0.001
18.6	-0.006	0.002
19.2	-0.005	0.002
19.8	-0.007	0.007
20.4	--	-0.001
21.0	--	--

A13
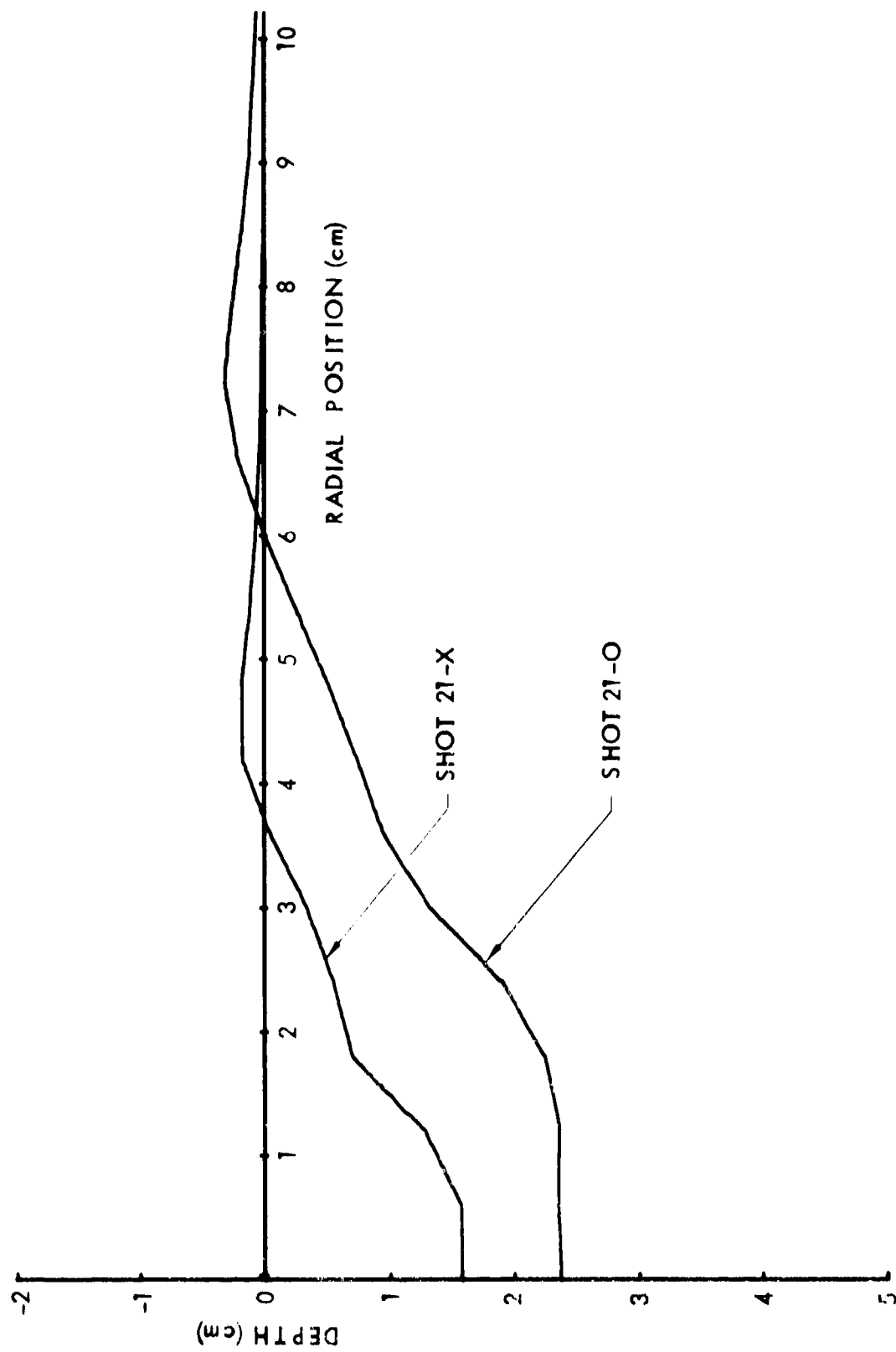
Fig. A7. Comparison of crater profiles.

Fig. A8. Shot 21-0, crater formed at 520 G by spherical 4.08-gm PETN charge half-buried in KAFB desert alluvium.

A15

Fig. A9.   Shot 21-X, crater formed at 520 G by spherical 1.70-gm PbN_6 charge half-buried in KAFB desert alluvium.

SHOT NUMBER	22-X-1	22-X-2
DATE	6/2/78	6/2/78
PURPOSE	Stress Gages	Stress Gages
CHARGE DESCRIPTION	CILAS-13(B-5)	CILAS-13(B-6)
CHARGE MASS (gm)	1.70 PbN$_6$	1.70 PbN$_6$
CHARGE RADIUS (cm)	0.508	0.508
CHARGE CONFIGURATION	Half-Buried Sphere	Half-Buried Sphere
TEST BED MATERIAL	Permoplast Clay (#53)	Permoplast Clay (#55)
TEST BED DENSITY (gm/cc)	1.53	1.53
MOISTURE CONTENT (%)	--	--
TEST BED GEOMETRY	Homogeneous	Homogeneous
CENTRIFUGE SPEED (rpm)	613	82
GROUND ZERO RADIUS (cm)	132.7	132.7
CENTRIFUGAL ACCELERATION (G)	557	10
CRATER VOLUME (cc)	40.4	53.4
CRATER RADIUS (cm)	3.32	3.24
MAX CRATER DEPTH (cm)	2.37	2.92
CRATER ASPECT RATIO (r/h)	1.40	1.11
CRATER C/L DEPTH (cm)	2.37	2.92
LIP RADIUS (cm)	4.20	4.20
LIP HEIGHT (cm)	0.52	1.09
LIP VOLUME (cc)	12.9	51.3
PI$_2$	3.39E-5	6.08E-7
PI$_V$	36.4	48.1
PI$_R$	3.21	3.13
PI$_H$	2.29	2.82

SHOT NUMBER	22-X-1	22-X-2
RANGE (cm)	DEPTH (cm)	DEPTH (cm)
0.0	2.372	2.918
0.6	2.283	2.807
1.2	2.042	2.596
1.8	1.727	2.266
2.4	1.168	1.661
3.0	0.362	0.533
3.6	-0.382	-0.810
4.2	-0.523	-1.088
4.8	-0.009	-0.289
5.4	0.005	-0.172
6.0	0.034	-0.115
6.6	0.058	-0.076
7.2	0.079	-0.050
7.8	0.084	-0.048
8.4	0.101	-0.027
9.0	0.089	-0.027
9.6	0.070	-0.010
10.2	0.033	0.009
10.8	-0.005	0.008
11.4	--	--
12.0	--	--
12.6	--	--
13.2	--	--
13.8	--	--
14.4	--	--
15.0	--	--
15.6	--	--
16.2	--	--
16.8	--	--
17.4	--	--
18.0	--	--
18.6	--	--
19.2	--	--
19.8	--	--
20.4	--	--
21.0	--	--
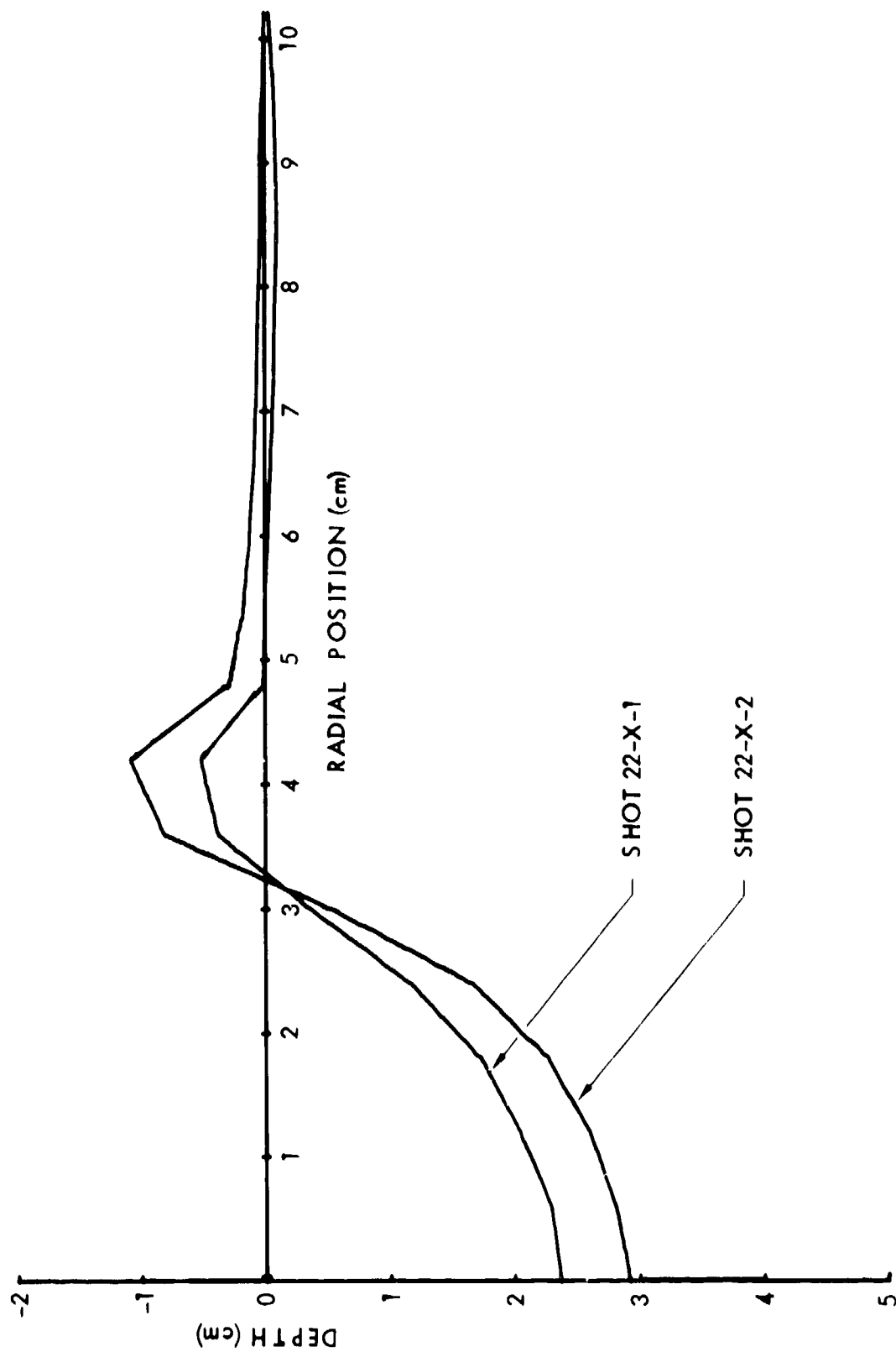
Fig. A10.   Comparison of crater profiles.

Fig. A11.   Pre-shot photograph (22-X-1) showing placement of three carbon stress gauges. Piezo pin used to generate scope trigger shown at 10 o'clock position.
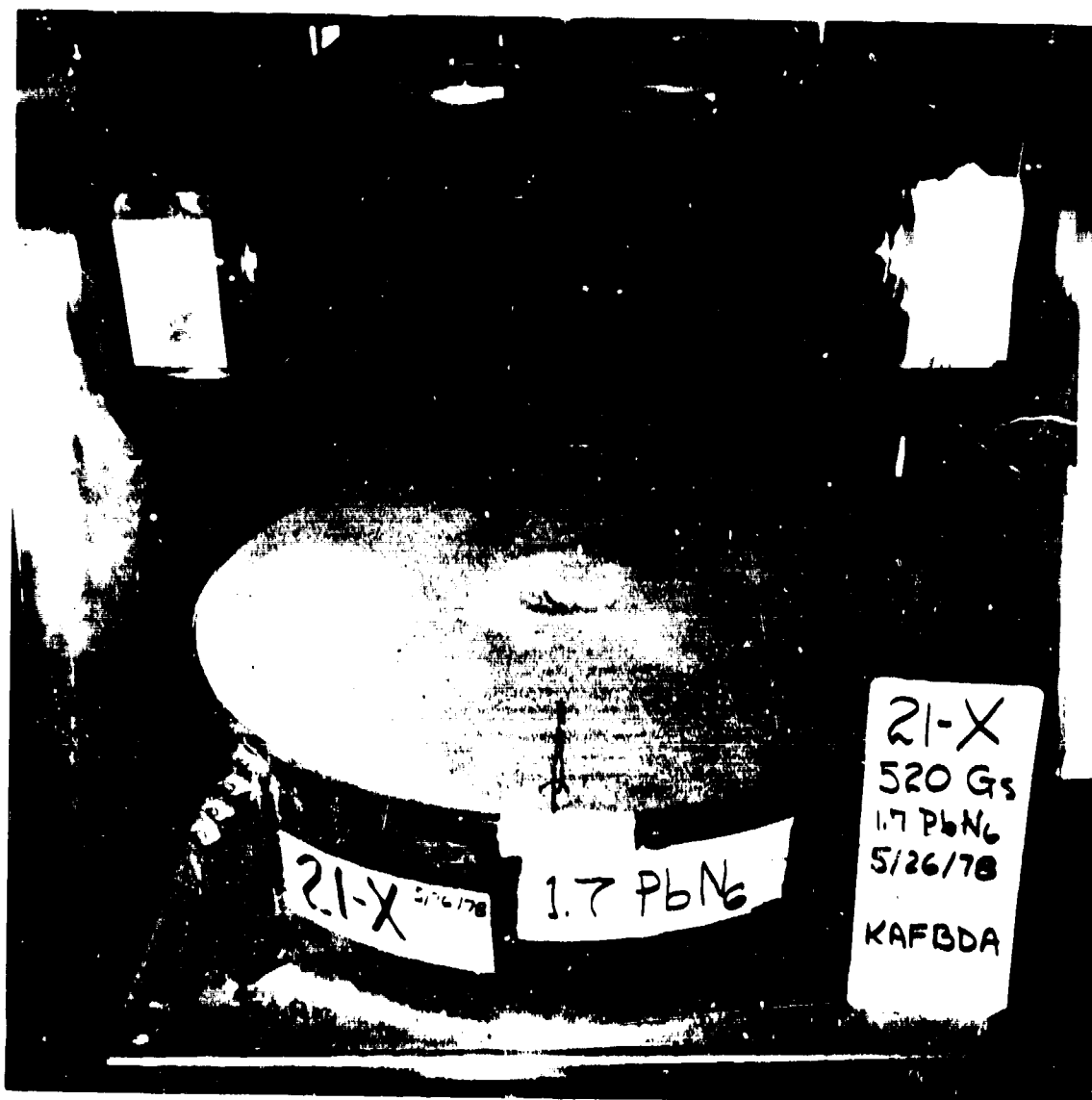
Fig. A12. Shot 22-X-1, crater formed at 557 G by spherical 1.70-gm PbN_6 charge half-buried in "Permoplast" oil-base clay.
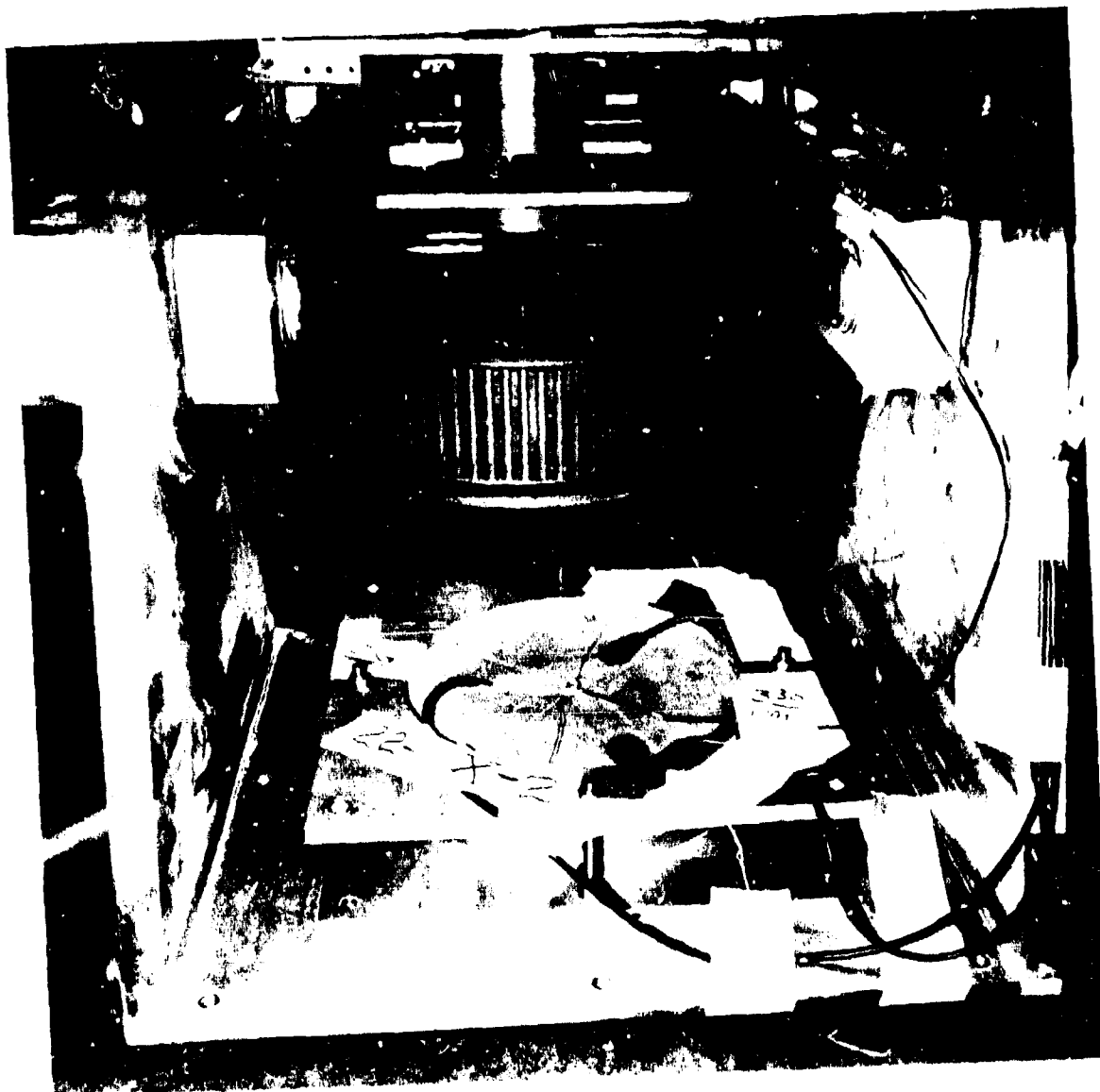
Fig. A13. Pre-shot photograph (22-X-2) showing placement of three carbon stress gauges. Piezo pin used to generate scope trigger shown at 4 o'clock position.
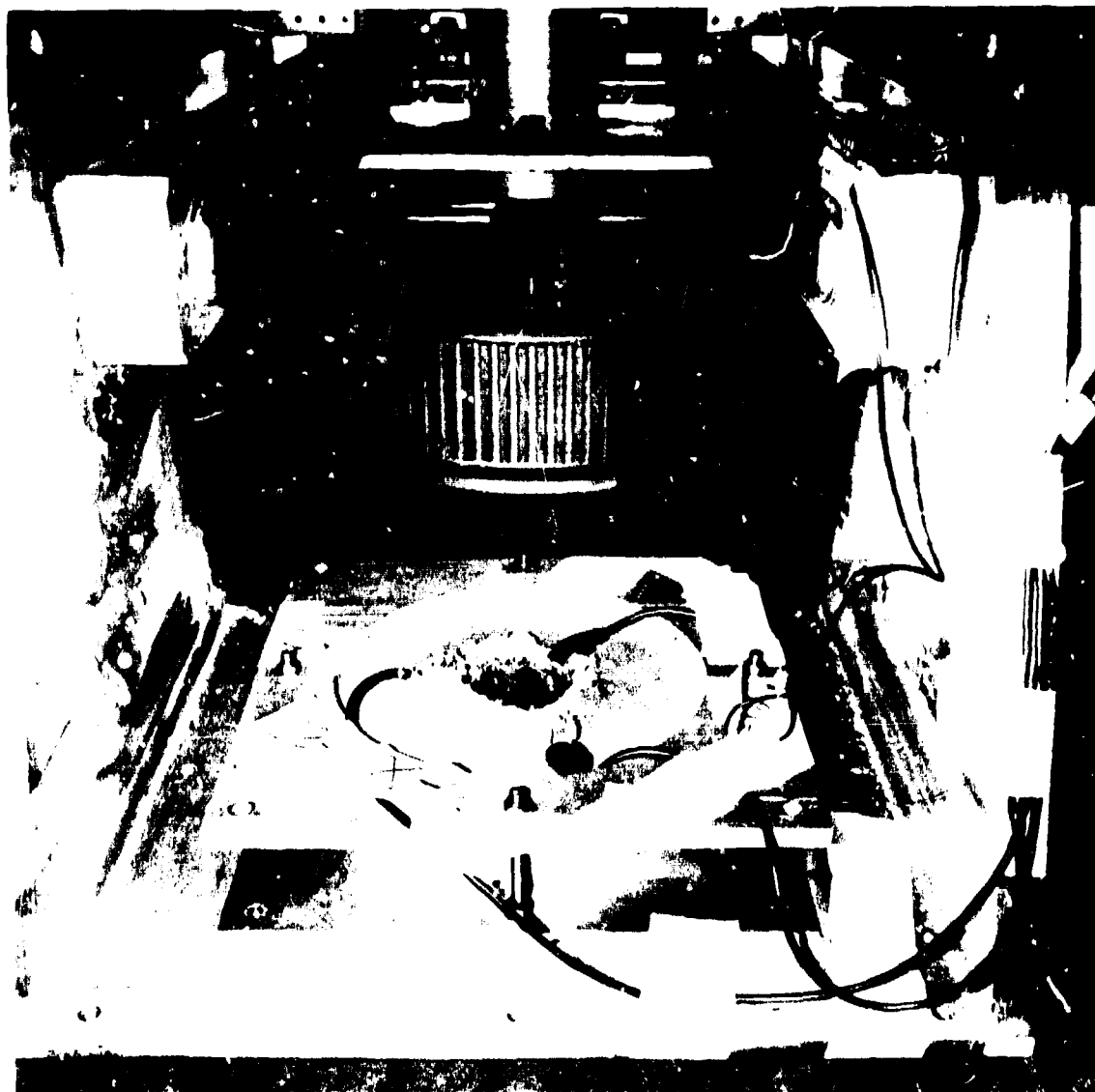
Fig. A14.   Shot 22-X-2, crater formed at 10 G by spherical 1.70-gm PbN_6 charge half-buried in "Permoplast" oil-base clay.

SHOT NUMBER	23-0	23-X
DATE	7/14/78	7/14/78
PURPOSE	Alluv	Alluvium Strength
CHARGE DESCRIPTION	CICS-5(B-2)	CICS-4.0(B-13)
CHARGE MASS (gm)	0.13 AgN$_3$/0.3	0.13 AgN$_3$/3.95 PETN
CHARGE RADIUS (cm)	0.390	0.826
CHARGE CONFIGURATION	Half-Buried Sphere	Half-Buried Sphere
TEST BED MATERIAL	KAFB D.A. #1R/#2R	KAFB D.A. #3R/#4R
TEST BED DENSITY (gm/cc)	1.566	1.570
MOISTURE CONTENT (%)	3.8	4.0
TEST BED GEOMETRY	Homogeneous	Homogeneous
CENTRIFUGE SPEED (rpm)	358	258
GROUND ZERO RADIUS (cm)	125	125
CENTRIFUGAL ACCELERATION (G)	179	93
CRATER VOLUME (cc)	19.1	169
CRATER RADIUS (cm)	3.96	7.52
MAX CRATER DEPTH (cm)	1.28	2.50
CRATER ASPECT RATIO (r/h)	3.09	3.01
CRATER C/L DEPTH (cm)	1.22	2.48
LIP RADIUS (cm)	4.80	9.60
LIP HEIGHT (cm)	0.11	0.40
LIP VOLUME (cc)	8.58	127
PI_2	2.45E-6	2.18E-6
PI_V	61.0	65.1
PI_R	5.83	5.47
PI_H	1.89	1.82

SHOT NUMBER	23-0	23-X
RANGE (cm)	DEPTH (cm)	DEPTH (cm)
0.0	1.221	2.482
0.6	1.282	2.495
1.2	0.967	2.503
1.8	0.644	2.470
2.4	0.406	2.226
3.0	0.223	1.744
3.6	0.072	1.415
4.2	-0.048	1.151
4.8	-0.107	0.952
5.4	-0.101	0.799
6.0	-0.063	0.592
6.6	-0.039	0.337
7.2	-0.018	0.101
7.8	-0.006	-0.092
8.4	-0.004	-0.263
9.0	0.005	-0.355
9.6	0.008	-0.399
10.2	0.012	-0.371
10.8	0.015	-0.311
11.4	0.016	-0.252
12.0	0.020	-0.192
12.6	0.018	-0.150
13.2	0.022	-0.127
13.8	0.023	-0.101
14.4	0.028	-0.077
15.0	0.024	-0.062
15.6	0.028	-0.047
16.2	0.033	-0.038
16.8	0.033	-0.034
17.4	0.038	-0.030
18.0	0.032	-0.028
18.6	0.037	-0.021
19.2	0.037	-0.022
19.8	0.028	-0.026
20.4	0.030	-0.024
21.0	--	--

A25
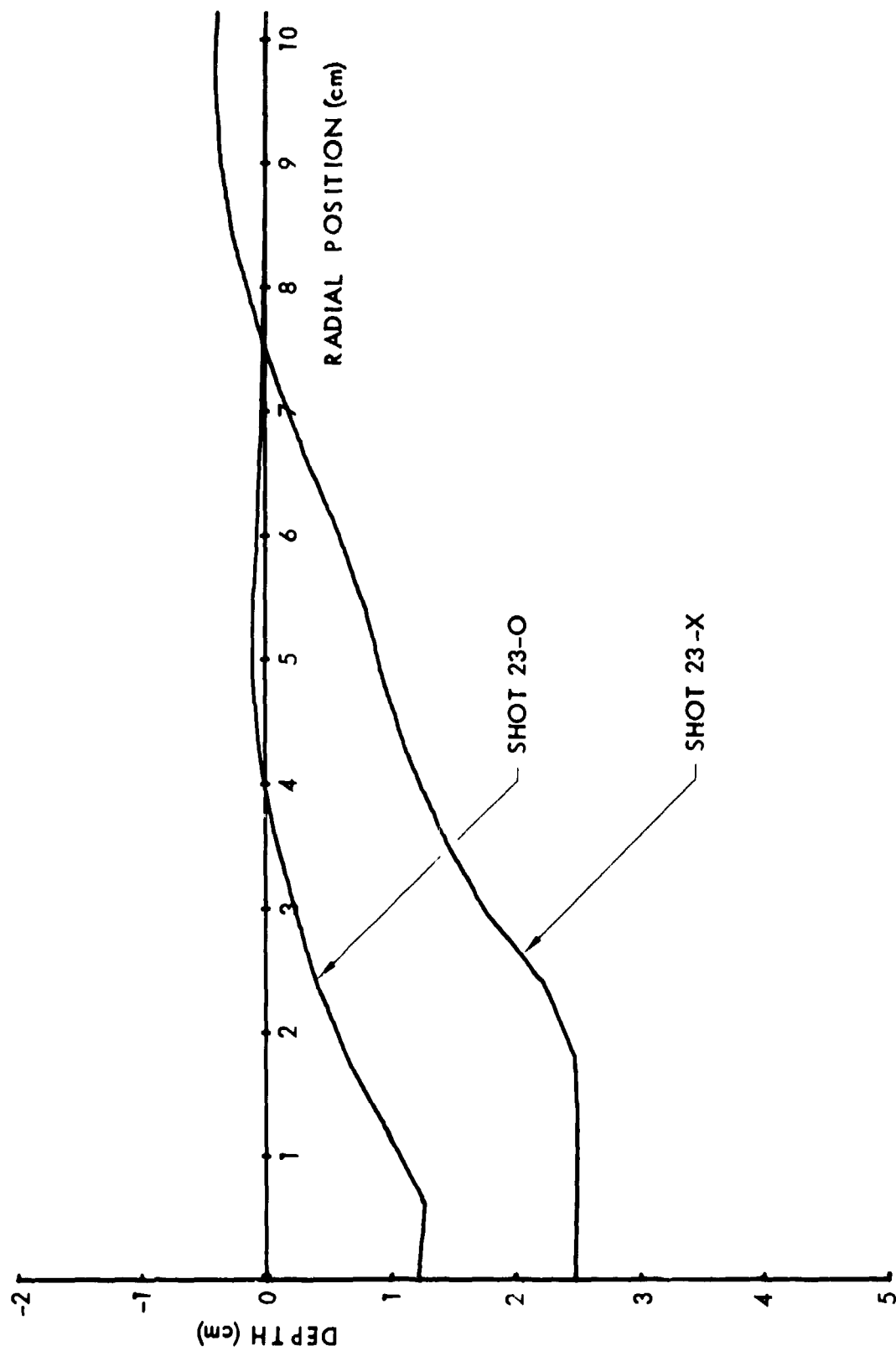
Fig. A15. Comparison of crater profiles.

SHOT 23-O

SHOT 23-X

RADIAL POSITION (cm)

DEPTH (cm)

A26
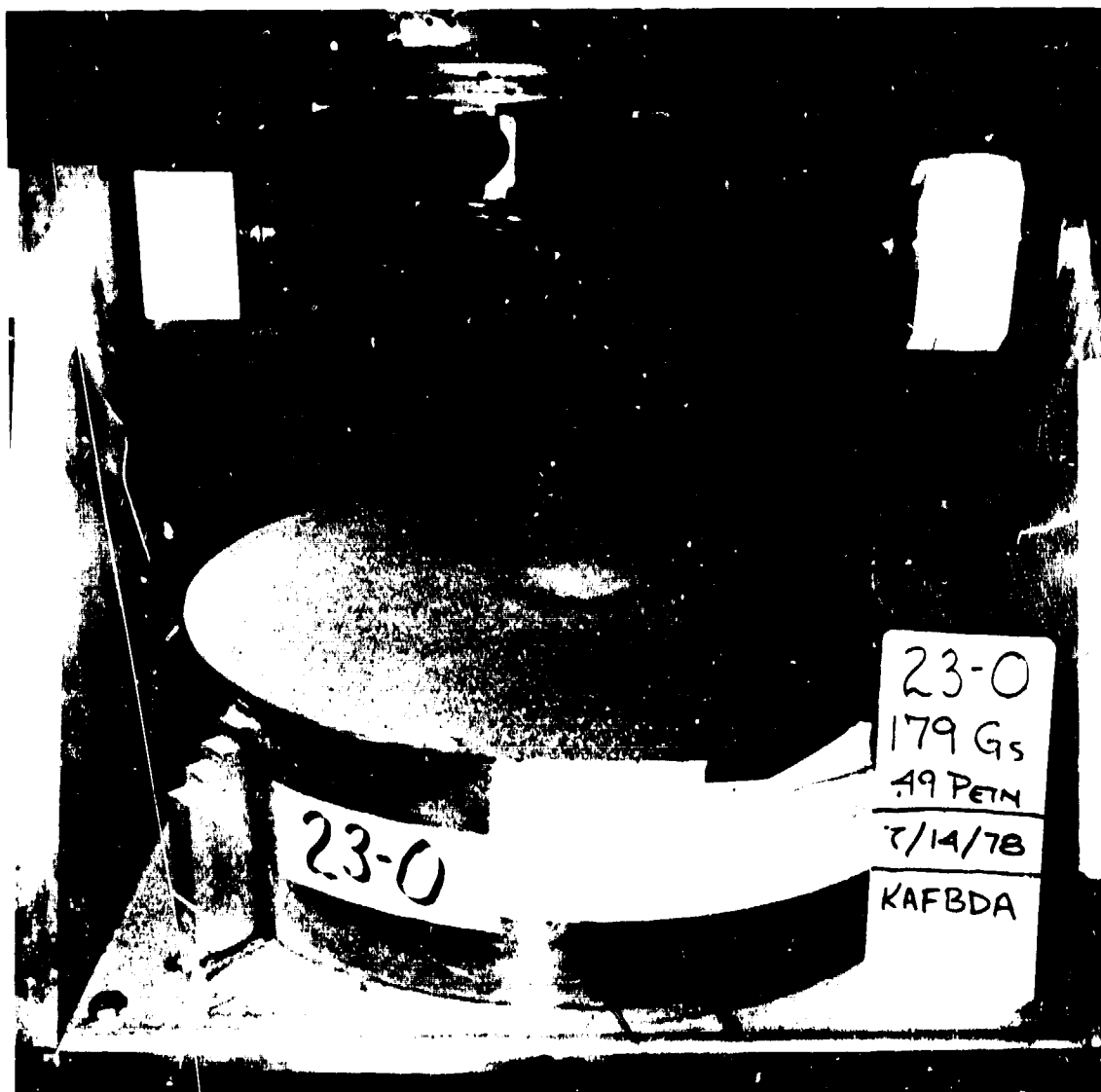
Fig. A16.   Shot 23-0, crater formed at 179 G by spherical 0.49-gm PETN charge half-buried in KAFB desert alluvium.
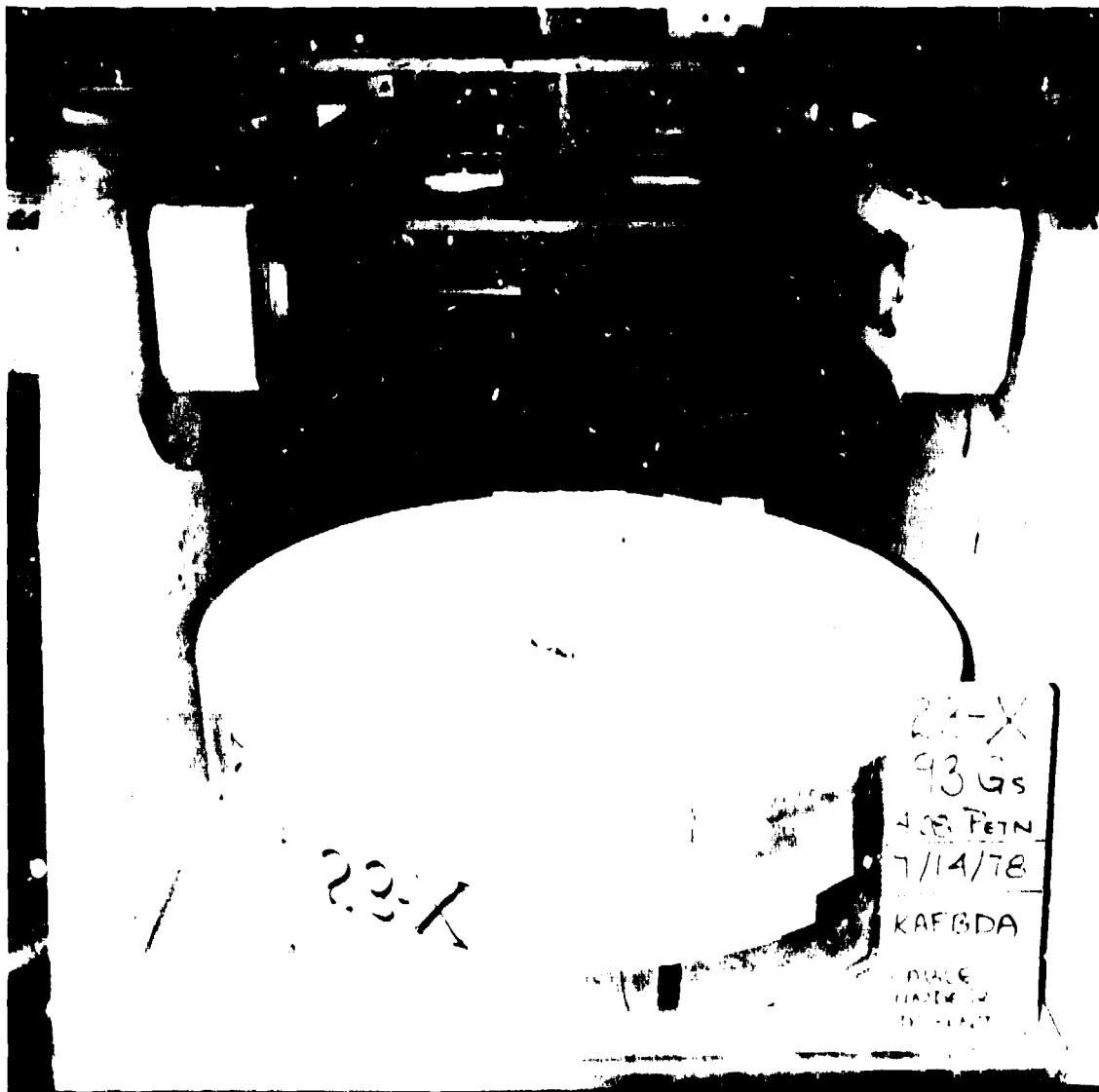
Fig. A17.   Shot 23-X, crater formed at 93 G by spherical 4.08-gm PETN charge half-buried in KAFB desert alluvium.

SHOT NUMBER	24-0	24-X
DATE	8/3/78	8/3/78
PURPOSE	Effect of Moisture (Dry)	Effect of Moisture (8%)
CHARGE DESCRIPTION	CICS-4(B-15)	CICS-4(B-14)
CHARGE MASS (gm)	0.13 AgN_3/3.95 PETN	0.13 AgN_3/3.96 PETN
CHARGE RADIUS (cm)	0.826	0.826
CHARGE CONFIGURATION	Half-Buried Sphere	Half-Buried Sphere
TEST BED MATERIAL	KAFB D.A. #11/#12	KAFB D.A. #7/#8
TEST BED DENSITY (gm/cc)	1.540	1.657
MOISTURE CONTENT (%)	<0.7	7.5
TEST BED GEOMETRY	Homogeneous	Homogeneous
CENTRIFUGE SPEED (rpm)	468	468
GROUND ZERO RADIUS (cm)	125	125
CENTRIFUGAL ACCELERATION (G)	306	306
CRATER VOLUME (cc)	108	136
CRATER RADIUS (cm)	6.71	6.10
MAX CRATER DEPTH (cm)	1.91	3.25
CRATER ASPECT RATIO (r/h)	3.51	1.88
CRATER C/L DEPTH (cm)	1.91	3.25
LIP RADIUS (cm)	8.40	7.20
LIP HEIGHT (cm)	0.39	0.32
LIP VOLUME (cc)	90.0	54.1
PI_2	7.19E-6	7.19E-6
PI_V	40.7	55.2
PI_R	4.85	4.52
PI_H	1.38	2.41

A29

| SHOT NUMBER | 24-0 | 24-X |
RANGE (cm)	DEPTH (cm)	DEPTH (cm)
0.0	1.912	3.252
0.6	1.877	3.236
1.2	1.836	3.147
1.8	1.661	2.915
2.4	1.439	2.685
3.0	1.225	2.196
3.6	1.031	1.129
4.2	0.862	0.754
4.8	0.672	0.538
5.4	0.481	0.300
6.0	0.272	0.038
6.6	0.042	-0.180
7.2	-0.197	-0.321
7.8	-0.372	-0.307
8.4	-0.388	-0.222
9.0	-0.304	-0.157
9.6	-0.227	-0.111
10.2	-0.165	-0.080
10.8	-0.128	-0.052
11.4	-0.090	-0.052
12.0	-0.071	-0.036
12.6	-0.051	-0.024
13.2	-0.038	-0.021
13.8	-0.049	-0.017
14.4	-0.037	-0.013
15.0	-0.038	-0.012
15.6	-0.035	-0.007
16.2	-0.028	-0.015
16.8	-0.032	-0.015
17.4	-0.026	-0.015
18.0	-0.027	-0.009
18.6	-0.023	-0.005
19.2	-0.020	-0.002
19.8	-0.023	-0.011
20.4	-0.026	0.001
21.0	--	--

A30
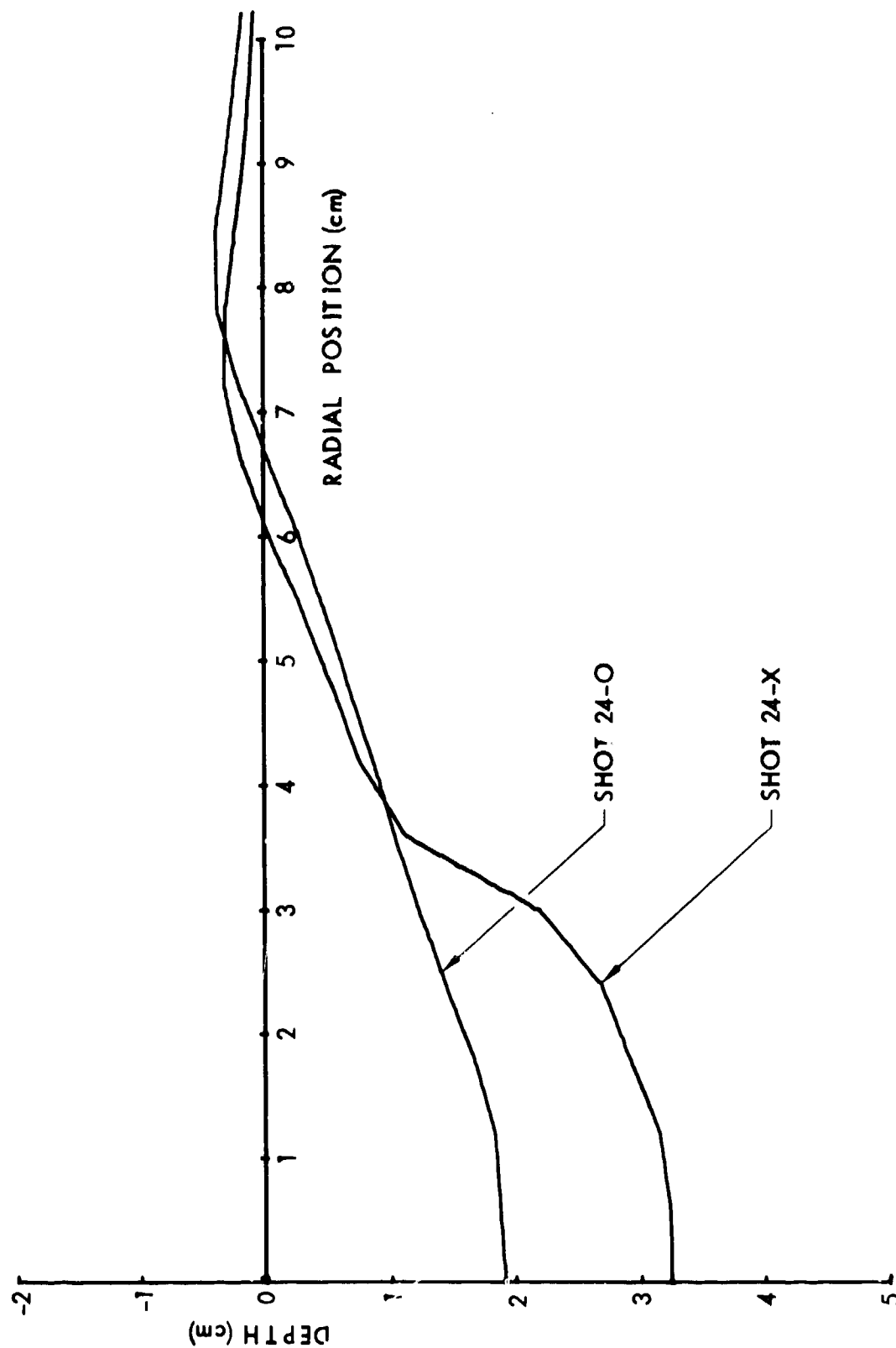
Fig. A18. Comparison of crater profiles.
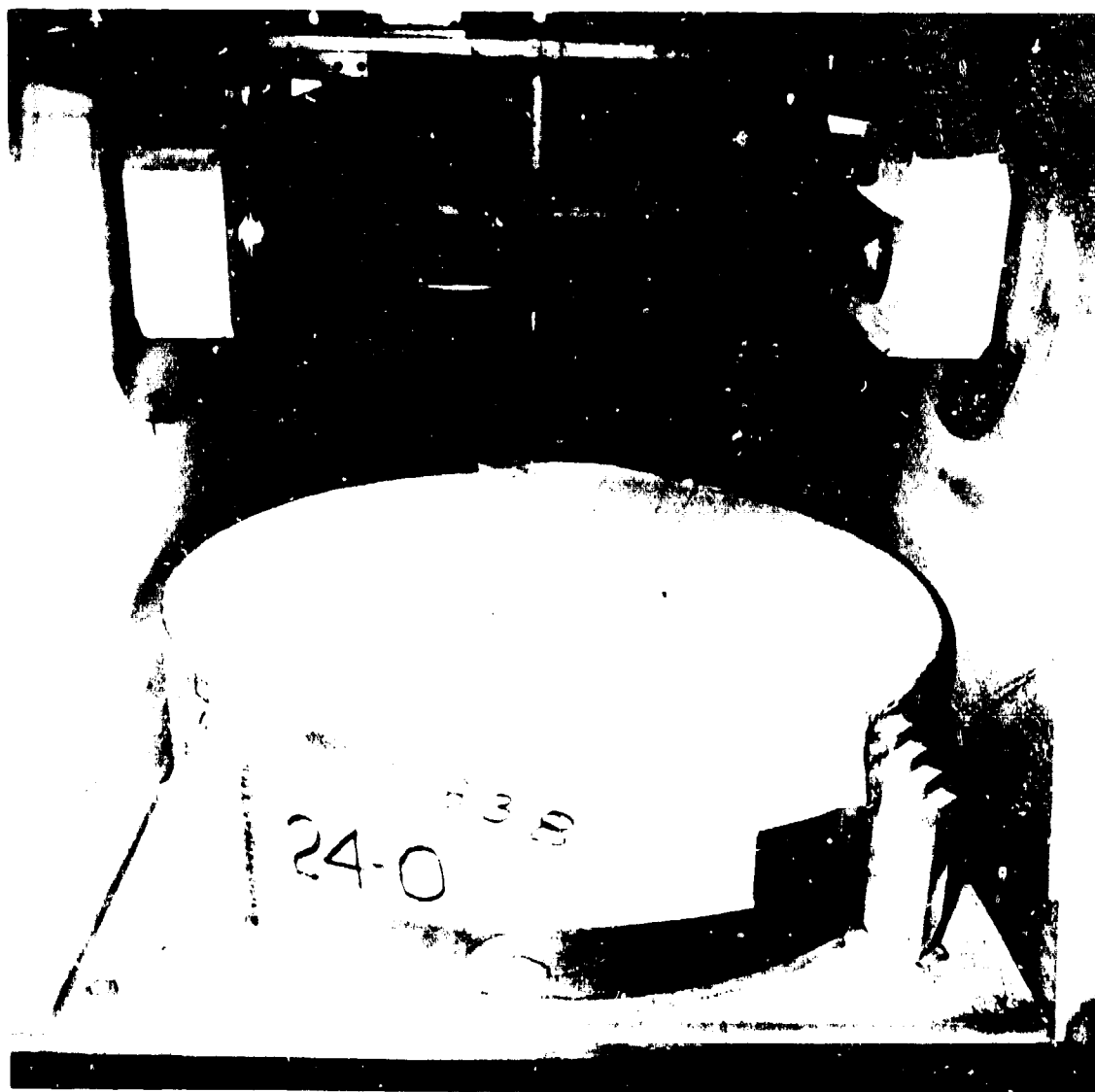
Fig. A19.   Shot 24-0, crater formed at 306 G by spherical 4.08-gm PETN
            charge half-buried in KAFB desert alluvium (<0.7-percent
            moisture content). Note flat shallow crater shape and
            compare with Fig. A20.

Fig. A20.   Shot 24-X, crater formed at 306 G by spherical 4.08-gm PETN
             charge half-buried in KAFB desert alluvium (7.5-percent
             moisture content). Note deep crater with bench in wall and
             compare with Fig. A19.

A33

SHOT NUMBER	25-0	25-X
DATE	8/14/78	8/14/78
PURPOSE	Small π_2	Large π_2
CHARGE DESCRIPTION	CICS-4(B-17)	CICS-4(B-18)
CHARGE MASS (gm)	0.13 AgN_3/3.97 PETN	0.13 AgN_3/3.96 PETN
CHARGE RADIUS (cm)	0.826	0.826
CHARGE CONFIGURATION	Half-Buried Sphere	Half-Buried Sphere
TEST BED MATERIAL	Permoplast Clay (#58)	Permoplast Clay (#59)
TEST BED DENSITY (gm/cc)	1.53	1.53
MOISTURE CONTENT (%)	--	--
TEST BED GEOMETRY	Homogeneous	Homogeneous
CENTRIFUGE SPEED (rpm)	85	609
GROUND ZERO RADIUS (cm)	124.6	124.8
CENTRIFUGAL ACCELERATION (G)	10.1	517
CRATER VOLUME (cc)	498	150
CRATER RADIUS (cm)	6.82	5.74
MAX CRATER DEPTH (cm)	6.01	2.73
CRATER ASPECT RATIO (r/h)	1.13	2.10
CRATER C/L DEPTH (cm)	6.01	2.73
LIP RADIUS (cm)	9.00	7.20
LIP HEIGHT (cm)	2.19	0.65
LIP VOLUME (cc)	340	45.5
PI_2	2.37E-7	1.21E-5
PI_V	187	56.2
PI_R	4.92	4.14
PI_H	4.33	1.97

SHOT NUMBER	25-0*	25-X*
DATE	10/16/78	10/16/78
PURPOSE	TEST FOR STABILITY OF CRATER SHAPE (100 SEC AT 518 G)	

CENTRIFUGE SPEED (rpm)	610	610
GROUND ZERO RADIUS (cm)	124.6	124.6
CENTRIFUGAL ACCELERATION (G)	518	518
CRATER VOLUME (cc)	235	142
CRATER RADIUS (cm)	6.77	5.72
MAX CRATER DEPTH (cm)	3.23	2.53
CRATER ASPECT RATIO (r/h)	2.10	2.26
CRATER C/L DEPTH (cm)	3.23	2.50
LIP RADIUS (cm)	7.80	7.20
LIP HEIGHT (cm)	0.52	0.62
LIP VOLUME (cc)	48.5	30.7
PI_2	1.22E-5	1.22E-5
PI_V	88.1	53.2
PI_R	4.88	4.12
PI_H	2.33	1.82

A35

SHOT NUMBER RANGE (cm)	25-0 DEPTH (cm)	25-0* DEPTH (cm)
0.0	6.006	3.231
0.6	5.954	3.135
1.2	5.846	3.088
1.8	5.690	2.997
2.4	5.542	2.839
3.0	5.252	2.516
3.6	4.971	2.249
4.2	4.382	2.033
4.8	3.712	1.696
5.4	2.850	1.254
6.0	1.692	0.708
6.6	0.400	0.146
7.2	-0.840	-0.234
7.8	-1.704	-0.520
8.4	-2.125	-0.468
9.0	-2.185	-0.230
9.6	-2.049	0.015
10.2	-0.918	0.168
10.8	-0.287	0.120
11.4	-0.069	0.105
12.0	-0.020	0.083
12.6	0.020	0.068
13.2	0.048	0.059
13.8	0.064	0.053
14.4	0.079	0.045
15.0	0.091	0.028
15.6	0.085	0.013
16.2	0.081	-0.001
16.8	0.075	-0.028
17.4	0.048	-0.059
18.0	-0.007	-0.110
18.6	--	--
19.2	--	--
19.8	--	--

*After test for stability of crater shape: 100 sec at 518 G

A36

SHOT NUMBER	25-X	25-X*
RANGE (cm)	DEPTH (cm)	DEPTH (cm)
0.0	2.725	2.496
0.6	2.752	2.528
1.2	2.707	2.466
1.8	2.557	2.338
2.4	2.402	2.231
3.0	2.155	1.994
3.6	1.832	1.700
4.2	1.383	1.290
4.8	0.899	0.862
5.4	0.283	0.264
6.0	-0.253	-0.264
6.6	-0.577	-0.534
7.2	-0.654	-0.624
7.8	-0.329	-0.191
8.4	-0.028	0.072
9.0	0.081	0.068
9.6	0.078	0.062
10.2	0.068	0.044
10.8	0.061	0.032
11.4	0.060	0.027
12.0	0.042	0.013
12.6	0.049	0.008
13.2	0.044	0.010
13.8	0.056	0.008
14.4	0.058	0.016
15.0	0.066	0.015
15.6	0.074	0.020
16.2	0.073	0.015
16.8	0.059	0.002
17.4	0.031	-0.032
18.0	-0.010	-0.074
18.6	--	--
19.2	--	--
19.8	--	--

*After test for stability of crater shape: 100 sec at 518 G

A37

Fig. A21. Comparison of crater profiles.

SHOT 25-O
(After test for stability of crater shape:
100 sec at 518 G)

SHOT 25-O
(Fired at 10 G)

RADIAL POSITION (cm)

DEPTH (cm)
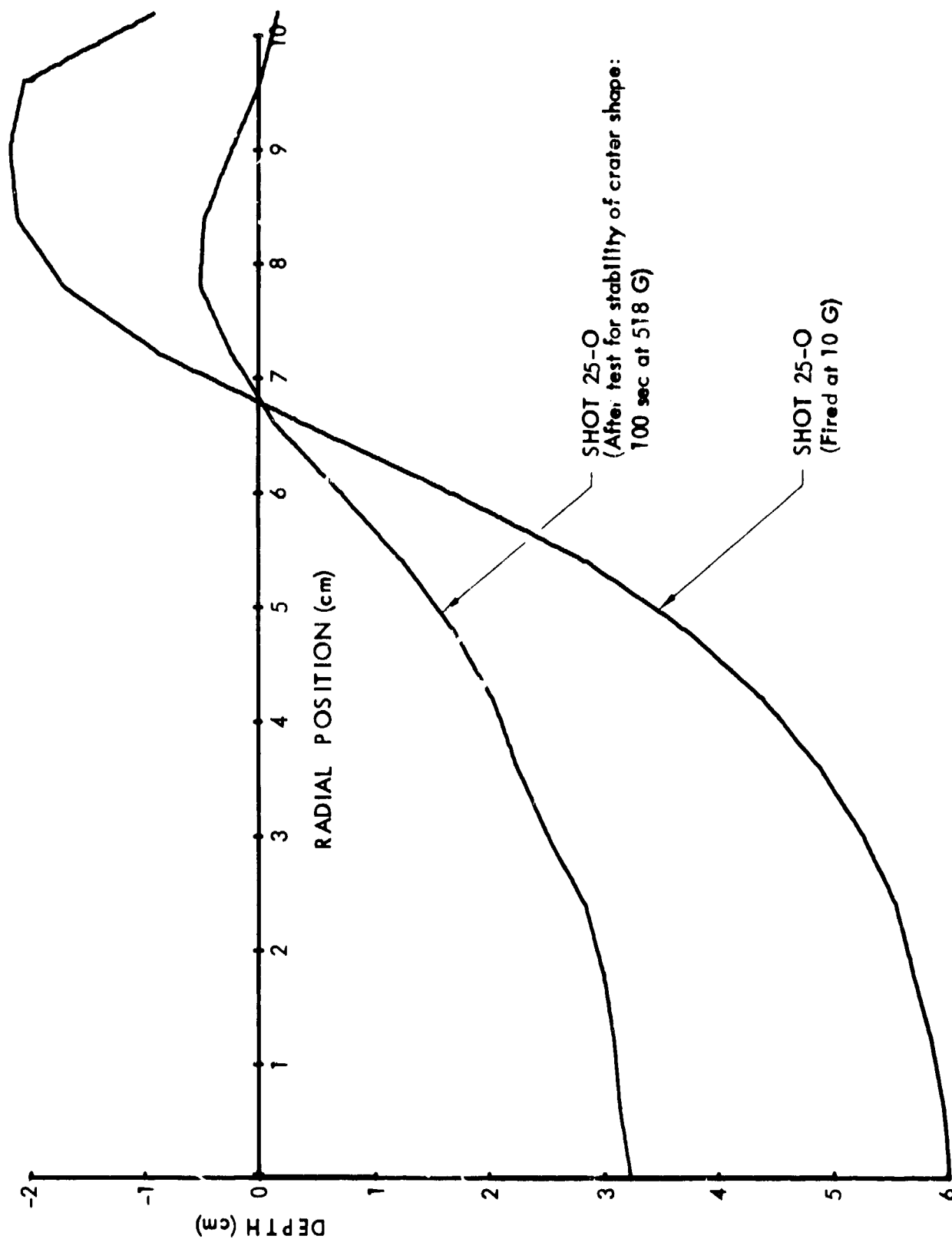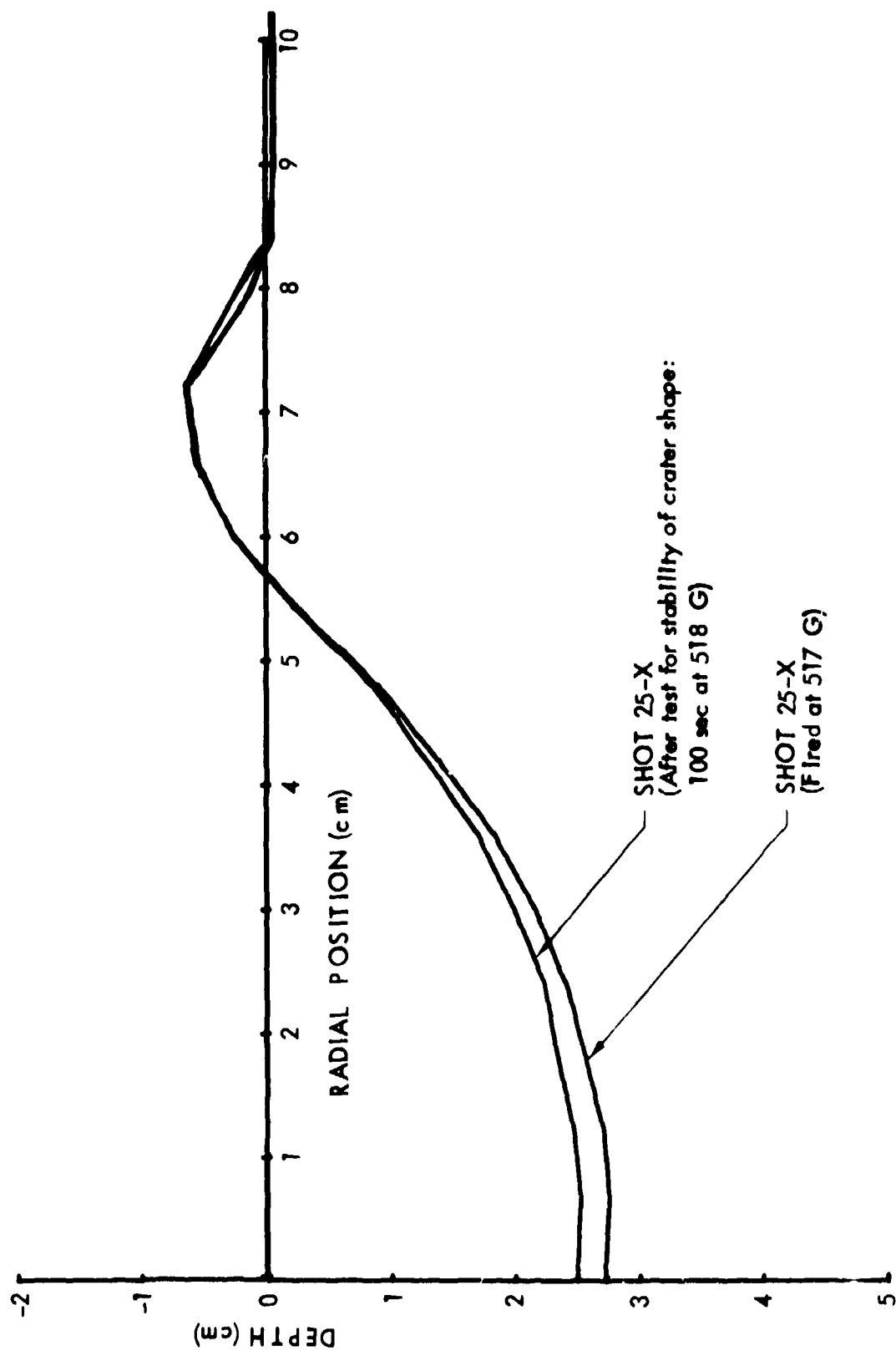
Fig. A22. Comparison of crater profiles.

SHOT 25-X
(After test for stability of crater shape:
100 sec at 518 G)

SHOT 25-X
(Fired at 517 G)

RADIAL POSITION (cm)

DEPTH (cm)

Fig. A23. Shot 25-0, crater formed at 10 G by spherical 4.08-gm PETN charge half-buried in "Permoplast" oil-base clay.
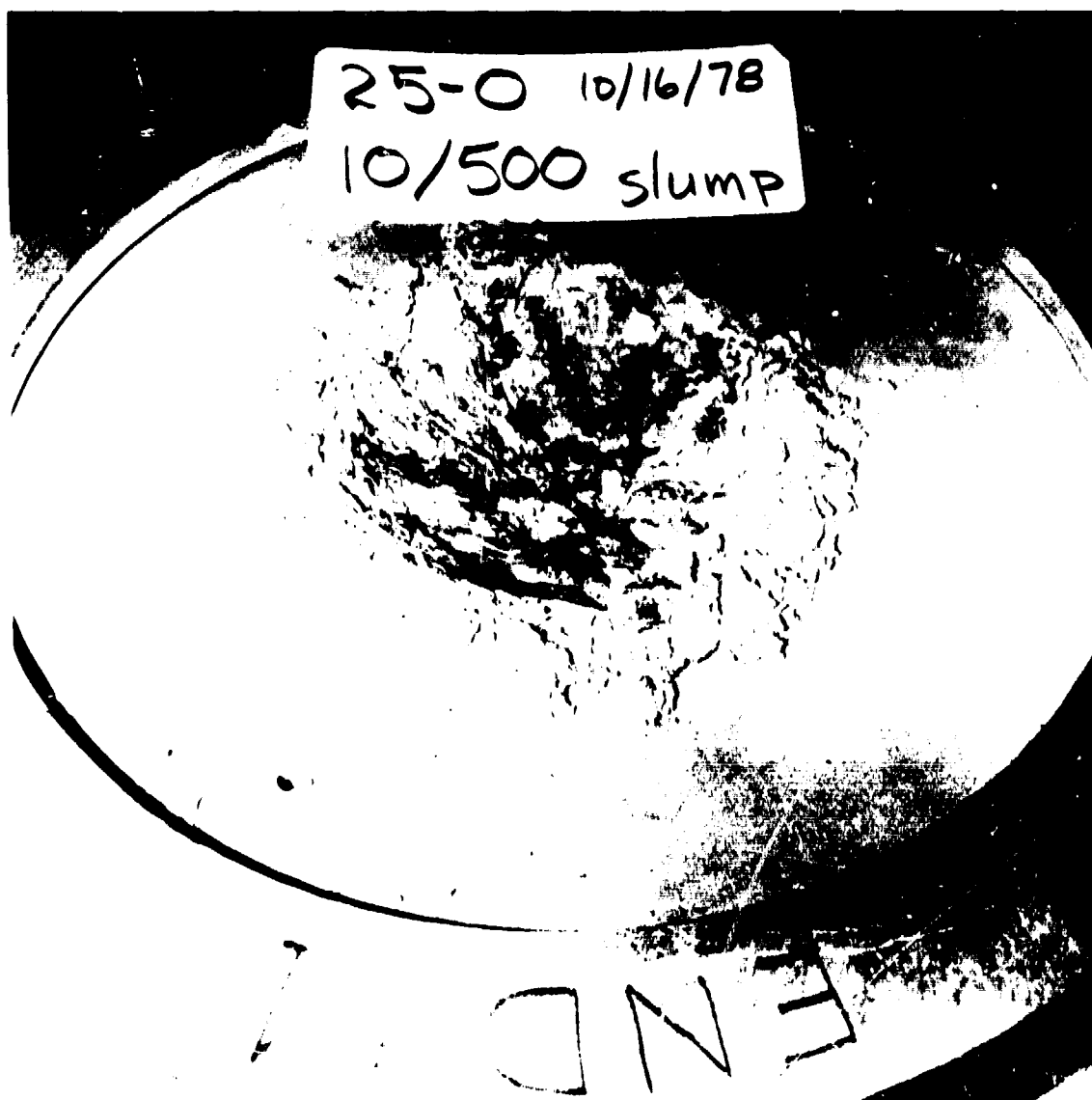
Fig. A24.   Final crater shape from shot 25-0 after 100 sec at 518 G.
Note depression of lip and irregular structure of crater
floor.   (Also see Fig. A23 and Figs. 4.7 and 4.8 in text.)
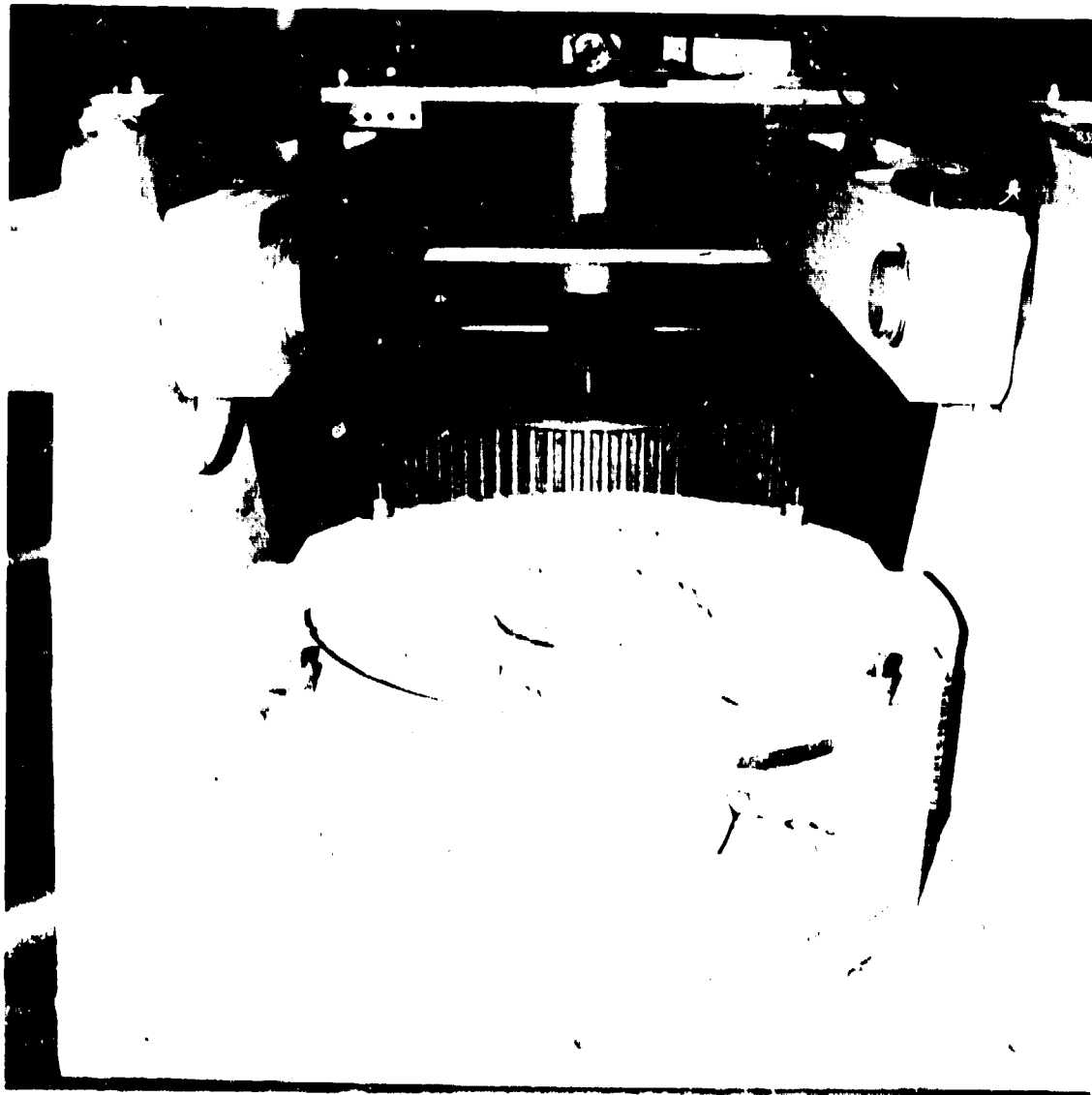
Fig. A25.   Shot 25-X, crater formed at 517 G by spherical 4.08-gm PETN
charge half-buried in "Permoplast" oil-base clay.
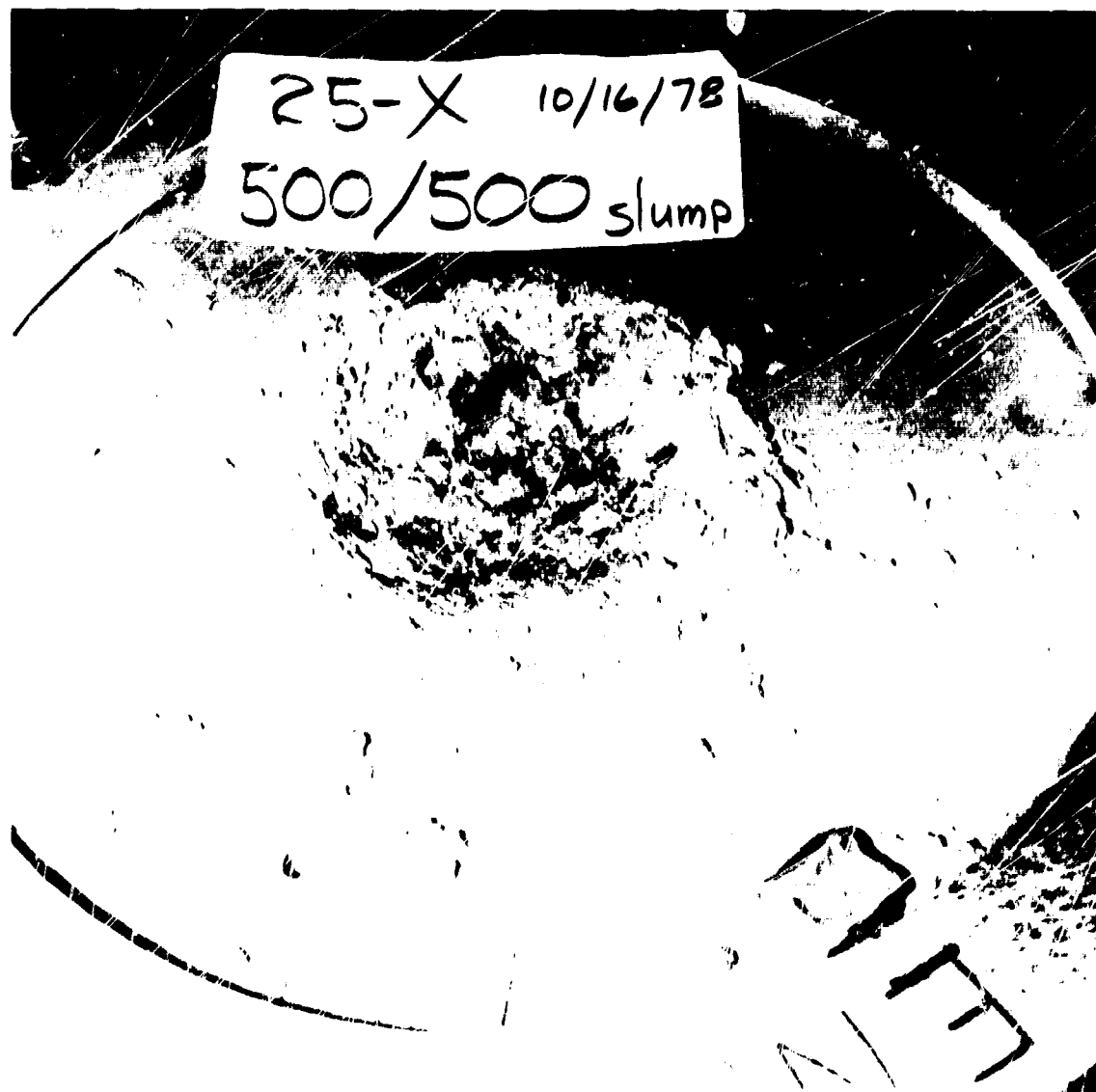
Fig. A26. No significant shape change due to slumping or flow was observed. Crater as originally formed was stable and did not show any evidence of a transient cavity that was larger than the final shape. (Also see Fig. A25 and Figs. 4.7 and 4.8 in text.)

A43

SHOT NUMBER	26-0	26-X
DATE	9/22/78	9/22/78
PURPOSE	Grain Size Effect	Grain Size Effect
	(Dense Saturated Sand)	(Dense Saturated Sand)
CHARGE DESCRIPTION	CILAS-13(B-7)	CILAS-13(B-8)
CHARGE MASS (gm)	1.70 PbN_6	1.70 PbN_6
CHARGE RADIUS (cm)	0.508	0.508
CHARGE CONFIGURATION	Half-Buried Sphere	Half-Buried Sphere
TEST BED MATERIAL	Sat. Sawing Sand	Sat. Banding Sand
TEST BED DENSITY (gm/cc)	2.078	2.056
MOISTURE CONTENT (%)	>97	>97
TEST BED GEOMETRY	Homogeneous	Homogeneous
CENTRIFUGE SPEED (rpm)	265	265
GROUND ZERO RADIUS (cm)	127.1	127.1
CENTRIFUGAL ACCELERATION (G)	100	100
CRATER VOLUME (cc)	122	54.8
CRATER RADIUS (cm)	6.88	4.80
MAX CRATER DEPTH (cm)	2.09	1.91
CRATER ASPECT RATIO (r/h)	3.29	2.51
CRATER C/L DEPTH (cm)	2.09	1.91
LIP RADIUS (cm)	7.80	6.00
LIP HEIGHT (cm)	0.25	0.20
LIP VOLUME (cc)	53.8	36.6
PI_2	6.08E-6	6.08E-6
PI_V	149	66.3
PI_R	7.36	5.11
PI_H	2.23	2.03

A44

| SHOT NUMBER	26-0	26-X
RANGE (cm)	DEPTH (cm)	DEPTH (cm)
0.0	2.094	1.909
0.6	2.011	1.892
1.2	1.781	1.675
1.8	1.645	1.421
2.4	1.531	1.188
3.0	1.388	0.847
3.6	1.232	0.539
4.2	1.057	0.284
4.8	0.815	-0.007
5.4	0.528	-0.190
6.0	0.299	-0.202
6.6	0.081	-0.162
7.2	-0.116	-0.136
7.8	-0.249	-0.112
8.4	-0.229	-0.095
9.0	-0.191	-0.059
9.6	-0 41	-0.045
10.2	-0.120	-0.031
10.8	-0.087	-0.030
11.4	-0.066	-0.022
12.0	-0.060	-0.016
12.6	-0.034	-0.015
13.2	-0.023	-0.020
13.8	-0.021	-0.013
14.4	-0.009	-0.007
15.0	-0.010	-0.006
15.6	-0.014	-0.007
16.2	-0.008	0.002
16.8	-0.006	0.001
17.4	0.002	0.004
18.0	0.010	0.004
18.6	0.014	0.003
19.2	0.024	0.002
19.8	0.022	0.004
20.4	0.021	-0.001
21.0	0.023	-0.008
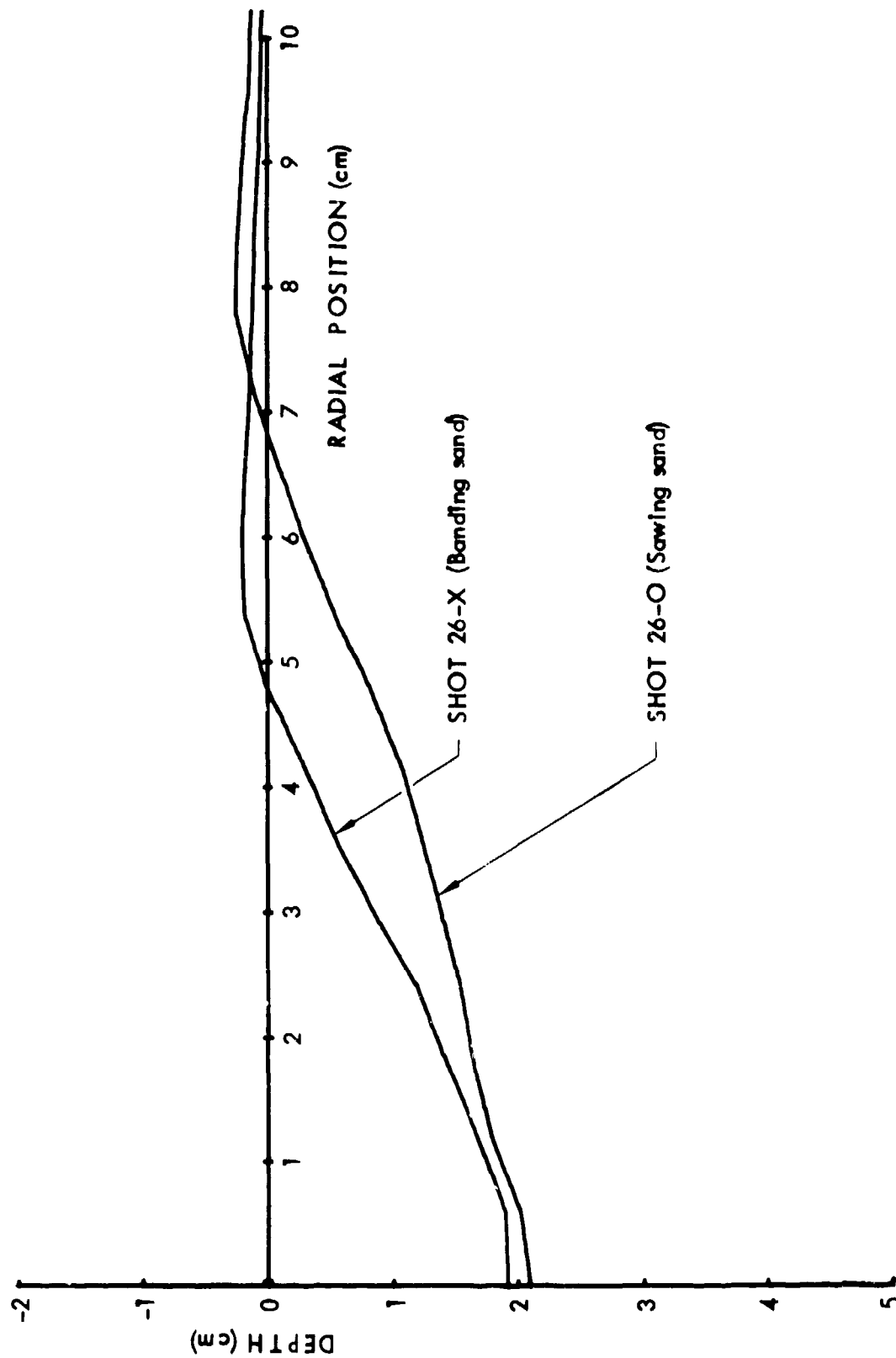
Fig. A27.   Comparison of crater profiles.

Fig. A28.   Pre-shot photograph (26-0) showing charge placement and
            initial water level.
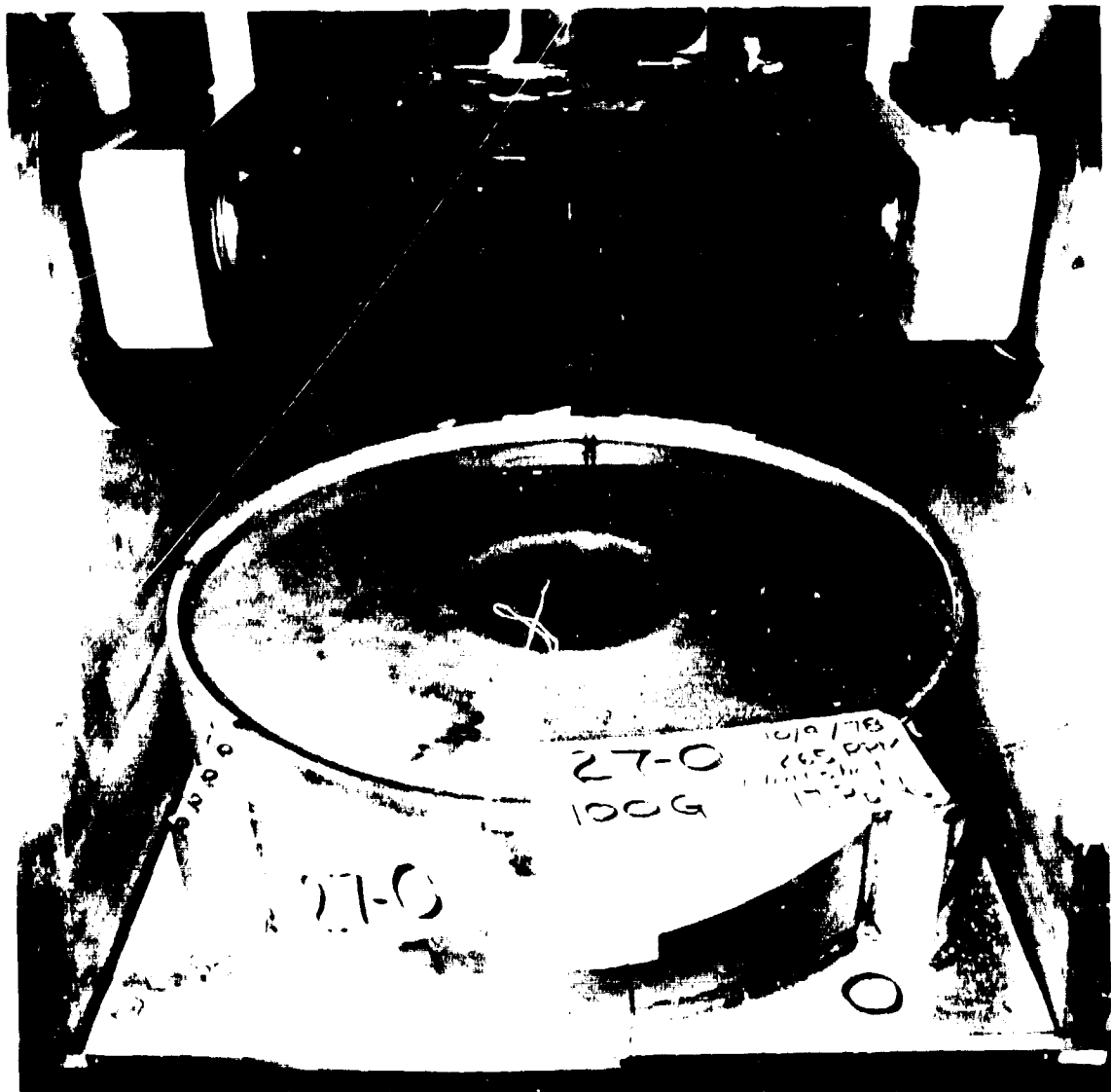
Fig. A29.   Shot 26-0, crater formed at 100 G by spherical 1.70-gm PbN$_6$ charge half-buried in nearly-saturated dense Ottawa Sawing sand.   Water has been drained to a level below crater floor to facilitate crater measurement.
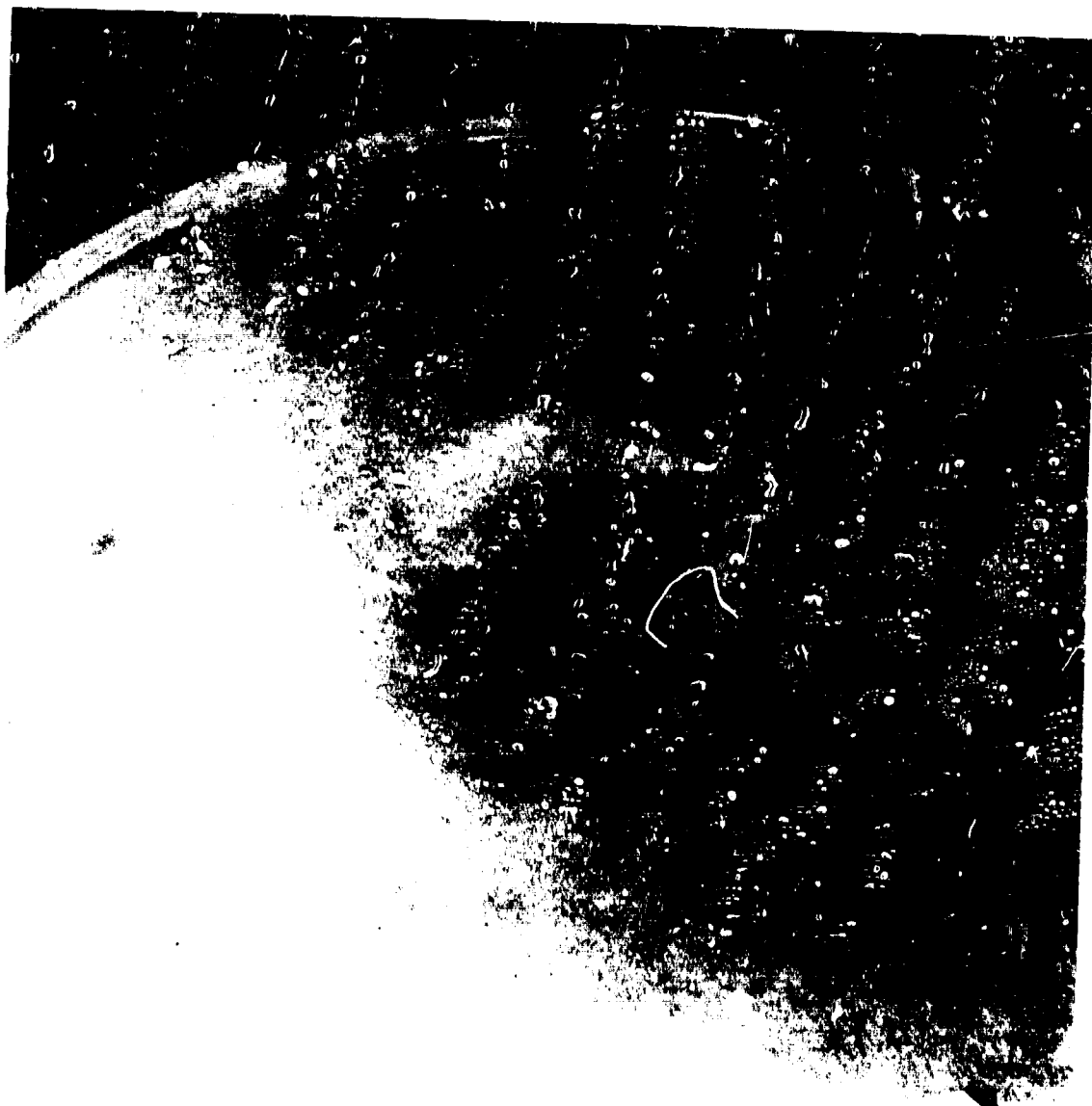
Fig. A30. Shot 26-0, close-up photograph of crater formed at 100 G by spherical 1.70-gm PbN_6 charge half-buried in nearly-saturated dense Ottawa Sawing sand. Water has been drained to a level below crater floor to facilitate crater measurement.
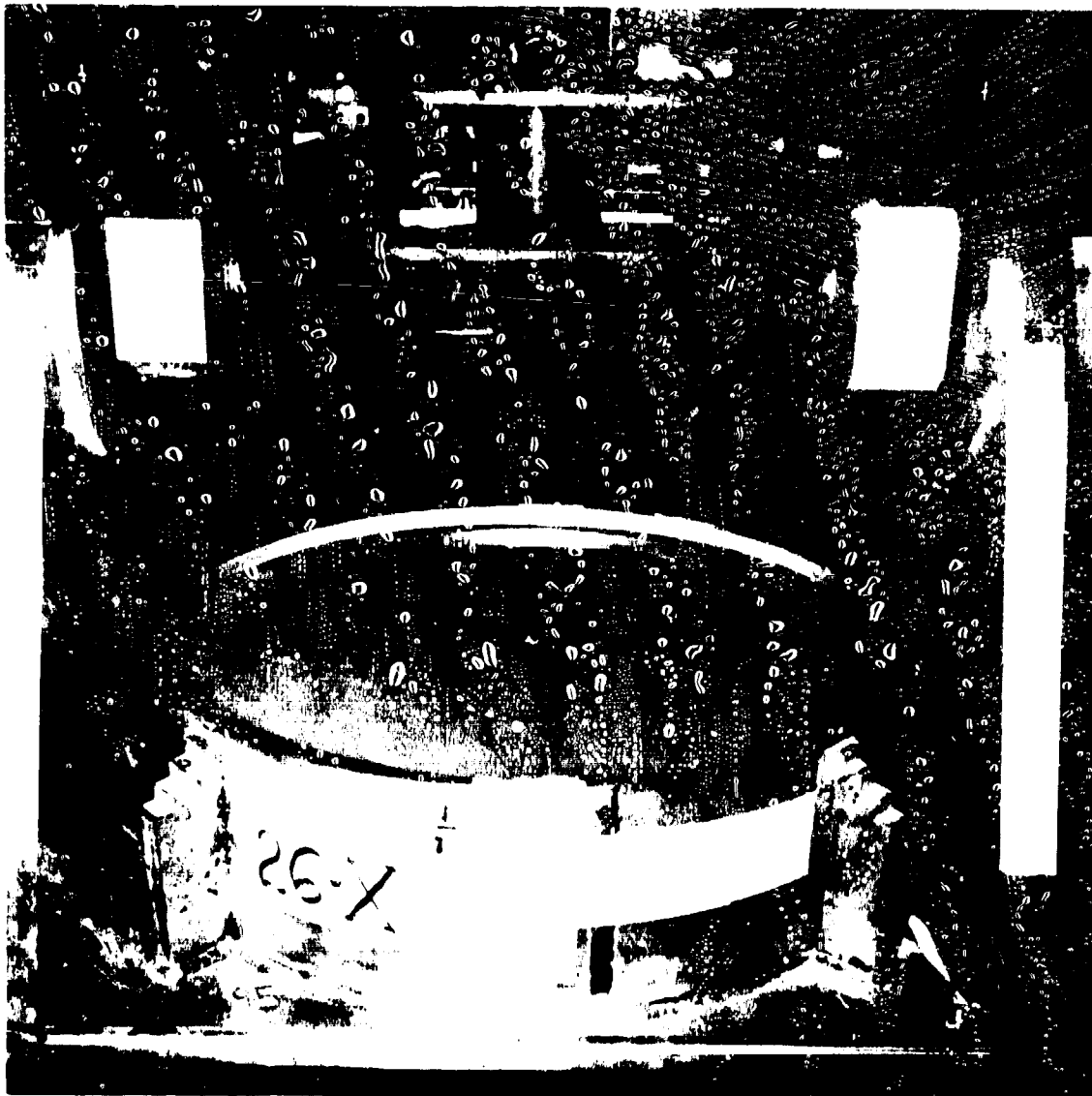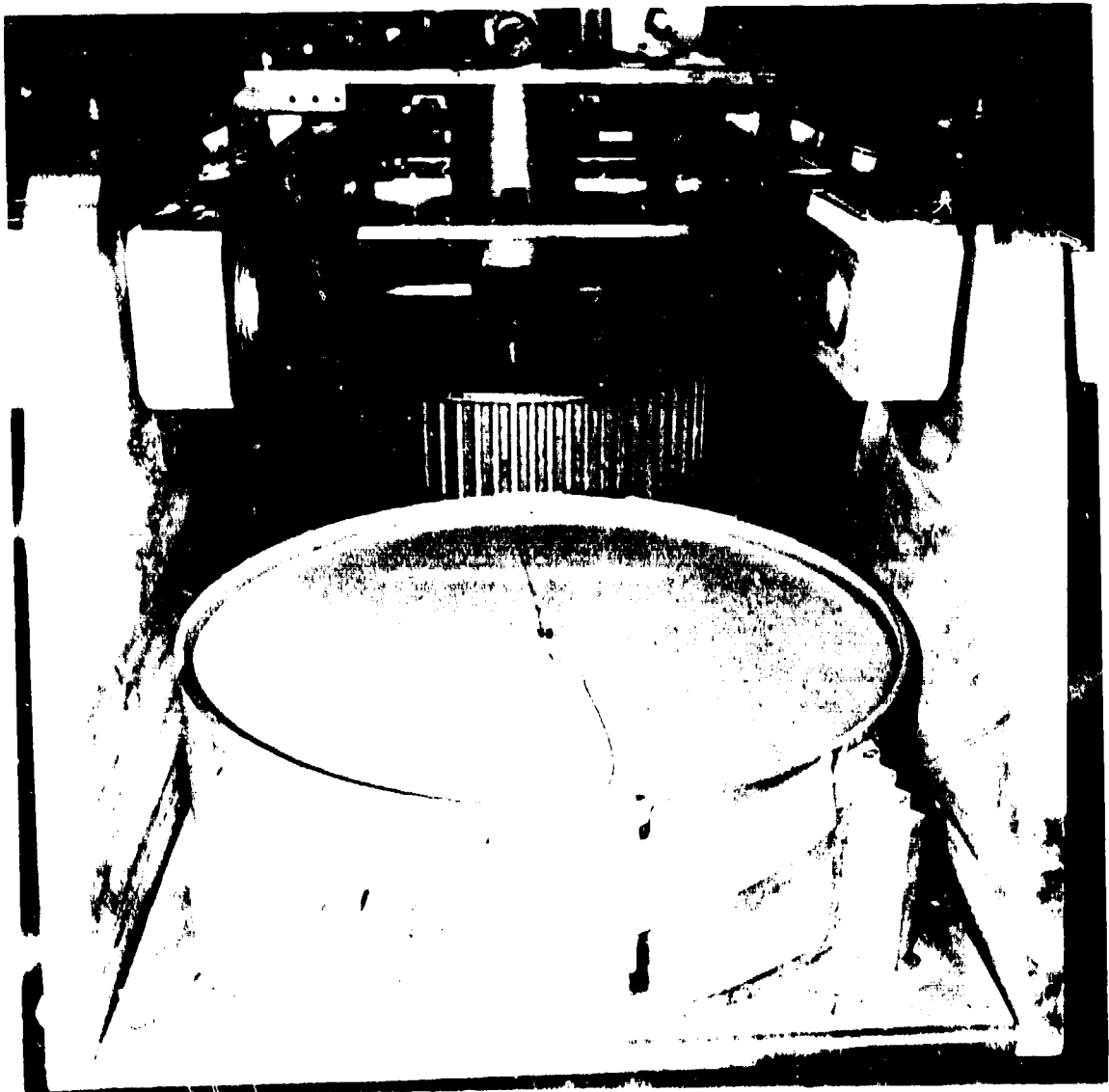
Fig. A31.   Pre-shot photograph (26-X) showing charge placement and initial water level.

Fig. A32.   Shot 26-X, crater formed at 100 G by spherical 1.70-gm PbN$_6$ charge half-buried in nearly-saturated dense Ottawa Banding sand. Water has been drained to a level below crater floor to facilitate crater measurement.

A51
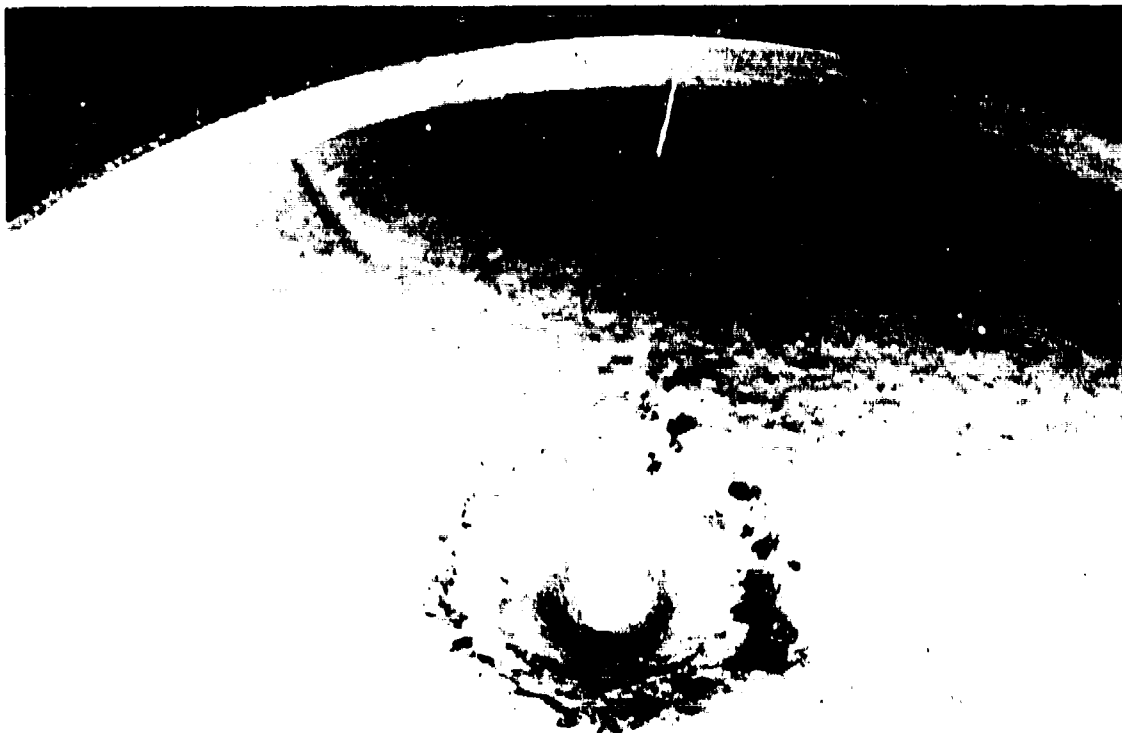
Fig. A33.   Shot 26-X, close-up photograph of crater formed at 100 G by
             spherical 1.70-gm PbN_6 charge half-buried in nearly-saturated
             dense Ottawa Banding sand. Water has been drained to a level
             below crater floor to facilitate crater measurement.

SHOT NUMBER	27-0	27-X
DATE	10/9/78	10/9/78
PURPOSE	Saturated Sand Reproducibility	Saturated Sand Reproducibility
CHARGE DESCRIPTION	CILAS-13(B-10)	CILAS-13(B-9)
CHARGE MASS (gm)	1.70 PbN$_6$	1.71 PbN$_6$
CHARGE RADIUS (cm)	0.508	0.508
CHARGE CONFIGURATION	Half-Buried Sphere	Half-Buried Sphere
TEST BED MATERIAL	Sat. Flintshot Sand	Sat. Flintshot Sand
TEST BED DENSITY (gm/cc)	2.113	2.113
MOISTURE CONTENT (%)	>97	>97
TEST BED GEOMETRY	Homogeneous	Homogeneous
CENTRIFUGE SPEED (rpm)	265	265
GROUND ZERO RADIUS (cm)	127.1	127.1
CENTRIFUGAL ACCELERATION (G)	100	100
CRATER VOLUME (cc)	73.8	86.6
CRATER RADIUS (cm)	6.03	6.09
MAX CRATER DEPTH (cm)	1.77	1.78
CRATER ASPECT RATIO (r/h)	3.41	3.42
CRATER C/L DEPTH (cm)	1.77	1.78
LIP RADIUS (cm)	7.80	7.80
LIP HEIGHT (cm)	0.31	0.36
LIP VOLUME (cc)	59.2	74.8
PI_2	6.08E-6	6.08E-6
PI_V	91.7	108
PI_R	6.48	6.55
PI_H	1.90	1.91

SHOT NUMBER	27-0	27-X
RANGE (cm)	DEPTH (cm)	DEPTH (cm)
0.0	1.766	1.775
0.6	1.701	1.757
1.2	1.548	1.644
1.8	1.408	1.524
2.4	1.249	1.393
3.0	1.056	1.198
3.6	0.799	0.982
4.2	0.544	0.707
4.8	0.334	0.437
5.4	0.162	0.234
6.0	0.007	0.026
6.6	-0.157	-0.161
7.2	-0.296	-0.318
7.8	-0.313	-0.363
8.4	-0.231	-0.288
9.0	-0.173	-0.225
9.6	-0.113	-0.180
10.2	-0.087	-0.123
10.8	-0.067	-0.108
11.4	-0.052	-0.095
12.0	-0.047	-0.063
12.6	-0.036	-0.038
13.2	-0.035	-0.030
13.8	-0.030	-0.027
14.4	-0.017	-0.014
15.0	-0.017	-0.015
15.6	-0.020	-0.012
16.2	0.003	-0.005
16.8	0.002	0.014
17.4	0.010	0.015
18.0	0.012	0.009
18.6	0.011	-0.001
19.2	0.004	0.006
19.8	0.003	0.001
20.4	-0.003	0.000
21.0	-0.005	-0.010
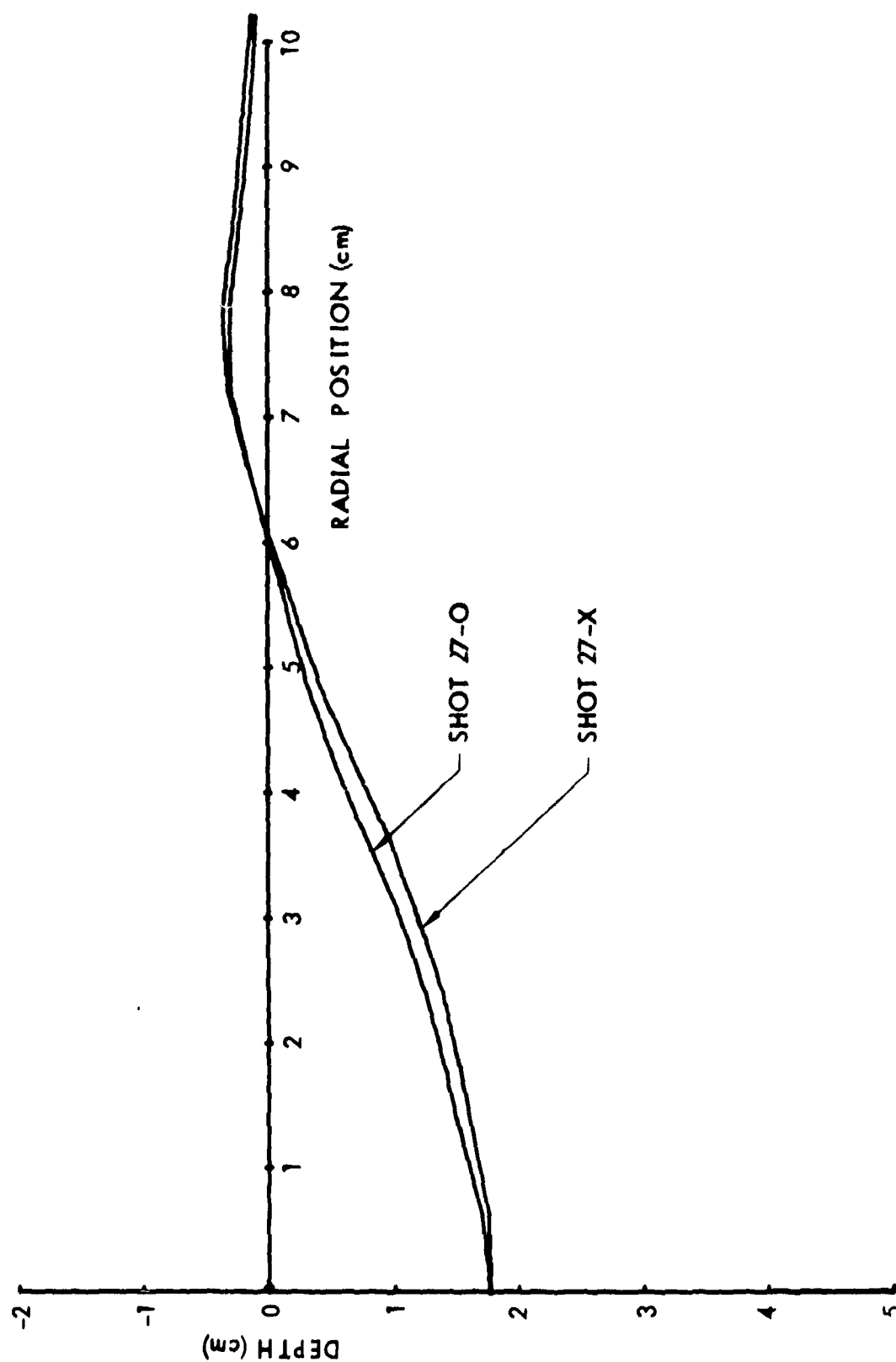
Fig. A34. Comparison of crater profiles.

Fig. A35. Pre-shot photograph (27-0) showing charge placement and initial water level.
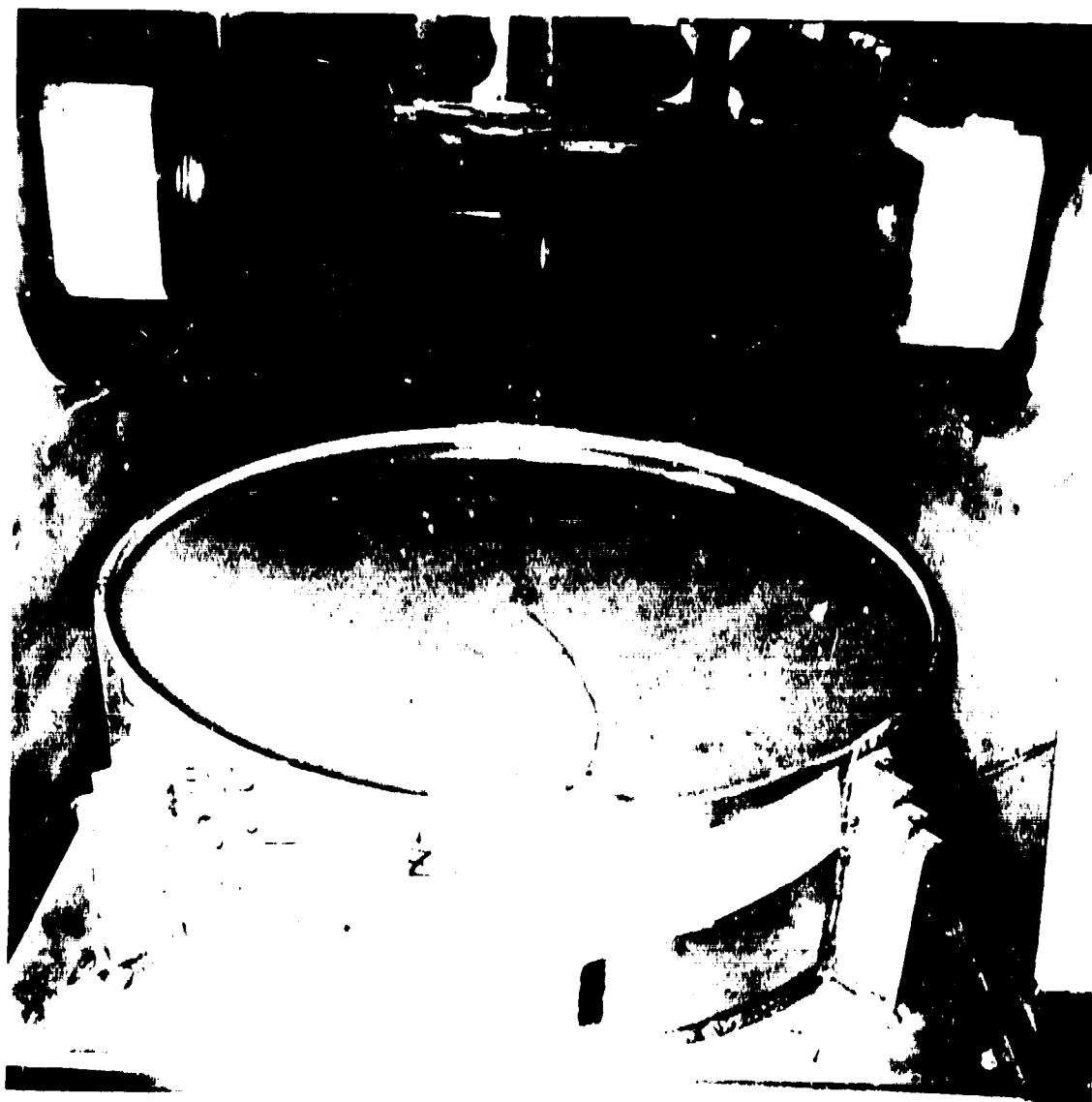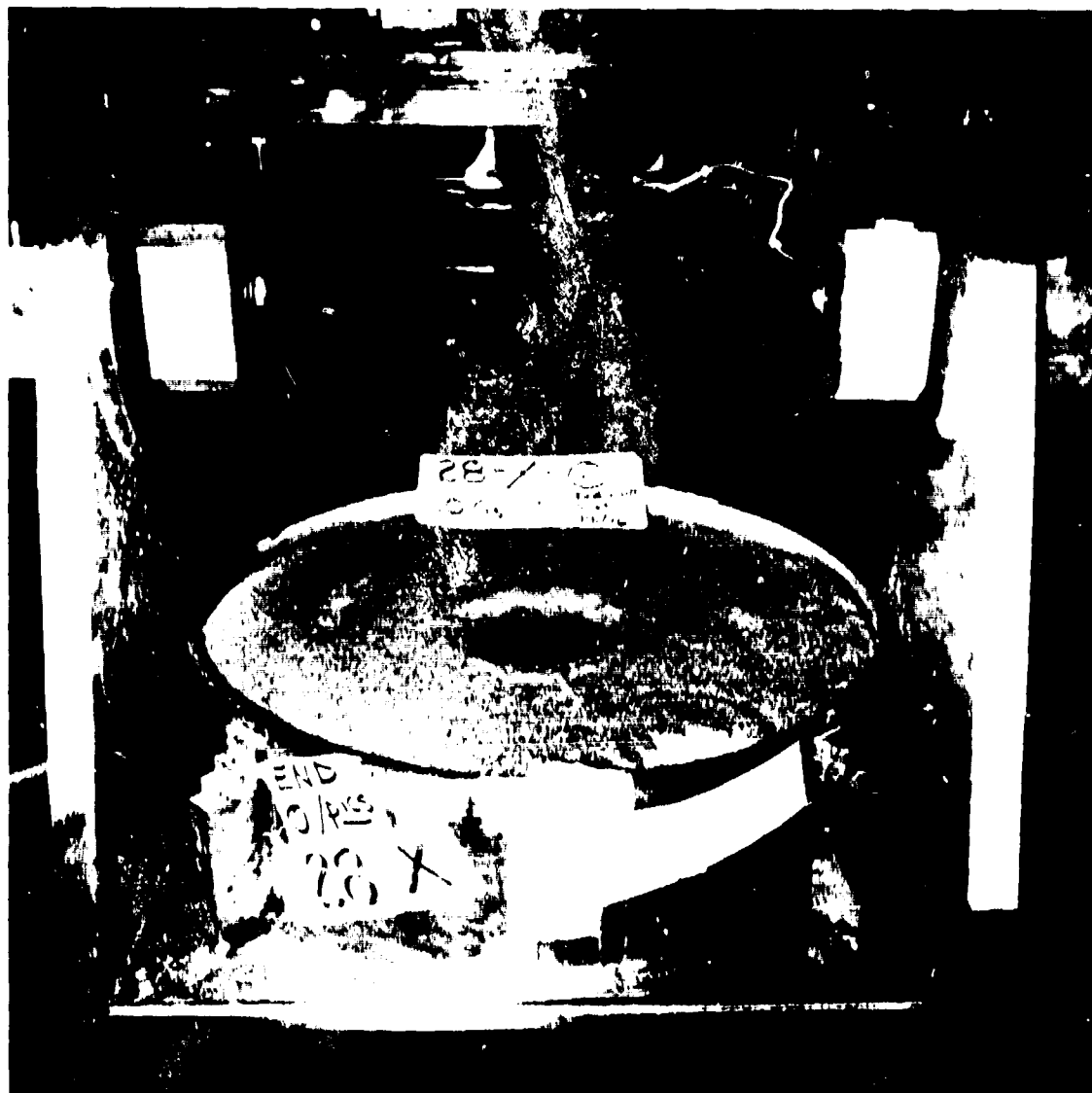
Fig. A36. Shot 27-0, crater formed at 100 G by spherical 1.70-gm PbN_6 charge half-buried in nearly-saturated dense Ottawa Flintshot sand. At shot time, water table was tangent to surface at the charge location.
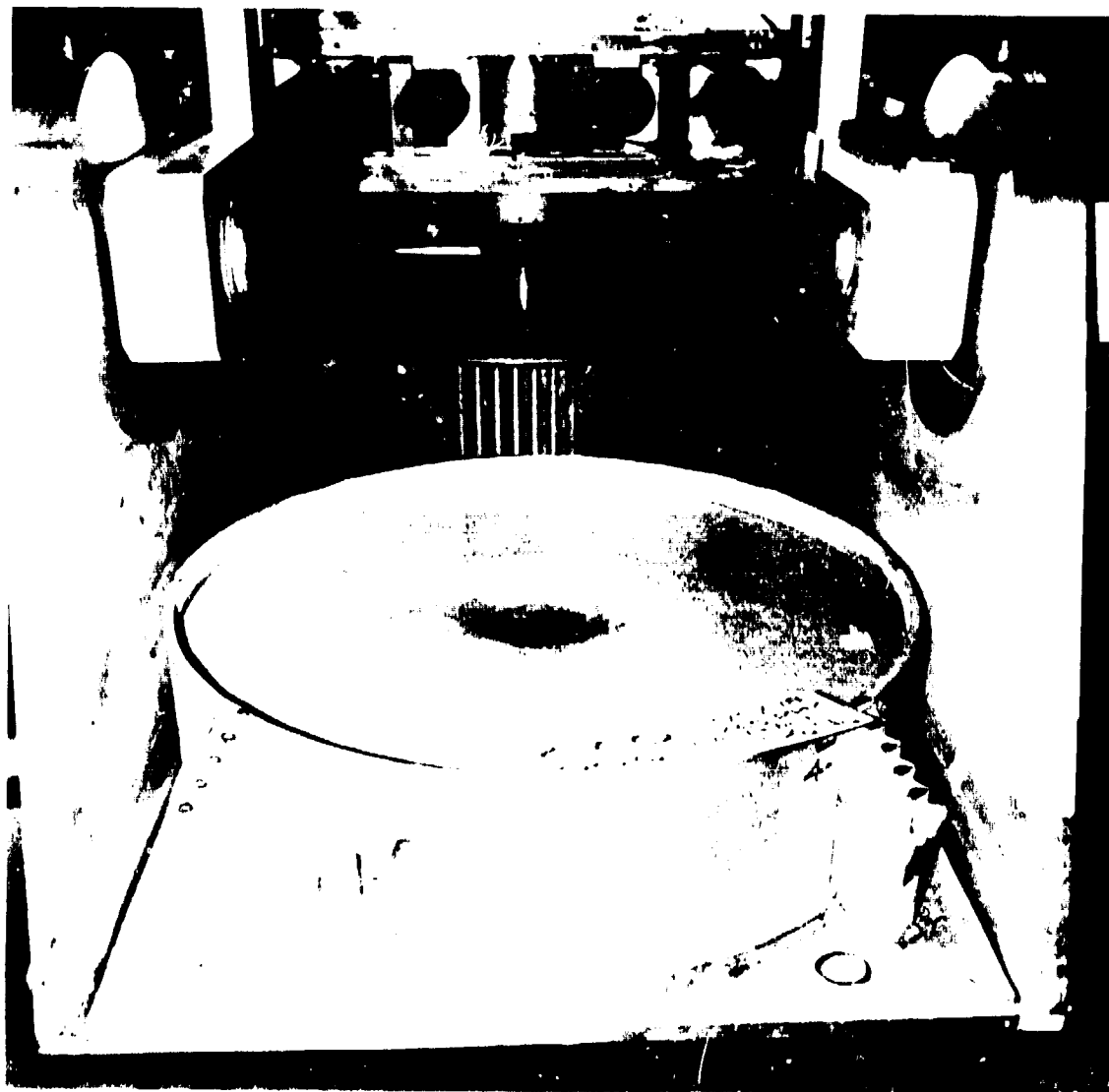
Fig. A37.   This photograph shows crater (27-0) after water was drained
             to a level below crater floor to facilitate measurement.
             See Fig. A36.

A58

Fig. A38. Pre-shot photograph (27-X) showing charge placement and initial water level.

Fig. A39.   Shot 27-X, crater formed at 100 G by spherical 1.70-gm PbN_6
            charge half-buried in nearly-saturated dense Ottawa
            Flintshot sand. At shot time, water table was tangent
   to surface at the charge location.
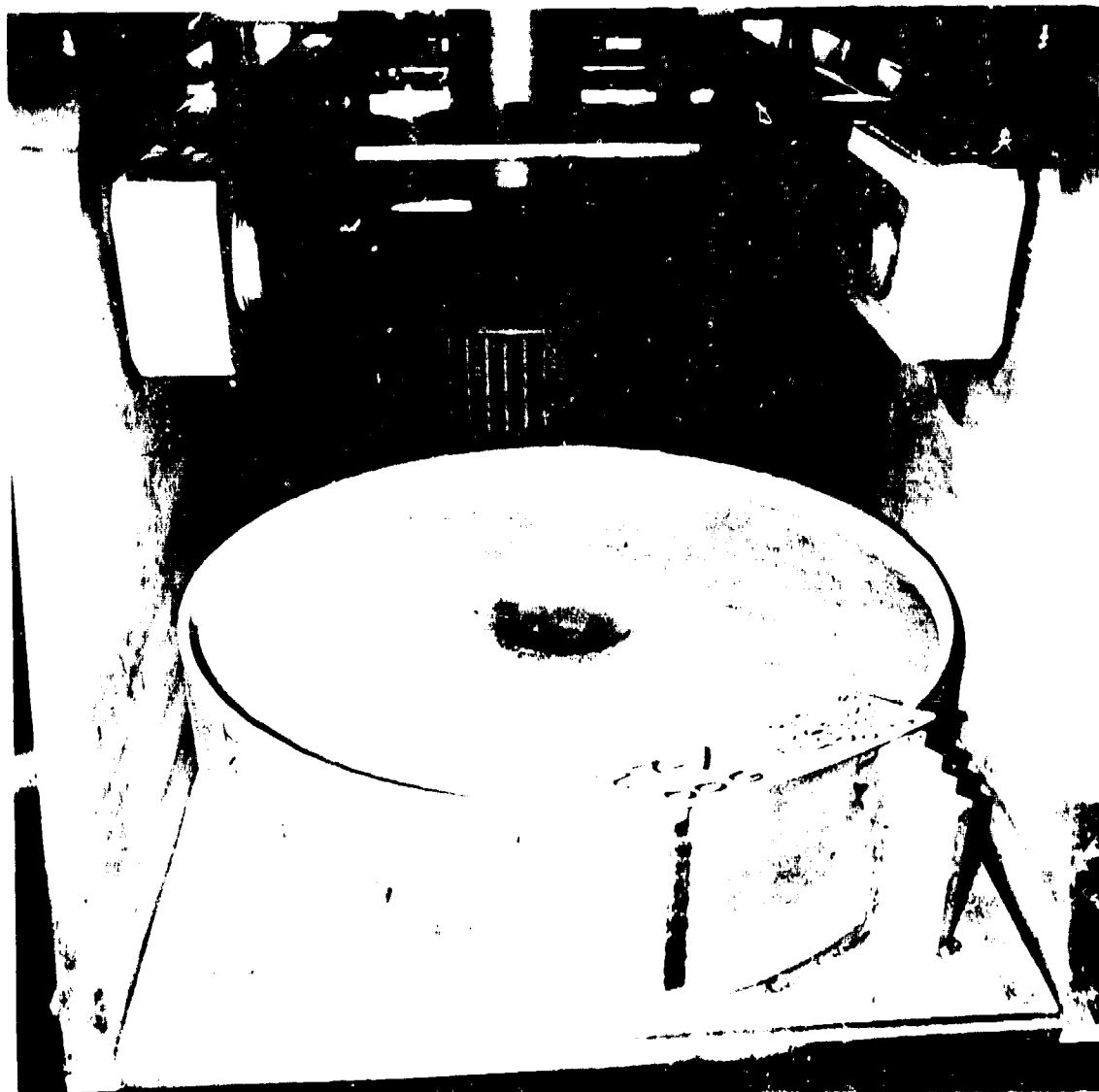
Fig. A40. This photograph shows crater (27-X) after water was drained to a level below crater floor to facilitate measurement. See Fig. A39.

SHOT NUMBER	28-0	28-X*
DATE	11/2/78	11/2/78
PURPOSE	High-G	Low-G
CHARGE DESCRIPTION	CILAS(B-13)	CILAS(B-13)
CHARGE MASS (gm)	1.70 PbN_6	1.70 PbN_6
CHARGE RADIUS (cm)	0.508	0.508
CHARGE CONFIGURATION	Half-Buried Sphere	Half-Buried Sphere
TEST BED MATERIAL	Sat. Flintshot Sand	Sat. Flintshot Sand
TEST BED DENSITY (gm/cc)	2.107	2.109
MOISTURE CONTENT (%)	>97	>97
TEST BED GEOMETRY	Homogeneous	Homogeneous
CENTRIFUGE SPEED (rpm)	605	84
GROUND ZERO RADIUS (cm)	127.1	127.1
CENTRIFUGAL ACCELERATION (G)	500	10
CRATER VOLUME (cc)	34.1	67.5
CRATER RADIUS (cm)	4.68	5.81
MAX CRATER DEPTH (cm)	1.13	1.45
CRATER ASPECT RATIO (r/h)	4.14	4.01
CRATER C/L DEPTH (cm)	1.13	1.30
LIP RADIUS (cm)	6.00	7.80
LIP HEIGHT (cm)	0.27	0.12
LIP VOLUME (cc)	36.2	15.5
PI_2	3.16E-5	6.08E-7
PI_V	42.3	83.7
PI_R	5.03	6.24
PI_H	1.21	1.56

*2 diameter only

A62

| SHOT NUMBER	28-0	28-X*
RANGE (cm)	DEPTH (cm)	DEPTH (cm)
0.0	1.129	1.299
0.6	1.018	1.455
1.2	0.862	1.445
1.8	0.779	1.339
2.4	0.698	1.176
3.0	0.595	0.895
3.6	0.453	0.722
4.2	0.197	0.510
4.8	-0.050	0.264
5.4	-0.198	0.124
6.0	-0.270	-0.014
6.6	-0.206	-0.052
7.2	-0.138	-0.072
7.8	-0.118	-0.124
8.4	-0.078	-0.061
9.0	-0.070	-0.022
9.6	-0.055	-0.031
10.2	-0.039	-0.017
10.8	-0.035	-0.046
11.4	-0.018	-0.022
12.0	-0.009	-0.021
12.6	-0.005	0.022
13.2	-0.006	0.016
13.8	-0.008	0.013
14.4	-0.001	0.038
15.0	0.002	0.035
15.6	0.002	0.030
16.2	0.002	0.025
16.8	0.002	0.033
17.4	0.004	0.030
18.0	0.002	0.030
18.6	0.003	0.017
19.2	0.003	0.024
19.8	0.001	0.013
20.4	-0.002	0.008
21.0	-0.020	-0.008
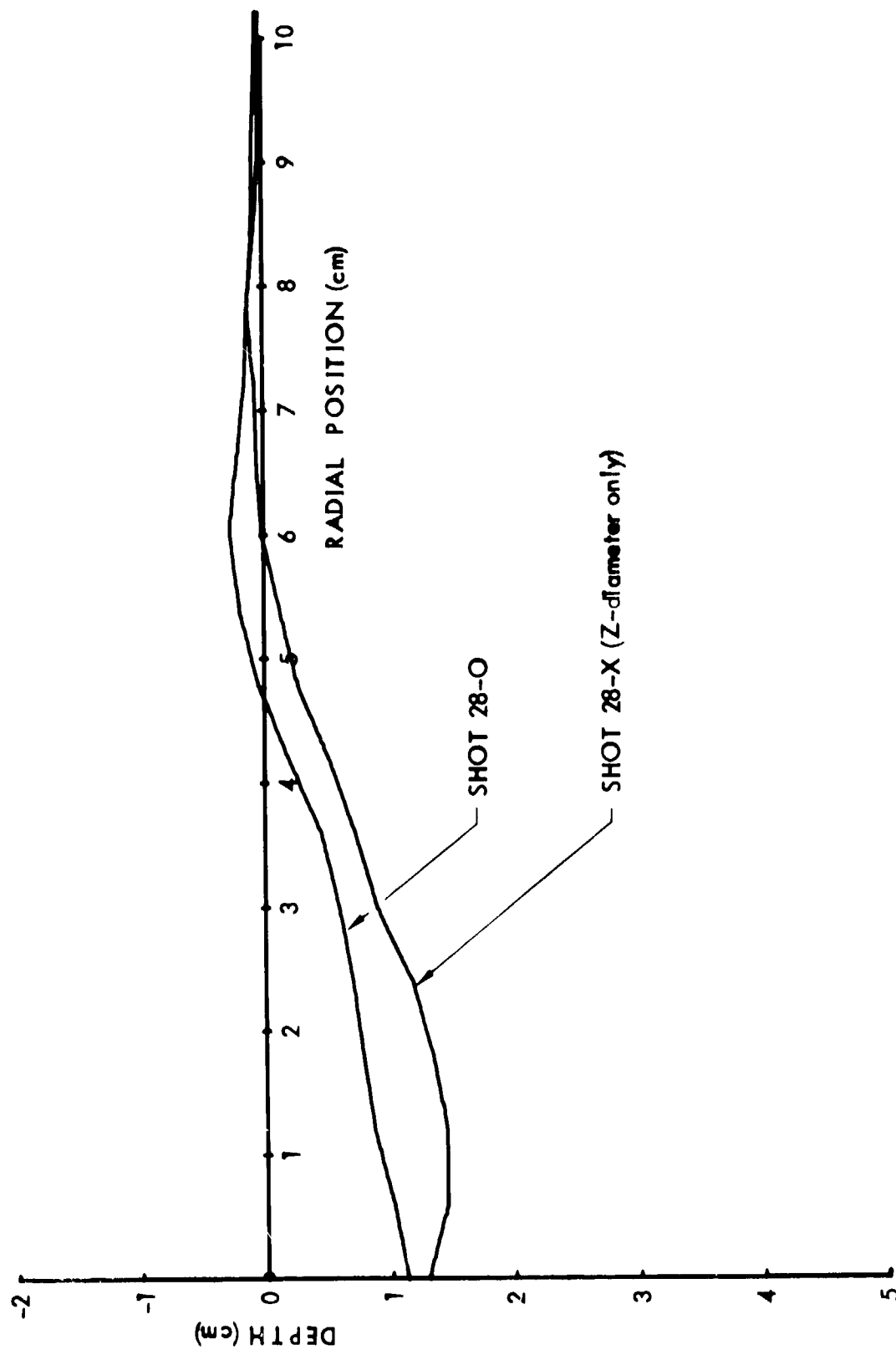
Fig. A41. Comparison of crater profiles.

Fig. A42. Shot 28-0, crater formed at 520 G by spherical 1.70-gm PbN_6 charge half-buried in nearly-saturated dense Ottawa Flintshot sand.

Fig. A43. Pre-shot photograph (28-X) showing charge placement and initial water level.

Fig. A44.   Shot 28-X, crater formed at 10 G by spherical 1.70-gm PbN$_6$
            charge half-buried in nearly-saturated dense Ottawa
            Flintshot sand. At shot time, water table was tangent
            to surface at the charge location.
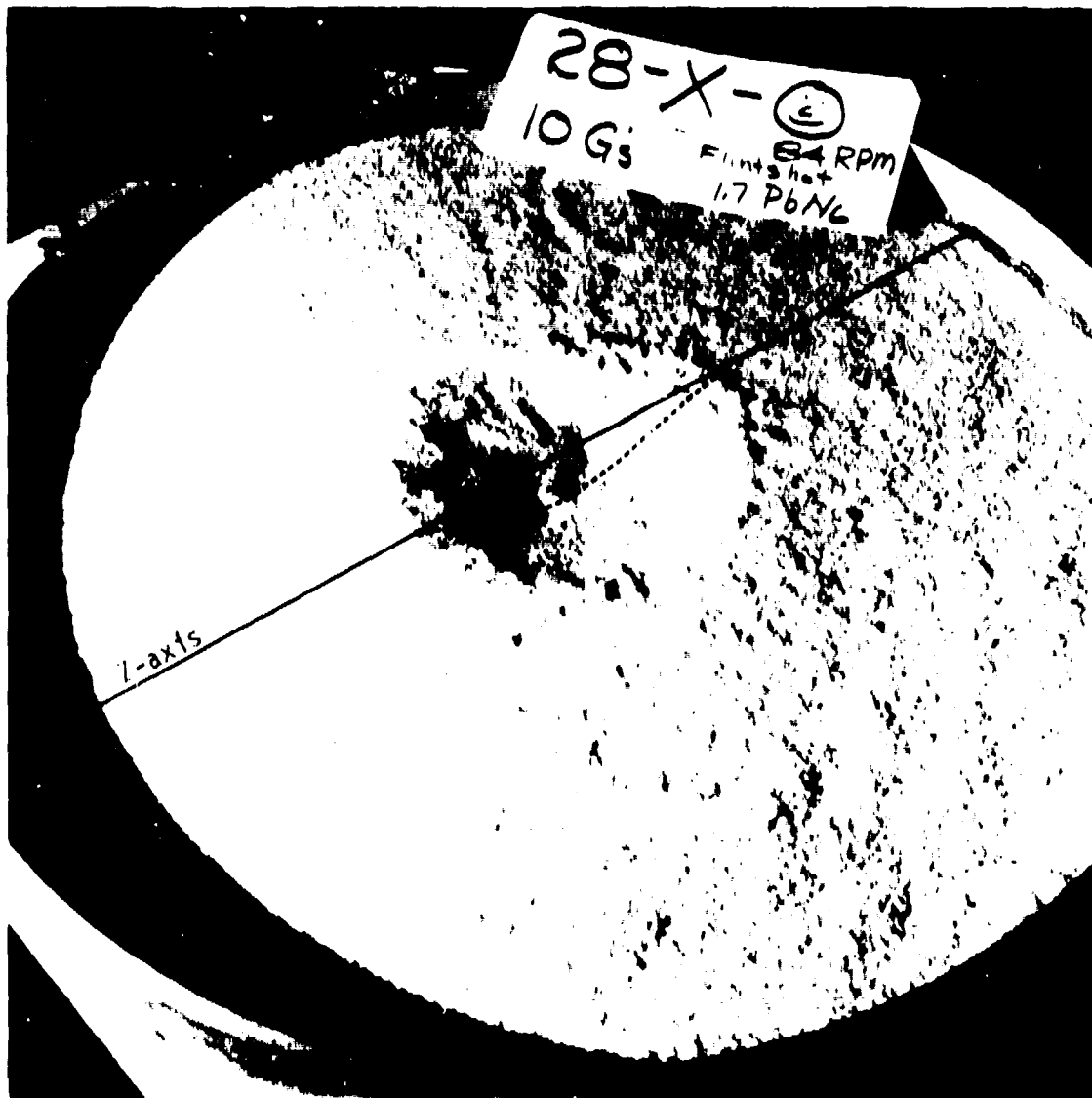
Fig. A45. Shot 28-X, close-up photograph showing effects of water wave washing of crater walls. L-axis shown on photo is line of tangency of water table in flight. See Fig. A44.

SHOT NUMBER	29-0	29-X
DATE	11/16/78	11/16/78
PURPOSE	Ground Motion	Ground Motion
CHARGE DESCRIPTION	CICS-4(B-20)	CICS-5(B-6)
CHARGE MASS (gm)	0.13 AgN$_3$/3.96 PETN	0.13 AgN$_3$/0.36 PETN
CHARGE RADIUS (cm)	0.826	0.390
CHARGE CONFIGURATION	Half-Buried Sphere	Half-Buried Sphere
TEST BED MATERIAL	Permoplast Clay (#61)	Permoplast Clay (#60)
TEST BED DENSITY (gm/cc)	1.53	1.53
MOISTURE CONTENT (%)	--	--
TEST BED GEOMETRY	Homogeneous	Homogeneous
CENTRIFUGE SPEED (rpm)	460	602
GROUND ZERO RADIUS (cm)	124.5	124.5
CENTRIFUGAL ACCELERATION (G)	294	504
CRATER VOLUME (cc)	211	17.6
CRATER RADIUS (cm)	5.70	2.56
MAX CRATER DEPTH (cm)	3.77	1.84
CRATER ASPECT RATIO (r/h)	1.51	1.39
CRATER C/L DEPTH (cm)	3.77	1.84
LIP RADIUS (cm)	7.20	3.00
LIP HEIGHT (cm)	0.90	0.40
LIP VOLUME (cc)	77.9	9.93
PI_2	6.90E-6	6.90E-6
PI_V	79.1	55.0
PI_R	4.11	3.74
PI_H	2.72	2.69

SHOT NUMBER RANGE (cm)	29-0 DEPTH (cm)	29-X DEPTH (cm)
0.0	3.767	1.839
0.6	3.772	1.638
1.2	3.696	1.358
1.8	3.548	0.884
2.4	3.320	0.135
3.0	2.956	-0.400
3.6	2.527	-0.369
4.2	2.029	-0.048
4.8	1.300	0.012
5.4	0.392	0.045
6.0	-0.385	0.071
6.6	-0.752	0.079
7.2	-0.903	0.096
7.8	-0.589	0.103
8.4	-0.285	0.119
9.0	0.014	0.116
9.6	0.050	0.119
10.2	0.065	0.122
10.8	0.070	0.119
11.4	0.083	0.119
12.0	0.079	0.110
12.6	0.078	0.104
13.2	0.067	0.080
13.8	0.046	0.063
14.4	0.041	0.046
15.0	0.020	0.014
15.6	-0.001	-0.008
16.2	-0.022	-0.039
16.8	-0.054	-0.096
17.4	-0.095	-0.137
18.0	-0.150	-0.202
18.6	--	--
19.2	--	--
19.8	--	--
20.4	--	--
21.0	--	--

A70
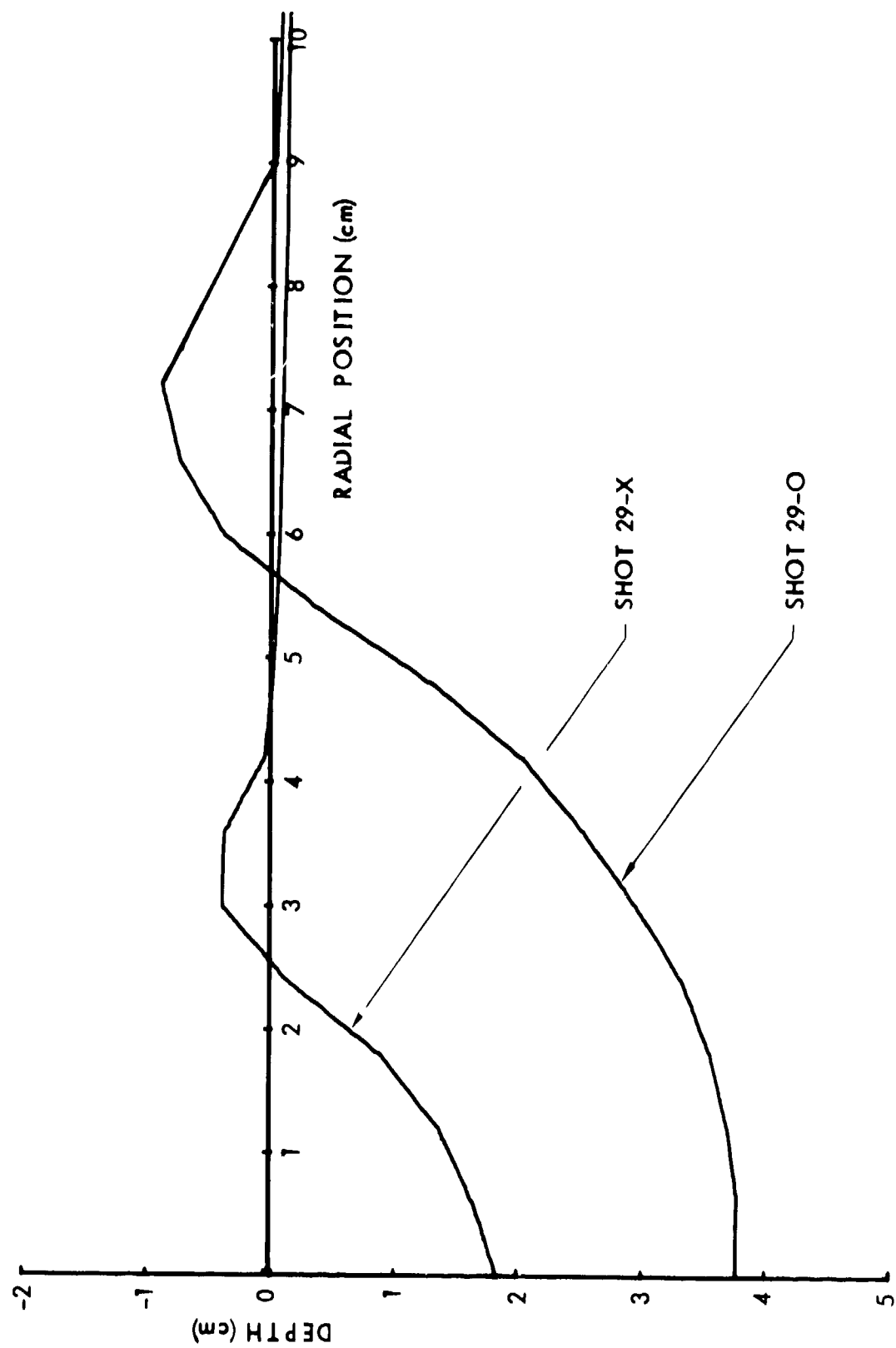
Fig. A46. Comparison of crater profiles.
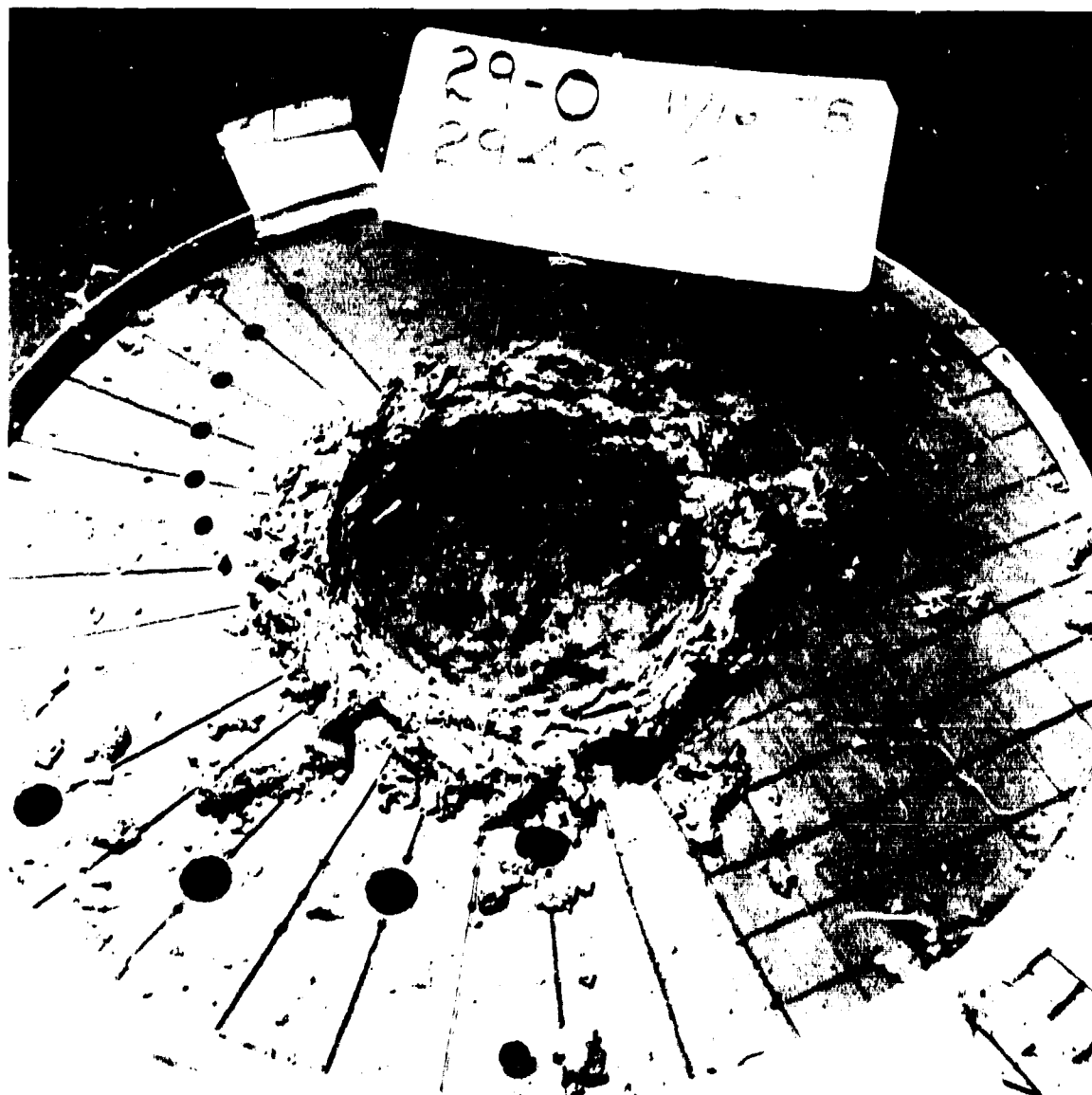
Fig. A47.   Shot 29-0, crater formed at 294 G by spherical 4.08-gm PETN
             charge half-buried in "Permoplast" oil-base clay. Gridwork,
             holes and sand columns were used to record residual ground
             displacement in near field. Compare with 1/2-scale event
             shown in Fig. A48.

A72
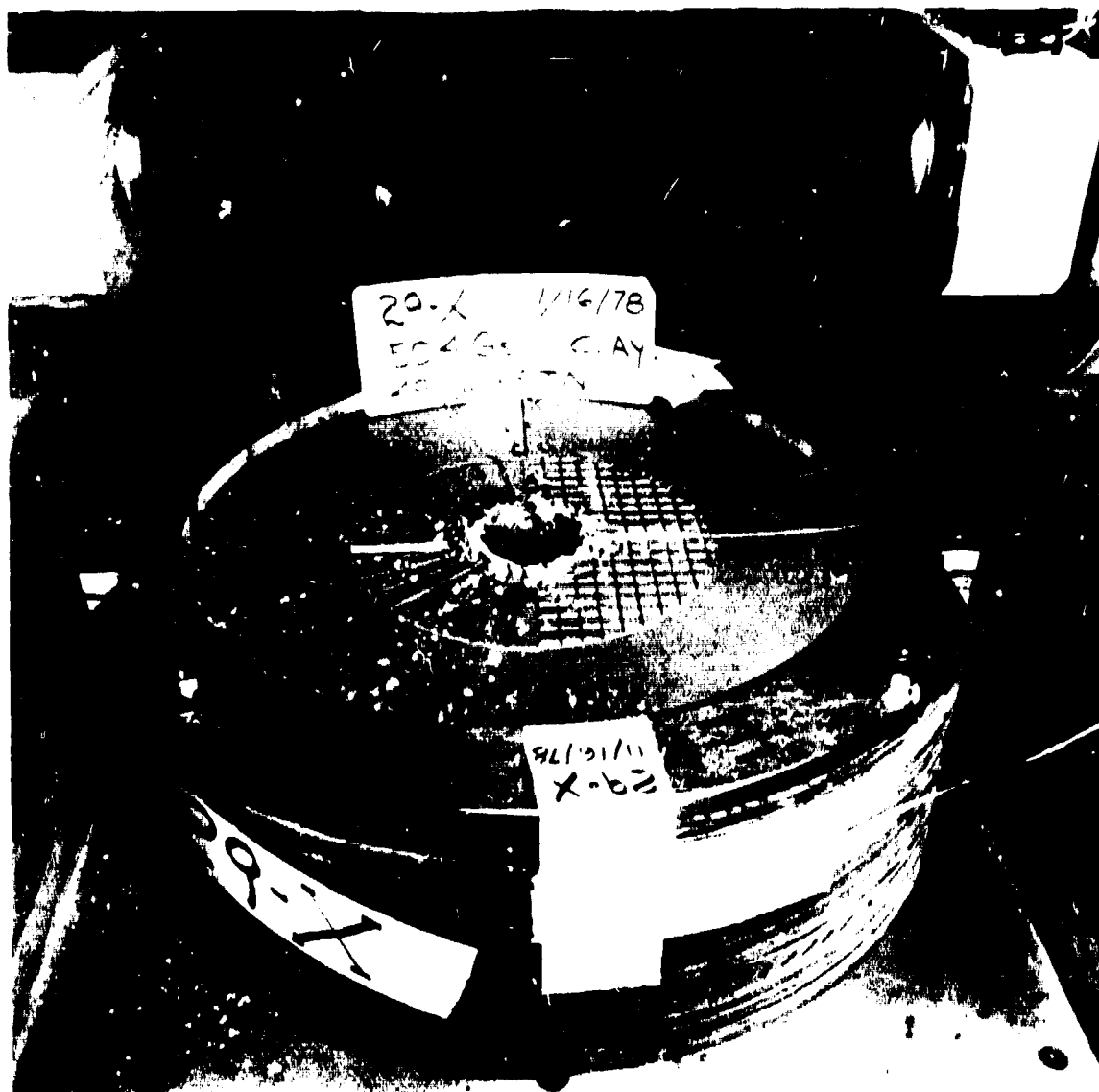
Fig. A48.   Shot 29-X, crater formed at 504 G by spherical 0.49-gm PETN
            charge half-buried in "Permoplast" oil-base clay. Gridwork,
            holes and sand columns were used to record residual ground
            displacement in near field. Compare with twice-scale event
            shown in Fig. A47.

Blank

A74

APPENDIX B
MATERIAL PROPERTIES OF TEST SOILS

REPORT ON
LABORATORY TESTS
CENTRIFUGE CRATERING STUDY II
FOR
BOEING AEROSPACE COMPANY

NOVEMBER, 1978

SHANNON & WILSON, INC.
Geotechnical Consultants
1105 North 38th Street
Seattle, Washington 98103

REPORT ON
LABORATORY TESTS
PERFORMED ON SOIL MATERIALS
FOR
CENTRIFUGE CRATERING STUDY II

I. PURPOSE AND SCOPE

This report presents the results of a series of unconsolidated-undrained (UU) triaxial compression tests and direct shear tests performed on five soil samples provided by Boeing Aerospace Company. Three UU tests and one direct shear test were performed on each material type to determine the shear strength parameters of the materials. The samples were designated as follows: Ottawa Sand No. 20, Ottawa Sand No. 30, Ottawa Sand No. 70, KAFBDA and Modeling Clay.

II. TEST PROCEDURES

A.   Unconsolidated-Undrained Triaxial Tests

Three (UU) test specimens were prepared for each sample. Test specimens of the sand were prepared by sifting the dry sand through a No. 16 mesh sieve from a height of 32 inches into a split mold to obtain the density specified by your office. For the alluvium type soil, KAFBDA, the density of the test specimens were obtained by vibrating a known weight of material at its natural water content into a split mold of known volume. Test specimen of the modeling clay were prepared by placing a known weight of clay in ten equal layers into a split mold and hand tamping each layer with a rod to obtain the desired density. The mold used was lined with a thin rubber membrane that was expanded against the split mold by vacuum.

After each UU test specimen was prepared, it was mounted in a triaxial test chamber and subjected to a specified triaxial confining pressure. It was then sheared under strain-controlled conditions, while maintaining a constant confining pressure and without allowing drainage. For each material type,

triaxial confining pressures of 10, 20 and 30 psi were used on the first, second and third test specimens, respectively, as specified. Water was used as the confining medium for all tests.

Simultaneous readings of load and deformation were obtained at regular time intervals throughout the shearing period. Deviator stress and axial strain values were then computed from these readings.

B.   Direct Shear Tests

Direct shear tests were performed in general accordance with ASTM D-3080-72. One direct shear test was performed on each material type. Test specimens of the sand were prepared in a similar manner as those for the UU specimens except they were prepared in a 4 x 4-inch shear box. The alluvium and modeling clay samples were packed in the box to the designated density.

After each specimen was compacted in the shear box, a very normal load was applied. Each specimen was sheared horizontaly in a constant strain shear device under drained conditions.
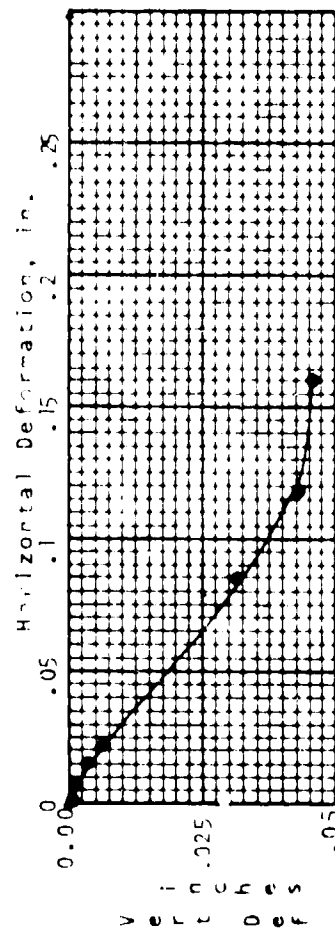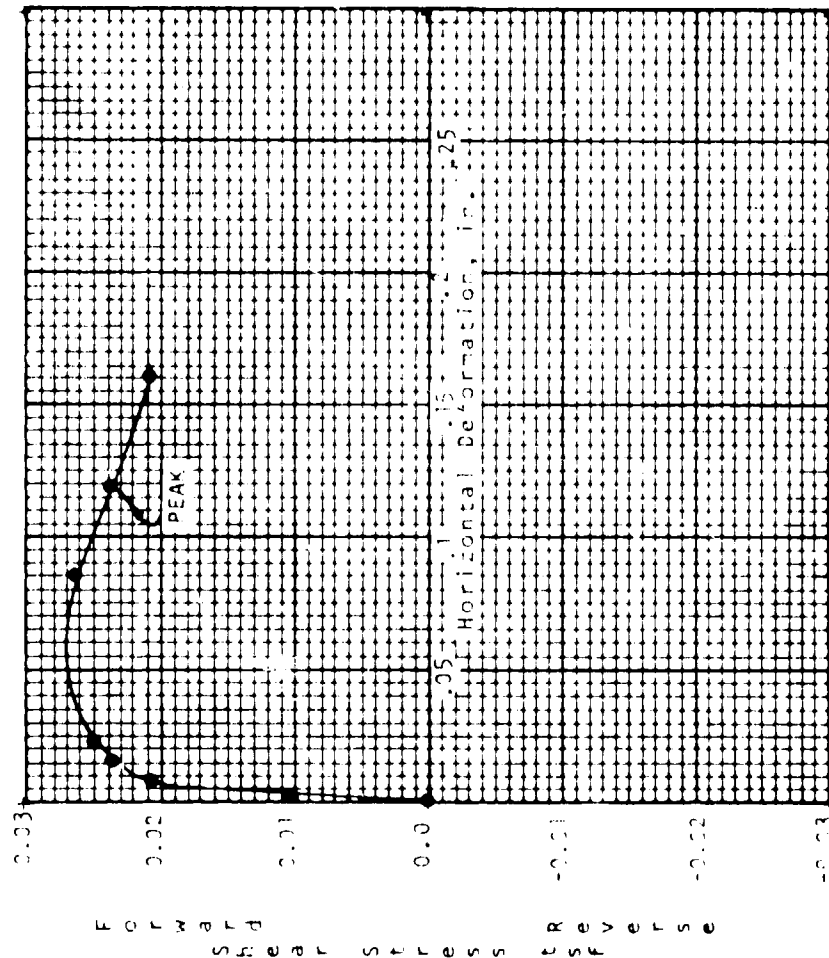
SPECIMEN DATA:
Height .... 1.75 in.
Length=Width .... 4.00 in.
Unit Wt., Dry ...... 111.7 pcf
Water Content
  Before Test ...... 0.0 %
  After Test .... 0.0 %
Degree of
  Saturation .... ---

CLASSIFICATION:
White, clean SAND, uniformly graded.

TEST DATA:
Initial Normal
  Stress .... .01 tsf
Rate of
  Strain .... .004966 in./min
Specimen Compacted
Specimen Dry

Fig. B1
Ottawa sand "FLINTSHOT"

DIRECT SHEAR TEST - 1
CENTRIFUGE CRATERING STUDY II

October 1979   W-3306-02
Shannon & Wilson, Inc.
Geotechnical Consultants

Forward Shear Stress tsf Reverse

Horizontal Deformation, in.

Vertical Deflection, inches

B4

Fig. B2
Ottawa sand "FLINTSHOT"

UNCONSOLIDATED, UNDRAINED,
TRIAXIAL COMPRESSION TEST
CENTRIFUGE CRATERING STUDY II
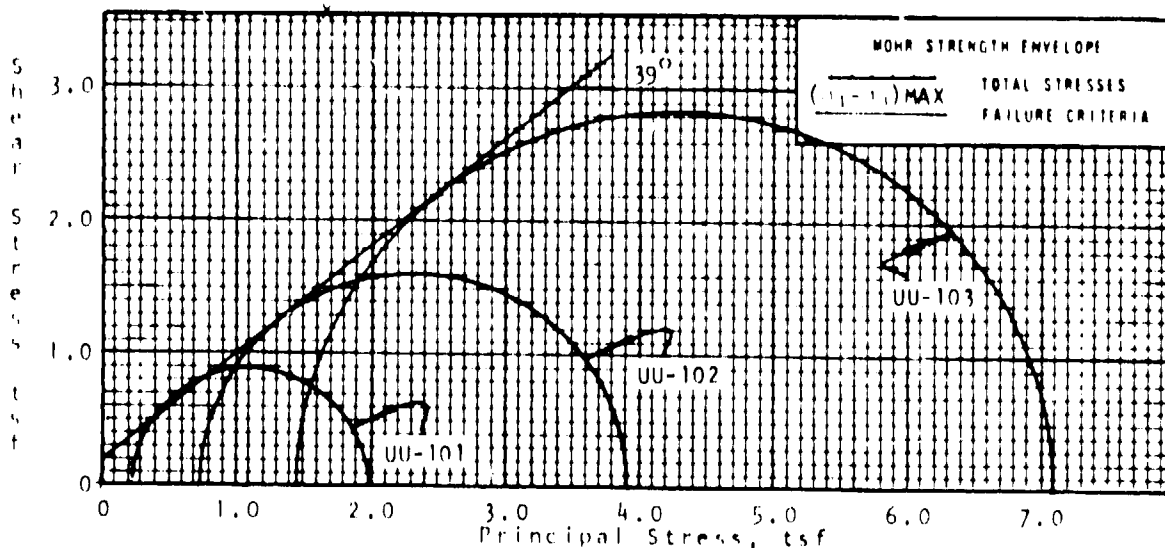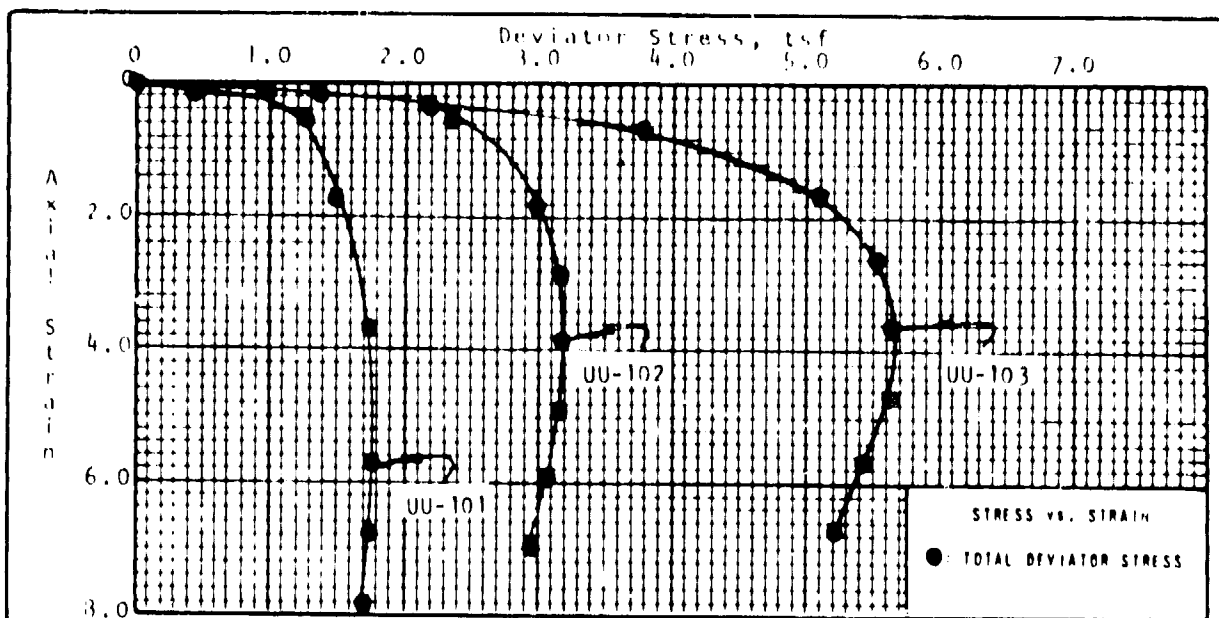
Test No.	UU-101	UU-102	UU-103
Confining Pressure, tsf	.22	.72	1.44
Ht., in.	4.93	4.93	4.93
Dia., in.	2.07	2.07	2.07
Ht./Dia. Ratio	2.38	2.38	2.38
Dry Unit Wt., pcf	111.5	112.1	112.1
Water Content, %			
Before Test	0.0	0.0	0.0
After Test	0.0	0.0	0.0
Degree of Saturation, %	--	--	--
Avg. % Strain/Min.	.989	1.003	.962

Specimens Compacted
Strain Controlled Test

October 1978   W-3306-02

Shannon & Wilson, Inc.
Geotechnical Consultants

Deviator Stress, tsf

0   20.0   40.0   60.0   80.0   100.0   120.0   140.0

Axial Strain %

5.0

10.0

15.0

20.0

UU-601 $(\sigma_1 - \sigma_3)$

UU-602 $(\sigma_1 - \sigma_3)$

UU-603 $(\sigma_1 - \sigma_3)$

UU-601 — UU-602 — UU-603
FAILURE SKETCHES

STRESS vs. STRAIN
● = TOTAL DEVIATOR STRESS

MOHR STRENGTH ENVELOPE
——— TOTAL STRESSES
$(\sigma_1 - \sigma_3)$ MAX   FAILURE CRITERIA

Shear Stress, tsf

S60.0

S40.0

S20.0

0

36°

UU-601   UU-602   UU-603

0   20.0   40.0   60.0   80.0   100.0   120.0   140.0

Principal Stress, tsf
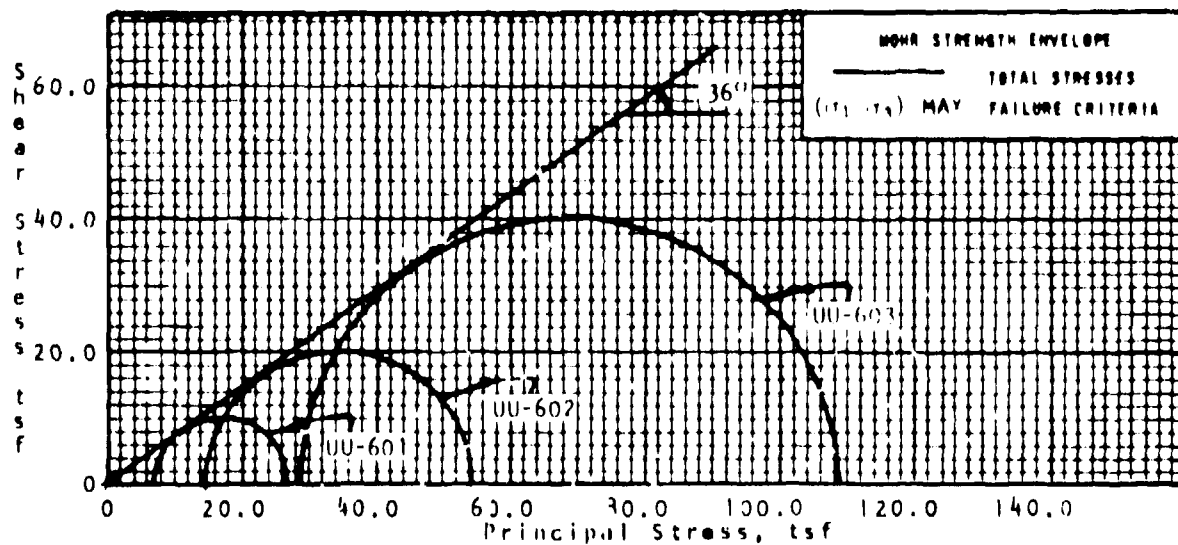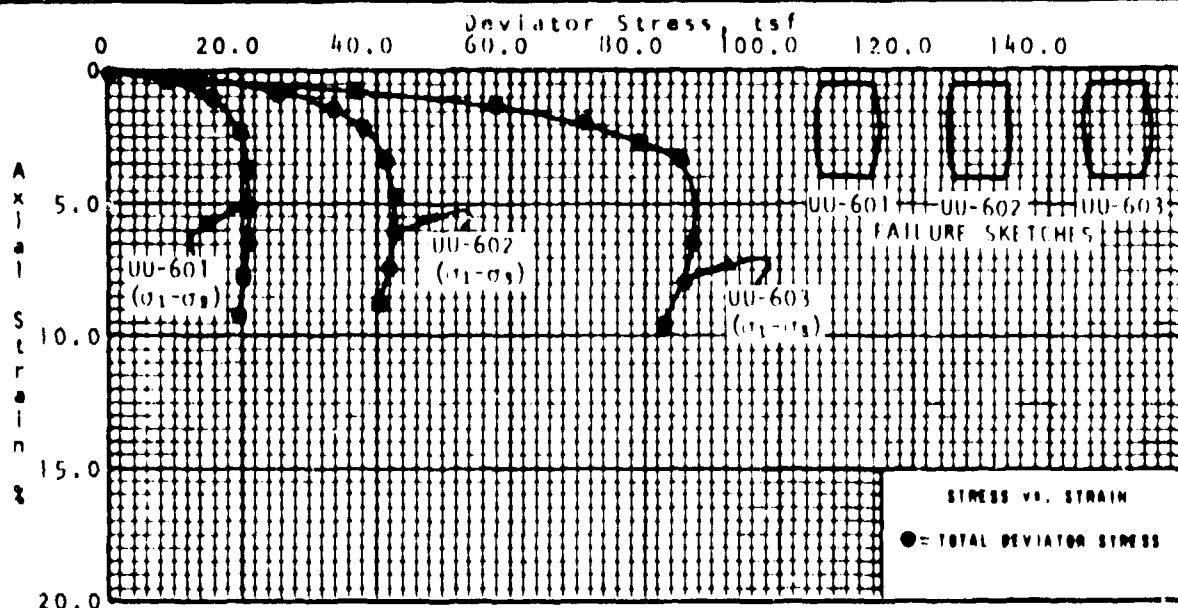
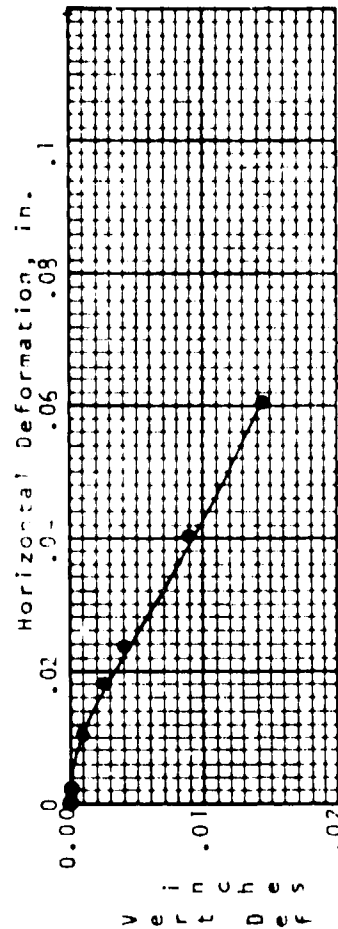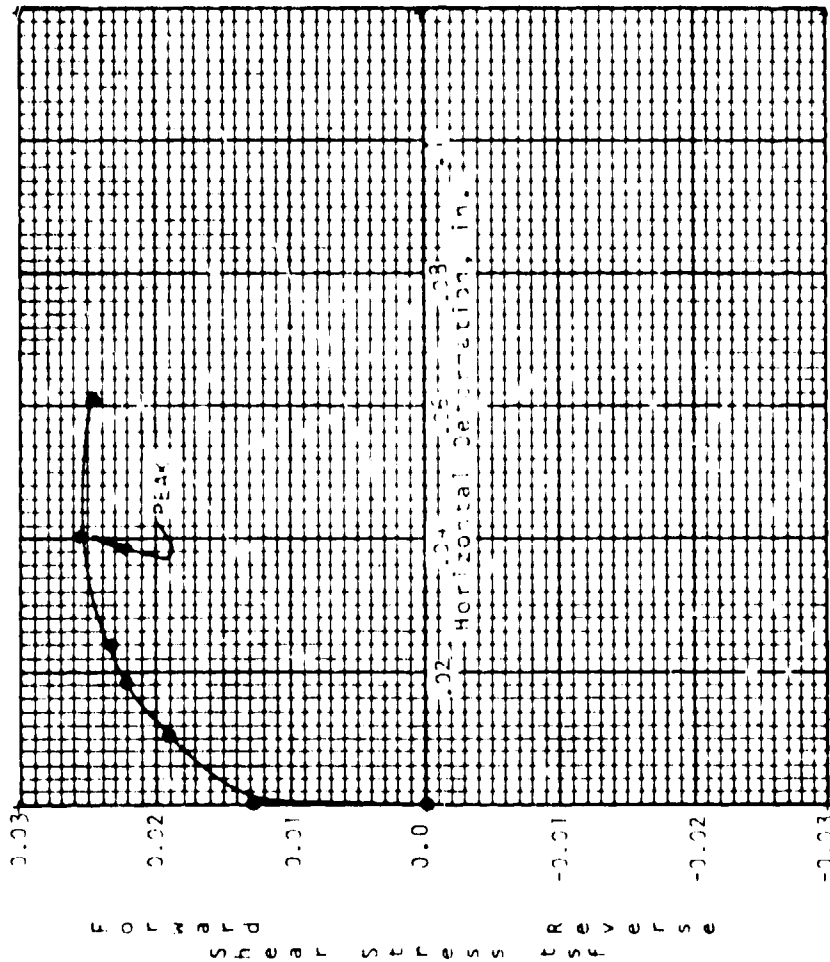| Test No.	UU-601	UU-602	UU-603
Confining Pressure, tsf	7.19	14.39	28.78
Ht., in.	6.91	6.89	6.89
Dia., in.	3.02	3.01	3.01
Ht./Dia. Ratio	2.28	2.28	2.28
Dry Unit Wt., pcf	109.6	110.0	110.2
Avg. % Strain/Min.	.658	.630	.683

Specimens Compacted
Strain Controlled Test

Fig. B3
Ottawa sand "FLINTSHOT"

UNCONSOLIDATED, UNDRAINED,
TRIAXIAL COMPRESSION TEST
LARGE CONFINING PRESSURES

Dec. 1977   W-3306-01
Shannon & Wilson, Inc.
Geotechnical Consultants
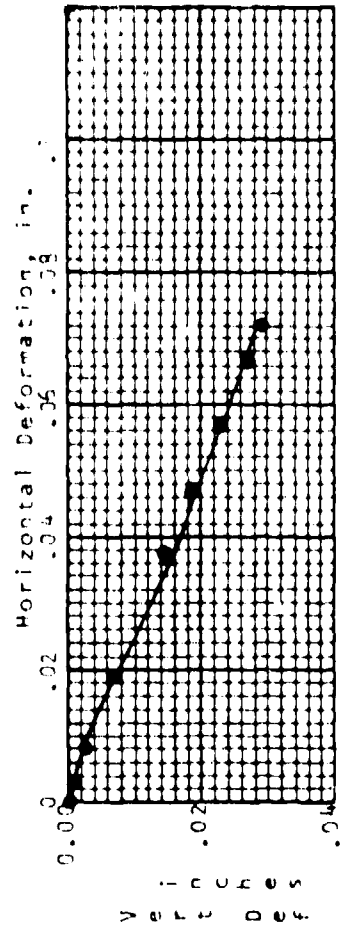
CLASSIFICATION:
White, clean SAND, uniformly graded.

Fig. B4
Ottawa sand "SAWING"

DIRECT SHEAR TEST

Shannon & Wilson, Inc.
Geotechnical Consultants

Horizontal Deformation, in.

Fig. B5
Ottawa sand "SAWING"

UNCONSOLIDATED, UNDRAINED,
TRIAXIAL COMPRESSION TEST
CENTRIFUGE CRATERING STUDY II
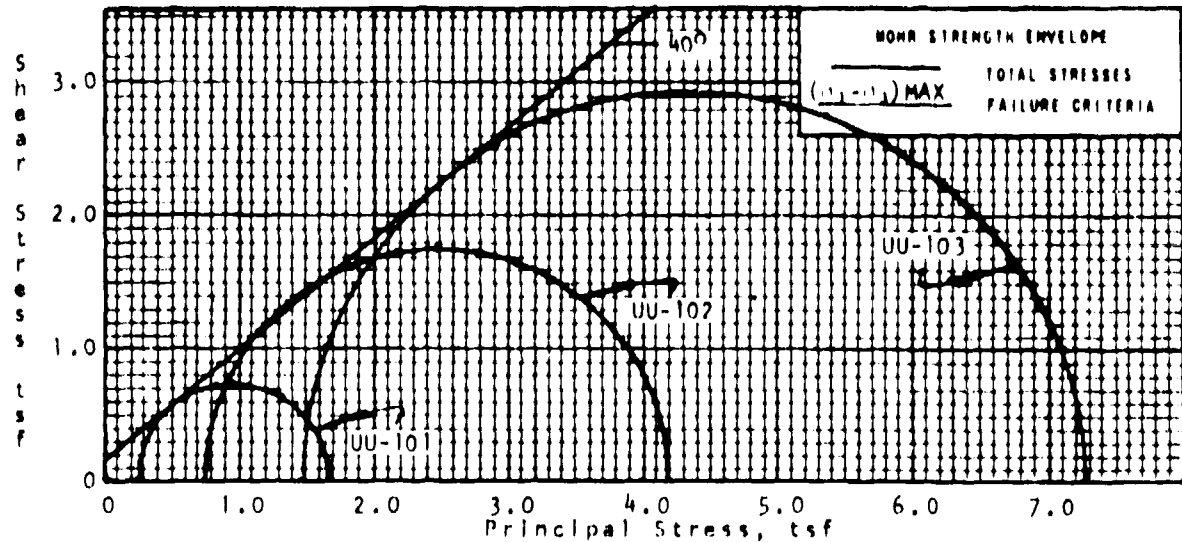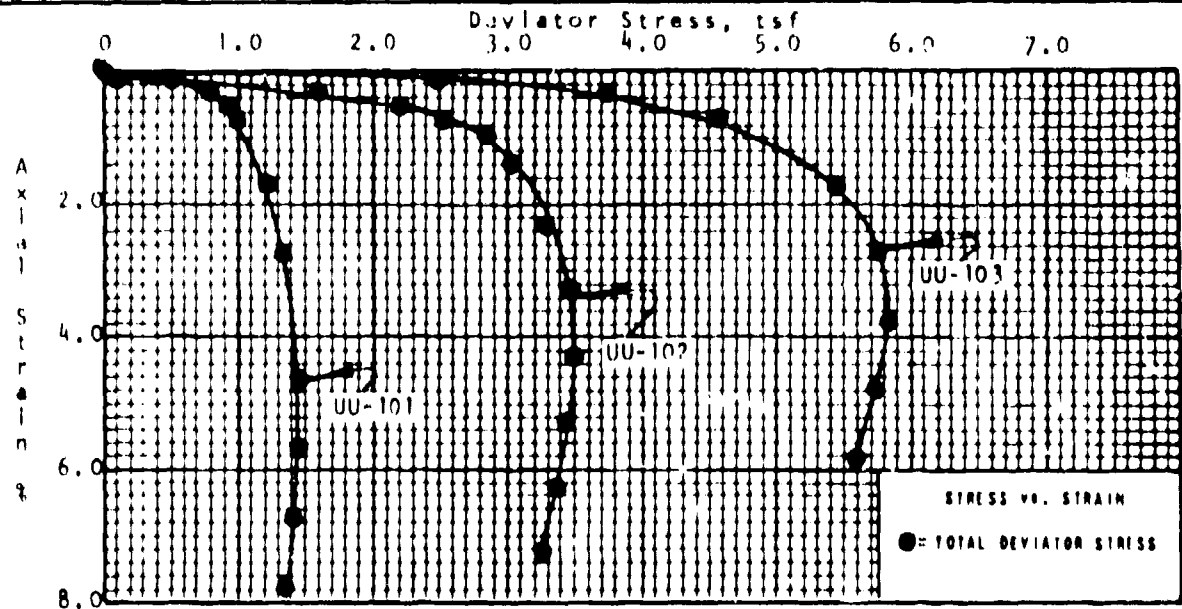
Test No.	UU-101	UU-102	UU-103
Confining Pressure, tsf	.22	.72	1.44
Ht., in.	4.93	4.93	4.93
Dia., in.	2.07	2.07	2.07
Ht./Dia. Ratio	2.38	2.38	2.38
Dry Unit Wt., pcf	111.0	110.5	110.6
Water Content, %			
Before Test	0.0	0.0	0.0
After Test	0.0	0.0	0.0
Degree of Saturation, %	--	--	--
Avg. % Strain/Min.	.976	.910	.975

Specimens Compacted
Strain Controlled Test

October 1978   W-3306-02
Shannon & Wilson, Inc.
Geotechnical Consultants

Fig. B6

Ottawa sand "SAWING"

UNCONSOLIDATED, UNDRAINED, TRIAXIAL COMPRESSION TEST

LARGE CONFINING PRESSURES
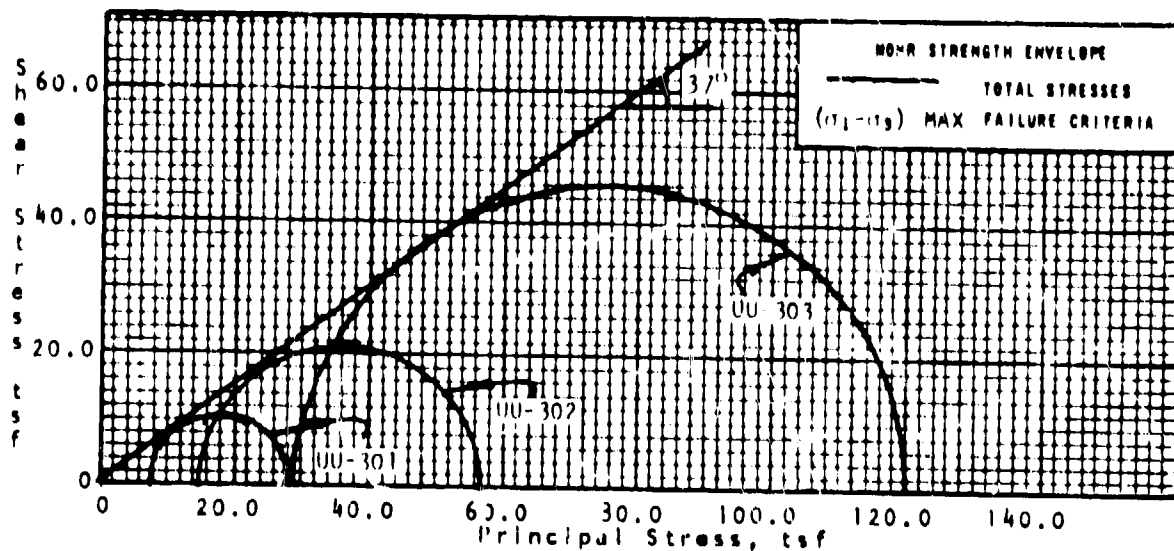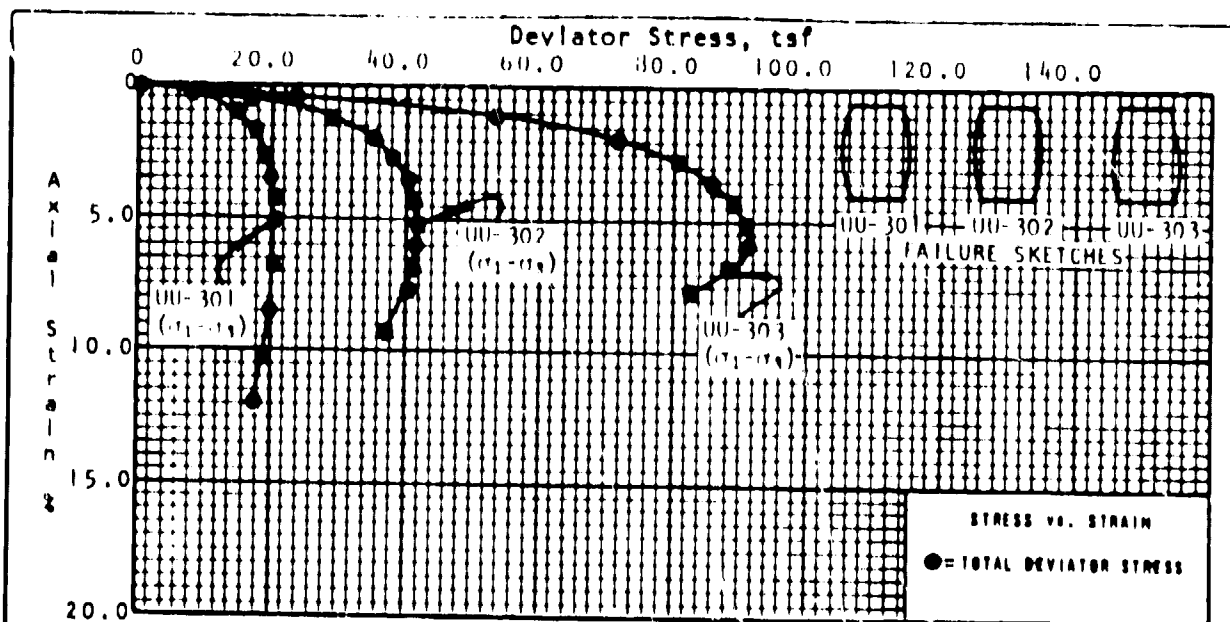
Test No.	UU-301	UU-302	UU-303
Confining Pressure, tsf	7.19	14.39	28.73
Ht., in.	6.85	6.35	6.87
Dia., in.	3.01	3.01	3.01
Ht./Dia. Ratio	2.27	2.27	2.23
Dry Unit Wt., pcf	110.5	110.3	110.3
Water Content, %			
Before Test	0	0	0
After Test	0	0	0
Avg. % Strain/Min.	.798	.733	.771

Specimens Compacted
Strain Controlled Test

Dec. 1977   W-3306-01
Shannon & Wilson, Inc.
Geotechnical Consultants

SPECIMEN DATA:
Height   1.75 in.
Length=Width   4.00 in.
Unit Wt., Dry   105.0 pcf
Water Content
  Before Test   0.0 %
  After Test   0.0 %
Degree of
  Saturation   --

CLASSIFICATION:
White, clean SAND, uniformly graded.

TEST DATA:
Initial Normal
  Stress   .01 tsf
Rate of
  Strain   .003930 in./min
Specimen Compacted
Specimen Dry

Fig. B7
Ottawa sand "BANDING"

DIRECT SHEAR TEST DS-1
CENTRIFUGE CRATERING STUDY II

October 1979   W-3306-02
Shannon & Wilson, Inc.
Geotechnical Consultants

STRESS vs. STRAIN

● = TOTAL DEVIATOR STRESS

MOHR STRENGTH ENVELOPE

$(\sigma_1 - \sigma_3)$ MAX — TOTAL STRESSES FAILURE CRITERIA
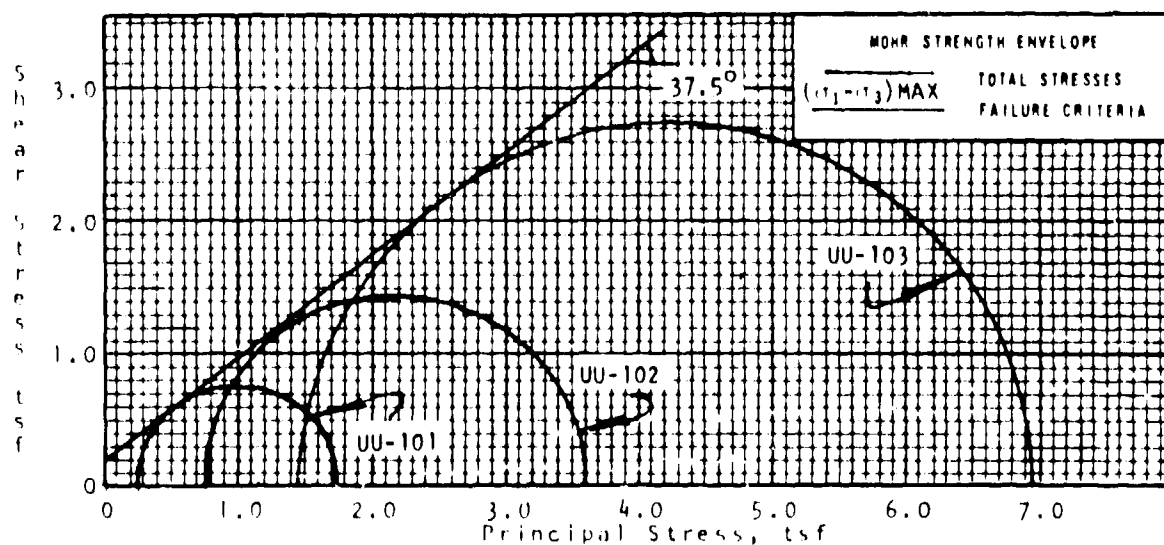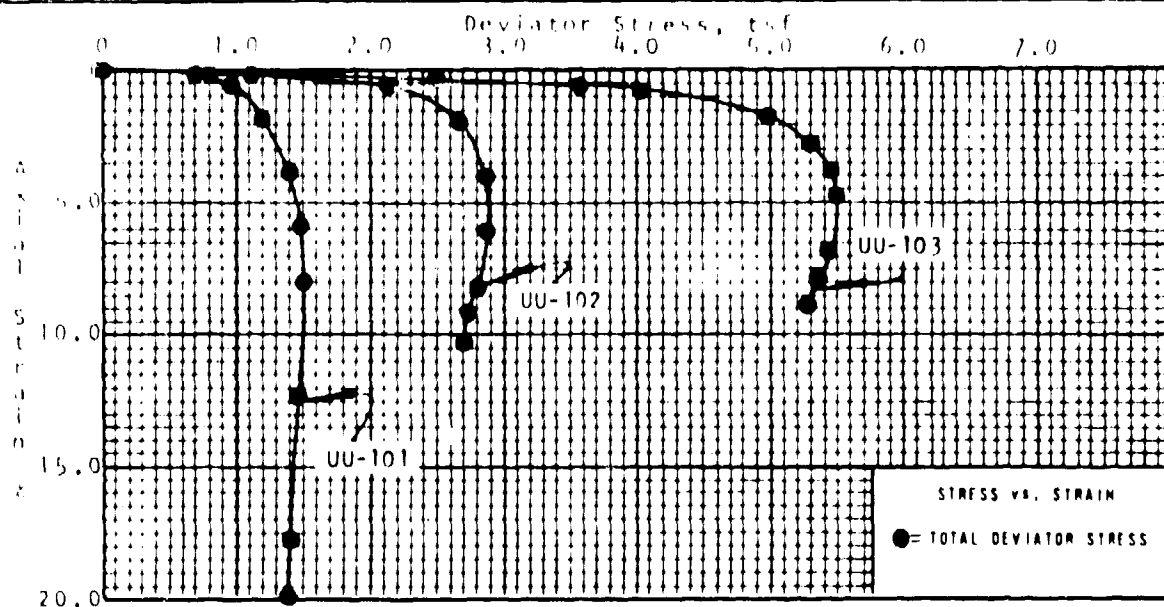
Test No.	UU-101	UU-102	UU-103
Confining Pressure, tsf	.22	.72	1.44
Ht., in.	4.91	4.93	4.93
Dia., in.	2.07	2.07	2.07
Ht./Dia. Ratio	2.37	2.38	2.38
Dry Unit Wt., pcf	105.5	105.1	105.1
Water Content, %			
Before Test	0.0	0.0	0.0
After Test	0.0	0.0	0.0
Degree of Saturation, %	--	--	--
Avg. % Strain/Min.	1.049	1.03	.995

Specimens Compacted
Strain Controlled Test

Fig. B8
Ottawa sand "BANDING"

UNCONSOLIDATED, UNDRAINED,
TRIAXIAL COMPRESSION TEST
CENTRIFUGE CRATERING STUDY II

October 1978   W-3306-02

Shannon & Wilson, Inc.
Geotechnical Consultants

Fig. B9
Ottawa sand "BANDING"

UNCONSOLIDATED, UNDRAINED,
TRIAXIAL COMPRESSION TEST
LARGE CONFINING PRESSURES
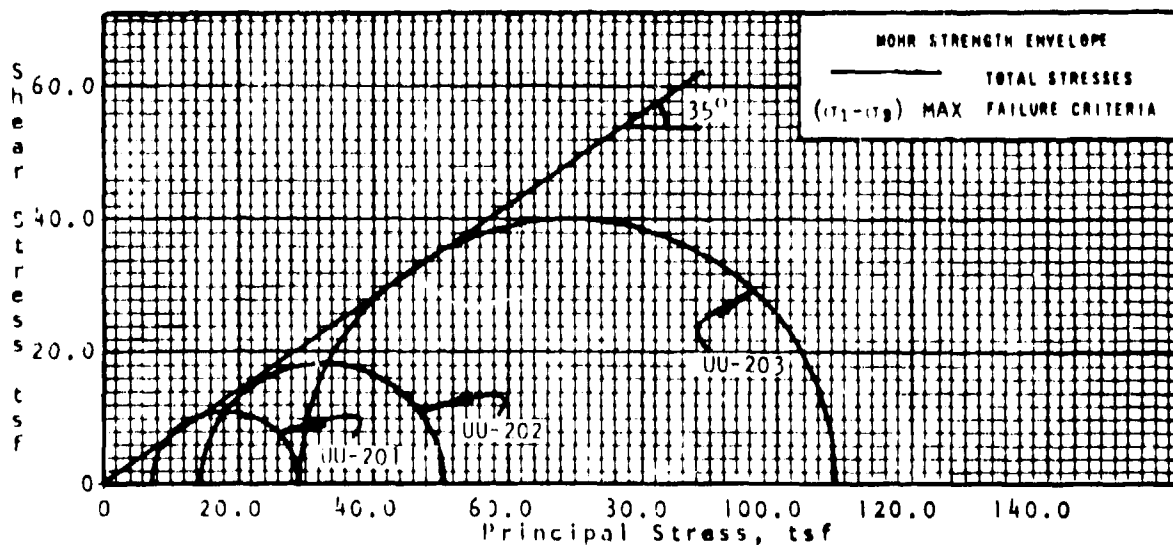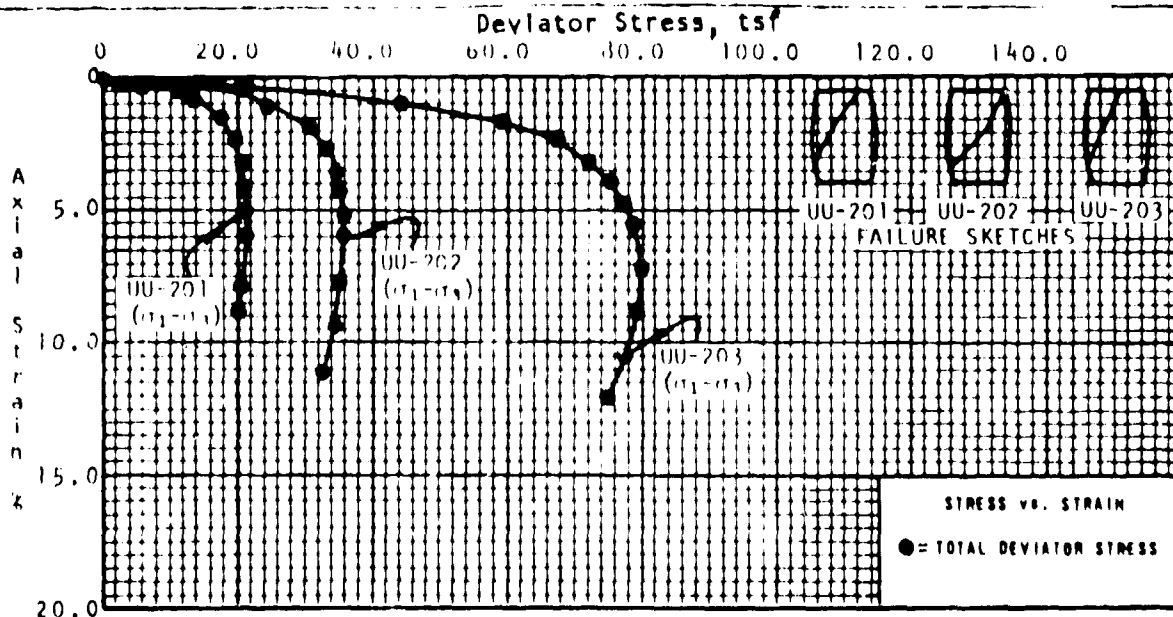
Test No.	UU-201	UU-202	UU-203
Confining Pressure, tsf	7.19	14.39	28.73
Ht., in.	6.85	6.85	6.89
Dia., in.	3.01	3.01	3.01
Ht./Dia. Ratio	2.27	2.27	2.28
Dry Unit Wt., pcf	104.4	104.3	103.9
Water Content, %			
Before Test	0.4	0.4	0.4
After Test	0.4	0.4	0.4
Avg. % Strain/Min.	.810	.794	.755

Specimens Compacted
Strain Controlled Test

Dec. 1977   W-3306-01
Shannon & Wilson, Inc.
Geotechnical Consultants
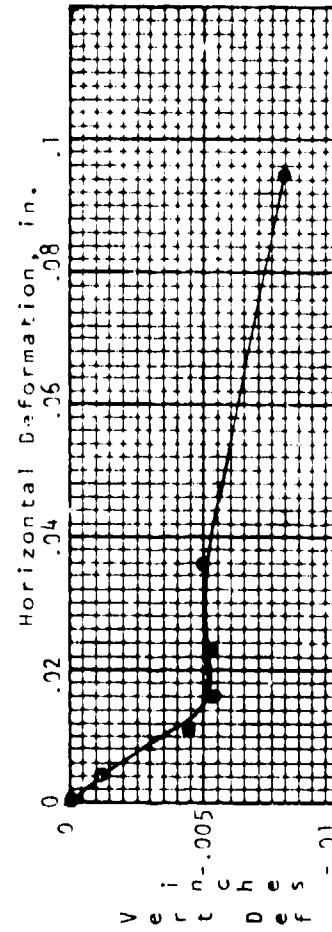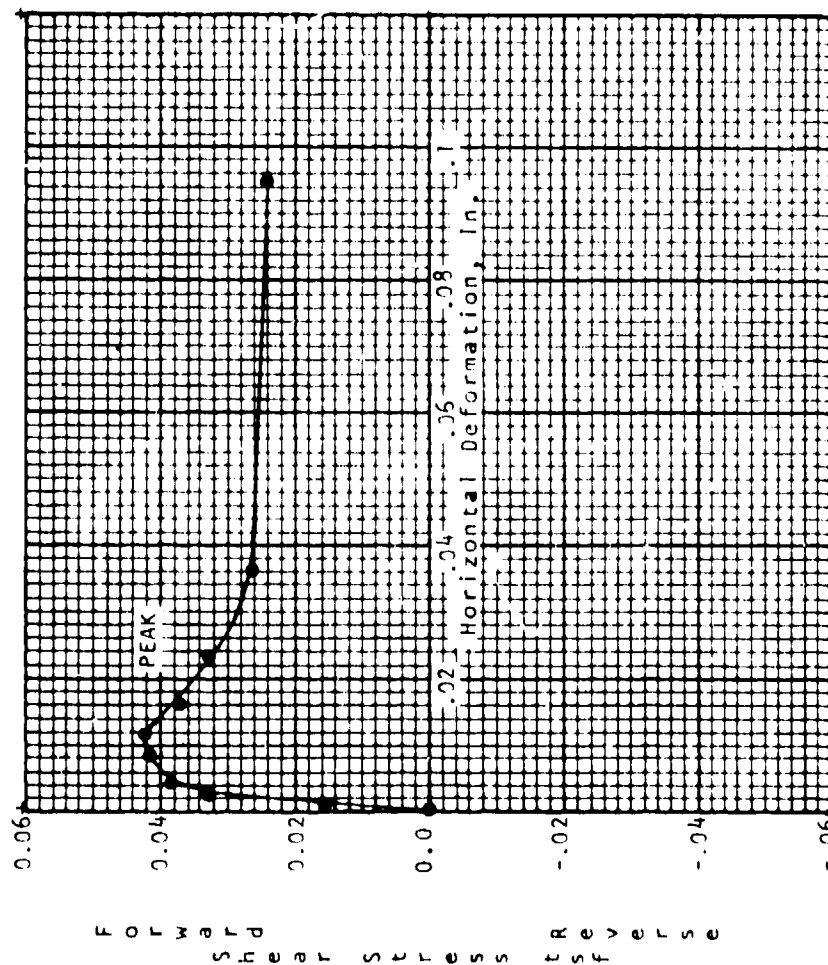
SPECIMEN DATA:
Height   1.75 in.
Length=Width   4.00 in.
Unit Wt. Dry   98.0 pcf
Water Content
  Before Test   .3 %
  After Test   .3 %
Degree of
  Saturation   -- %
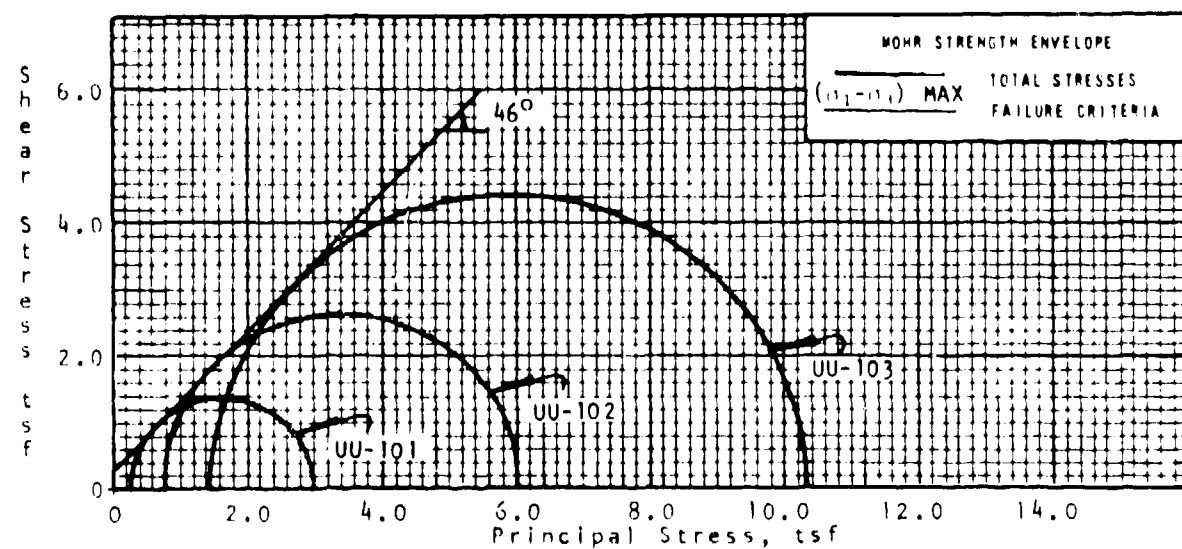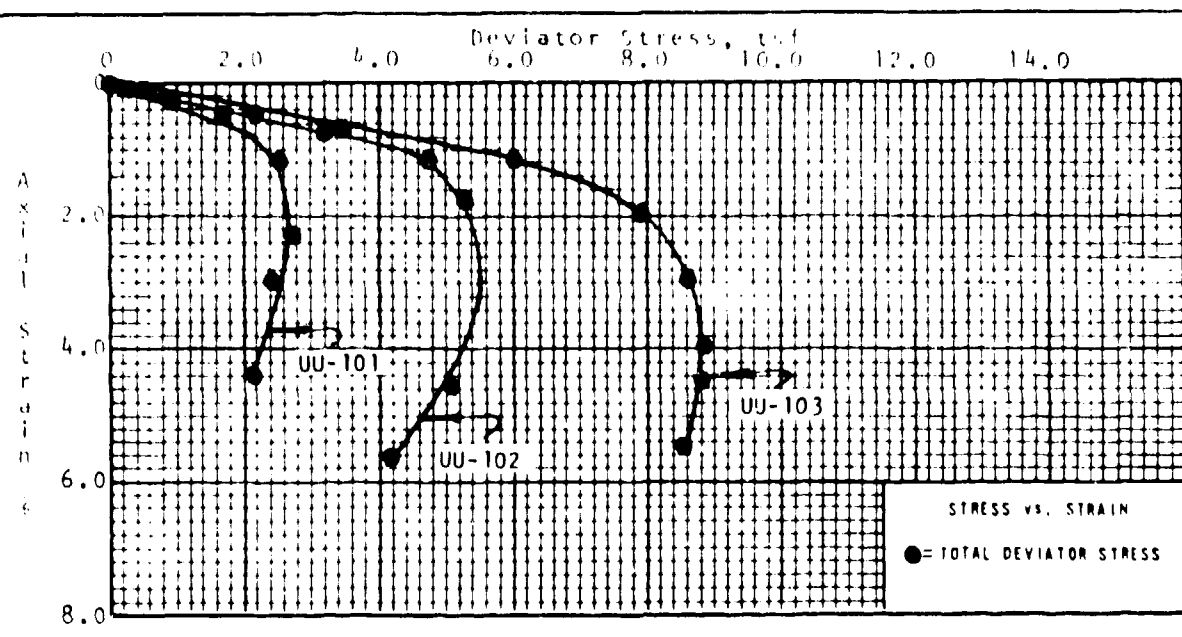
CLASSIFICATION:
Light brown, sandy SILT.

TEST DATA:
Initial Normal
  Stress   .01 tsf
Rate of
  Strain   .004938 in./min
Specimen Compacted
Specimen At Nat WC

Fig. B10
KAFB Alluvium (<1% moisture)

DIRECT SHEAR TEST DS-1

CENTRIFUGE CRATERING STUDY II

October 1979
Shannon & Wilson, Inc.   W-3306-02
Geotechnical Consultants

B13

Fig. B11
KAFB Alluvium (<1% moisture)

UNCONSOLIDATED, UNDRAINED,
TRIAXIAL COMPRESSION TEST

CENTRIFUGE CRATERING STUDY II

Test No.	UU-101	UU-102	UU-103
Confining Pressure, tsf	.22	.72	1.44
Ht., in.	4.97	4.98	4.99
Dia., in.	2.08	2.08	2.08
Ht./Dia. Ratio	2.38	2.39	2.39
Dry Unit Wt., pcf	98.8	98.0	96.5
Water Content, %			
Before Test	0.24	0.72	0.60
After Test	0.24	0.72	0.60
Degree of Saturation, %	---	---	---
Avg. Strain/Min.	.891	1.261	.896

Specimens Compacted
Strain Controlled Test

October 1978   W-3306-02
Shannon & Wilson, Inc.
Geotechnical Consultants

Fig. B12

KAFB Alluvium (2.4% moisture)

UNCONSOLIDATED, UNDRAINED,
TRIAXIAL COMPRESSION TEST

LARGE CONFINING PRESSURES
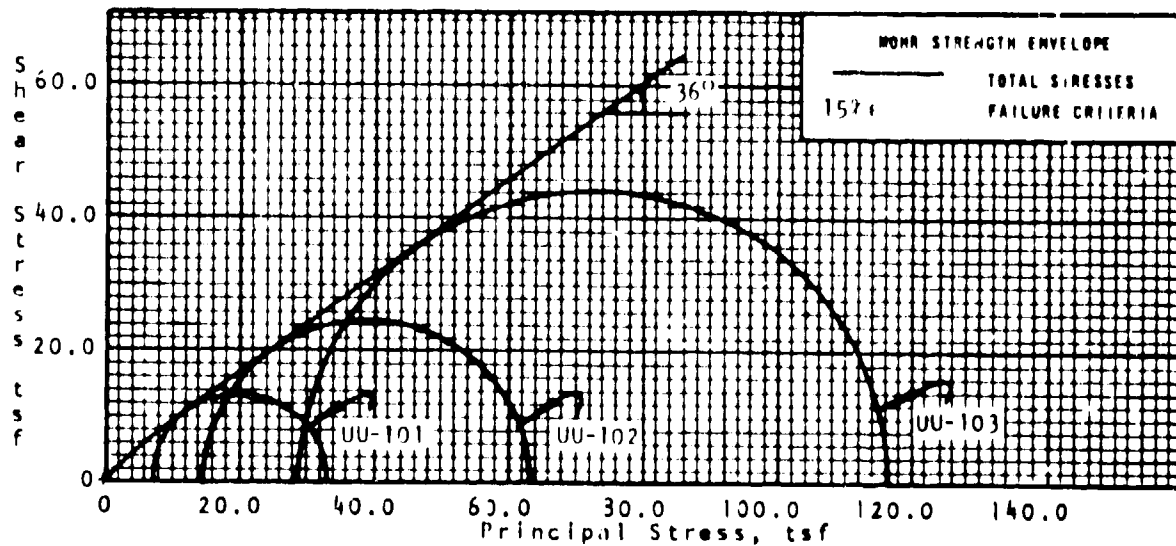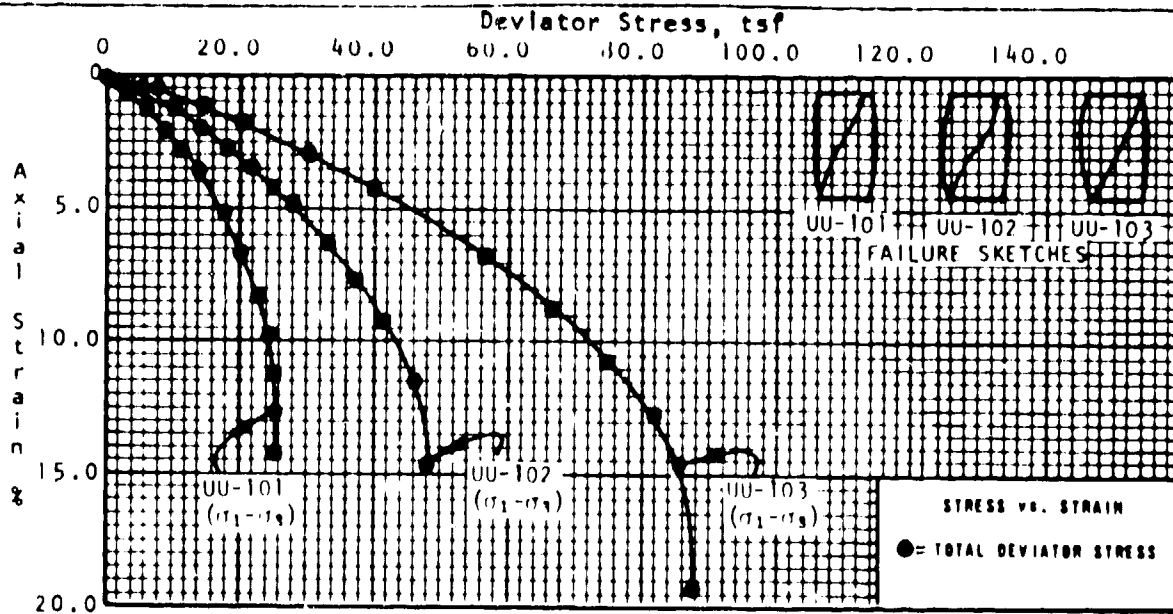
Test No.	UU-101	UU-102	UU-103
Confining Pressure, tsf	7.19	14.39	28.73
Ht., in.	6.83	6.34	6.83
Dia., in.	3.00	3.01	2.93
Ht./Dia. Ratio	2.27	2.27	2.23
Dry Unit Wt., pcf	99.0	99.7	100.0
Water Content, %			
Before Test	2.4	2.4	2.4
After Test	2.4	2.4	2.4
Avg. % Strain/Min.	.753	.733	.644

Specimens Compacted
Strain Controlled Test

Dec. 1977   W-3306-01
Shannon & Wilson, Inc.
Geotechnical Consultants

SPECIMEN DATA:
Height   1.75 in.
Length=Width   4.00 in.
Unit Wt., Dry   95.1 pcf
Water Content
  Before Test   4.0 %
  After Test   4.0 %
Degree of
  Saturation   --- %

CLASSIFICATION:
Light brown, sandy SILT.

TEST DATA:
Initial Normal
  Stress   .01 tsf
Rate of
  Strain   .004733 in./min
Specimen Compacted
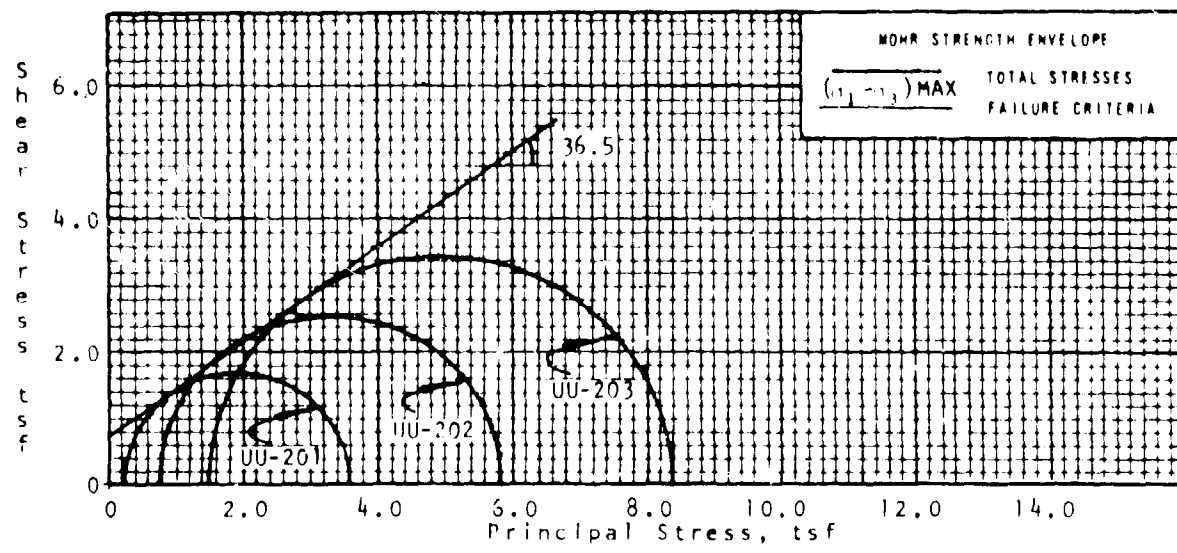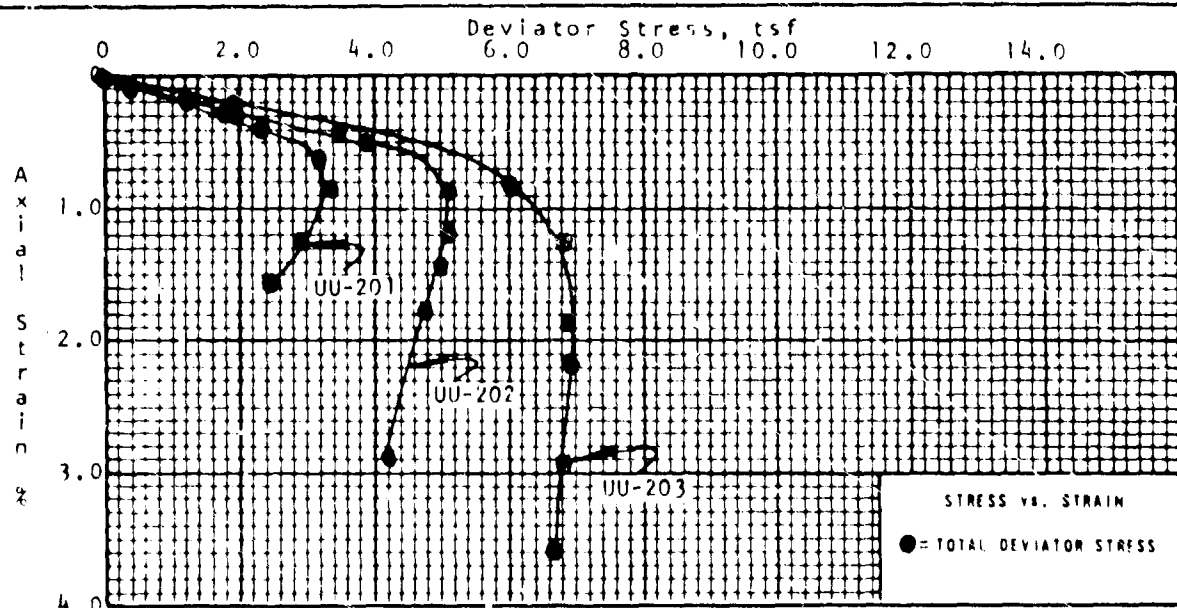Specimen At Nat WC
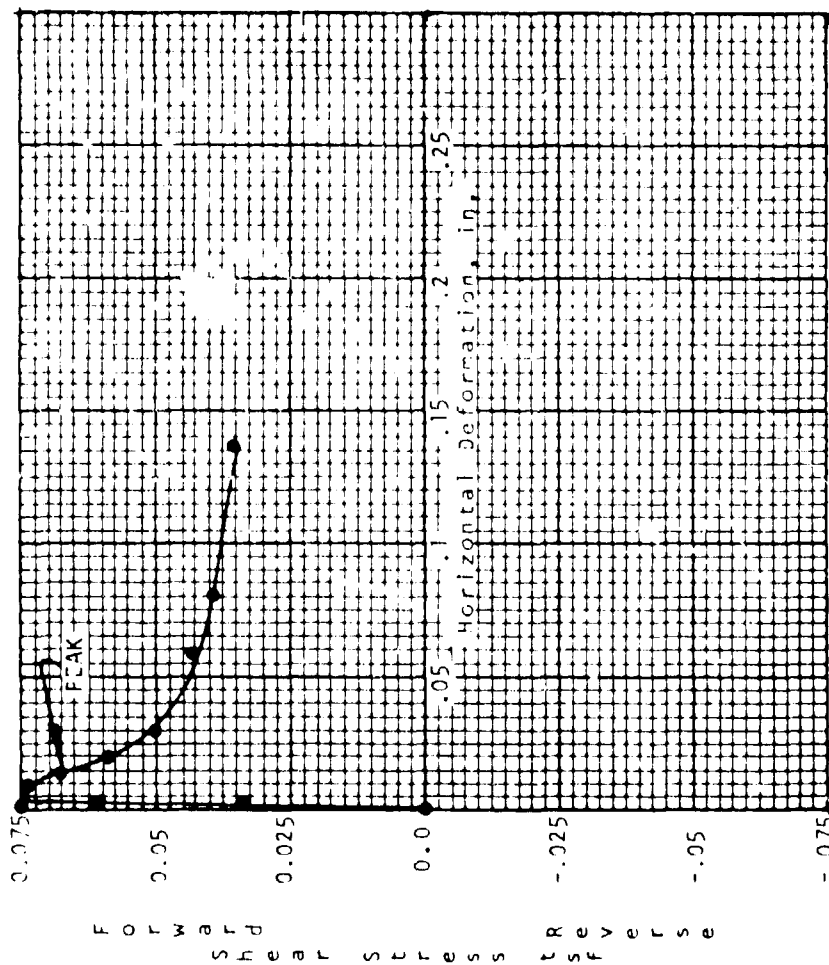
Fig. B13
KAFB Alluvium (3-4% moisture)

DIRECT SHEAR TEST DS-1
CENTRIFUGE CRATERING STUDY II

October 1978   W-3306-02
Shannon & Wilson, Inc.
Geotechnical Consultants

Fig. B14
KAFB Alluvium (3-4% moisture)

UNCONSOLIDATED, UNDRAINED,
TRIAXIAL COMPRESSION TEST

CENTRIFUGE CRATERING STUDY II

Test No.	UU-201	UU-202	UU-203
Confining Pressure, tsf	.22	.72	1.44
Ht., in.	4.74	4.48	4.76
Dia., in.	2.10	2.10	2.10
Ht./Dia. Ratio	2.25	2.13	2.26
Dry Unit Wt., pcf	97.0	95.0	94.6
Water Content, %			
Before Test	3.5	3.5	3.5
After Test	3.0	3.4	3.4
Degree of Saturation, %	--	--	--
Avg. % Strain/Min.	.791	.996	.903

Specimens Compacted
Strain Controlled Test

October 1978   W-3306-02
Shannon & Wilson, Inc.
Geotechnical Consultants

Fig. B15
KAFB Alluvium (4.4% moisture)

UNCONSOLIDATED, UNDRAINED,
TRIAXIAL COMPRESSION TEST

LARGE CONFINING PRESSURES
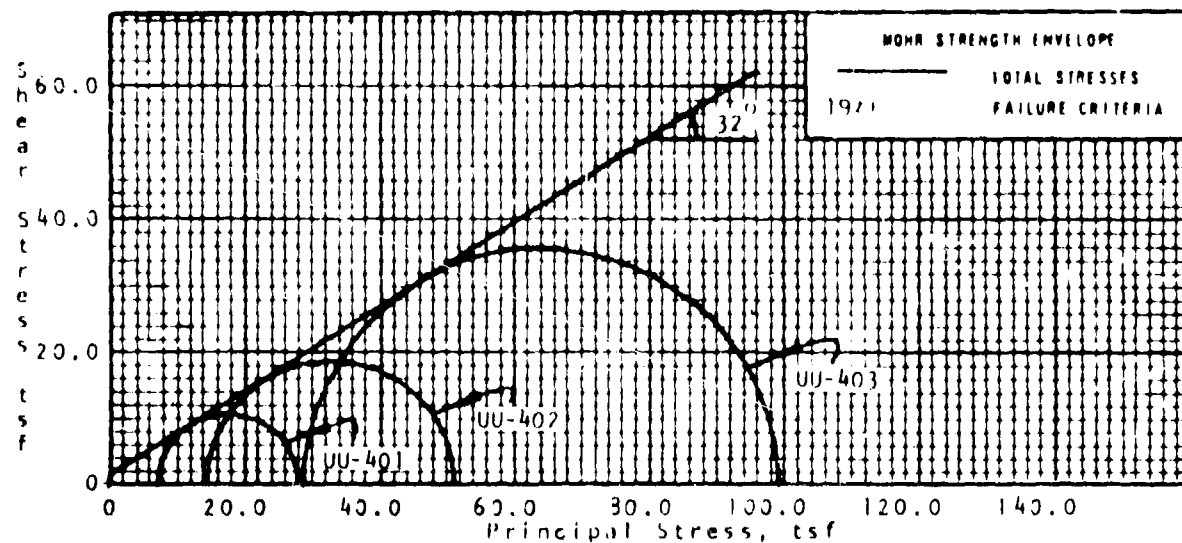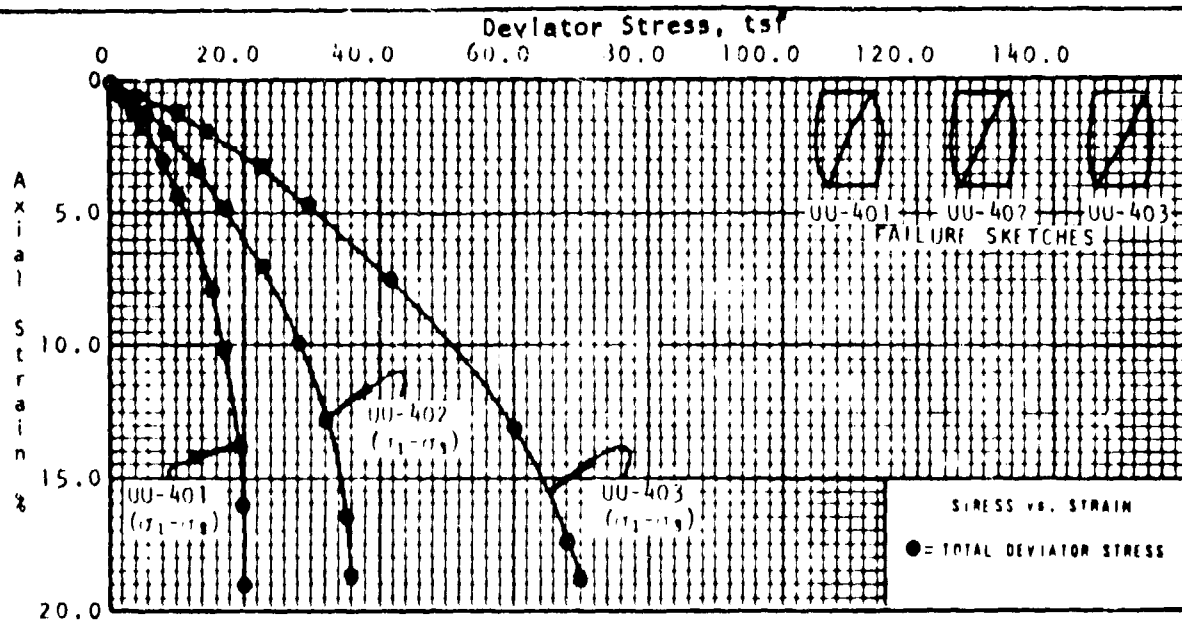
Test No.	UU-401	UU-402	UU-403
Confining Pressure, tsf	7.19	14.39	28.73
Ht., in.	6.89	6.89	6.85
Dia., in.	3.01	3.00	3.00
Ht./Dia. Ratio	2.28	2.29	2.28
Dry Unit Wt., pcf	92.0	93.4	92.3
Water Content, %			
Before Test	4.4	4.4	4.4
After Test	4.4	4.4	4.4
Avg. % Strain/Min.	.706	.721	.699

Compaction, %
Specimens Compacted
Strain Controlled Test

Dec. 1977   W-3306-01
Shannon & Wilson, Inc.
Geotechnical Consultants
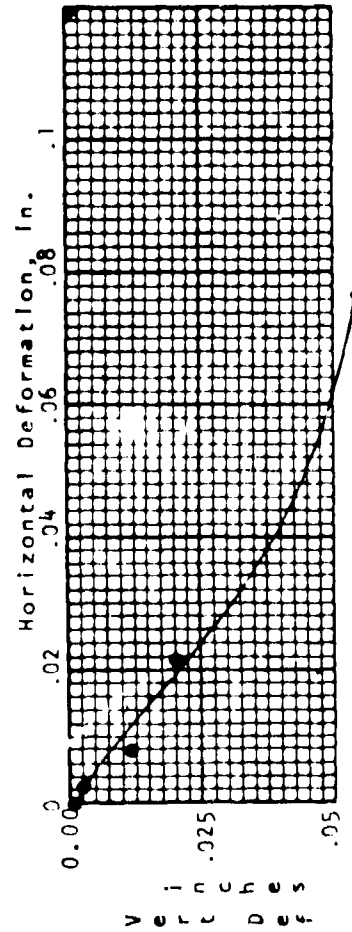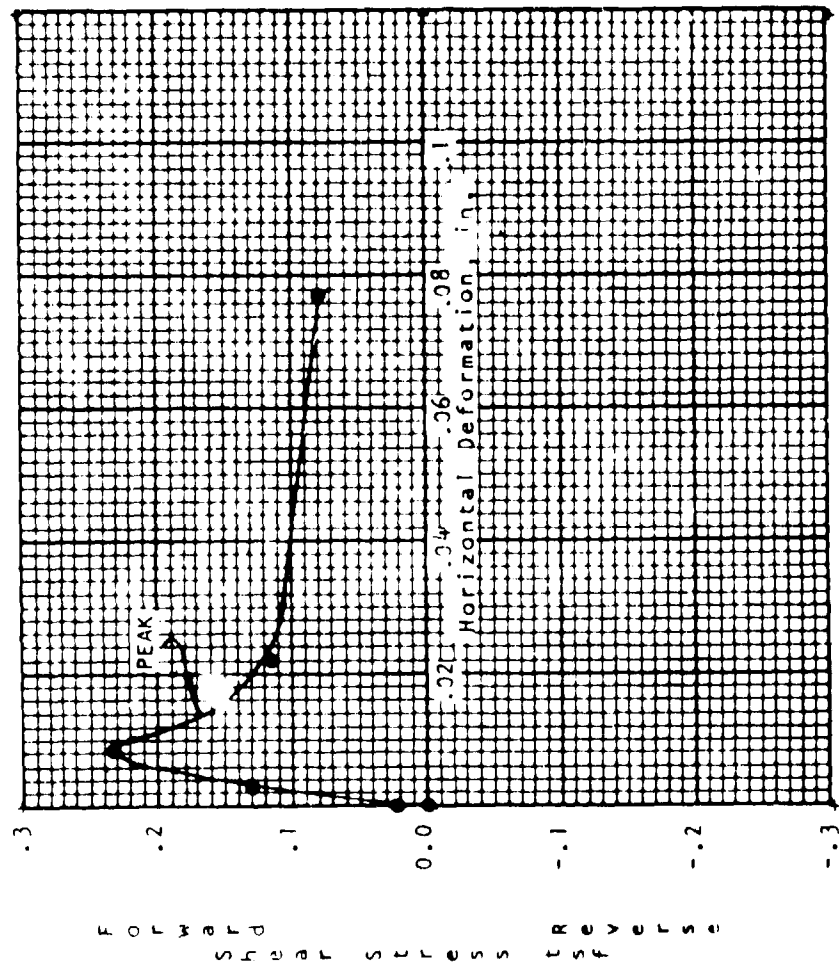
SPECIMEN DATA:
Height   1.75 in.
Length=Width   4.00 in.
Unit Wt., Dry   96.1 pcf
Water Content
  Before Test   7.2 %
  After Test   7.0 %
Degree of
  Saturation   --- %

CLASSIFICATION:
Light brown, sandy SILT.

TEST DATA:
Initial Normal
  Stress   .01 tsf
Rate of
  Strain   .004394 in./min
Specimen Compacted
Specimen At Nat WC

Fig. B16
KAFB Alluvium (7% moisture)

DIRECT SHEAR TEST DS-1
CENTRIFUGE CRATERING STUDY II

October 1978   W-3306-02
Shannon & Wilson, Inc.
Geotechnical Consultants

Fig. B17
KAFB Alluvium (7% moisture)

UNCONSOLIDATED, UNDRAINED,
TRIAXIAL COMPRESSION TEST

CENTRIFUGE CRATERING STUDY II

October 1978   W-3306-02

Shannon & Wilson, Inc.
Geotechnical Consultants
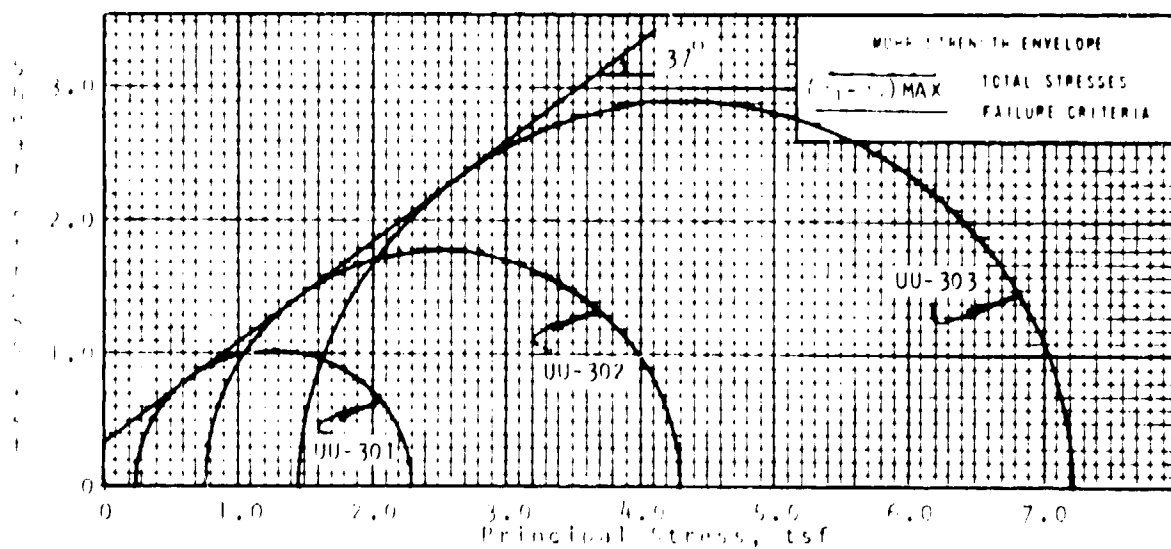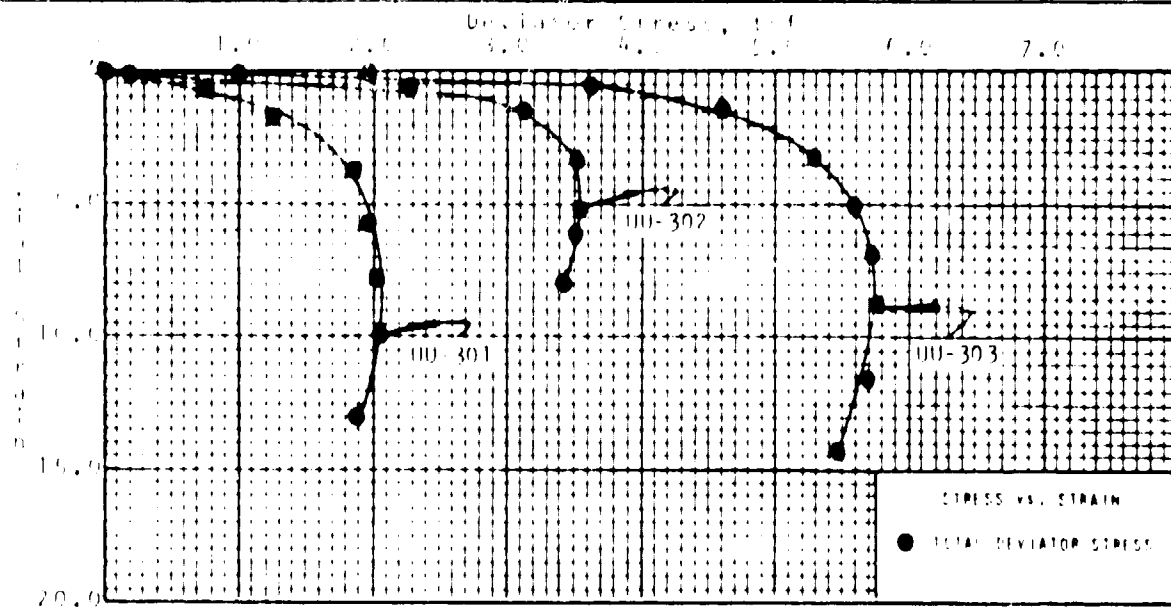
Test No.	UU-301	UU-302	UU-303
Confining Pressure, tsf	.22	.72	1.44
Ht., in.	4.93	5.00	5.00
Dia., in.	2.08	2.10	2.10
Ht./Dia. Ratio	2.37	2.38	2.38
Dry Unit Wt., pcf	96.3	95.2	96.4
Water Content,			
Before Test	7.2	7.2	7.2
After Test	7.2	7.2	7.2
Initial Saturation,	--	--	--
Avg. Strain/Min.	1.00%	.80%	.80%

Specimen - Compacted
Strain - Controlled Test
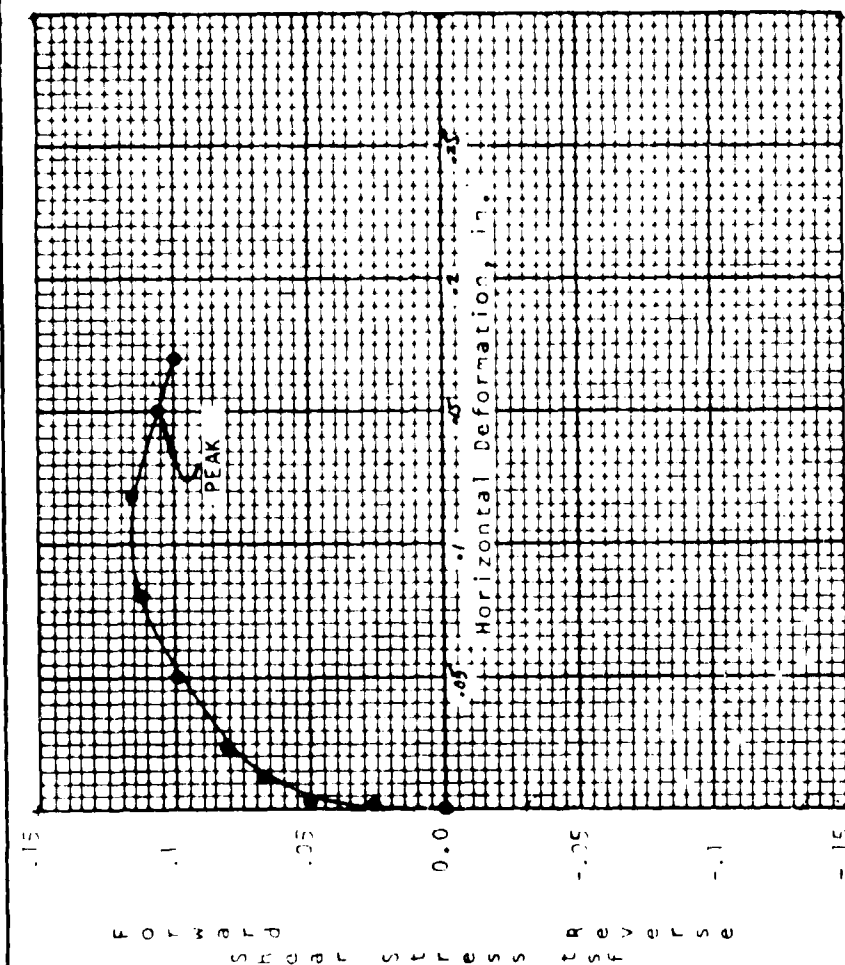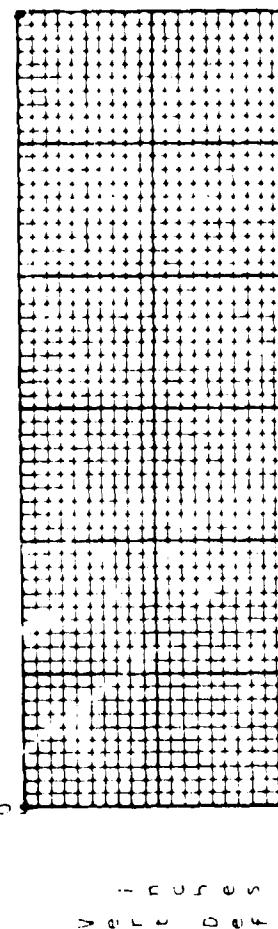
SPECIMEN DATA:
Height .... 1.75 in.
Length=Width .... 4.00 in.
Unit Wt., Wet .... 96.1 pcf
Water Content
  Before Test .... --
  After Test .... --
Degree of
  Saturation .... --

CLASSIFICATION:
Gray, oil-base CLAY.

TEST DATA:
Initial Normal
  Stress .... .01 tsf
Rate of
  Strain .... .000728 in./min
Specimen Compacted
Specimen At Nat WC

Fig. B18
"PERMOPLAST" Modeling clay

DIRECT SHEAR TEST DS-1
CENTRIFUGE CRATERING STUDY II

November 1979   W-3306-02

Shannon & Wilson, Inc.
Geotechnical Consultants

Horizontal Deformation, in.

Horizontal Deformation, in.

PEAK

Forward Shear Stress tr Reverse

Vertical Deformation, in.

Deviator Stress, tsf

STRESS vs. STRAIN
● = TOTAL DEVIATOR STRESS

UU-101
UU-102
UU-103

MOHR STRENGTH ENVELOPE
TOTAL STRESSES
FAILURE CRITERIA
$\left(\dfrac{\sigma_1 - \sigma_3}{2}\right)$ MAX

UU-101
UU-102
UU-103

Principal Stress, tsf

Test No.	UU-101	UU-102	UU-103
Confining Pressure, tsf	.22	.72	1.44
Ht., in.	4.99	4.99	4.98
Dia., in.	2.11	2.10	2.10
Ht./Dia. Ratio	2.36	2.37	2.37
Wet Unit Wt., pcf	95.1	96.4	96.3
Water Content, %			
Before Test	--	--	--
After Test	--	--	--
Degree of Saturation, %	--	--	--
Avg. % Strain/Min.	0.698	0.752	0.763
Compaction, %			
Specimens Compacted	--	--	--
Strain Controlled Test			

Fig. B19
"PERMOPLAST" Modeling clay

UNCONSOLIDATED, UNDRAINED,
TRIAXIAL COMPRESSION TEST
CENTRIFUGE CRATERING STUDY II

November 1978   W-3306-02
Shannon & Wilson, Inc.
Geotechnical Consultants

Fig. B20
"PERMOPLAST" Modeling clay

UNCONSOLIDATED, UNDRAINED,
TRIAXIAL COMPRESSION TEST
LARGE CONFINING PRESSURES

Test No.	UU-501	UU-502	UU-503
Confining Pressure, tsf	7.19	14.39	28.73
Ht., in.	4.51	4.63	4.93
Dia., in.	2.09	2.07	2.03
Ht./Dia. Ratio	2.15	2.23	2.39
Wet Unit Wt., pcf	91.4	93.5	92.5
Avg. % Strain/Min.	1.010	.947	.372

Specimens Undisturbed
Strain Controlled Test

Dec. 1977   W-3306-01
Shannon & Wilson, Inc.
Geotechnical Consultants

B23
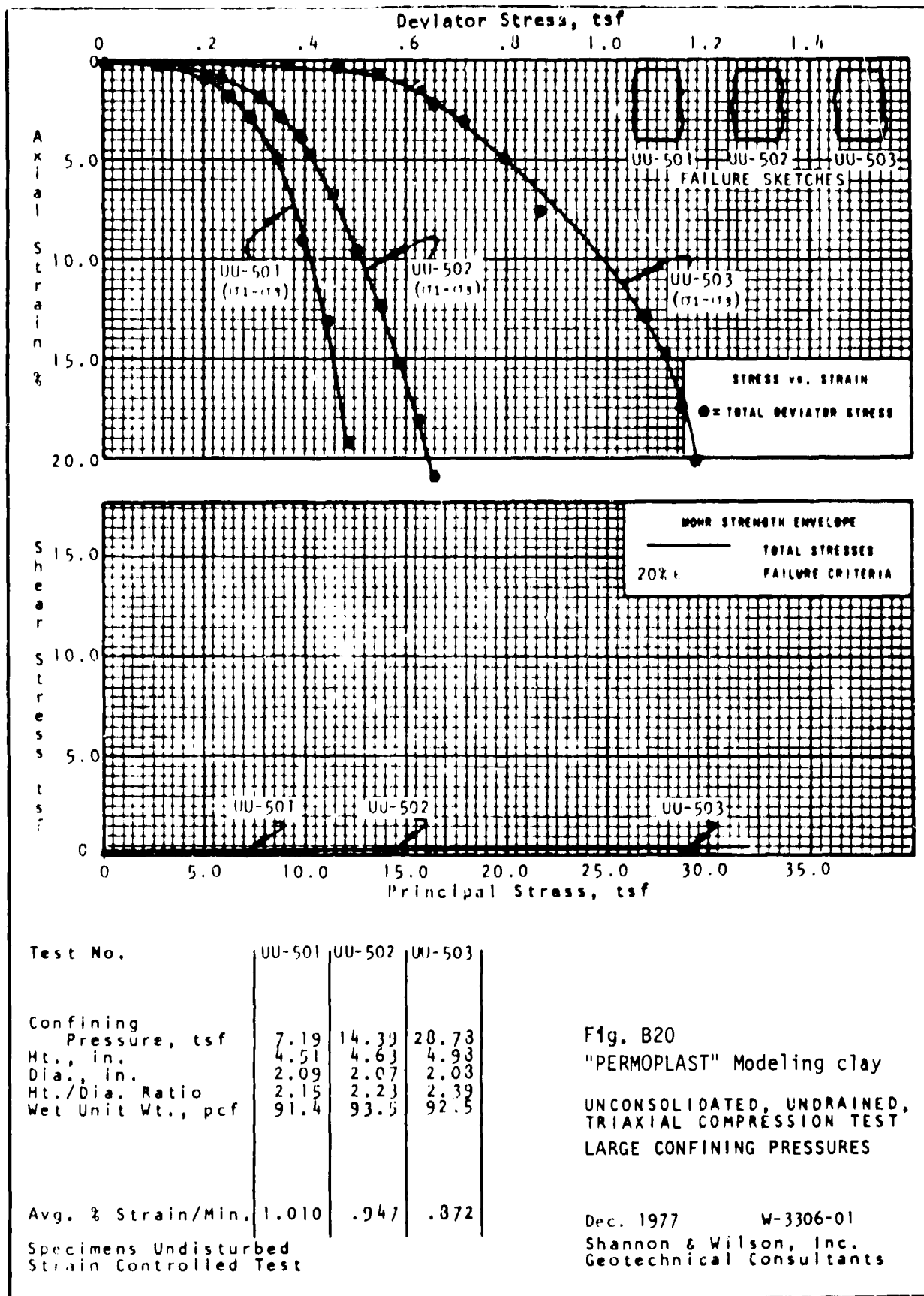
Blank

DISTRIBUTION LIST

DEPARTMENT OF DEFENSE

Assistant to the Secretary of Defense
Atomic Energy
    ATTN: Executive Assistant

Defense Intelligence Agency
    ATTN: DT-1C
    ATTN: DB-4C, E. O'Farrell
    ATTN: DT-2
    ATTN: DB-4N

Defense Nuclear Agency
    ATTN: STSP
3 cy ATTN: SPSS
4 cy ATTN: TITL

Defense Technical Information Center
12 cy ATTN: DD

Department of Defense Explo Safety Board
    ATTN: Chairman

Field Command
Defense Nuclear Agency
    ATTN: FCP
    ATTN: FCT
    ATTN: FCTK
    ATTN: FCTMOF

Field Command
Defense Nuclear Agency
Livermore Branch
    ATTN: FCPRL

Field Command Test Directorate
Defense Nuclear Agency
    ATTN: FCTC

Interservice Nuclear Weapons School
    ATTN: TTV

Joint Strat Tgt Planning Staff
    ATTN: JLA
    ATTN: NRI STINFO, Library

NATO School (SHAPE)
    ATTN: U.S. Documents Officer

Under Secretary of Defense for Rsch & Engrg
    ATTN: Strategic & Space Sys (OS)

DEPARTMENT OF THE ARMY

BMD Advanced Technology Center
Department of the Army
    ATTN: ICRDABH-X

Chief of Engineers
Department of the Army
    ATTN: DAEN-MCE-D
    ATTN: DAEN-RDL

Harry Diamond Laboratories
Department of the Army
    ATTN: DELHD-N-P
    ATTN: 00100 Commander/Tech Dir/TSO

DEPARTMENT OF THE ARMY (Continued)

U.S. Army Ballistic Research Labs
    ATTN: DRDAR-BLT, J. Keefer
    ATTN: DRDAR-BLT, W. Taylor
    ATTN: DRDAR-TSB-S
    ATTN: DRDAR-BLV

U.S. Army Concepts Analysis Agency
    ATTN: CSSA-ADL

U.S. Army Engineer Center
    ATTN: DT-LRC

U.S. Army Engineer Div, Huntsville
    ATTN: HNDED-SR

U.S. Army Engineer Div, Ohio River
    ATTN: ORDAS-L

U.S. Army Engr Waterways Exper Station
    ATTN: WESSE, L. Ingram
    ATTN: WESSD, J. Jackson
    ATTN: J. Strange
    ATTN: Library
    ATTN: WESSA, W. Flathau
    ATTN: L. Davis

U.S. Army M'erial & Mechanics Rsch Ctr
    ATTN: Technical Library

U.S. Army Materiel Dev & Readiness Cmd
    ATTN: DRXAM-TL

U.S. Army Missile Command
    ATTN: RSIC

U.S. Army Mobility Equip R&D Cmd
    ATTN: DRDME-WC

U.S. Army Nuclear & Chemical Agency
    ATTN: Library

XVIII Airborne Corps
Department of the Army
    ATTN: F. Ford

DEPARTMENT OF THE NAVY

David Taylor Naval Ship R&D Ctr
    ATTN: Code 1844
    ATTN: Code 17
    ATTN: Code L42-3
2 cy ATTN: Code 1740.5, B. Whang

Naval Civil Engineering Laboratory
    ATTN: L51, R. Murtha
    ATTN: Code L51, J. Crawford
    ATTN: Code L08A

Naval Electronic Systems Command
    ATTN: PME 117-21

Naval Facilities Engineering Command
    ATTN: Code 04B

Naval Material Command
    ATTN: MAT 08T-22

DEPARTMENT OF THE NAVY (Continued)

Naval Postgraduate School
    ATTN: Code 1424, Library

Naval Research Laboratory
    ATTN: Code 8440, G. O'Hara
    ATTN: Code 2627

Naval Sea Systems Command
    ATTN: SEA-09G53
    ATTN: SEA-0322
    ATTN: SEA-0351

Naval Surface Weapons Center
    ATTN: Code R14
    ATTN: Code F31
    ATTN: Code R14, I. Blatstein

Naval Surface Weapons Center
    ATTN: Tech Library & Info Svcs Br

Naval War College
    ATTN: Code E-11 (Tech Service)

Naval Weapons Evaluation Facility
    ATTN: Code 10

Office of Naval Research
    ATTN: Code 474, N. Perrone

Office of the Chief of Naval Operations
    ATTN: OP 981
    ATTN: OP 03EG

Strategic Systems Project Office
Department of the Navy
    ATTN: NSP-272
    ATTN: NSP-43

DEPARTMENT OF THE AIR FORCE

Air Force Geophysics Laboratory
    ATTN: LWW, K. Thompson

Air Force Institute of Technology
    ATTN: Library

Air Force Systems Command
    ATTN: DLW

Air Force Weapons Laboratory
Air Force Systems Command
    ATTN: NTE
    ATTN: SUL
    ATTN: NTE, M. Plamondon
    ATTN: NTED-C
    ATTN: NTES-C, R. Henny
    ATTN: DEX

Air University Library
Department of the Air Force
    ATTN: AUL-LSE

Assistant Chief of Staff
Intelligence
Department of the Air Force
    ATTN: INT

DEPARTMENT OF THE AIR FORCE (Continued)

Ballistic Missile Office
Air Force Systems Command
    ATTN: MMH
    ATTN: SYDT

Deputy Chief of Staff
Research, Development, & Acq
Department of the Air Force
    ATTN: AFRDQI

Deputy Chief of Staff
Logistics & Engineering
Department of the Air Force
    ATTN: LEEE

Foreign Technology Division
Air Force Systems Command
    ATTN: NIIS, Library

Rome Air Development Center
Air Force Systems Command
    ATTN: TSLD

Strategic Air Command
Department of the Air Force
    ATTN: NRI STINFO, Library

VELA Seismological Center
Department of the Air Force
    ATTN: G. Ullrich

DEPARTMENT OF ENERGY

Department of Energy
Albuquerque Operations Office
    ATTN: CTID

Department of Energy
    ATTN: OMA/RD&T

Department of Energy
Nevada Operations Office
    ATTN: Mail & Records for Technical Library

Lovelace Biomed & Env Rsch Inst, Inc
    ATTN: D. Richmond

OTHER GOVERNMENT AGENCIES

Central Intelligence Agency
    ATTN: OSWR/NED

Department of the Interior
Bureau of Mines
    ATTN: Tech Lib

Department of the Interior
U.S. Geological Survey
    ATTN: D. Roddy

Federal Emergency Management Agency
National Sec Ofc Mitigation & Rsch
    ATTN: Assistant Associated Dir

DEPARTMENT OF ENERGY CONTRACTORS

Lawrence Livermore National Lab
 ATTN: W. Crowley
 ATTN: Technical Info Dept, Library
 ATTN: L-10, H. Kruger

Los Alamos National Laboratory
 ATTN: M. Henderson
 ATTN: MS 670, J. Hopkins
 ATTN: MS362, Librariar
 ATTN: R. Bridwell
 ATTN: G. Spillman
 ATTN: MS 364 (Class Reports Lib)

Oak Ridge National Laboratory
 ATTN: Central Rsch Library
 ATTN: Civil Def Res Proj

Sandia National Laboratories
Livermore Laboratory
 ATTN: Library & Security Classification Div

Sandia National Laboratories
 ATTN: A. Chabia
 ATTN: 3141
 ATTN: R. Schmidt 5732
 ATTN: T. Bergstresser 5533
 ATTN: H. Sutherland 4732

DEPARTMENT OF DEFENSE CONTRACTORS

Aerospace Corp
 ATTN: Technical Information Services

Agbabian Associates
 ATTN: M. Agbabian

Applied Research Associates, Inc
 ATTN: J. Bratton
 ATTN: N. Higgins

Applied Theory, Inc
 2 cy ATTN: J. Trulio

AVCO Research & Systems Group
 ATTN: Library A830

University of Arizona
 ATTN: W. McKinnon

University of Arizona State
 ATTN: R. Greeley
 ATTN: J. Fink

BDM Corp
 ATTN: Corporate Library
 ATTN: T. Neighbors

Boeing Co
 ATTN: Aerospace Library

Boeing Co
 4 cy ATTN: K. Holsapple
 20 cy ATTN: R. Schmidt

California Institute of Technology
 ATTN: T. Ahrens

DEPARTMENT OF DEFENSE CONTRACTORS (Continued)

California Research & Technology, Inc
 ATTN: Library
 ATTN: K. Kreyenhagen
 ATTN: S. Schuster
 ATTN: M. Rosenblatt

University of California
 ATTN: J. Cheney

California Research & Technology, Inc
 ATTN: D. Orphal

Calspan Corp
 ATTN: Library

University of Denver
 ATTN: J. Wisotski

EG&G Wash. Analytical Svcs Ctr, Inc
 ATTN: Library

Electromech Sys of New Mexico, Inc
 ATTN: L. Piper

Electromech Sys of New Mexico, Inc
 ATTN: R. Shunk

Eric H. Wang
Civil Engineering Rsch Fac
University of New Mexico
 ATTN: N. Baum

Gard, Inc
 ATTN: G. Neidhardt

Geocenters, Inc
 ATTN: E. Marram

H-Tech Labs, Inc
 ATTN: B. Hartenbaum

Horizons Technology, Inc
 ATTN: R. Kruger

IIT Research Institute
 ATTN: Documents Library

Institute for Defense Analyses
 ATTN: Classified Library

JAYCOR
 ATTN: H. Linnerud

Kaman AviDyne
 ATTN: Library

Kaman Sciences Corp
 ATTN: Library

Kaman Tempo
 ATTN: DASIAC

Lockheed Missiles & Space Co, Inc
 ATTN: Technical Information Center
 ATTN: T. Geers
 ATTN: Technical Library

DEPARTMENT OF DEFENSE CONTRACTORS (Continued)

Lockheed Missiles & Space Co, Inc
    ATTN: TIC-Library

Martin Marietta Corp
    ATTN: G. Freyer

Lunar and Planetary Institute
    ATTN: P. Schultz

McDonnell Douglas Corp
    ATTN: R. Halprin

Merritt CASES, Inc
    ATTN: Library
    ATTN: J. Merritt

University of New Mexico
    ATTN: CERF, G. Leigh
    ATTN: CERF, N. Baum

Pacific-Sierra Research Corp
    ATTN: H. Brode

Pacifica Technology
    ATTN: G. Kent
    ATTN: Tech Library

Patel Enterprises, Inc
    ATTN: M. Patel

Physics Applications, Inc
    ATTN: F. Ford

Physics International Co
    ATTN: J. Thomsen
    ATTN: F. Sauer
    ATTN: Technical Library
    ATTN: L. Behrmann
    ATTN: E. Moore

R & D Associates
    ATTN: J. Lewis
    ATTN: Technical Information Center
    ATTN: R. Port
    ATTN: J. Carpenter
    ATTN: W. Wright
    ATTN: P. Haas

Science Applications, Inc
    ATTN: J. Dishon

Science Applications, Inc
    ATTN: Technical Library
    ATTN: H. Wilson

Science Applications, Inc
    ATTN: D. Bernstein
    ATTN: D. Maxwell

DEPARTMENT OF DEFENSE CONTRACTORS (Continued)

Science Applications, Inc
    ATTN: W. Layson
    ATTN: J. Cockayne
    ATTN: M. Knasel

Southwest Research Institute
    ATTN: A. Wenzel
    ATTN: W. Baker

Science & Engineering Associates, Inc
    ATTN: J. Stockton

SRI International
    ATTN: B. Gasten
    ATTN: G. Abrahamson

Systems, Science & Software, Inc
    ATTN: T. Riney
    ATTN: D. Grine
    ATTN: T. Cherry
    ATTN: K. Pyatt
    ATTN: R. Lafrenz
    ATTN: Library

Terra Tek, Inc
    ATTN: Library
    ATTN: S. Green

Tetra Tech, Inc
    ATTN: L. Hwang

TRW Defense & Space Sys Group
    ATTN: Technical Information Center
    ATTN: I. Alber
    ATTN: R. Plebuch
    ATTN: D. Baer
    ATTN: J. O'Keefe
2 cy ATTN: N. Lipner

TRW Defense & Space Sys Group
    ATTN: E. Wong
    ATTN: P. Dai

Universal Analytics, Inc
    ATTN: E. Field

Weidlinger Assoc, Consulting Engrg
    ATTN: J. Wright
    ATTN: M. Baron

Weidlinger Assoc, Consulting Engrg
    ATTN: J. Isenberg

Weidlinger Assoc, Consulting Engrg
    ATTN: A. Misovec